Simulating Weak Gravitational Lensing for Cosmology

by

Alina Kiessling

A Dissertation
Presented in fulfillment of the requirements
for the degree of
Doctor of Philosophy (Astrophysics)
at The University of Edinburgh

31st March 2011

Abstract

This thesis will present a new cosmic shear analysis pipeline SUNGLASS (Simulated UNiverses for Gravitational Lensing Analysis and Shear Surveys). SUNGLASS is a pipeline that rapidly generates simulated universes for weak lensing and cosmic shear analysis. The pipeline forms suites of cosmological N-body simulations and performs tomographic cosmic shear analysis using a novel line-of-sight integration through the simulations while saving the particle lightcone information. Galaxy shear and convergence catalogues with realistic 3-D galaxy redshift distributions are produced for the purposes of testing weak lensing analysis techniques and generating covariance matrices for data analysis and cosmological parameter estimation. This thesis presents a suite of fast medium-resolution simulations with shear and convergence maps for a generic 100 square degree survey out to a redshift of $z = 1.5$, with angular power spectra agreeing with the theoretical expectations to better than a few percent accuracy up to $\ell = 10^3$ for all source redshifts up to $z = 1.5$ and wavenumbers up to $\ell = 2000$ for source redshifts $z \geq 1.1$. A two-parameter Gaussian likelihood analysis of Ω_m and σ_8 is also performed on the suite of simulations for a 2-D weak lensing survey, demonstrating that the cosmological parameters are recovered from the simulations and the covariance matrices are stable for data analysis, with negligible bias.

An investigation into the accuracy of traditional Fisher matrix calculations is presented. Fisher Information Matrix methods are commonly used in cosmology to estimate the accuracy that cosmological parameters can be measured with a given experiment, and to optimise the design of experiments. However, the standard approach usually assumes both data and parameter estimates are Gaussian-distributed. Further, for survey forecasts and optimisation it is usually assumed the power-spectra covariance matrix is diagonal in Fourier-space. But in the low-redshift Universe, non-linear mode-coupling will tend to correlate small-scale power, moving informa-

tion from lower to higher-order moments of the field. This movement of information will change the predictions of cosmological parameter accuracy. In this thesis, the loss of information is quantified by comparing naïve Gaussian Fisher matrix forecasts with a Maximum Likelihood parameter estimation analysis of the suite of mock weak lensing catalogues derived from the SUNGLASS pipeline, for 2-D and tomographic shear analyses of a Euclid-like survey. In both cases the 68% confidence area of the $\Omega_m - \sigma_8$ plane is found to increase by a factor 5. However, the marginal errors increase by just 20 to 40%. A new method is proposed to model the effects of non-linear shear-power mode-coupling in the Fisher Matrix by approximating the shear-power distribution as a multivariate Gaussian with a covariance matrix derived from the mock weak lensing survey. The findings in this thesis show that this approximation can reproduce the 68% confidence regions of the full Maximum Likelihood analysis in the $\Omega_m - \sigma_8$ plane to high accuracy for both 2-D and tomographic weak lensing surveys. Finally, three multi-parameter analyses of $(\Omega_m,\ \sigma_8,\ n_s)$, $(\Omega_m,\ \sigma_8,\ n_s,\ \Omega_\Lambda)$ and $(\Omega_m,\ \sigma_8,\ h,\ n_s,\ w_0,\ w_a)$ are performed to compare the Gaussian and non-linear mode-coupled Fisher matrix contours. The multi-parameter volumes of the 1σ error contours for the six-parameter non-linear Fisher analysis are consistently larger than for the Gaussian case, and the shape of the 68% confidence volume is modified. These results strongly suggest that future Fisher Matrix estimates of cosmological parameter accuracies should include mode-coupling effects.

Acknowledgments

It is a real pleasure for me to be able to thank the people who helped make this thesis possible. First and foremost, I want to thank my supervisors Andy Taylor and Alan Heavens. Without your supervision, completing this PhD would not have been possible. I am so very lucky to have had the opportunity to learn from you both and I am so grateful for your patience and support. I hope that we will continue to work together in future and look forward to working on new and exciting projects with both of you.

I would also like to thank the Marie Curie Research Training Network Dark Universe with Extragalactic Lensing (DUEL) for supporting me with a fellowship throughout my PhD. Being a member of this network allowed me to interact with lensing experts from all over the world and provided me with opportunities that I otherwise would not have been able to pursue.

I would very much like to thank my thesis examiners David Bacon and Philip Best for what was actually a very enjoyable viva with lively discussion and many interesting questions and suggestions. I never expected to enjoy the viva, but the two of you ensured that I was relaxed throughout and made certain that the event that I had been dreading was in fact an incredibly positive experience.

I owe a huge thanks to Marc Duldig and the council of the Astronomical Society of Australia from 2005-2007. Marc, I can't thank you enough for your mentoring and counsel when I needed it the most. I truly admire your generosity and wisdom and hope that one day, I too can inspire people the way that you inspire me. To the ASA council, I want to thank you for your unwavering support while I was the student representative from 2005-2007. Each one of you encouraged me and provided friendship and I will always be grateful for my time as a part of the council.

To Richard Massey and Tom Kitching who have acted as mentors to me here in Edinburgh, I owe many thanks. I am very grateful for the time that you have both spent giving me advice about progressing my career, getting me involved in collaborations and the help that you have given me in my research.

Next, a very heartfelt thanks to Eric Tittley, Jonathan Dearden, John Barrow and

Declaration

This thesis contains no material that has been accepted for the award of any other degree or diploma. To the best of my knowledge, this thesis contains no material previously published or written by another author, except where due reference is made in the text of the thesis. All work presented is primarily that of the author.

Parts of this thesis have been accepted for publication in refereed scientific journals.

Chapter 5 is based on work presented in the paper:

SUNGLASS: A New Weak Lensing Simulation Pipeline
A. Kiessling, A. F. Heavens, A. N. Taylor, B. Joachimi, 2011, *MNRAS*, 414, 2235

Chapter 6 is based on work presented in the paper:

Simulating the Effect of Non-Linear Mode-Coupling in Cosmological Parameter Estimation
A. Kiessling, A. N. Taylor, A. F. Heavens, 2011, *MNRAS, accepted*, arXiv:1103.3245

Minor alterations have been made to these studies in order to maintain consistency of style.

Alina Kiessling

31st Mar 2011

Contents

List of Figures

List of Tables

'Can you imagine what I would do if I could do all I can?'

Sun Tzu
The Art of War, 6th century BC

Chapter 1

Background

The Universe is filled with galaxies, enormous collections of gas, dust and billions of stars all held together by gravity. These giant objects delineate the large scale structure of the Universe. Galaxies group together in clusters (eg Zwicky, 1938; Zwicky et al., 1961). Many galaxy clusters appear to be fairly static and relatively uniform, the dynamics of which are described by the virial theorem[1] (eg Abell, 1965; Peebles, 1970; White, 1976).

Although stars and galaxies dominate the night sky, the standard model of cosmology tells us that all of the baryons in the Universe comprise just 4% of the total matter density. The remaining matter density is made from dark 'stuff' that we still know very little about, approximately 23% is dark matter and 73% is dark energy[2]. There are also many other cosmological parameters that can be used to describe the Universe. I have developed a set of tools, based on the bending of light, that will help to understand the dark Universe and the cosmological parameters that govern it and this thesis will explore these.

A key prediction of Einstein's General Theory of Relativity is that a massive object curves space-time in its vicinity. A result of this curvature is that light will deflect around a massive object (the 'lens'), producing effects such as changing the brightness, shape or even the number of images of a background source. Thus, light traveling through the Universe is deflected by mass distributions such as galaxies and clusters of galaxies, causing distortions and magnifications to the image. This

---

[1]See Section 2.7.1 for further explanation of the virial theorem
[2]See Chapter 2 for more information on dark matter and dark energy

effect is known as gravitational lensing. Gravitational lensing offers a method for probing the mass distribution of the Universe, without any dependence on luminous tracers or physical assumptions such as hydrostatic equilibrium and virialisation. This makes it an ideal tool for measuring the total mass (dark and luminous) and mass distribution of galaxy clusters and other astronomical objects.

Gravitational lensing can be defined in two main categories; Multiple images, microlensing and arcs in clusters are all a result of *strong gravitational lensing*, which occurs when the surface mass density of the lensing object, convergence $\kappa \geq 1$, and for when light from a distant object travels very close to the lensing mass, within the Einstein ring[3]. In the *weak gravitational lensing* regime the distortions and magnifications are very weak with just $\sim 1\%$ shape changes. This occurs when the surface mass density is small and for a point-like lens when light from a source travels well outside the Einstein ring. These effects must be identified statistically, not by looking at individual sources. While strong lensing can only be detected near the centres of very dense mass concentrations, weak lensing can be detected in all of the Universe.

The idea that gravitational lensing should occur in the Universe, and the equations describing the phenomenon, are not new. However, observations of lensing are still reasonably recent. The following section will give a historical background to the field of gravitational lensing to show the origins of the field and the rapid progress that has been made in the last three decades.

1.1   History

As early as 1704, Newton suggested that the gravitational field of a massive object could possibly bend light rays, considering that light may be composed of elementary particles. Around 100 years later, Soldner found that within Newtonian mechanics, a light ray passing near the limb of the Sun should undergo an angular deflection. Unfortunately, the wave description of light was popular during the 18th and 19th centuries and neither Newton nor Soldner's results were ever taken seriously.

---

[3]See Chapter 3 for definitions of shear, convergence and the Einstein ring

Using his theory of general relativity, Einstein predicted that a massive object would curve the space-time in its vicinity. The result of this curvature is that free particles, massive or not (i.e. photons), will move along the geodesics of this curved space. In 1915, using the full equations of General Relativity, Einstein obtained a value twice the Newtonian value for the deflection angle of light as it passed the Sun.

Measurements of the solar field were taken during the solar eclipse immediately following World War I in May 1919 and again six months later. Using the results of these measurements, Eddington confirmed the deflection angle predicted by Einstein with errors of around 30%. With the development of very precise radio interferometric observations of quasars, the Einstein deflection angle has now been verified to within 1% (Fomalont & Sramek, 1975, 1976; Robertson et al., 1991).

In the mid-1920's, the hypothesis was made that if a background and foreground star were perfectly aligned with an observer, a ring-shaped image of the background star, centered on the foreground star, would result (Chwolson, 1924). While these ring phenomena should be known as 'Chwolson rings', they are usually called 'Einstein rings', even though Einstein believed that there was no great chance of observing them (Einstein, 1936).

Another major step forward in the understanding of gravitational lensing came when it was demonstrated that gravitational lensing does not change the surface brightness of the source (Etherington, 1933). Thus, it follows that the amplification of a source is equal to the magnification ratio of its image size to the original source size.

An advocate of the discovery of cosmological gravitational lenses was Fritz Zwicky, who believed that the probability of detecting lensing is very high. He was the first person to propose the use of galaxies, rather than stars, as gravitational lenses (Zwicky, 1937a,b). He also emphasised the possibility of determining the mass of distant galaxies using gravitational lensing, using lensing to test general relativity and finally, using the magnification effects of lensing to view galaxies further away than ordinary telescopes would usually see. A statement was made by Zwicky (1937b) that 'the probability that galactic nebulae which act as gravitational lenses will be found becomes practically a certainty'. It is therefore no surprise that he was puzzled that lenses had still not been observed some 20 years later (Zwicky, 1957).

Gravitational lensing went out of fashion for a couple of decades after Zwicky's ideas of using galaxies as lenses. A revival in interest came with several independent publications (Klimov, 1963; Liebes, 1964; Zel'dovich, 1964; Refsdal, 1964a,b, 1966a,b). With the discovery of quasars (Schmidt, 1963), some of the proposed applications proved to be extremely promising. It would now be much easier to prove the lensing origin of these point-like objects with their prominent spectral features, high redshift and high luminosity, rather than extended, diffuse galaxies.

Theoretical work slowly progressed throughout the 1970s until the momentous observational detection of the first cosmological gravitational lens by Walsh et al. (1979). This discovery of a distant quasar (0957+561), multiply-imaged by a foreground massive lensing galaxy, prompted huge interest in the field of gravitational lensing. The range of publications on the subject increased significantly numbering in the hundreds per year (see the bibliography of Pospieszalska-Surdej et al., 2001, for an almost complete list of lensing publications up to 2001).

The next significant discovery came less than ten years later with the discovery of narrow arc-like shapes of enormous length, located in clusters of galaxies with a curvature toward the apparent centre of gravity of the cluster (Fort et al., 1988). These arcs are now known to be the highly distorted images of high-redshift galaxies, seen through a massive foreground cluster of galaxies. After this discovery, theory developed to suggest that further away from the lens, there should be many more galaxy images with much less distortion. This distortion is so small that it can only be detected by averaging over many such images. This hypothesis was confirmed when Tyson et al. (1990) reported statistical distortion effects in two clusters.

Following this discovery Kaiser & Squires (1993) showed how to reconstruct the projected mass distribution in clusters from the measurements of distorted shapes of galaxies. This technique was used recently in the reconstruction of mass around merging cluster 1E0657-558 (shown in Figure 1.1), commonly known as the Bullet Cluster, by Clowe et al. (2006). Importantly, this study showed that there was a displacement between the baryonic matter and the gravitational potentials. For the weak lensing peaks to be located in these offset positions requires a large unseen concentration of matter at these points, that is also far more massive than the vis-
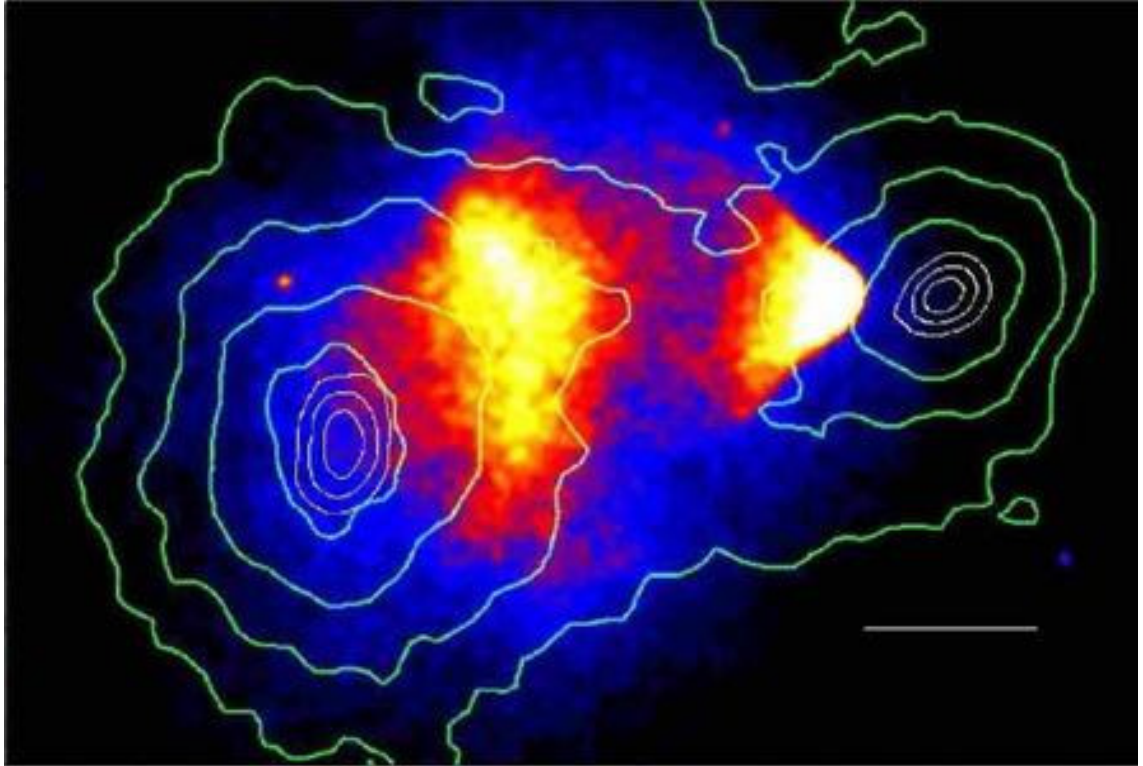
Figure 1.1: X-ray Chandra image of the merging cluster IE0657-558 (the Bullet Cluster). The hot gas as detected by Chandra is shown in the background and the green contours overlaid represent the weak lensing mass reconstruction of the merging clusters. The image clearly shows a displacement of the hot gas from the center of the gravitational potentials of the clusters providing good empirical evidence for the existence of Dark Matter.

Image Credit: Clowe et al. (2006)

ible gas. This requirement is compelling evidence for the existence of dark matter, which provides the simplest solution to this offset.

During this time of increasing interest in gravitational lensing, it was realised that light traveling through an inhomogeneous universe would be deflected due to the gravitational fields produced by large scale structure (LSS, Gunn, 1967a). This fact meant that it would be very difficult to determine the true position of a distant source with any accuracy. The equations that describe the changes in the cross-sections and shapes of ray bundles had already been determined in relation to the propagation of gravitational waves through an inhomogeneous universe (Sachs, 1961). These equations were further applied to show the statistical effects of local inhomogeneities on the propagation of light through the Universe (Zel'dovich, 1964;

Dashevskii & Zel'dovich, 1965; Dashevskii & Slysh, 1966; Gunn, 1967b). These phenomena were later realised to reflect the statistical properties of the LSS and recognised as a unique way of studying the properties of the dark matter distribution of the Universe (Blandford et al., 1991; Miralda-Escude, 1991; Kaiser, 1992). Even though the theory for lensing by LSS had been in place for many years, it wasn't until the year 2000 that 'cosmic shear' was observed by four independent groups (Kaiser et al., 2000; Wittman et al., 2000; Van Waerbeke et al., 2000; Bacon et al., 2000). Today, we regularly measure the cosmic shear signal (e.g. Bacon et al., 2003; Hoekstra et al., 2006; Hetterscheidt et al., 2007; Massey et al., 2007; Huff et al., 2010) and have been using the information derived from weak lensing cosmic shear analysis to further our understanding of the Universe (e.g. Daniel & Linder, 2010; Jarosik et al., 2011; Semboloni et al., 2011).

For overviews of gravitational lensing and its history see Schneider et al. (1992); Blandford & Narayan (1992); Refsdal & Surdej (1994); Narayan & Bartelmann (1997); Mellier (1999); Bartelmann & Schneider (2001); Refregier (2003b); Schneider (2006); Munshi et al. (2008); Massey et al. (2010) and references therein.

1.2   Thesis Outline

The technology required to undertake weak lensing studies observationally is continually being improved (e.g. wide-field cameras and many-object redshift surveys). Ground- and space-based telescopes are becoming increasingly more sensitive. The development of next generation telescopes such as the Panoramic Survey Telescope and Rapid Response System (Pan-STARRS) and the space-based telescope Euclid, will provide a tremendous step toward more accurate studies of weak lensing signatures and better constraints on cosmological parameters. Our understanding and interpretation of the observational data is limited by the robustness of the underlying theories and our ability to model the systematics and errors that plague the data. In order to address these issues, simulations are required to provide mock weak lensing data. These will model not only systematics and errors but can also help interpreting data, predicting errors on future surveys and testing new analysis techniques. Over the course of this PhD I have written and tested a weak lensing simulation pipeline for future weak lensing studies. This thesis will detail all aspects

of this pipeline and also show how it can be used to predict errors on parameters for future telescope surveys.

The outline of this thesis is as follows; Chapter 2 introduces the basic scientific concepts involved in the study of cosmology. Chapter 3 builds on the cosmological framework to detail the weak lensing formalisms. Chapter 4 gives a technical introduction to cosmological N-body simulations and gives a brief overview of how simulations can be utilised to better interpret current weak lensing telescope surveys and prepare for future missions. Chapter 5 presents the SUNGLASS, Simulated UNiverses for Gravitational Lensing Analysis and Shear Surveys, pipeline and details the extensive testing that the pipeline has undergone to ensure both its accuracy and reliability. This chapter also illustrates how the mock galaxy shear catalogues produced with SUNGLASS have been used to perform parameter estimates using a maximum likelihood analysis in the $\Omega_m - \sigma_8$ plane with 2-D binning. Chapter 6 demonstrates cosmological multi-parameter error estimates of the mock catalogues using a Fisher matrix analysis and tests the effect of using a non-Gaussian covariance matrix generated with these simulated catalogues against a Fisher matrix analysis using a Gaussian covariance matrix. Chapter 7 summarises the important results presented in this thesis and discusses where the development of this work is going and how I plan on improving and extending the pipeline over the next several years. Appendix A shows a derivation of the lensing deflection angle $\hat{\boldsymbol{\alpha}}$ for a point mass and Appendix B gives detailed instructions on how to install the GADGET2 simulation package with all the relevant libraries. Finally, Appendix C lists the publications that have resulted from work in this thesis to date.

Chapter 2

Introduction to Cosmology

2.1 Introduction

The workings of the large-scale Universe are described by cosmology. The groundwork for modern cosmological theory was first given in the General Theory of Relativity (Einstein, 1916) – which is fundamental to our understanding of gravity, the only known force that acts on cosmological length scales. In the last few decades, analysis of huge surveys of the large-scale structure of the Universe and the cosmic microwave background have shown agreement, to remarkable precision, with many predictions from cosmological theory. Now, almost 100 years after Einstein's first descriptions of gravity, cosmology remains one of the fundamental areas of research into our understanding of the Universe. The work in this thesis is directed toward furthering our comprehension.

Cosmology is a vast subject so the introduction that follows in this chapter has a necessary bias toward the work undertaken in this thesis. First, the fundamentals of cosmology are introduced with the Standard Model of Cosmology and the Robertson-Walker metric. Then the dynamics of the Universe will be discussed along with an introduction to cosmological observables. The significant epochs of the early Universe are examined and a discussion on the matter dominated Universe and the Dark Universe follows. Finally a review of the current best estimates for the cosmological parameters completes the chapter, summarising the state of the Standard Model of Cosmology as we understand it today.

2.2   The Standard Model of Cosmology

Observational data today has led to an almost universal consensus among cosmologists for the 'Standard Cosmological Model'. This model states that the Universe is spatially flat and around 13.7 billion years old. It is principally composed of photons, neutrinos, electrons, baryons, dark matter and dark energy and is expanding at an accelerating rate.

The very early Universe was an incredibly hot and dense plasma. In the first 10^{-34} seconds (or thereabouts), the Universe underwent a brief period of extremely fast expansion, known as inflation, resulting in the homogeneity and isotropy that we see today (Linde, 1982). Quantum mechanical fluctuations present during the inflationary process were imprinted on the Universe as density perturbations, as observed in the temperature fluctuations of the Cosmic Microwave Background (CMB). After inflation switched off, the Universe consisted of plasma and elementary particles and it continued to expand and cool at a much slower rate producing light elements via big bang nucleosynthesis (Wagoner et al., 1967). The density perturbations grew via gravitational instability to form larger structures that merged hierarchically to eventually form the large-scale structures such as galaxy clusters that we see in the Universe today. A large unseen matter component needs to exist to allow structures to form in this hierarchical manner and the favoured form of this matter is massive particles that are weakly interacting and travel at non-relativistic speeds, commonly called Cold Dark Matter (CDM; Blumenthal et al., 1984). Observational evidence also shows that the expansion of the Universe is accelerating, providing evidence for some kind of vacuum energy (Λ) or dark energy.

2.2.1   The Field Equations from General Relativity

In the General Theory of Relativity, the force of gravity occurs as a result of the curvature of space-time by matter and energy. This effect is described in the Einstein Field Equations (Einstein, 1916):

$$G_{\mu\nu} + \Lambda g_{\mu\nu} = \frac{8\pi G}{c^4} T_{\mu\nu}, \qquad (2.1)$$

where $G_{\mu\nu}$ is the Einstein tensor, Λ is the cosmological constant (see Section 2.8.2), $g_{\mu\nu}$ is the metric tensor, $T_{\mu\nu}$ is the stress-energy tensor, c is the speed of light and

G is the gravitational constant. The Einstein tensor is defined as

$$G_{\mu\nu} = R_{\mu\nu} - \frac{1}{2}Rg_{\mu\nu}, \tag{2.2}$$

where $R_{\mu\nu}$ is the Ricci curvature tensor and R is the Ricci scalar curvature. The metric tensor, $g_{\mu\nu}$, describes the geometry of the 4D space-time (3 spatial dimensions + time). The stress-energy tensor, $T_{\mu\nu}$, describes the energy and matter content of the Universe. In an isotropic and homogeneous Universe, this may take the perfect fluid form:

$$T_{\mu\nu} = \left(\rho(t) + \frac{p(t)}{c^2}\right)u_\mu u_\nu - p(t)g_{\mu\nu}, \tag{2.3}$$

where u_μ is the four-velocity and $\rho(t)$ and $p(t)$ are the density and pressure of the fluid respectively.

The geometry of space-time changes in the presence of matter and this is observed when the trajectory of a particle is altered in the presence of a massive object when compared with the trajectory in empty space. This is interpreted as gravity in the Newtonian limit.

2.2.2 The Robertson-Walker Metric

A key postulate in our understanding of the Universe is the **Copernican Principle**, which states that our place in the Universe is in no way special. This idea, in addition to an assumption of isotropy gives the **Cosmological Principle**, which suggests that the Universe is statistically both *isotropic* and *homogeneous*, i.e. on average looks the same regardless of the direction that you look in and regardless of your location in the Universe. Locally this postulate breaks down but on larger scales, regions containing many hundreds of thousands of galaxies (though still significantly smaller than the size of the Universe itself), the Universe looks essentially the same in every direction, i.e. is isotropic. When combined with the Copernican principle, the implication is that the Universe is also homogeneous. Using the cosmological principle and general relativity, the dynamics of space-time can be investigated. The assumption that the Universe is isotropic, homogeneous and expanding allows us to write the space-time line element in the form

$$ds^2 = c^2\,d\tau^2 = c^2\,dt^2 - a^2(t)\left[\,dr^2 + S_k^2(r)(\,d\theta^2 + \sin^2\theta\,d\phi^2)\right], \tag{2.4}$$

MAP990006
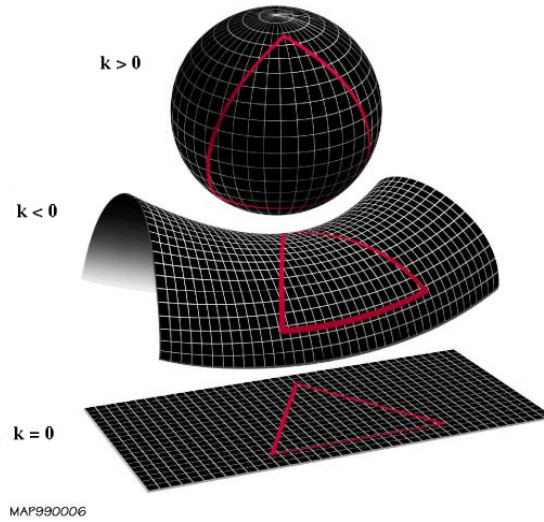
Figure 2.1: This image illustrates the three allowed geometries for the Universe in a RW cosmology. The top picture shows a 'closed' Universe where the curvature $k > 0$, the middle picture illustrated an 'open' Universe where $k < 0$ and the final picture shows a 'flat' Universe where $k = 0$.

Image Credit: NASA

known as the **Robertson-Walker** (RW) line element where r is a comoving spatial coordinate, θ and ϕ are transverse angular coordinates, $d\tau^2$ is the proper time interval squared (the time experienced by an observer moving through the Universe), dt^2 is the coordinate time interval squared (the time experienced by observers at fixed comoving coordinates and in freefall), $S_k(r)$ is the curvature of the Universe in 3D space and $a(t)$ is the dimensionless scale factor of the Universe

$$a(t) = \frac{R(t)}{R_0}, \tag{2.5}$$

where $R(t)$ is the scale factor of the Universe and R_0 is the present day value of the scale factor. A subscript of 0 on any variable implies a present day value throughout this text. By definition, $a(t_0) = 1$ today. From the cosmological principle, the curvature of the Universe must be the same everywhere, which leaves just three curvature solutions. Thus $S_k(r)$ can be expressed as

$$S_k = \begin{cases} \sinh(r), & k = -1 \\ r, & k = 0 \\ \sin(r), & k = 1. \end{cases} \tag{2.6}$$
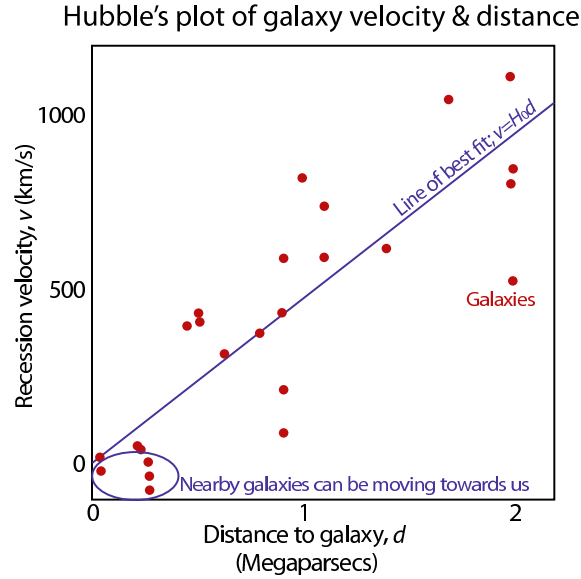
Figure 2.2: Hubble's distance velocity relationship using galaxies from his original data set. This relationship is evidence for the expansion of the Universe.

Image Credit: CSIRO Australia

In this scheme, the Universe has either positive ($k > 0$, spherical), negative ($k < 0$, saddle) or zero ($k = 0$, flat) curvature (see Figure 2.1).

2.2.3 The Hubble Law

Almost everything in the Universe appears to be moving away from us, and everything else. This originated from Slipher's discovery that galaxies are receding from us, and one another, as the Universe expands (Slipher, 1917; Hubble, 1929; Hubble & Humason, 1931). The separation between cosmological objects is often given in *comoving coordinates* which are related to physical coordinates[1], x, by

$$r = \frac{x}{a(t)}. \tag{2.7}$$

The comoving distance is a fundamental distance measure in cosmology as it remains the same for two objects locked in the Hubble flow (the expansion of the Universe).

---

[1]Physical coordinates measure the distance between two objects at an instant in time, as would be measured by a set of rulers at rest with respect to comoving observers between the two objects.

The time evolution of the separation can then be given in terms of

$$\frac{dx}{dt} = \dot{a}(t)\, r = \frac{\dot{a}(t)}{a(t)}\, x. \tag{2.8}$$

We can then define the Hubble parameter as $H(t) = \frac{\dot{a}(t)}{a(t)}$ and define the current value of the Hubble parameter, the Hubble constant as

$$H_0 = H(t_0) = 100\ h\ \text{km s}^{-1}\ \text{Mpc}^{-1}, \tag{2.9}$$

where h is a dimensionless number (for the most current values of H_0 and h, see Section 2.10). Thus, the expansion of the local Universe, the *Hubble Law*, is obtained

$$v = H_0\, x, \tag{2.10}$$

where v is the velocity of the galaxy. Figure 2.2 shows the original data that lead to the derivation of the Hubble law. Hubble used Cepheid variable stars to determine the distances to the galaxies. Cepheid variable stars undergo oscillations in their periods at regular intervals and there is a tight correlation between the period of oscillation and the luminosity of the star (Leavitt & Pickering, 1912). Given that the luminosity is known, the distance to the star can be measured. From the figure we can see that some nearby galaxies appear to be moving toward us while the distant galaxies are moving away. The measurement of this relation has become far more precise since Hubble's first measurement with the Hubble Key Project's distance measurements using Cepheid variables (Freedman et al., 2001) and more recently with the Wilkinson Microwave Anisotropy Probe (WMAP) characterisation of the Cosmic Microwave Background (CMB, see Section 2.5.1) (Jarosik et al., 2011). Hubble's law has also contributed to our understanding that the Universe is not only expanding, it is also accelerating in its expansion (see Section 2.8).

2.2.4   Cosmological Redshift

From General Relativity, we know that light rays travel along null geodesics, $ds^2 = 0$. Thus, we can see from equation 2.4 that the comoving distance can also be defined as

$$r = \int_{t_e}^{t_0} \frac{c\, dt}{a(t)}, \tag{2.11}$$

where t_e is the time the photon was emitted and t_0 is the time that the photon is observed. If we imagine a scenario where two photons are emitted from a source, separated by a short time, the second photon will take longer to reach the observer because the Universe is expanding. However, because we are measuring a comoving distance, the distance that each photon travels will be exactly the same

$$r = \int_{t_e + \Delta t_e}^{t_0 + \Delta t_0} \frac{c \, dt}{a(t)}, \tag{2.12}$$

so we must still satisfy the relation

$$\frac{\Delta t_e}{\Delta t_0} = \frac{a(t_e)}{a(t_0)}, \tag{2.13}$$

remembering that by definition $a(t_0) = 1$. We can also express this time dilation in terms of frequencies, ν, and wavelengths, λ,

$$\frac{\nu_e}{\nu_0} = \frac{1}{a(t)} = \frac{\lambda_0}{\lambda_e}. \tag{2.14}$$

The redshift is defined as the relative change in the wavelength between emission and observation

$$z = \frac{\lambda_0 - \lambda_e}{\lambda_e}, \tag{2.15}$$

so the redshift is related to the scale factor by

$$a(t) = \frac{1}{1 + z}. \tag{2.16}$$

2.3 The Dynamics of Expansion

It is possible to apply the RW line element to determine analytic solutions to Einstein's Field Equations in order to describe a Universe that is expanding or contracting. The solution gives the Friedmann Equation and the Acceleration Equation

$$H^2(t) = \left(\frac{\dot{a}}{a}\right)^2 = \frac{8\pi G \rho}{3} - \frac{kc^2}{a^2}, \tag{2.17}$$

$$\frac{\ddot{a}}{a} = \frac{-4\pi G}{3} \left(\rho + \frac{3p}{c^2}\right), \tag{2.18}$$

where p is the sum of the pressures of each component of the Universe (the total pressure), k is the curvature of the Universe, H is the Hubble Parameter, G is the Gravitational Constant, ρ is the sum of the matter (ρ_m), radiation (ρ_r) and dark energy (ρ_Λ) in the Universe (the total energy density) and

$$\rho_\Lambda = \frac{\Lambda c^2}{8\pi G},\tag{2.19}$$

where Λ is the cosmological constant.

From Equation (2.17), we can determine that there must be a critical density that will result in a flat Universe, $k = 0$, and this is

$$\rho_c(t) = \frac{3H^2(t)}{8\pi G}.\tag{2.20}$$

A density not equal to this critical density would result in a Universe with a curved geometry. Since the Universe is not necessarily flat, it is sensible to define a parameter that is relative to this critical density, the *density parameter*

$$\Omega_{tot} = \frac{\rho}{\rho_c} = \frac{8\pi G\rho}{3H^2(t)}.\tag{2.21}$$

From the Friedmann equation and the Acceleration equation, we can derive the *adiabatic energy equation*, $dE = -pdV$,

$$\frac{d(a^3\rho c^2)}{dt} + p\frac{da^3}{dt} = 0,\tag{2.22}$$

which describes the dependence of the density on the scale factor. In a matter dominated Universe, $\rho \propto a^{-3}$; In a radiation dominated Universe $\rho \propto a^{-4}$; and finally, in a dark energy dominated Universe $\rho = \frac{\Lambda}{8\pi G}$.

2.4   Observational Quantities

Verifying the theories of cosmology requires observation of the real Universe for comparison. This section will describe the observables that are traditionally used in cosmological analyses.

2.4.1 The Hubble Parameter

The Hubble parameter relates the the recessional velocity of a galaxy to its distance from us. The Hubble parameter changes with time. A useful form of the Hubble parameter is derived from the Friedmann equation, using density parameters. The dimensionless density of matter in the Universe is simply defined as

$$\Omega_m = \frac{\rho_{m_0}}{\rho_c} = \frac{8\pi G}{H_0^2}\,\rho_{m_0}, \tag{2.23}$$

and we know from the previous section that in a matter dominated Universe

$$\rho_m(a) \propto \frac{\rho_{m_0}}{a^3}. \tag{2.24}$$

We can also define the dimensionless curvature density parameter as

$$\Omega_k = \frac{-kc^2}{(a_0 H_0)^2}, \tag{2.25}$$

and the dimensionless dark energy density parameter as

$$\Omega_\Lambda = \frac{\Lambda c^2}{3H_0^2}. \tag{2.26}$$

This can be generalised such that the dimensionless density parameter for any species i is given as

$$\Omega_i(t) = \frac{\rho_i(t)}{\rho_c(t)} = \frac{8\pi G \rho_i(t)}{3H^2(t)}. \tag{2.27}$$

The total dimensionless density of the Universe is

$$\Omega_{tot} = \sum_i \Omega_i. \tag{2.28}$$

Substituting all of these into the Friedmann equation and replacing the scale factor with redshift gives the Hubble parameter

$$H(z) = H_0 \sqrt{(\Omega_r(1+z)^4 + \Omega_m(1+z)^3 + \Omega_k(1+z)^2 + \Omega_\Lambda)}, \tag{2.29}$$

where Ω_r is the dimensionless density of the radiation in the Universe (see Section 2.10 for current values of the dimensionless density parameters).

2.4.2 Distances in Cosmology

In a Universe that is both curved and expanding, the distance between two objects is constantly changing, making the notion of distance particularly ambiguous. Consequently, there are several different distance measures in cosmology that are clearly defined and this section will introduce a subset that are directly relevant to this work. For a review of these and other distance measures, see Hogg (2000).

Proper Distance: The proper distance is the distance between two objects as measured with a 'ruler' at an instant in time

$$x = a(t) \; r. \tag{2.30}$$

Comoving Distance: The comoving distance is defined in Equation (2.11) in terms of time. Another definition in terms of redshift is

$$r = \int_0^z \frac{c \; dz'}{H(z)}. \tag{2.31}$$

Angular Diameter Distance: The angular diameter distance is the distance defined by the ratio of the objects physical size, y, to its angular size in radians, θ, as viewed by an observer

$$D_A = \frac{dy}{d\theta} = a(t) \; S_k, \tag{2.32}$$

(e.g. Weinberg, 1972). In terms of redshift, in a flat Universe this is just

$$D_A(z) = \frac{r(z)}{1 + z}. \tag{2.33}$$

Luminosity Distance: The luminosity distance is related to the absolute magnitude, M, of an object and the apparent magnitude, m, of the object by

$$D_L = 10^{\frac{m-M}{5}+1}, \tag{2.34}$$

where D_L is measured in parsecs. The luminosity distance also happens to be related to the comoving distance and angular diameter distance by

$$D_L = r(1 + z) = D_A(1 + z)^2 \tag{2.35}$$

(e.g. Weinberg, 1972).

2.5 The Early Universe

The early Universe is defined by a number of distinct epochs. Each of these periods directly influenced the evolution of structures in the Universe and are responsible for how it appears today. This Section will introduce some of these epochs.

2.5.1 The Cosmic Microwave Background

In parallel with the development of our understanding of the dynamics of the Universe, our knowledge of the underlying cosmological framework has evolved. The Cosmological Principle and Einstein's theory of General Relativity form the theoretical basis for **Big Bang Cosmology**, the most broadly accepted model for the evolution of the Universe. Historically, the Big Bang framework originated with Friedmann's discovery of the expanding Universe. This expanding Universe model inspired Lemaître, using the second law of thermodynamics, to hypothesise that the expansion of the Universe is actually an increase in the disorder of the system, originating in a singularity called the primeval atom. This nucleus would then explode where an increase in the entropy of the Universe would be apparent (Lemaître, 1931). George Gamow expanded on this work, originally assuming that the primeval atom was comprised entirely of neutrons before moving on to include protons and electrons in the nucleus (Gamow, 1948, 1949).

The single most important discovery that gave solid evidence to the Big Bang framework occurred in 1965 when Arno Penzias and Robert Wilson of Bell Laboratories accidently discovered the *Cosmic Microwave Background* (CMB) which had been hypothesised by Gamow and extended by Robert Dicke and James Peebles (Penzias & Wilson, 1965; Dicke et al., 1965). In this framework, when the Universe was very young, temperatures would have been extremely high, so atoms would not have been able to exist. Consequently, the Universe would have consisted of free nuclei and electrons. Photons from the Big Bang traveling through the Universe would have been rapidly scattered by the free electrons via Thomson scattering, rendering this epoch virtually opaque. As the Universe expanded and cooled, atoms were able to form and electrons dropped to their ground state, so the photons no longer inter-
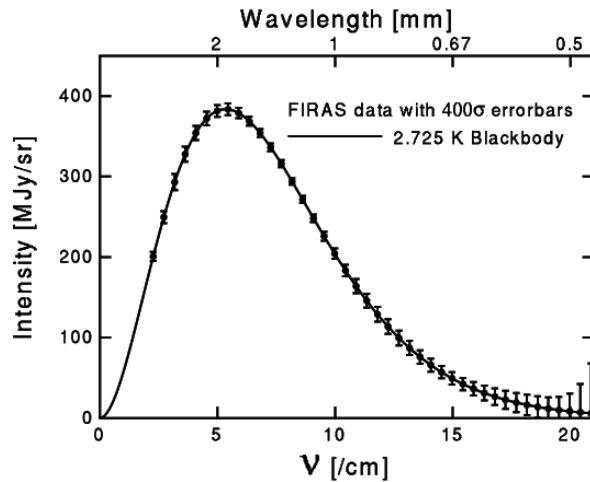
Figure 2.3: This image shows the theoretical spectrum for the Cosmic Microwave Background (CMB) with the data taken by the FIRAS instrument on COBE overlaid. The x-axis variable is the wavenumber (1/wavelength in cm) and the y-axis variable is the power per unit area per unit frequency per unit solid angle in MegaJanskies per steradian. The agreement between the theory and the observations is so good that the error bars on this plot needed to be multiplied by 400 in order to be able to see them.

Image Credit: Ned Wright

acted with them. At this time, known as the epoch of Recombination, the Universe became transparent and the photons have been traveling uninterrupted since then. We detect these photons coming from every direction toward us, all with almost the same temperature. One possible idea for the origin of these photons was that they came from stars throughout the Universe. However, the observed spectrum of the photons is a black body and it would be very unlikely for photons from stars all through the Universe to combine to produce an almost perfect black body spectrum. The black body nature of these photons is strong evidence that the CMB is the left over electromagnetic radiation from the Big Bang and that it fills the entire Universe. The CMB has a thermal blackbody spectrum of 2.726K which peaks in the microwave (Figure 2.3).

The CMB has small fluctuations in temperature that occurred during inflation (see Section 2.5.3). These temperature anisotropies arise from two separate physical processes. The first is the existence of gravitational potential fluctuations at the surface of last scattering, or the Sachs-Wolfe effect (Sachs & Wolfe, 1967), which causes photons escaping from the last scattering surface to be redshifted by the non-

uniform gravitational potential. This effect dominates on angular scales larger than $\theta \simeq 1°$ and contributes to the temperature anisotropy by $\Delta T/T = \frac{1}{3}\Phi$, where Φ is the gravitational potential (White & Hu, 1997). The second process that contributes to the temperature anisotropies is related to small scale fluctuations in the matter-radiation fluid at the epoch of recombination. When a slight overdensity caused matter to be gravitationally attracted to it but the heat of the photon-matter interactions caused an outward pressure, an oscillation began. These oscillations are analogous to sound waves because they are caused by changes in pressure and the imprint that they left on the CMB after photons and baryons decoupled has been named Baryon Acoustic Oscillations (BAOs). The acoustic peak has a characteristic scale around $\theta \simeq 1°$ (see Figure 2.4), which is the maximum distance an acoustic wave could travel before recombination. The sound horizon at the time of recombination provides strong constraints on the matter content of the Universe.

Most CMB anisotropies were generated in the very early Universe. However, some anisotropies are formed at late times via the Integrated Sachs-Wolfe effect (ISW) (Sachs & Wolfe, 1967). These temperature fluctuations are generated when photons traveling through the Universe pass through evolving gravitational potentials. Also, by measuring the angular size of the sound horizon in the CMB and combining this with our understanding of the speed of sound in a hot plasma, it can be shown that the geometry of the Universe is flat.

The Cosmic Background Explorer (COBE) satellite was launched into space in 1989 to measure these anisotropies (amongst other things) and in 1992, anisotropies on scales larger than $7°$ were detected at a level of $\Delta T/T \sim 10^{-5}$ (Smoot et al., 1992). This measurement, along with the measurement of the thermal blackbody spectrum, earned the PI's George Smoot and John Mather a Nobel prize. The COBE satellite was followed up by the Wilkinson Microwave Anisotropy Probe (WMAP) which measured anisotropies on scales of around 13 arcmin with a similar sensitivity (Jarosik et al., 2011) (see Figure 2.5). To improve on the resolution obtained with the WMAP satellite, the Planck satellite was launched in 2009. Planck has a 5 arcmin resolution and will measure the temperature on this scale to an accuracy of $\Delta T/T \sim 2 \times 10^{-6}$ (The Planck Collaboration, 2006).

Today, there are three main observations that validate the Big Bang theory and these
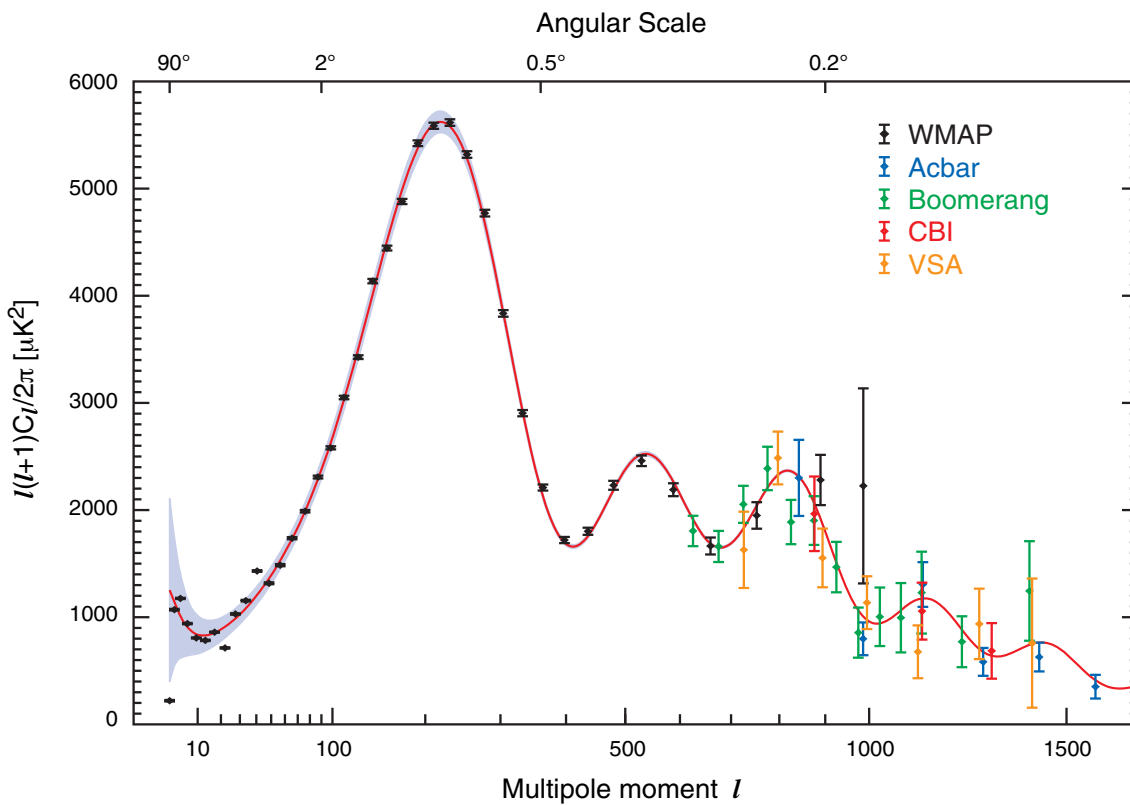
Figure 2.4: Angular power spectrum of the Cosmic Microwave Background showing results from the WMAP 3-year (Hinshaw et al., 2007), Boomerang (Jones et al., 2006), Acbar (Kuo et al., 2004), CBI (Readhead et al., 2004) and the VSA (Dickinson et al., 2004) CMB experiments.

Image Credit: Hinshaw et al. (2007)

are the expansion of the Universe (discussed further in section 2.8), the observed Planck spectrum of the CMB (Figure 2.3) and the abundance of primordial elements (discussed in section 2.5.3). Together, these observations show that the Universe began in a hot and dense state.

2.5.2 Nucleosynthesis

Around 1 second after the Big Bang, the Universe had expanded, and consequently cooled down, enough for stable protons and neutrons to form. This was the start of the process known as Big Bang Nucleosynthesis which was responsible for the formation of deuterium, the helium isotopes He-3 and He-4 and the lithium isotopes Li-6 and Li-7. In addition to these stable nuclei, some unstable isotopes were also produced: tritium (H-3); beryllium-7 (Be-7), and beryllium-8 (Be-8). These unstable isotopes either decayed or fused with other nuclei to make one of the stable isotopes.

The relative abundances of these isotopes follow from thermodynamical arguments, combined with the way that the mean temperature of the Universe changes over time. Combining thermodynamics and the changes brought about by the expansion of the Universe, it is possible to calculate the fraction of protons and neutrons based on the temperature at this point. At around three minutes after the Big Bang, the Universe became too cool for any further nuclear fusion to occur (until the star formation epoch). At this point, the elemental abundances were fixed and only changed as some of the radioactive products, such as tritium, decayed.

During the 1970s it was realised that the density of baryons as calculated by Big Bang Nucleosynthesis was much less than the observed mass of the Universe based on calculations of the cluster mass density. The introduction of dark matter played a large role in solving this discrepancy. Today, observations of the CMB using the Wilkinson Microwave Anisotropy Probe (WMAP) have been able to independently confirm the baryon density of the Universe required to account for Big Bang Nucleosynthesis.

2.5.3 Inflation

Big Bang cosmology has several problems including the Horizon problem (why is the CMB temperature so uniform when opposite points on the sky could not have
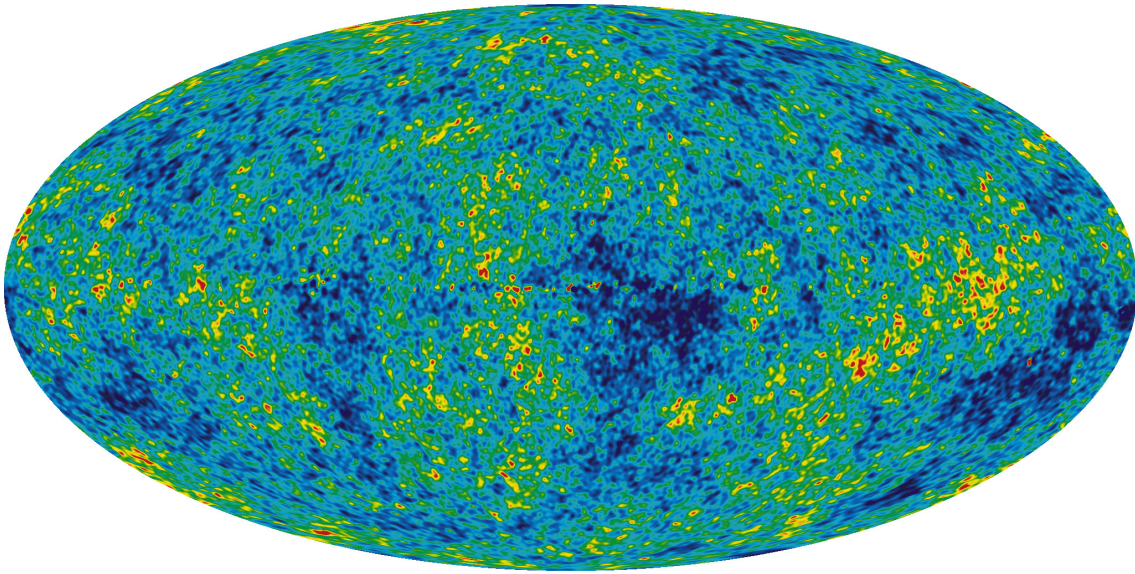
Figure 2.5: The Cosmic Microwave Background (CMB) as viewed by the Wilkinson Microwave Anisotropy Probe (WMAP). This image shows the fluctuations in the CMB that appeared as a result of quantum fluctuations during the period of inflation in the very early Universe. These fluctuations are extremely faint, amounting to only one part in 100,000 with respect to the 2.726K temperature of the background radiation field.

Image Credit: NASA/WMAP Science Team

been causally connected?), flatness (why does the geometry of the Universe appear to be flat?), the origin of perturbations and an absence of observed relics such as monopoles. These problems included the fact that the Universe would need to have started from very specific initial conditions at the time of the Big Bang in order to allow the Universe to appear as it does today.

The Structure Problem

Although the background radiation is largely uniform, the very existence of structure in the Universe today demands that there be some anisotropies in the temperature of the CMB. The introduction of Inflation is an attempt to resolve all of these problems by providing a dynamical mechanism to drive the Universe into what we observe today. The basic theory behind inflation is that the very early Universe underwent a period of accelerated expansion. During this rapid expansion, minute quantum mechanical fluctuations imprinted themselves on the Universe as density perturbations and the structure of these perturbations has been observed as temperature anisotropies by the incredibly detailed data taken by the WMAP satellite (Figure

2.5).

The Horizon Problem

When looking at the CMB on scales larger than the horizon at that time, regions are expected to be causally isolated from one another. The distances involved are too great for light to have traveled from one point to the other. However, the observed homogeneity of the Universe suggests that at some time, all points of the sky were causally connected. So, if the early Universe was causally connected in small patches, a period of Inflation can expand these to account for the homogeneity and isotropy of the observable Universe today (Guth, 1981).

The Flatness Problem

The Friedman equation suggests that a very small initial curvature in the Universe would become far more pronounced over time. So, in order for the Universe to have the flat geometry that we measure today, the curvature at the Planck time must have been $|\Omega_k| < 10^{-15}$. Inflation accounts for the observed flatness of the Universe because the rapid exponential expansion would drive any initial curvature in the Universe to scales beyond the horizon scale (Guth, 1981).

The Monopole Problem

Grand Unified Theories suggest that the very early Universe should have produced very heavy, stable magnetic monopoles that would have persisted to the present day and should, in fact, dominate the energy density of the Universe today. However, no magnetic monopoles have ever been observed. The absence of magnetic monopoles can be explained by a period of Inflation separating any monopoles and lowering their observed density by many orders of magnitude so that none exist in the observable Universe (Olive, 1990).

2.6 The 3-D Matter Density Power Spectrum

Predicting the density of the Universe at every point in space is not possible given the initial conditions are subject to stochasticity and are therefore not known exactly. However, the statistics of the fluctuations in the density field can be predicted

and measured.

If we have a density field (or any field) that is statistically homogeneous, isotropic and random, we can determine the excess probability of two points having a given separation, $\boldsymbol{r}$, by its two-point correlation function

$$\xi_\delta(r) = \langle \delta(\boldsymbol{x}) \, \delta^*(\boldsymbol{x}') \rangle, \tag{2.36}$$

where $r = |\boldsymbol{x} - \boldsymbol{x}'|$ and the angled brackets represent the ensemble average over realisations. For the case of the Universe, where there is only one realisation, we must assume the *ergodic principle* which states that an average over a sufficiently large field is equal to an ensemble average.

In Fourier space, the two-point correlation function becomes

$$\langle \delta(\boldsymbol{k}) \, \delta^*(\boldsymbol{k}') \rangle = \int d^3x \, \mathrm{e}^{-i\boldsymbol{x}\cdot\boldsymbol{k}} \int d^3x' \, \mathrm{e}^{-i\boldsymbol{x}'\cdot\boldsymbol{k}'} \, \langle \delta(\boldsymbol{x}) \, \delta^*(\boldsymbol{x}') \rangle, \tag{2.37}$$

where k is the wavenumber in Fourier space. Substituting in equation 2.36 gives

$$\begin{aligned}
\langle \delta(\boldsymbol{k}) \, \delta^*(\boldsymbol{k}') \rangle &= (2\pi)^3 \, \delta_D(\boldsymbol{k} - \boldsymbol{k}') \int d^3r \, \mathrm{e}^{-i\boldsymbol{r}\cdot\boldsymbol{k}'} \xi_\delta(r) \\
&= (2\pi)^3 \, P_\delta(k) \, \delta_D(\boldsymbol{k} - \boldsymbol{k}'),
\end{aligned} \tag{2.38}$$

where δ_D is the Dirac delta function and $P_\delta(k)$ is the matter density power spectrum. P_δ is only a function of $|\boldsymbol{k}|$ due to isotropy. In dimensionless form, the matter density power spectrum becomes

$$\Delta^2(k) = \frac{k^3 P_\delta(k)}{2\pi^2}. \tag{2.39}$$

The shape of the power spectrum is determined by the values of a variety cosmological parameters including Ω_m, Ω_Λ, Ω_b (the baryon density), σ_8 (the normalisation, see Section 2.6.3) and n_s (the spectral index). The spectral index determines the slope of the primordial power spectrum, $P(k) \propto k^{n_s}$.

2.6.1 The Matter Transfer Function

The matter transfer function relates the ratio of the amplitude of matter fluctuations at early times to the amplitude of the fluctuations today:

$$T(k) \equiv \frac{\delta(k, z = 0)}{\delta(k, z = \infty)} \frac{\delta(0, z = \infty)}{\delta(0, z = 0)}, \qquad (2.40)$$

where k is the 3-D wavenumber and δ is the matter overdensity. By construction $T \to 1$ as $k \to 0$. The 3-D matter density power spectrum, $P_\delta(r)$, is proportional to the square of the transfer function multiplied by the primordial (initial) power spectrum. Thus, knowing the initial power spectrum and the transfer function allows you to calculate the power spectrum at a later redshift. A popular fitting function for the matter transfer function was determined by Eisenstein & Hu (1998), who also include corrections due to baryon effects.

2.6.2 The Non-Linear Power Spectrum

The equations mentioned in the previous section describe the density field when the clustering of objects is still in the linear regime, $\delta \ll 1$. In the non-linear regime, on small scales where complex structures form, things become significantly more difficult to determine analytically. A common way for predicting the matter density power spectrum in the non-linear regime is through measuring the power spectra of N-body simulations and using fitting formulae. Currently, the most commonly used non-linear correction is from Smith et al. (2003), who use a method known as the *halo model*. The halo model assumes that the density field can be separated into clumps of matter of different mass but with a universal density profile. Using input from simulations, such as the matter density power spectrum or halo density profile and linear perturbation theory, the halo model successfully accounts for the cosmological density field for many cosmological models (see Cooray & Sheth, 2002, for a review of the halo model).

2.6.3 Normalisation

The amplitude of the power spectrum is achieved through implementing a normalisation factor. This normalisation can not be predicted from theory, it must be measured. One commonly used approach, which is adopted in this thesis, is to

define a region of the density field that is smoothed with a normalised, spherical top-hat filter of radius R,

$$\sigma^2(R) = \int \frac{d^3k}{(2\pi)^3} P_\delta(k) W_R^2(k), \tag{2.41}$$

where $W_R(k)$ is the Fourier transform of the filter function. Traditionally, $R = 8\ h^{-1}$ Mpc and the resulting dispersion is defined as σ_8. A different approach, often used in CMB studies, scales the matter density power spectrum with a constant

$$\Delta^2(k) = \left(\frac{k}{k_0}\right)^{n_s+3} T^2(k), \tag{2.42}$$

where k_0 is a pivot scale, n_s is the spectral index and $T(k)$ is the matter transfer function.

2.7   Dark Matter

Matter can be split into two types – baryonic and non-baryonic. All of the matter that we can see in the Universe is baryonic matter, but this only comprises a very small fraction of the total matter in the Universe. The other form of matter is known as *dark matter* for reasons that are explained in the following sections. Also discussed is the evidence that we have for the existence of dark matter and a selection of plausible dark matter candidates.

2.7.1   Evidence for Dark Matter

Given that many galaxy clusters appear to be reasonably static and uniform, it is possible to describe their dynamics with the virial theorem. So, assuming that a galaxy cluster is stable and contains a number of galaxies with average velocity dispersion we can employ the virial theorem[2] to determine the virial mass of the cluster by measuring the velocity dispersion of the galaxies within the cluster,

$$M_{tot} = 2\frac{R_{tot}\langle v^2\rangle}{G}, \tag{2.43}$$

---

[2]The virial theorem states that for a system that is equilibrium, $2\ K.E. + P.E. = 0$

where R_{tot} is the virial radius of the cluster, G is the gravitational constant and M_{tot} is the virial mass of the cluster.

Experimentally, cluster masses determined using this method are much greater than masses determined using their stellar masses. This discrepancy in masses can be much more than an order of magnitude. If the normal physical laws were applied, the galaxies would be disrupted by the high rotational speeds because the gravity they exert would not be sufficient for the systems to remain bound, i.e. the velocity dispersion of the galaxies within clusters is too high for the cluster to remain bound when considering mass contributed only by the luminous galaxies. This is known as the 'missing mass problem'. Based on these conclusions, it was suggested that there must be some other form of matter existing in the galaxy clusters which had not been detected – matter which provides sufficient mass and gravity to bind the galaxies together. (e.g. Zwicky, 1933, 1937a; Schwarzschild, 1954). A substantial non-visible, dark matter, component is the simplest solution to this apparent mismatch in energies, with the visible material comprising only a small part of the cluster (e.g. Zwicky, 1933, 1937a).

This idea was not widely accepted until the 1970s when scientists began measuring the rotational properties of spiral galaxies (i.e. their rotation curves, Figure 2.6). The main finding of these studies was that the rotation curves remained relatively flat, indicating that velocities were remaining constant as radius increased (e.g. Rubin & Ford, 1970). The expectation was that the rotation curves would decrease with increasing radius based on the mass of the stars and gas in the galaxy and the predictions from Newtonian dynamics. The implication of the flat rotation curves was that there must be a significant amount of matter in the Galaxy that extends beyond the luminous component to form a large halo that we are unable to see, i.e. Dark Matter.

Concurrent with this observational work, simulations of galaxy formation were taking their first, formative, steps. Initial simulations of disk galaxies without a dark matter component were found to be 'rapidly and grossly unstable', whereas simulations that included a dark halo remained stable (Ostriker & Peebles, 1973). The conclusion to this work was that if the Milky Way (and other spirals) did not have a large unobserved mass in the disk component, then the halo mass interior must
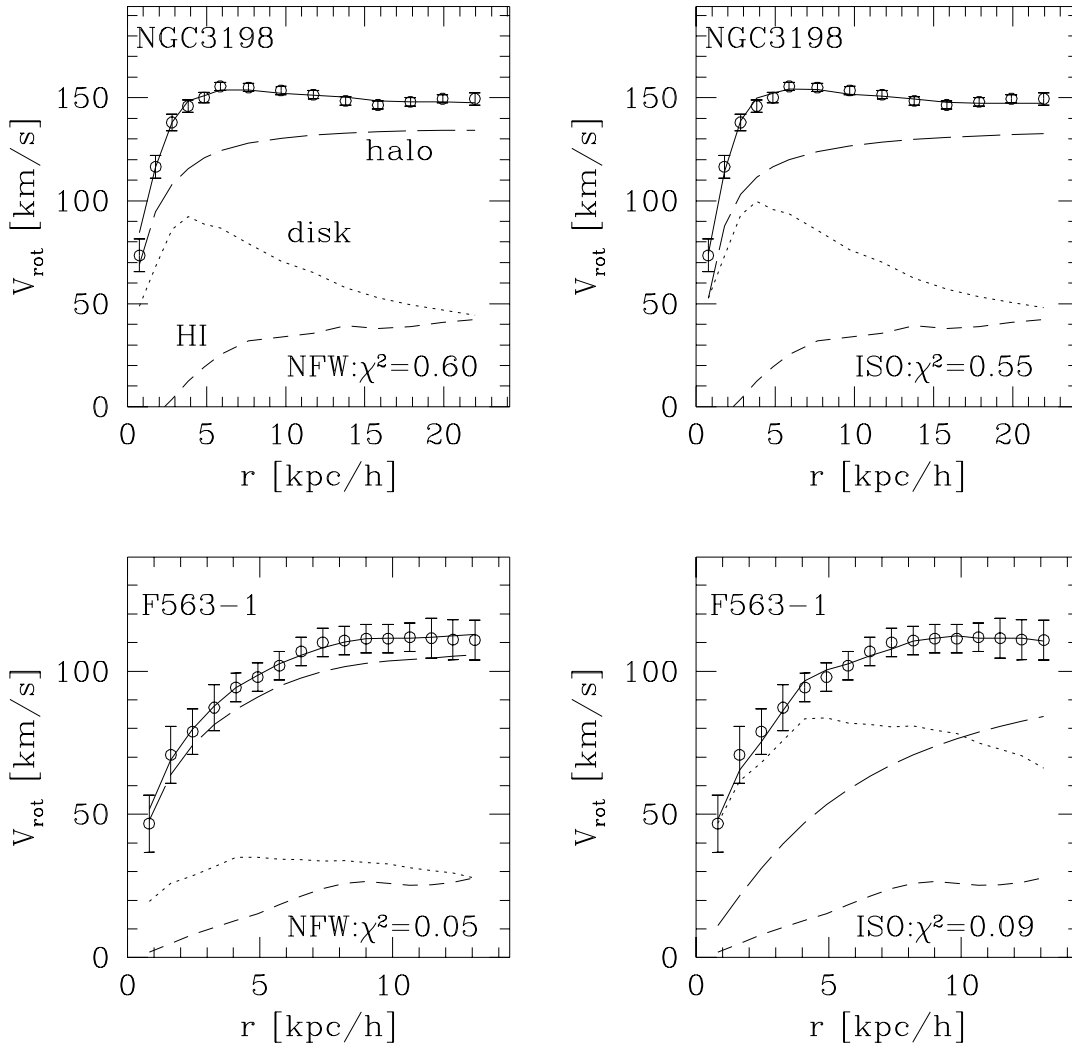
Figure 2.6: Galaxy rotation curve fits using the Navarro, Frenk and White dark matter halo profile (NFW) (Navarro et al., 1995, 1996, 1997) and the Isothermal Sphere halo model. The top two panels show a high-surface brightness galaxy (NGC 3198, Begeman (1987)) and the bottom two panels show a low-surface brightness galaxy (F563-1, de Blok (1997)). The various lines show the different components of the rotation with the top line being the total rotational velocity of the system which, in both cases, is very flat. It is interesting that while both models produce good fits, they require different disk contributions.

Image Credit: Navarro (1998)

be comparable to the disk mass. Thus the halo masses exterior to the disk must be extremely large.

Dark matter remains the most viable explanation for many phenomena observed in the Universe, ranging from gravitational lensing (discussed in detail in section 3.1) to X-ray emissions from clusters (Mulchaey et al., 1993), the acoustic peaks in the CMB power spectrum (Jarosik et al., 2011) and Big Bang nucleosynthesis (BBN), where constraints on the baryon density of the Universe from BBN models and observational data imply that the bulk of the matter in the Universe is dark if $\Omega_{tot} = 1$ and requires that this dark component is dominated by non-baryonic matter (Walker et al., 1991).

2.7.2 Dark Matter Candidates

While a small component of dark matter may be made up of non-radiating baryons in the form of MACHOs (MAssive Compact Halo Objects like black holes and brown dwarfs), there is little doubt that a large fraction of dark matter must be non-baryonic in nature. This is evidenced by the upper bound on the amount of baryonic matter in the Universe from nucleosynthesis and from galaxy redshift surveys. However, a suitable candidate for the non-baryonic dark matter has not been determined. Dark matter can be broadly grouped into three categories – Hot Dark Matter (HDM), Cold Dark Matter (CDM) and Warm Dark Matter (WDM).

Hot Dark Matter: HDM refers to particles that are moving close to the speed of light at the time of formation and/or matter-radiation equality. The most common candidate for HDM is the neutrino. For a short time HDM was the most favoured dark matter candidate (e.g. Zel'Dovich, 1970b; Bond et al., 1980; Silk et al., 1983), however the 'top down' structure formation that results from a HDM-dominated Universe (where very large 'pancake' structures form first and then fragment into the galaxies and clusters of galaxies) was shown to be inconsistent with the presence of galaxies at early times and the observed distribution of structures in the Universe today that imply structure formation is hierarchical (e.g. Cole et al., 2005; Schaeffer & Silk, 1988; White et al., 1983). While HDM is no longer favoured as the dominant dark matter candidate, neutrinos certainly exist in the Universe, and an upper limit to the sum of their masses has been determined, by combining the data from a

number of cosmological surveys, corresponding to $\Omega_\nu < 0.006$ (Thomas et al., 2010).

Cold Dark Matter: CDM particles are slow-moving particles but no candidates have ever been detected. The most likely candidates in theory are axions (e.g. Sikivie, 2011), axinos (e.g. Strumia, 2010), Weakly Interacting Massive Particles (WIMPS, e.g. Bertone, 2010) or other Supersymmetric (SUSY) particles like the neutralino (e.g. Das et al., 2010). Structures in the CDM paradigm form 'bottom-up', or hierarchically, with small structures forming first and accreting mass or merging to become larger structures, which is consistent with our observations of the Universe today (Davis et al., 1985; Gott et al., 1989; White & Frenk, 1991). For a short time the question of 'downsizing', where galaxies in the early Universe appear to be more massive than galaxies today, seemed to derail the bottom-up structure formation scenario (Cowie et al., 1996). However, downsizing can be explained in a hierarchical structure formation model since the largest overdensities will tend to collapse first, forming the largest structures earliest (Neistein et al., 2006). The term 'downsizing' has also been used to describe other observational trends, not necessarily related to CDM, such as the fact that the most massive galaxies appear to be dominated by old stellar populations, while small faint galaxies appear to have a continuous star formation history with stellar populations dominated by young stars. Fontanot et al. (2009) give a summary of several different types of downsizing that have been described in the literature, for which the physical processes causing many of the effects are still not well understood.

CDM is currently the most favoured dark matter model, however, there are still some inconsistencies in the model on scales where the dark matter is strongly clustered, such as in the central parts of dark matter halos where galaxies reside. Simulations often feature a cuspy density profile (e.g. Navarro et al., 1997) while kinematical observations favour a cored profile (Salucci & Burkert, 2000; Gentile et al., 2004). The CDM models also predict a large number of small scale structures like satellite and dwarf galaxies that may not be observed in the real Universe (Diemand et al., 2007, and references therein). Furthermore, the angular momentum of simulated dark matter halos is significantly lower than that observed in spiral galaxies (Maller & Dekel, 2002; Chen & Jing, 2002) and the distribution of sizes of voids does not match observations (Gottlöber et al., 2003). Whether baryonic effects on small scales can resolve these discrepancies is a matter of current debate (e.g. Debattista et al., 2008;

Knebe et al., 2010). Recent work has shown that baryons begin to affect the matter density power spectrum at scales of a few Mpc (van Daalen et al., 2011; Semboloni et al., 2011). These scales are higher resolution than the simulations in this thesis so for the purposes of this work, baryons will be ignored.

Warm Dark Matter: WDM is the final dark matter model and it has been described as 'just HDM cooled down' (Bode et al., 2001). WDM particles interact more weakly than the active HDM neutrinos and their mass is expected to be roughly an order of magnitude higher than HDM particles, from 1 keV - 30 keV (Gorbunov et al., 2008). No WDM candidates have been observed but theories predict that the gravitino is the most likely candidate (Gorbunov et al., 2008). WDM can solve some issues found in CDM, like reducing the number of small satellites in halos (Götz & Sommer-Larsen, 2003), smoothing out the cusps at the center of halos (Bode et al., 2001), resolving the angular momentum observed in dark matter halos (Sommer-Larsen & Dolgov, 2001) and the distribution of sizes of voids in the Universe (Tikhonov et al., 2009). WDM has an initial velocity that is not so fast as to break the observed hierarchical structuring of the Universe but fast enough that free streaming in the early Universe damps out some of the smaller scale structures that form in CDM scenarios, which may be more consistent with the observed Universe (see Figure 2.7). However, the damping effect can go too far and remove many of the substructures that are observed in the Universe so the hottest varieties of WDM are ruled out. So if WDM is the correct dark matter model, rather than CDM, it must still be reasonably cool, or tepid.

It is clear that there is much more research to be done before we either detect a dark matter particle or converge on a dark matter model that completely matches the observed Universe. The current status is that CDM is the preferred model but research into the exact nature of dark matter is still an ongoing endeavour.

2.8 Dark Energy

In 1917, Einstein introduced a constant into the General Relativity field equations in order to produce a static and finite Universe (Einstein, 1917). This constant was known as Λ and it was quickly dismissed by Einstein after Slipher's discovery
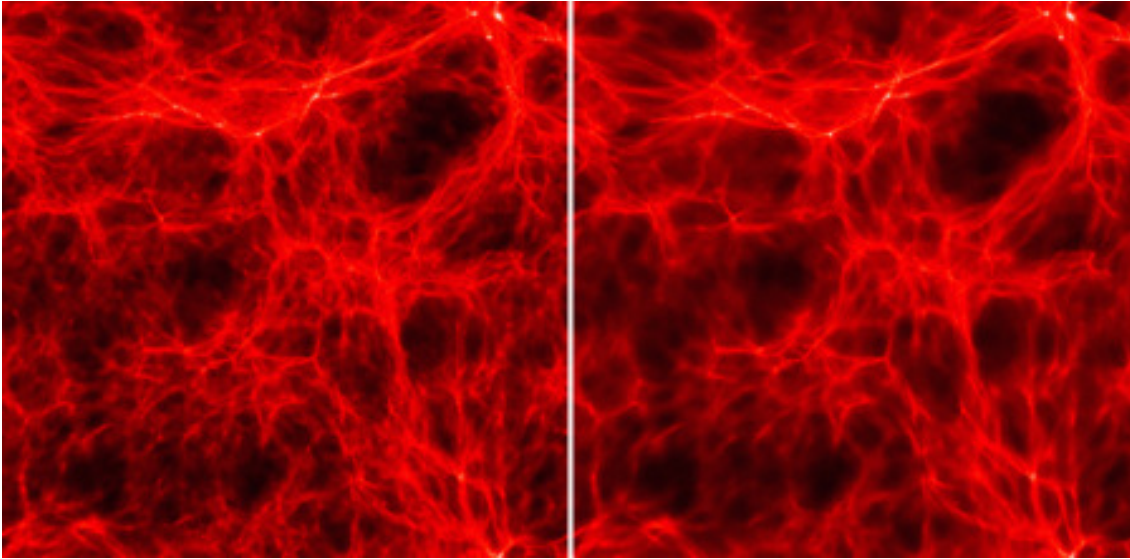
Figure 2.7: **Comparison between a Cold Dark Matter (CDM) and a Warm Dark Matter (WDM) cosmological simulation with a sidelength of $1h^{-1}$Mpc. The left panel shows a CDM simulation while the right panel shows a WDM simulation. The WDM scenario appears to be far smoother than the CDM simulation, with the very small scale structures being damped out due to free streaming of the WDM in the very early Universe.**

Image Credit: Matteo Viel

that the Universe was expanding. Ever since this discovery astronomers have been trying to determine the deceleration parameter, the slowing of the expansion of the Universe due to gravity (e.g. Sandage, 1962).

For more complete reviews of dark energy and its problems from a particle physics perspective, see Bass (2011); or from a cosmological perspective, see Frieman et al. (2008).

2.8.1   Evidence for Dark Energy

Compelling evidence for the existence of dark energy was only discovered just over a decade ago. However, in this last decade, many observations have been undertaken that further confirm the existence of dark energy.

In 1998 two independent teams published some startling results, evidence from Supernovae Type Ia (SNIa) that the Universe is not decelerating, it is in fact speeding up (Figure 2.8) (Riess et al., 1998; Perlmutter et al., 1999). Supernovae are ex-
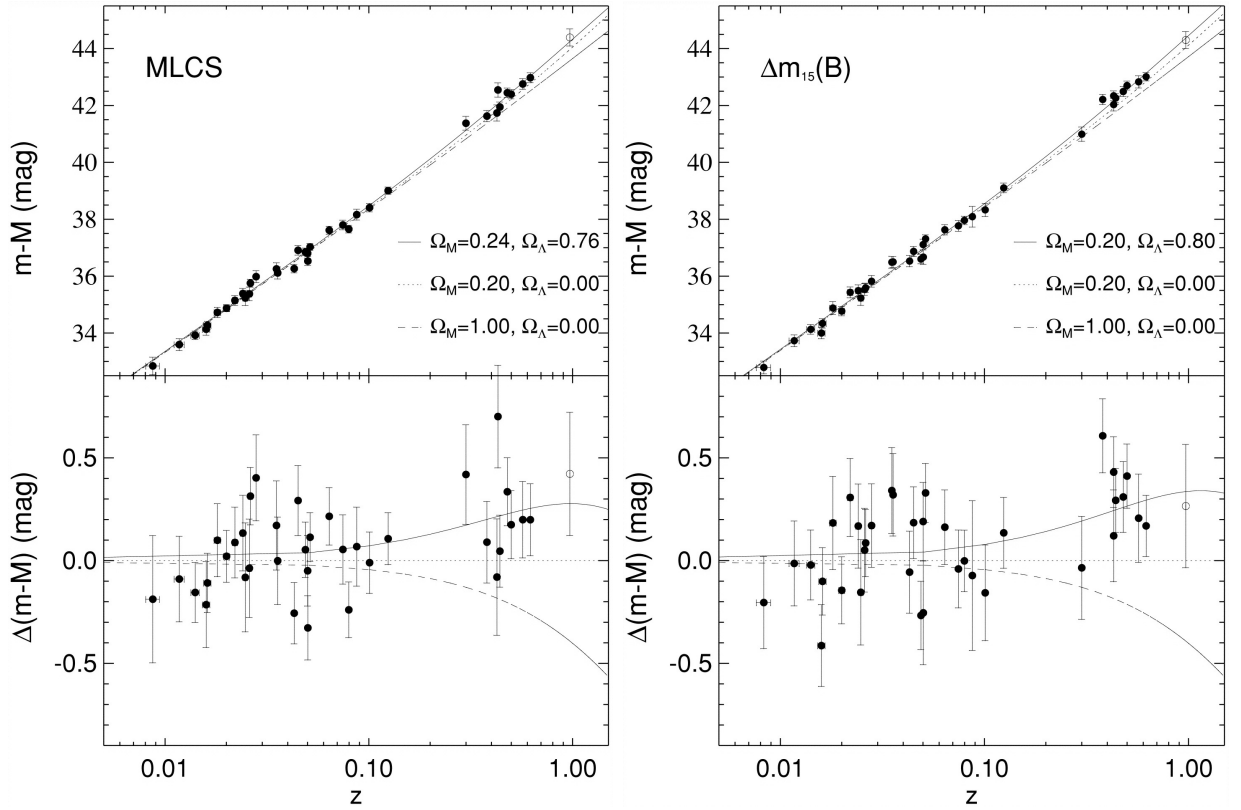
Figure 2.8: *Left Panel:* **Hubble diagram showing distances and magnitudes of SNIa using the MLCS method (Riess et al., 1995, 1996). The upper panel shows low and high redshift SNIa overplotted on three different cosmologies as indicated in the plot. The bottom panel shows the difference between the data and the models with the data indicating a fit with a Universe that is accelerating.**

Right Panel: **Hubble diagram showing distances and magnitudes of SNIa using the template fitting method parametrised by Δm_{15} (Hamuy et al., 1995, 1996). Three different cosmologies are overplotted with the parameters as indicated in the plot. The bottom panel again shows the difference between the data and the models, also indicating a fit with an accelerating Universe.**

Credit: Riess et al. (1998)

tremely luminous explosions that can be categorised into a number of types. The supernovae classified as type Ia occur in binary systems which consist of a white dwarf and a companion star (typically thought to be low mass red giants or slightly evolved main sequence stars). The white dwarf accretes mass from the companion until it reaches the Chandrasekhar limit (Chandrasekhar, 1931) ($\sim 1.4 M_{\odot}$). As the mass exceeds this limit, the white dwarf explodes. SNIa have an absolute luminosity that can be calibrated to have a constant peak brightness, providing a 'standard candle' against which to observationally measure luminosity distances. The results

found in 1998 both showed that the luminosity of the SNIa were fainter than expected for their redshifts. This is consistent with what would be observed in a Universe with accelerating expansion. Subsequent SNIa studies have also shown evidence for dark energy. (e.g. Astier et al., 2006; Riess et al., 2007; Wood-Vasey et al., 2007).

Further to the evidence provided by SNIa, separate studies have shown that the presence of dark energy affects CMB scales. As shown in Figure 2.4, the CMB power spectrum matches the predicted ΛCDM cosmology to remarkable accuracy. The geometry of the Universe can be determined from these precision measurements and the WMAP observations have independently shown that the dark energy density is non-zero (Larson et al., 2011). When combined with the data from other experiments, this dark energy density has been constrained to a high degree of accuracy (see Table 2.1 in the Summary of this chapter) (Komatsu et al., 2011). Also, in the presence of dark energy, gravitational potentials in the Universe evolve at late times and this can be determined observationally by measuring the CMB anisotropies formed due to the Integrated Sachs Wolfe effect (e.g. Giannantonio et al., 2008).

Section 2.5.1 introduced the origin of BAOs. The peak of the BAO signal will occur on a characteristic length scale, known as a 'standard ruler'. Observations of the CMB show the size of the baryon oscillations, which can then be measured in the large-scale structure by looking at the clustering of galaxies. The BAO peak has been measured to occur at 100 h^{-1} Mpc (Eisenstein et al., 2005). The apparent BAO length scale depends on the nature of dark energy and measurements in the last few years are consistent with the ΛCDM predictions (e.g. Percival et al., 2010).

In an expanding Universe, the evolution of the energy density is controlled by the ratio of pressure to the energy density, $w \equiv p/(\rho c^2)$, known as its equation of state parameter. An equation of state relates the pressure, p, to the density, ρ, of a fluid. In this case the fluid is Dark Energy and its equation of state dictates the expansion of the Universe. In order for sufficient growth of primordial fluctuations to allow large scale structure formation, dark energy must only have come to dominate the Universe recently. This occurs only if it has a negative pressure, $w < 0$.

To determine how negative w needs to be to cause the acceleration of the expansion of

the Universe, the equation of state can be substituted into the Acceleration Equation (2.18) to give

$$\ddot{a} \quad \propto \quad -\left[\rho + 3\frac{p}{c^2}\right] \tag{2.44}$$

$$\propto \quad -(1+3w)\rho. \tag{2.45}$$

So, for dark energy to be capable of generating accelerated expansion of the Universe, the equation of state for dark energy must be

$$w < -\frac{1}{3}. \tag{2.46}$$

In the general case, this ratio can evolve over time. The specific case of the cosmological constant is discussed in Section 2.8.2.

The accelerating expansion of the Universe is now well established and the simplest explanation for this acceleration is dark energy. The other possibility is that General Relativity breaks down on cosmological scales and we must find a more complex theory of gravity.

2.8.2 The Cosmological Constant

In the preferred model for cosmology, the cosmological constant Λ has been generalised to be called 'dark energy'. On its own, the cosmological constant has no underlying physics. To provide physical motivation, the cosmological constant can be described as a smoothly distributed vacuum energy. For the specific case of the cosmological constant, w is also a constant. ΛCDM cosmology adopts a vacuum energy with an equation of state of

$$p_{VAC} = -\rho_{VAC} = -\frac{\Lambda}{8\pi G}, \tag{2.47}$$

and

$$w = -1. \tag{2.48}$$

However, this cosmological constant causes problems when trying to connect very small scales with very large scales. This is known as the *cosmological constant problem* (Weinberg, 1989) and it asks the question – Why is the vacuum energy

density (ρ_{VAC}) predicted by particle physics so much larger than what is observed in the real world? In fact, the observed vacuum energy density $\rho_{vac} = (0.002 \text{ eV})^4$ is 10^{120} orders of magnitude smaller than the predicted vacuum energy density when we assume that physics and quantum field theory can be trusted up to the Planck scale (where we expect quantum gravity effects to become important). We may get closer to a solution to this problem if SUSY exists, although detections have not yet been made at the Large Hadron Collider and straightforward predictions do not remove the problem completely (see Peacock, 1999, for a more detailed discussion). So while $w_{VAC} = -1$ is the simplest description of Dark Energy, there is no explanation in the theory as to why the density should have the value it does.

2.8.3   Dark Energy Candidates

The cosmological constant problem is being investigated by looking at alternative models for dark energy where w is equal to something other than -1 and can also vary in time. There are a very large number of these alternative dark energy candidates and theories and this section will introduce a small number of the more well known candidates. The first few candidates, Quintessence, k-essence and Phantoms, rely on the energy-momentum tensor $T_{\mu\nu}$, containing an exotic form of matter with a negative pressure. The final candidate, modified gravity, relies on a modification to the Einstein tensor $G_{\mu\nu}$.

Quintessence: The main alternative theory is known as Quintessence (Peebles & Ratra, 1988; Ratra & Peebles, 1988). In these models, the accelerated expansion of the Universe is caused by the potential energy of a dynamic scalar field $V(\phi)$, much like inflation. Quintessence models vary from the cosmological constant in that the equation of state parameter, w, can vary in time and space. The equation of state for the scalar field is given by

$$w_\phi = \frac{p}{\rho} = \frac{\dot{\phi}^2 - 2V(\phi)}{\dot{\phi}^2 + 2V(\phi)}, \qquad (2.49)$$

which limits the equation of state to $-1 \leq w_\phi \leq 1$. There is currently no evidence to confirm a Quintessence model.

k-essence: The k-essence dark energy theories are also scalar fields. However,

in this scenario cosmic acceleration is driven by the kinetic energy of the field (Armendariz-Picon et al., 2000, 2001). Many constructions of k-essence models suffer from unphysical artifacts (like sound speeds faster than the speed of light) and inconsistency with the particle physics framework (Amendola & Tsujikawa, 2010). While a k-essence model is a possible dark energy candidate, it is currently seen as very unlikely.

Phantoms: If the equation of state for dark energy is less than -1, this is known as a phantom equation of state. With $w < -1$, the accelerating expansion of the Universe continues until all cosmic structure is 'ripped' apart, resulting in the end of the Universe in an event called the 'Big Rip' (Caldwell et al., 2003). Recent studies have ruled out phantom models as dark energy candidates (e.g. Jamil, 2010).

Modified Gravity: A very different alternative is that cosmic acceleration can be explained by modifying gravity rather than trying to explain a mysterious dark energy. Modified gravity models require a new version of the Friedmann equation that will govern the evolution of the scale factor of the Universe, $a(t)$ and a modification to the equations that govern the growth of density perturbations. While it is attractive not having to explain an unknown energy density, it is not clear that a consistent modified gravity model actually exists (e.g. Gregory et al., 2007).

There were a number of dark energy models introduced here and there are many more in existence. To date, we have been able to place constraints on the dark energy density of the Universe and the dark energy equation of state through observations (see Figure 2.10), but we still have not converged on a single model. As the summary of this chapter will show, the data tends toward a dark energy equation of state that is constant in time, $w = -1$ and is most likely vacuum energy (the cosmological constant). However, with upcoming precision surveys, confirmation of a dark energy model should be conclusively determined.

2.9 Baryons

Dark matter and dark energy together comprise around 96% of the Universe. The final ~4% is baryons and this makes up the matter that we can see and interact

with like stars, planets, dust and gas. Baryons consist of protons, neutrons and electrons[3] and typically move at non-relativistic speeds.

An unanswered question about the baryon content of the early Universe is that of baryon asymmetry. Theory states that the Big Bang should have created equal amounts of baryons and antibaryons, resulting in complete annihilation of both, leaving a universe filled with photons but no matter. However, the Universe is currently filled with baryons proving that there was an asymmetry in abundances that was likely caused by physical laws acting on the baryons and antibaryons differently. Supersymmetry has been suggested as a possible solution to the origin of baryon asymmetry and experimental tests are ongoing to investigate this (Dine & Kusenko, 2003).

Baryons in the Universe fuse together to create the atoms represented in the periodic table of chemical elements. These elements are formed via nucleosynthesis that initially started just after the Big Bang (see section 2.5.2) and later through fusion in stars and supernovae. These supernovae explosions produce the heaviest elements found in the Universe today (Woosley et al., 2002).

It is possible to model the large-scale Universe reasonably accurately while neglecting the effect of baryons. However, on smaller scales, the effects of baryons become far more important. The matter density power spectrum is affected by baryons at small scales around a few Mpc (van Daalen et al., 2011) and galaxy formation and evolution is strongly influenced by baryonic effects such as dissipation and radiative cooling which act to increase the matter density power spectrum at small scales and star formation, active galactic nuclei and supernovae feedback which act to suppress the matter density power spectrum at small scales (Larson, 1992). The exact impact of each of these processes on the matter density power spectrum is unknown and is the basis of ongoing research (Dalla Vecchia & Schaye, 2008; Booth & Schaye, 2009; Wiersma et al., 2009). However, baryons are very difficult to simulate accurately, which is why they are so often neglected. The work in this thesis is focused on scales that are much larger than those affected by baryons and thus baryons have been ignored in this work.

---

[3]Strictly speaking electrons are not baryons. However cosmologists use the term baryon to include protons, neutrons and electrons.

2.10 Summary

Today's cosmological model can be described by anywhere between 6 and 20 free parameters and results depend on which set of parameters are chosen and the mix of data used to describe them. One standard choice to describe a ΛCDM cosmology is the combination of the following parameters : H_0, Ω_B, Ω_M, Ω_Λ, σ_8 and n_s; the Hubble parameter, baryonic matter density, total matter density, dark energy density, the RMS amplitude of mass fluctuations on an $8h^{-1}$Mpc scale and the spectral index which indicates the scale variance of the primordial density perturbations respectively.

These free parameters are restricted by observations and the most accurate constraints are determined by combining results from many different experiments. Figures 2.9 and 2.10 show how several of the parameters can be constrained when combining measurements from the CMB, BAO and SNIa. The more measurements that can be taken using different and complementary methods, the tighter the constraints can become. Table 2.1, an abridged version of the table given in Jarosik et al. (2011), shows the cosmological constraints derived from the WMAP Seven-year CMB data release and a combined result from WMAP Seven-year CMB data, Sloan Digital Sky Survey (SDSS) BAO data (Percival et al., 2010) and Hubble Space Telescope (HST) H_0 data (Riess et al., 2009). The advantage of showing the results for two different analyses is that we can begin to see the dependence and sensitivity of certain parameters.

There are many surveys to explore the cosmology of the Universe proposed for the coming decades including the Panoramic Survey Telescope and Rapid Response System (Pan-STARRS), the Very Large Telescope Survey Telescope Kilo-Degree Survey (VST-KIDS), the Dark Energy Survey (DES), the Large Synoptic Survey Telescope (LSST), Euclid and the Wide-Field Infrared Survey Telescope (WFIRST), the Big Baryon Oscillation Spectroscopic Survey (BigBOSS), the WiggleZ Dark Energy Survey and the Subaru Measurement of Image and Redshifts survey (SuMIRe).

The important information to take from this introduction to cosmology and the ΛCDM model is that the data available suggests that the Universe today is close to flat, $\Omega_k \simeq 0$ and very close to critical density, $\rho_c = 3H_0^2/8\pi G$ or $\Omega_{tot} = \rho/\rho_c \simeq 1$.

Table 2.1   *WMAP* Seven-year Cosmological Parameter Summary[a]

Description	Symbol	*WMAP* -only	*WMAP* +BAO+H_0
Parameters for Standard ΛCDM Model			
Age of Universe	t_0	13.75 ± 0.13 Gyr	13.75 ± 0.11 Gyr
Hubble constant	H_0	71.0 ± 2.5 km/s/Mpc	$70.4^{+1.3}_{-1.4}$ km/s/Mpc
Baryon density	Ω_b	0.0449 ± 0.0028	0.0456 ± 0.0016
Physical baryon density	$\Omega_b h^2$	$0.02258^{+0.00057}_{-0.00056}$	0.02260 ± 0.00053
Dark energy density	Ω_Λ	0.734 ± 0.029	$0.728^{+0.015}_{-0.016}$
Fluctuation amplitude at $8h^{-1}$ Mpc	σ_8	0.801 ± 0.030	0.809 ± 0.024
Scalar spectral index	n_s	0.963 ± 0.014	0.963 ± 0.012
Redshift of matter-radiation equality	z_{eq}	3196^{+134}_{-133}	3232 ± 87
Angular diameter distance to matter-radiation eq.	$d_A(z_{\mathrm{eq}})$	14281^{+158}_{-161} Mpc	14238^{+128}_{-129} Mpc
Reionization optical depth	τ	0.088 ± 0.015	0.087 ± 0.014
Redshift of reionization	z_{reion}	10.5 ± 1.2	10.4 ± 1.2
Parameters for Extended Models			
Total density	Ω_{tot}	$1.080^{+0.093}_{-0.071}$	$1.0023^{+0.0056}_{-0.0054}$
Equation of state	w	$-1.12^{+0.42}_{-0.43}$	-0.980 ± 0.053
Neutrino density	$\Omega_\nu h^2$	< 0.014 (95% CL)	< 0.0062 (95% CL)
Neutrino mass	$\sum m_\nu$	< 1.3 eV (95% CL)	< 0.58 eV (95% CL)

[a]This table is an abridged summary of parameters given in Jarosik et al. (2011). The parameters in the first section assume the 6 parameter flat ΛCDM model, first using *WMAP* data only (Larson et al., 2011), then using *WMAP* +BAO+H_0 data (Komatsu et al., 2011).
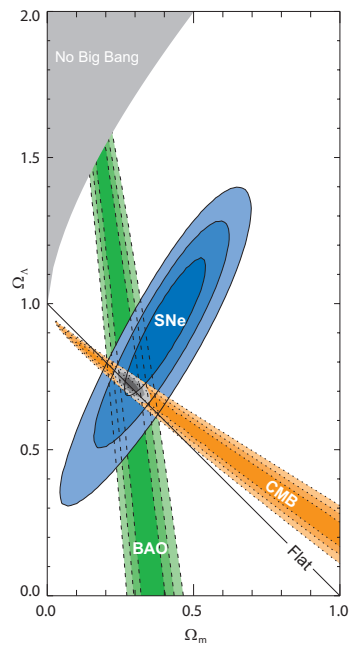
Figure 2.9: Constraints upon Ω_m and Ω_Λ in the ΛCDM model using BAO, CMB, and SNIa measurements.

Credit: Kowalski et al. (2008)
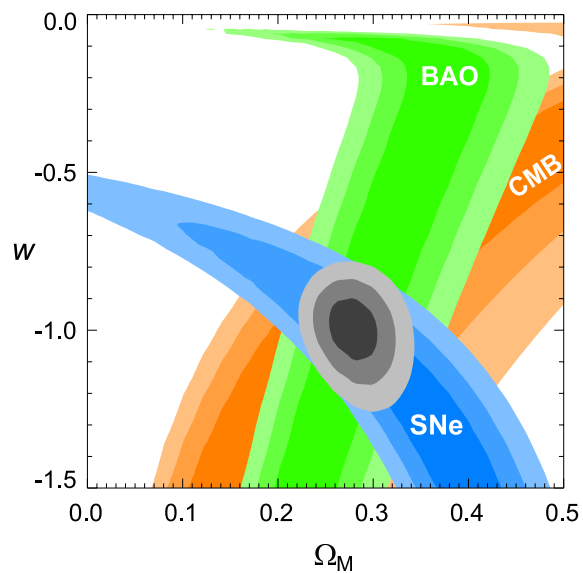
Figure 2.10: Constraints upon Ω_m and w in the ΛCDM model using BAO, CMB, and SNIa measurements in a dark energy model where $k = 0$, $\Omega_{tot} = 1$ and w is a constant but not necessarily -1.

Credit: Kowalski et al. (2008)

Around 27% of its density is attributed to matter with only 4% of this matter comprised of baryons. The other 23% is comprised of dark matter. The remaining 73% of this critical density is contributed by a smoothly distributed vacuum energy which acts to accelerate the expansion of the Universe (Jarosik et al., 2011).

Cosmology today is involved in both verifying this Standard ΛCDM Cosmological Model, as well as testing alternative dark energy and dark matter models and gravity itself. The nature of dark matter and dark energy remain the big unanswered questions in cosmology and gravitational lensing provides an excellent method for further investigating this dark Universe. The future of this field lies in precision measurements of the basic cosmological parameters and investigating the very nature of the Universe.

Chapter 3

Introduction to Gravitational Lensing

3.1 Gravitational Lensing

Einstein's General Theory of Relativity tells us that light travels along null geodesics in space-time. However, massive objects bend space-time – so light traveling through the Universe appears to be deflected when it propagates through these inhomogeneous gravitational fields. This phenomenon, known as gravitational lensing, is observed as microlensing events, gravitational arcs or multiple images (see Figure 3.1 for an example of multiple images) which are strong lensing events. Another gravitational lensing regime exists which is the *weak gravitational lensing* regime. Weak lensing probes effects such as magnification and distortion in a purely statistical manner, i.e. weak lensing effects are only noticeable across an ensemble of sources. Lensing is an attractive method for probing the dark Universe because it does not rely on assumptions such as hydrostatic equilibrium, luminous tracers or galaxy distribution. The physics underlying gravitational lensing are also robust and very well understood, providing a method for constraining cosmological parameters as well as mapping the dark matter distribution in the Universe.

Section 1.1 gave a historical background to the field of gravitational lensing and in this section, I will detail the theoretical basis and concepts involved in the bending of light as it travels through the Universe and is deflected by gravitational fields. For more detailed insight into the physics and equations that govern gravitational
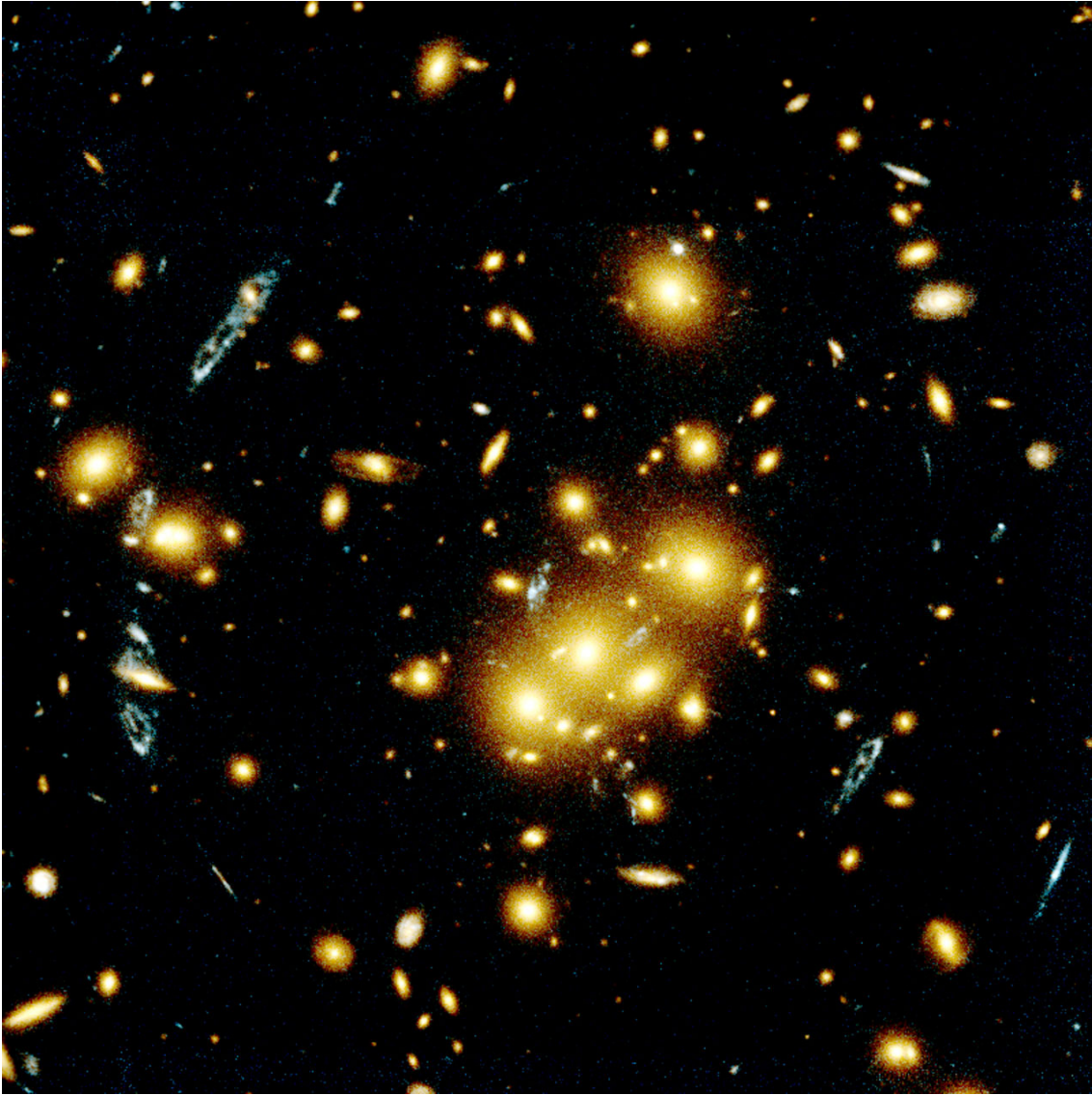
Figure 3.1: **HST image of the galaxy cluster CL0024+1654. Many of the blue ring-like galaxies in this image are in fact a single background galaxy, multiply lensed as a result of strong gravitational lensing by the foreground cluster.**

Image Credit: NASA, ESA, W.N. Colley and E. Turner (Princeton University), J.A. Tyson (Bell Labs, Lucent Technologies)

lensing, the following reviews focus on the technical aspects of gravitational lensing Munshi et al. (2008), Schneider (2006), Refregier (2003b), Wittman (2002), Bartelmann & Schneider (2001) and Mellier (1999).

3.1.1 The Deflection Angle

The deflection angle is the angle that describes the deflection experienced by a light ray traveling from a distant source as it passes a gravitational lens. Figure 3.2 shows the typical geometry of a gravitational lens and α is the deflection angle. If we assume that the light ray does not pass into the strong lensing regime, we can derive the deflection by an extended source by first considering the deflection by a point source. A full derivation of the deflection angle for a point source is given in Appendix A; For now, we will just start with the result:

$$\hat{\alpha} = \frac{4GM}{c^2 D_L \theta}, \tag{3.1}$$

where G is the gravitational constant, M is the mass of the point source, c is the speed of light, D_L is the angular diameter distance between the observer and the lens and θ is the angle on the sky seen by the observer. Note: D_L should not be confused with the luminosity distance. $D_L \theta$ is the distance from the lens to the deflection point and is known as the impact parameter.

To generalise this equation to be true for an extended source, we take a small increment of mass

$$dM = \Sigma \, d^2\theta' \, D_L^2, \tag{3.2}$$

where Σ is the surface mass density of the volume, $d^2\theta'$ is the angular area of the volume and D_L^2 is the distance to the volume. The surface mass density is given by

$$\Sigma = \int dl \rho, \tag{3.3}$$

where ρ is the density and dl indicates a line-of-sight integral. Putting these into Equation (3.1) and summing over all lenses gives

$$\hat{\boldsymbol{\alpha}}(\boldsymbol{\theta}) = \frac{4GD_L}{c^2} \int d^2\theta' \frac{\Sigma(\theta')(\boldsymbol{\theta} - \boldsymbol{\theta'})}{(\boldsymbol{\theta} - \boldsymbol{\theta'})^2}, \tag{3.4}$$
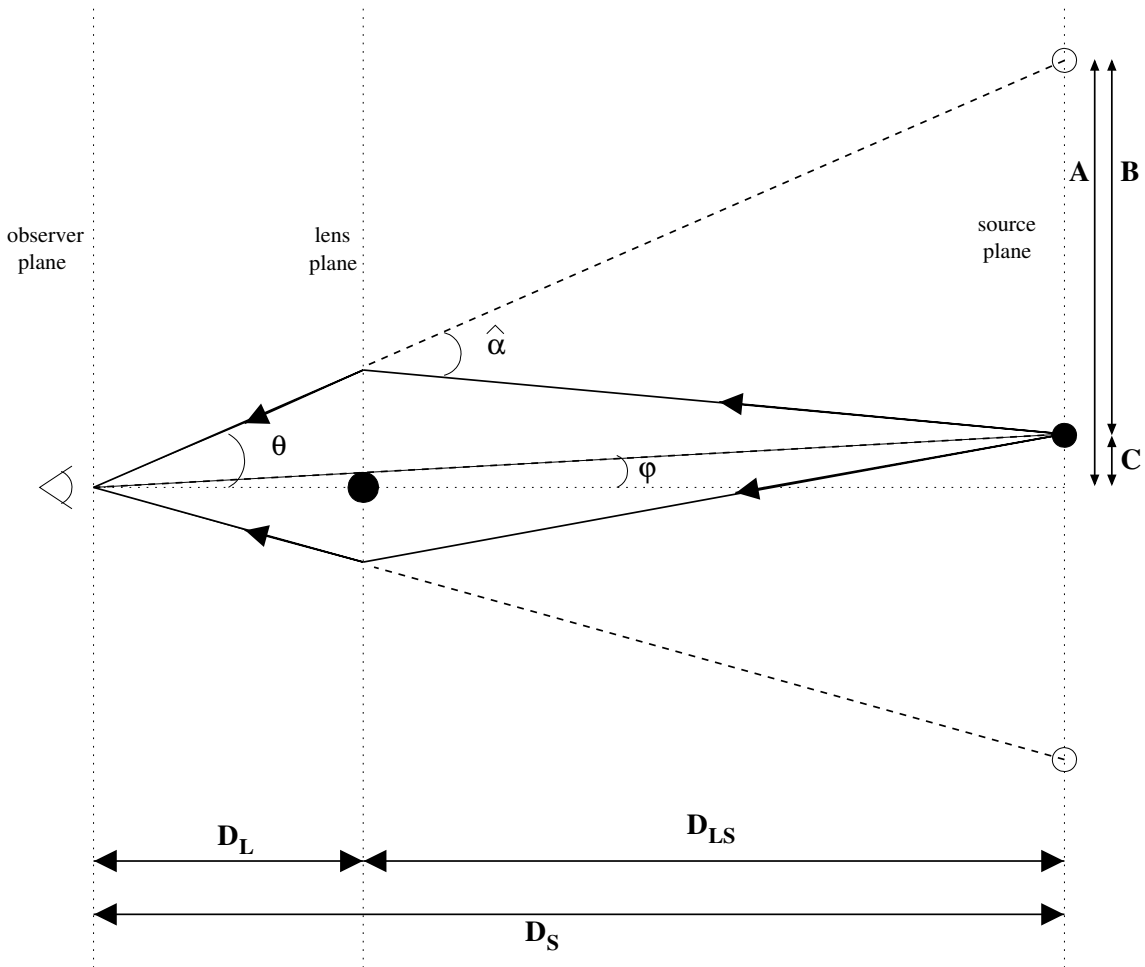
Figure 3.2: This plot shows the geometry of a gravitational lens. A light ray from the source is deflected by an angle α at the lens. The angles between the optical axis and the true source and the optical axis and the image are φ and θ respectively. The angular diameter distances between the observer and lens, lens and source and observer and source are D_L, D_{LS} and D_S respectively. The lengths A, B and C allow us to derive the lens equation (shown in Section 3.1.2).

which is the deflection angle for an extended lens distribution. We can also define a vector such that

$$\boldsymbol{\alpha} = \hat{\boldsymbol{\alpha}} \frac{D_{LS}}{D_S}, \tag{3.5}$$

where the distances D_S and D_{LS} are the angular diameter distances between the observer and source and the lens and source respectively. So the deflection angle for an extended lens becomes

$$\boldsymbol{\alpha}(\boldsymbol{\theta}) = \left(\frac{4 G D_L D_{LS}}{c^2 D_S} \right) \int d^2\theta' \frac{\Sigma(\boldsymbol{\theta} - \boldsymbol{\theta}')}{(\boldsymbol{\theta} - \boldsymbol{\theta}')^2}. \tag{3.6}$$

Now, it is useful to define a dimensionless surface mass density,

$$\kappa = \frac{\Sigma}{\Sigma_{\text{crit}}}, \tag{3.7}$$

where κ is also known as the convergence (discussed in more detail in Section 3.1.4). Σ_{crit} is the critical surface mass density which is given by

$$\Sigma_{\text{crit}} = \frac{c^2}{4\pi G} \frac{D_S}{D_L D_{LS}}. \tag{3.8}$$

From these, we define a scaled deflection angle:

$$\boldsymbol{\alpha}(\boldsymbol{\theta}) = \frac{1}{\pi} \int d^2\theta' \kappa(\boldsymbol{\theta}') \frac{(\boldsymbol{\theta} - \boldsymbol{\theta}')}{(\boldsymbol{\theta} - \boldsymbol{\theta}')^2}. \tag{3.9}$$

These expressions are only valid when the deviation of the light ray is small compared with the scale on which the mass distribution changes significantly. This assumption is relevant for almost all astrophysical situations such as lensing by galaxies, clusters of galaxies and large scale structure.

3.1.2 The Lens Equation

Given the deflection angle, we can now relate the position of a lensed object on the sky to its true, unlensed, position. The basic geometry of a lensing event is shown in Figure 3.2. The *thin lens approximation* states: 'If the size of the lensing object is very much smaller than the distance between the observer, lens and source, we can assume that all lensing occurs at a single lens plane'. The basic lensing equation can be derived from Figure 3.2 easily, since from the figure we see that $A = B + C$

and $A = \theta D_S$, $B = \hat{\alpha} D_{LS}$ and $C = \varphi D_S$. Rearranging gives the lens equation

$$\boldsymbol{\varphi} = \boldsymbol{\theta} - \hat{\boldsymbol{\alpha}}(\boldsymbol{\theta}) \, \frac{D_{LS}}{D_S} \tag{3.10}$$

where the angle $\boldsymbol{\theta}$ is the position of the lensed image on the sky, $\boldsymbol{\varphi}$ is the true (unlensed) angular position of the source on the sky. To simplify this equation, simply replace the deflection angle with Equation (3.5) so the lens equation becomes

$$\boldsymbol{\varphi} = \boldsymbol{\theta} - \boldsymbol{\alpha}(\boldsymbol{\theta}). \tag{3.11}$$

If more than one solution exists to this equation, then multiple images of the source object will be observed, which only occurs in the strong lensing regime. Analytic solutions for the lens equation only exist for some lens models (e.g. the isothermal sphere). When an analytical solution is not available, numerical techniques such as ray tracing or line-of-sight integrations are used to determine the light path. The research in this thesis uses line-of-sight integrations in numerical N-body simulations to determine the lensing signal. This method will be explained in further detail in Chapter 5.

3.1.3   Lensing Potential

To determine the path of the light ray, we consider what happens to the photons as they pass by a lensing mass. For a particle traveling in the Newtonian gauge (which is a perturbed form of the RW line element in Equation (2.4)), with r as the radial coordinate, θ as an angle on the sky and $d\phi = 0$:

$$c^2 d\tau^2 = a^2(\eta) \left[(1 + 2\Phi_N) d\eta^2 - (1 - 2\Phi_N)(dr^2 + r^2 d\theta^2) \right], \tag{3.12}$$

where η is the conformal time[1], we have a comoving coordinate space, where Φ_N is the Newtonian potential which is given by the solution to Poisson's equation,

$$\nabla^2 \Phi_N = 4\pi G \rho \delta a^2, \tag{3.13}$$

---

[1] The conformal time is defined by $d\eta = \frac{c \, dt}{a(t)}$, where $a(t)$ is the scale factor of the Universe.

where a is the expansion factor of the Universe and δ is the mean overdensity which is given by

$$\delta = \frac{\rho - \bar{\rho}}{\bar{\rho}}, \tag{3.14}$$

where $\bar{\rho}$ is the mean density.

It is not possible for a photon to be accelerated in the radial direction as it is already traveling at the speed of light, however a photon may be accelerated in the transverse direction. Putting Equation (3.12) in to the geodesic equation

$$\ddot{x}^{\mu} + \Gamma^{\mu}_{\alpha\beta}\dot{x}^{\alpha}\dot{x}^{\beta} = 0, \tag{3.15}$$

(e.g. Peacock, 1999), where x^{μ} is a space-time position four-vector and $\dot{x}^{\mu} = dx^{\mu}/dp$ where p is an affine parameter which we make equal to the coordinate time t for a photon, gives the relativistic acceleration equation:

$$\ddot{\boldsymbol{\alpha}} = \frac{\partial}{\partial\eta}r^2\frac{\partial}{\partial\eta}\boldsymbol{\alpha} = -2\frac{\partial}{\partial\boldsymbol{\theta}}\Phi_N, \tag{3.16}$$

where r is the radial coordinate of the photon.

The right-hand side of Equation (3.16) is the transverse gradient of a potential, which implies that the left-hand side must also be a transverse gradient of the potential:

$$\boldsymbol{\alpha} = \nabla_{\perp}\phi(r) = \frac{\partial}{\partial\boldsymbol{\theta}}\phi(r). \tag{3.17}$$

Now, putting Equation (3.17) into equation (3.16) and substituting $\eta = -r$, which is true for a photon traveling on an unperturbed radial path (this is called the **Born approximation**) gives:

$$\frac{\partial}{\partial r}r^2\frac{\partial}{\partial r}\phi(r) = -2\Phi_N, \tag{3.18}$$

which can be solved for the lensing potential

$$\phi(r) = 2\int_0^r dr'\left(\frac{r - r'}{rr'}\right)\Phi_N(r'). \tag{3.19}$$

Taking the transverse divergence of Equation (3.17) gives

$$\nabla_\perp \cdot \boldsymbol{\alpha} = \nabla_\perp^2 \phi. \tag{3.20}$$

Equation 3.9 is the solution of $\nabla_\perp \boldsymbol{\alpha} = 2\kappa$. So,

$$\nabla_\perp^2 \phi = 2\kappa. \tag{3.21}$$

Taking the 3D Laplacian of both sides of Equation 3.19, where $r^2 \nabla^2 = (\partial_r r^2 \partial_r + \nabla_\perp^2)$, gives

$$\kappa(\boldsymbol{\theta}, r) = \frac{3H_0^2 \Omega_m}{2c^2} \int_0^r dr' \; \frac{(r - r')r'}{ra} \; \delta(\boldsymbol{\theta}, r'). \tag{3.22}$$

These equations all refer to how photons passing massive objects will be deflected from their path as they travel through the Universe.

3.1.4   Gravitational Lensing Distortions

Gravitational lensing not only deflects photons from a straight path, it also acts to distort the images. It is possible for the position of two objects on a plane relative to each other to change. When considering positions of objects on a plane, it is convention in gravitational lensing to relate deflection angles to each other as given in Equation (3.11). Thus, the separation of two objects on a plane after their deflection relates to their initial separation before deflection by:

$$\Delta\boldsymbol{\varphi}_i = \left(\frac{\partial\varphi_i}{\partial\theta_j}\right)\Delta\theta_j + \left(\frac{1}{2}\frac{\partial^2\varphi_i}{\partial\theta_j\partial\theta_k}\;\Delta\theta_j\Delta\theta_k\right). \tag{3.23}$$

If we are only interested in the first order effects, the separation becomes

$$\Delta\boldsymbol{\varphi}_i = \Delta\theta_j\left(\delta_{ij}^K - \frac{\partial}{\partial\theta_i}\alpha_j\right). \tag{3.24}$$

Substituting Equation (3.17) into this:

$$\Delta\boldsymbol{\varphi}_i = \Delta\theta_j\left(\delta_{ij}^K - \frac{\partial}{\partial\theta_i}\frac{\partial}{\partial\theta_j}\phi\right). \tag{3.25}$$

Splitting these forces up in to *local* and *non-local* forces:[2]

$$\Delta\varphi_i = \Delta\theta_j \left(\delta_{ij}^K - \frac{1}{2}\partial^2\phi \; \delta_{ij}^K - \left[\partial_i\partial_j\phi - \frac{1}{2}\partial^2\phi \; \delta_{ij}^K \right] \right), \qquad (3.26)$$

where

$$\partial^2 = \frac{\partial^2}{\partial\theta_1^2} + \frac{\partial^2}{\partial\theta_2^2}, \qquad (3.27)$$

and

$$\partial_i = \frac{\partial}{\partial\theta_i}. \qquad (3.28)$$

The local forces act to magnify or de-magnify the position of the two points on the plane and we see the role of the **Convergence** (κ) defined in Equation (3.22);

$$\kappa = \frac{1}{2}\partial^2\phi. \qquad (3.29)$$

Convergence is easily visualised when considering the image of an object getting larger (or smaller) when viewed after traveling through the Universe and being gravitationally lensed (rather than just considering the relative separation of two points).

The non-local force that acts on the photons causes a distortion to the image known as **Shear** (γ)

$$\gamma_{ij} = \partial_i\partial_j\phi - \frac{1}{2}\partial^2\phi \; \delta_{ij}^K. \qquad (3.30)$$

A simple explanation of shear is that it makes a circular object become elliptical after being gravitationally lensed. This ellipticity (tangential to the projected separation from the lensing object) is what observers look for when trying to detect gravitational lensing (see Figure 3.3 for a pictorial description of convergence and shear). The shear can be decomposed into two separate components:

$$\gamma = \begin{pmatrix} \gamma_1 & \gamma_2 \\ \gamma_2 & -\gamma_1 \end{pmatrix}, \qquad (3.31)$$

---

[2]One way of considering the difference between a local and a non-local force is to consider an example on the Earth. Gravity that makes us come back to the ground if we jump is a local force but tides that cause the oceans to come in and out are due to the moon which is a non-local force.
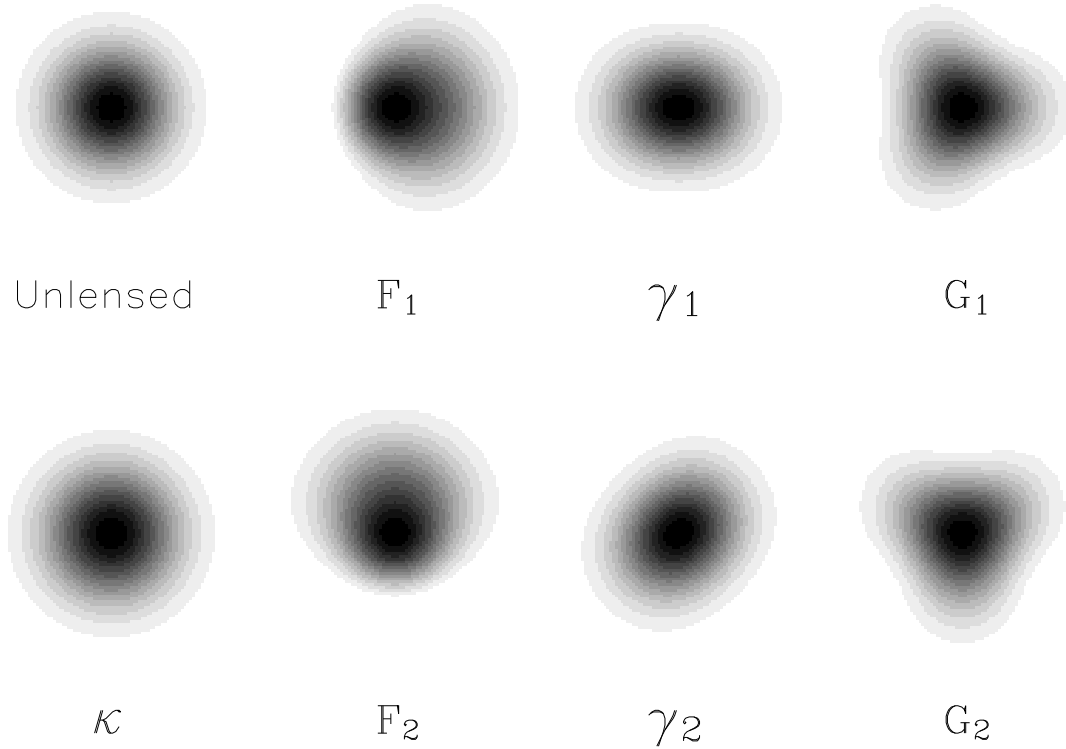
Figure 3.3: **This picture shows the different distortions that can happen to an object due to gravitational lensing. In 2D, this example shows an object that initially appears as a circle. It can then undergo one or all of seven distortions due to gravitational lensing. The first is convergence, κ, which in this case is acting to make the image appear larger. The second and third are shears, γ_1 and γ_2. The object can also undergo flexion where either the centroid is shifted $\mathcal{F}_1$ and $\mathcal{F}_2$ or its shape is modified by a spin-3 field $\mathcal{G}_1$ and $\mathcal{G}_2$.**

Image Credit: Bacon et al. (2006)

which can be related to the lensing potential by

$$\gamma_1 = \frac{1}{2}\left(\partial_1^2\phi - \partial_2^2\phi\right), \tag{3.32}$$

$$\gamma_2 = \partial_1\partial_2\phi. \tag{3.33}$$

So, the distortions to the relative separation of two points on a plane can be described to first order by:

$$\Delta\varphi_i = \Delta\theta_j\left(\delta_{ij}^K\left[1 - \kappa\right] - \gamma_{ij}\right). \tag{3.34}$$

The magnification of a lensed source can be determined by starting with **Liouville's**

theorem (e.g. Peacock, 1999), which states that the phase-space distribution function, f_N, is constant with time

$$\frac{df_\mathrm{N}}{dt} = 0, \tag{3.35}$$

which implies that for particles traveling on trajectories through phase space, there is no creation or destruction of particles within the volume. This can be expanded to

$$\frac{\partial}{\partial t} f_\mathrm{N} + \dot{\boldsymbol{x}}\frac{\partial}{\partial \boldsymbol{x}} f_\mathrm{N} + \dot{\boldsymbol{p}} \frac{\partial}{\partial \boldsymbol{p}} f_\mathrm{N} = 0, \tag{3.36}$$

where $\boldsymbol{p}$ is the momentum vector, $\boldsymbol{x}$ is the position vector and t is time. The first two terms of this equation are just a traditional equation of motion. The third term is the time derivative of the momentum, which is actually a force, in this case gravity. From this equation, we can determine that the surface brightness of lensed objects is conserved because the frequency of the light is unchanged by lensing. So, a bundle of photons traveling through the Universe may be distorted and the volume they occupy may change, but the number of photons in the bundle remains unchanged leading to a conservation of surface brightness. For the case where an object is magnified, the number of photons coming from the object actually increases because of the larger area, but the overall surface brightness is the same. The term for this brightness is *intensity*

$$I(\boldsymbol{\varphi}) = I(\boldsymbol{\theta}), \tag{3.37}$$

and this equation states that the intensity before lensing is the same as the intensity after lensing. Now, the definition of magnification is the ratio of the final intensity to the initial intensity

$$\mu = \frac{I(\boldsymbol{\theta})\, d^2\theta}{I(\boldsymbol{\varphi})\, d^2\varphi}, \tag{3.38}$$

and since $I(\boldsymbol{\theta}) = I(\boldsymbol{\varphi})$, the magnification is given by the change in the area of the image,

$$d^2\theta = \left[\det\left(\frac{\partial \varphi_i}{\partial \theta_j}\right) \right]^{-1} d^2\varphi = [\det \boldsymbol{J}]^{-1}\, d^2\varphi, \tag{3.39}$$

where $\mathbf{J}$ is the Jacobian;

$$\mathbf{J} = \begin{pmatrix} 1 - \kappa - \gamma_1 & -\gamma_2 \\ -\gamma_2 & 1 - \kappa + \gamma_1 \end{pmatrix}. \tag{3.40}$$

So the magnification is the determinant of the inverse Jacobian $\mu = [\det \boldsymbol{J}]^{-1}$,

$$\mu \;=\; \left|\frac{\partial \varphi_i}{\partial \theta_j}\right|^{-1} \tag{3.41}$$

$$\;=\; \left[(1-\kappa)^2 - |\gamma|^2\right]^{-1}, \tag{3.42}$$

where $\gamma = \gamma_1 + i\gamma_2$.

Much of this thesis work will involve using the weak lensing equations detailed above to analyse the lensing potential, shear and convergence of large simulations of the Universe. The third order effects of Equation (3.23) are not considered in this thesis but they could be included in the pipeline in future so will be explained here for completeness. The third order effects are known as Flexion and were first described in Goldberg & Bacon (2005) and Bacon et al. (2006). From the second term of Equation (3.23), we let

$$\frac{\partial^2 \varphi_i}{\partial \theta_j \partial \theta_k} = \boldsymbol{D}_k = \partial_k \boldsymbol{J}. \tag{3.43}$$

Using results from Kaiser (1995), it can be shown that

$$\boldsymbol{D}_1 \;=\; \begin{pmatrix} -2\gamma_{1,1} - \gamma_{2,2} & -\gamma_{2,1} \\ -\gamma_{2,1} & -\gamma_{2,2} \end{pmatrix}, \tag{3.44}$$

$$\boldsymbol{D}_2 \;=\; \begin{pmatrix} -\gamma_{2,1} & -\gamma_{2,2} \\ -\gamma_{2,2} & 2\gamma_{1,2} - \gamma_{2,1} \end{pmatrix}. \tag{3.45}$$

D_{ijk} can be expressed as the sum of two flexions

$$D_{ijk} = \mathcal{F}_{ijk} + \mathcal{G}_{ijk}, \tag{3.46}$$

where $\mathcal{F} = \mathcal{F}_1 + i\mathcal{F}_2$ and $\mathcal{G} = \mathcal{G}_1 + i\mathcal{G}_2$. The $\mathcal{F}$ flexion shape change manifests itself as a centroid shift and the $\mathcal{G}$ flexion spin-3 shape change induces a 'three-leaf clover' shape (Figure 3.3).

3.1.5   Critical Curves, Caustics and the Einstein Radius

A lens may have a closed, smooth curve defined by $\det(\mathbf{J}) = 0$. This is known as a *critical curve* in the lens plane and when mapped on to the source (image) plane,
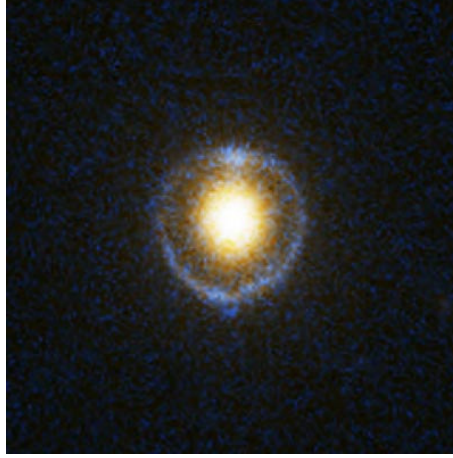
Figure 3.4: Einstein ring system SDSSJ162746.44-005357.5 as imaged by the Hubble Space Telescope Advanced Camera for Surveys. The unique, almost perfect, alignment of this system results in the background galaxy being lensed into an Einstein ring.

Image Credit: NASA, ESA, A. Bolton (Harvard-Smithsonian CfA) and the SLACS Team

the curve is is known as a *caustic* and is not necessarily smooth. For the special case of a point source, the critical curve is known as the *Einstein radius*. The Einstein radius is a characteristic angle for gravitational lensing. The Einstein radius is given as

$$\theta_E = \left(\frac{4GM}{c^2} \frac{D_{LS}}{D_L D_S} \right)^{1/2},$$

(e.g. Bartelmann, 2010), where G is the gravitational constant, M is the mass of the lens. Substituting this into Equation (3.10), the lens equation for a point mass becomes

$$\varphi = \theta - \frac{\theta_E^2}{\theta}, \tag{3.47}$$

which can be solved to show the position of the image on the sky

$$\theta = \frac{1}{2}\varphi \pm \sqrt{\frac{\varphi}{4} + \theta_E^2}. \tag{3.48}$$

The Einstein radius can be observed directly when $\varphi = 0$, so $\theta = \pm\theta_E$ which means the source, lens and observer are all perfectly aligned. The light from the source is distorted into a ring around the lens and is known as the Einstein ring. An example of an Einstein ring, where the background source is almost perfectly aligned with the foreground lens, is shown in Figure 3.4.

For a source lying on a caustic, Equation (3.42) predicts infinite magnification. However, this does not occur in reality because sources are extended. Indeed, infinite magnification would not occur for a point source either due to failure of the geometrical-optics approximation near critical curves. However, a source lying close to a caustic will still experience significant magnification, a characteristic of *strong gravitational lensing*. Other characteristics of strong gravitational lensing are multiple images and giant arcs. Multiple images occur when a source crosses a caustic and giant arcs occur when an extended image is located on the caustic, which causes the multiple images to merge.

If a source lies outside of the caustic, this is the *weak lensing regime* where the magnifications and distortions are very small and must be analysed statistically. This thesis deals exclusively with weak lensing and then next section will give further details on the weak lensing phenomenon.

3.2   Weak Lensing

As the previous sections have shown, gravitational lensing has two distinct regimes. Strong lensing occurs when a source is located inside or directly on a caustic, which is limited to the centres of very dense mass concentrations, and is characterised by significant magnification, multiple images and giant arcs. The weak lensing regime occurs when a source lies significantly outside the caustic. This is far more common than the case of strong lensing, occurring throughout most of the Universe. Weak lensing is characterised by magnifications and distortions that are so small, $\gamma \ll 1$ and $\kappa \ll 1$, that they must be identified statistically.

Analysis of weak lensing enables the direct study of the mass distribution (or gravitational potential) of the Universe. There are two weak lensing effects that can be used to perform these studies; The weak lensing magnification effect results in detection of a higher number density of background galaxies. Weak lensing shear typically results in a very small change of galaxy ellipticity of just $\sim 1\%$. If galaxies were circular, this would be a straightforward observation, however, galaxies are intrinsically elliptical so observationally we look for a mean tangential alignment

around lensing objects to determine a shear field, or more generally a correlated pattern of galaxy ellipticities. The ellipticity of a galaxy can be defined generally in terms of moments (e.g. Bartelmann & Schneider, 2001), but for a galaxy with elliptical isophotes, the ellipticity is related to its semi-major and semi-minor axes, a and b and its orientation θ by

$$e_1 = \frac{a-b}{a+b}\cos(2\theta) \tag{3.49}$$

$$e_2 = \frac{a-b}{a+b}\sin(2\theta), \tag{3.50}$$

and $e = e_1 + ie_2$. To first order in ellipticity, the measured ellipticity, e^{obs}, of a galaxy is a combination of the galaxies intrinsic ellipticity, e^S, and the shear

$$e^{\mathrm{obs}} \simeq e^S + \gamma. \tag{3.51}$$

Most studies look at the power spectrum of the signal (see Chapter 5) or the correlations of the observed ellipticities

$$\langle e_i^{\mathrm{obs}} e_j^{\mathrm{obs}} \rangle = \langle e_i^S e_j^S \rangle + \langle \gamma_i e_j^S \rangle + \langle e_i^S \gamma_j \rangle + \langle \gamma_i \gamma_j \rangle, \tag{3.52}$$

where $z_i < z_j$. The first term on the right is the intrinsic galaxy alignment, the second and third terms are the shear-ellipticity correlations and the final term is the cosmological signal that we are interested in. The second term is expected to be zero but the other terms can be significant and need to be considered (e.g. Schneider, 2006). Chapter 7 has further discussion on intrinsic galaxy alignments.

There are three regimes in which weak lensing occurs; galaxy-galaxy lensing, cluster-galaxy lensing and cosmic shear and the work in this thesis is based on the latter. For completeness, I will briefly introduce the basics of measuring the weak gravitational lensing shear signal observationally as well as briefly discussing the first two weak lensing regimes. I will then move on to the concepts of cosmic shear analysis that are particularly important for this work.

3.2.1   Measuring Weak Gravitational Lensing Shear

Galaxies generally have reasonably elliptical shapes. However, it is difficult to specifically measure a major and minor axis of a galaxy unless it is large on the sky and reasonably luminous. Also, images have noise and a point spread function (PSF). The PSF tends to make images larger, blurred and rounder than the actual image. Telescope correction can elongate an image and exposures that are taken off-axis can also elongate an image. Images are also pixelated, which means that the true ellipticity can not be measured because everything is discretised.

An example of a different parametrisation of the ellipticity from that given in equations (3.49) and (3.50) is

$$e_1 \quad = \quad \frac{a^2 - b^2}{a^2 + b^2} \cos(2\theta), \tag{3.53}$$

$$e_2 \quad = \quad \frac{a^2 - b^2}{a^2 + b^2} \sin(2\theta). \tag{3.54}$$

So,

$$e_i^{\mathrm{obs}} = e_i^{\mathrm{S}} + \left[2 - (e_i^{\mathrm{S}})^2 \right] \gamma, \tag{3.55}$$

where e_i^{obs} is the measured ellipticity, e_i^{S} is the intrinsic ellipticity (and the galaxy is intrinsically elliptical) and γ is the shear. In this parametrisation, an object can not continue to become more elliptical beyond a straight line. An amount of shear will change the ellipticity of an object. The same amount of shear applied again will produce less of a change in ellipticity. From this, we can determine a shear estimator

$$\tilde{\gamma} \equiv \frac{e_i}{P_{sh}}, \tag{3.56}$$

(Kaiser et al., 1995) where equation (3.55) gives

$$P_{sh} = \frac{\partial e_i}{\partial \gamma} = 2 - (e_i^{\mathrm{S}})^2. \tag{3.57}$$

So, to measure the shear of an image, you need an ellipticity and a P_{sh} and these will give a shear estimator (equation 3.56).
The ellipticity of an image can be related to the shear by measuring the second order surface brightness moments (quadrupole moments) of the image (Bartelmann & Schneider, 2001). For a galaxy with a surface brightness $I(\boldsymbol{\theta})$ at an angular

position $\boldsymbol{\theta}$,

$$\tilde{\boldsymbol{\theta}} \equiv \frac{\int d^2\theta W[I(\boldsymbol{\theta})]\boldsymbol{\theta}}{\int d^2\theta W[I(\boldsymbol{\theta})]}, \tag{3.58}$$

where $\tilde{\boldsymbol{\theta}}$ is the centre of the image and $W[I(\boldsymbol{\theta})]$ is a weight function chosen such that the integrals will converge. Thus, the quadrupole moments are

$$Q_{ij} = \frac{\int d^2\theta W[I(\boldsymbol{\theta})](\theta_i - \tilde{\theta}_i)(\theta_j - \tilde{\theta}_j)}{\int d^2\theta W[I(\boldsymbol{\theta})]}, \qquad i,j \in \{1,2\}. \tag{3.59}$$

From this, a complex ellipticity can be defined as

$$e \equiv \frac{Q_{11} - Q_{22} + 2iQ_{12}}{Q_{11} + Q_{22}}. \tag{3.60}$$

The measured ellipticity will also include the weight function and the point spread function. Quantifying shapes of well resolved galaxies is fairly straight forward. However, the blurring of the atmosphere is a serious complication. The transformation between the source and observed ellipticity is given by

$$e^{\mathrm{obs}} = \begin{cases} \dfrac{e^{\mathrm{S}} + g}{1 + g^* e^{\mathrm{S}}} & \text{for} \quad |g| \leq 1 \\[4mm] \dfrac{1 + g(e^{\mathrm{S}})^*}{(e^{\mathrm{S}})^* + g^*} & \text{for} \quad |g| > 1, \end{cases} \tag{3.61}$$

(Seitz & Schneider, 1997) where g is the reduced shear

$$g(\boldsymbol{\theta}) \equiv \frac{\gamma(\boldsymbol{\theta})}{1 - \kappa(\boldsymbol{\theta})}. \tag{3.62}$$

Very basically, the steps to create a shear catalogue are

- Reduce your data well

- Detect objects

- Separate stars from galaxies

- Model the PSF with the stars

- Remove the effect of the PSF

- Measure the galaxy shape

The most popular software for detecting objects is SExtractor[3]. To find objects in noisy data, one must smooth the data with a smoothing kernel where the optimal kernel is a smoothing with the object itself. However, the smoothing kernel is typically round which can bias the detection algorithm toward round objects. Objects may also partially overlap; this is called blending and the effect is most severe in deep ground-based images. Ideally, these objects would not be used in a lensing analysis. Spurious detections like cosmetic defects and diffraction spikes also need to be removed.

After the objects have been detected and the PSF has been corrected, the shape of the galaxies must be measured. There is also noise to account for (which occurs in both ground- and space-based observations). Clearly, it becomes harder to measure shapes if the galaxy is faint and the seeing is large (relative to the galaxy size). Dealing with these systematics is the largest difficulty in measuring the weak lensing signal as observational distortions are typically larger than the lensing signal.

The various shape measurement pipelines only differ in the final two steps mentioned above. There are a number of pipelines available but almost all are based on one of the three methods mentioned below.

KSB

The most widely used shape measurement technique is the Kaiser, Squires and Broadhurst (KSB) method (Kaiser et al., 1995). This method is based on the assumption that the PSF is circular with an anisotropic distortion (ie constant elliptical isophotes). It is several orders of magnitude faster than all other methods and allows for the accurate removal of smearing of galaxies due to the anisotropic PSF. This method is good for large, high signal-to-noise galaxies. However, it is unstable to small changes in the method and has galaxy size and magnitude dependent biases. For small, low signal-to-noise galaxies, it can be very inaccurate. Future surveys will need to improve on the systematic errors by an order of magnitude.

---

[3]SExtractor http://www.astromatic.net/software/sextractor

Shapelets

Shapelets are a series of orthogonal basis functions that can be summed together to model complex galaxy morphologies (Refregier, 2003a). The shapelets technique works reasonably well for large, bright galaxies but is not very good for smaller, fainter galaxies. The flexibility of shapelets to model any galaxy morphology feature is also the main drawback. Increasing the number of shapelets improves the fit - but you end up just fitting noise. Thus, shapelets are well suited to modeling high signal-to-noise objects but the faint, fuzzy objects that make up the majority of the lensing survey don't gain much from this type of analysis. This technique does not suffer from the poor PSF assumptions like KSB but it does give the galaxy model too much freedom.

Lensfit

Lensfit uses Bayesian model fitting to determine the shape of the galaxy (Miller et al., 2007; Kitching et al., 2008). If the wrong prior is used, lensfit can give a biased result. Thus, a second data set is generally used to set the prior. Lensfit is very promising on simulated data and is by far the best method tested by the Canada France Hawaii Telescope Legacy Survey (CFHTLS) systematics collaboration. This new way of thinking is a real breakthrough in shear measurement.

3.2.2 Galaxy-Galaxy Lensing

When probing the mass distribution of an individual galaxy, many people will measure rotation curves as a first step (see Sofue & Rubin (2001) for a review). This method relies heavily on luminous tracers and as such, can not measure the mass profile of radii beyond the luminous extent of the galaxy. To understand the shape and properties of dark matter halos, we need to probe the mass distribution over a wide range of projected radii (up to $\sim 250h^{-1}$ kpc). Globular clusters, planetary nebulae and satellite galaxies (Côté et al., 2003; Prada et al., 2003; Romanowsky et al., 2004; Battaglia et al., 2005) may also be used to estimate the mass of a galaxy out to further radii, but these methods also rely on luminous tracers.

Galaxy-galaxy lensing deals with the lensing of a background galaxy by an individual foreground galaxy. Currently only five galaxy-galaxy lenses are known where

the lensed source shows multiple images (i.e. is strongly lensed), has a confirmed redshift and is reasonably bright at optical wavelengths (Warren et al., 1996; Bolton et al., 2005; Cabanac et al., 2005; Willis et al., 2005). Far more common is weak galaxy-galaxy lensing. The galaxy-galaxy weak lensing signal is a statistically built, mean distortion of images of faint galaxies resulting in a weak preference toward the tangential alignment of faint galaxies around brighter galaxies. The strength of this signal relies on the distance between the source and lens galaxies, the mass of the lens galaxy and the angular separation of the lens and the source on the sky. This technique offers a way of measuring the mass of the lens galaxy well beyond the optical radii and this effect has been detected in several surveys (e.g., Brainerd et al., 1996; Hoekstra et al., 2003; Seljak et al., 2005).

Another anticipated use for galaxy-galaxy lensing came from the prediction that dark matter halo profiles in CDM simulations may be triaxial (Dubinski & Carlberg, 1991). Two independent groups have attempted to observationally measure this ellipticity using galaxy-galaxy lensing. Hoekstra et al. (2004) argued that there was a positive detection of ellipticity in their field while Mandelbaum et al. (2006) claim a null result, with no conclusive evidence of halo ellipticity being found. So the question of whether halo shapes can indeed be measured using galaxy-galaxy lensing is still wide open and the problem will need to be tackled by both observers and theorists.

3.2.3   Cluster - Galaxy Lensing

The mass of galaxy clusters was traditionally determined by using dynamical methods and the virial theorem (e.g Chapman et al., 1988; Carlberg et al., 1996; Girardi et al., 2000) or investigation of the X-ray gas residing in the cluster potential (e.g. Sarazin, 1986; David et al., 1994; Leahy & Yin, 2000). However, these methods make strong assumptions which leave them vulnerable to biased estimates. The dynamical methods rely on the clusters being virialised, which is not guaranteed since the typical dynamical time scale of a cluster is close to the Hubble time. The X-ray methods assume that the intra-cluster gas is in hydrostatic equilibrium which is difficult to accurately assess with a telescope.

Cluster-galaxy lensing makes no assumptions on the dynamical state of the lensing

cluster and is independent of luminous tracers. This source of lensing occurs when background source galaxies are gravitationally lensed by a foreground galaxy cluster. This is the most common configuration for strong lens events and many giant arcs and multiple images have been identified from cluster-galaxy lenses (e.g. Soucail et al., 1987; Pello et al., 1991; Kubo et al., 2010). The weak lensing signal around galaxy clusters is always present. Weak lensing by a cluster of galaxies allows us to form a parameter-free map of the projected (2-D) mass distribution of the lensing cluster. This in turn allows the mapping of the dark matter distribution directly (Kaiser & Squires, 1993; Kaiser et al., 1995). These cluster-galaxy lens analyses, in concert with X-ray gas analyses, were responsible for the identification of the Bullet cluster, one of the seminal discoveries in cosmology discussed in Chapter 1. This analysis provided direct empirical evidence for the existence of dark matter.

The ellipticity of the halos in clusters is dependent on cosmology (e.g. Splinter et al., 1997) and evolves with redshift (e.g. Allgood et al., 2006). Attempts at measuring the cluster dark matter halo ellipticity have been made and appear to agree with predictions from N-body simulations (e.g. Deb et al., 2010; Oguri et al., 2010). Measuring shapes of clusters is still a reasonably new analysis technique and work is still ongoing to perfect the measurements.

3.2.4 Cosmic Shear

The effects mentioned above all deal with lensing by a localised mass concentration like a galaxy or a cluster of galaxies. It is important to understand that light can also undergo weak lensing from large-scale structure (LSS). As light travels from a source through the Universe, it is continually deflected, magnified and distorted due to the inhomogeneity of the LSS. The result of these effects are that images of distant galaxies are distorted from their original size and shape. Collecting a large sample of these cosmologically lensed galaxies reveals the statistical properties of the LSS (Gunn, 1967b; Blandford et al., 1991; Chang et al., 2004). In contrast to the galaxy-galaxy and cluster-galaxy lensing mentioned above, light is not deflected at a specific lens plane, but rather by a 3-D matter distribution.

The work in this thesis is focused on the cosmic shear signal, which can be determined from the underlying matter density of the Universe. In a matter dominated

Universe, where $\rho \propto a^{-3}$, Poisson's Equation (3.13) can be written as

$$\nabla^2 \Phi = \frac{3H_0^2 \Omega_m \delta}{2a},\tag{3.63}$$

since $H^2 = \frac{8\pi G\rho}{3\Omega_m}$ (assuming that only the matter component clusters). If we remember that

$$\nabla^2 = \frac{1}{r^2}\frac{\partial}{\partial r}r^2\frac{\partial}{\partial r} + \frac{\partial^2}{\partial \theta^2},\tag{3.64}$$

and substitute this in to the lensing potential given in Equations (3.18) and (3.19), we find an effective convergence for cosmological lensing

$$\kappa(\boldsymbol{\theta}, r_s) = \frac{3H_0^2 \Omega_m}{2c^2}\int_0^{r_s} dr\ \frac{(r_s - r)r}{r_s a}\ \delta(\boldsymbol{\theta}, r),\tag{3.65}$$

where r_s is the comoving distance to the source redshift plane.

The shear can be determined on a flat-sky by Fourier transforming the convergence field. The shear and convergence Fourier coefficients are related by

$$\gamma_1(\boldsymbol{\ell}) = \kappa(\boldsymbol{\ell})\frac{(\ell_x^2 - \ell_y^2)}{(\ell_x^2 + \ell_y^2)},\tag{3.66}$$

$$\gamma_2(\boldsymbol{\ell}) = \kappa(\boldsymbol{\ell})\frac{2\ell_x\ell_y}{\ell_x^2 + \ell_y^2},\tag{3.67}$$

where $\kappa(\boldsymbol{\ell})$ is the Fourier transform of the effective convergence field and ℓ_x and ℓ_y are the Fourier variables. The statistical properties of these fields can be determined through calculating their power spectra. This is explained in far more detail in Chapter 5.

3.2.5   Cosmological Parameter Estimates

Cosmic shear probes the large-scale density distribution of the Universe without reliance on any luminous tracers. This makes cosmic shear the ideal tool to probe the dark Universe and put constraints on the parameters that make up the standard model of Cosmology. One way that we can probe this sensitivity is by comparing the cosmic shear power spectrum or correlation function with theoretical expectations. Hu (1999) pointed out that the constraining power of cosmic shear surveys will be increased by accounting for the redshift distribution of galaxies within the survey.

Consequently, tomographic and 3-D cosmic shear analyses are expected to provide up to a factor of ~ 2 improvement on parameter constraints (Kitching et al., 2010).

To further constrain the cosmological parameters, cosmic shear estimates can be combined with estimates from other methods such as Cosmic Microwave Background and Baryon Acoustic Oscillation studies as well as galaxy redshift surveys (e.g. Brown et al., 2003; Schrabback et al., 2010).

3.3 Summary

This chapter has introduced the concepts and formalisms that describe gravitational lensing, in particular weak gravitational lensing. Today, weak gravitational lensing is regularly observed in the Universe (e.g. Kubo et al., 2009; Tereno et al., 2009). Analysing the weak lensing signal is an excellent method for investigating the dark Universe because it occurs throughout all the Universe and is independent of any luminous tracers. In order to better interpret weak lensing observations, we require detailed weak lensing simulations for comparison. The work in this thesis addresses this requirement by developing a pipeline specifically to generate weak lensing simulations.

Chapter 4

Introduction to Simulations and Weak Lensing Surveys

4.1 Introduction

There are many well-motivated theories of cosmology, but to determine which represents the real Universe, we must inevitably compare the theories to observation. However, observations can not provide a complete picture because they are subject to noise, systematics and limitations on how much of the Universe can actually be seen. The only way to optimally interpret these observations is with numerical simulations that contain a full complement of cosmological information and with similar limitations to the observational data imposed. Observational data need a covariance matrix for maximum likelihood or full Bayesian analysis. As will be explored in Chapter 6, analytic approximations of the covariance matrix may be inadequate for analysis but simulations can provide a covariance matrix which includes the non-linear mode-coupling that is essential for precision analysis. Additionally, by modelling the sources of non-Gaussianity in our simulations and testing our cosmological analysis techniques on them, we can determine the strengths and weaknesses of each analysis tool and better interpret results from observational data sets. We can also use simulations to model the propagation of errors in cosmological analyses, which is often not possible with the observational data. Furthermore, cosmological simulations are an essential tool in the design phase of telescope missions – providing estimates on the cosmological parameter accuracies that a particular telescope design may achieve and allowing that design to be adjusted to increase measurement

precision. Numerical simulations of cosmological structure formation have also become an indispensable tool for investigating the non-linear evolution of the Universe, where analytic solutions to the equations are not possible. Advances in this field have been enormous over the last few decades with computer hardware becoming increasingly powerful and also with incredibly sophisticated algorithms being written to optimise and speed up the running of the software.

In this Chapter, Section 4.2 will give a brief introduction to cosmological N-body simulations and detail the underlying algorithms that allow them reproduce the statistics of our Universe. More specific details of the simulations used in this thesis can be found in Chapter 5. Section 4.3 goes on to describe some existing and future weak gravitational lensing surveys and how cosmological simulations will aid in both preparing for the surveys and ultimately analysing their data.

4.2   N-Body Simulations

N-body simulations mimic the statistical properties of the Universe by sampling the density field with discrete particles. Early computer simulations relied on using a direct summation method for calculating the forces between particles in the N-body problem (e.g. Peebles, 1970; Press & Schechter, 1974; White, 1976; Aarseth et al., 1979). However, as computing power increased, so did the number, N, of particles in the simulations and this $O(N^2)$ direct summation method was no longer efficient. In response to this, several different methods to calculate the forces between particles in collisionless systems were developed. These methods use Fourier techniques to determine the large scale gravitational fields and are known as Particle Mesh, PM, which scales as $O(N_g^3 \log N_g^3)$, where N_g is the number of grid points (see Section 4.2.5); Particle Particle Particle Mesh, P^{3}M, which scales as $O(N + N_g)$; and Adaptive Particle Particle Particle Mesh, AP^{3}M which scales as $\sim O(N_g \log N_g)$ (e.g. Eastwood & Hockney, 1974; Hockney & Eastwood, 1981; Efstathiou et al., 1985; Couchman, 1991; Bertschinger & Gelb, 1991; Macfarland et al., 1998). These methods determine forces between particles on small scales as a direct summation but on larger scales or highly clustered regions, they lay down a mesh and smooth the masses onto this grid. The more sophisticated versions of these codes use an adaptive mesh, one that is coarse in the sparsely populated regions and fine in the

highly clustered regions. An alternative to this scheme is the Tree algorithm, developed by Appel (1985) (see Section 4.2.5). This method reduces the computational cost of the full force calculation to an $O(N \log(N))$ scaling. The Tree algorithm can also be paired with a PM scheme to form an algorithm that combines the best of the two methods (Xu, 1995; Szapudi, 2005). In the TreePM algorithm, the short range forces are determined by the Tree and the long range forces by the PM. The TreePM scheme will be discussed further in Section 4.2.5.

N-body simulations have been used to test theories of structure formation in the Universe and have converged on a framework that is consistent with much of the available observational evidence. To ensure the Universe at the end of a simulation has the correct power spectrum, a set of initial conditions must be imposed on the pre-initial particle distribution (see Section 4.2.1). The initial conditions generator, N-GenIC (N-body Generate Initial Conditions), was developed by Volker Springel and was made available by him for use in my work. The cosmological N-body/SPH code GADGET2 (GAlaxies with Dark matter and Gas intEracT)[1] is a freely available piece of software that was also developed by Volker Springel to undertake cosmological simulations of structure formation (Springel et al., 2001; Springel, 2005). These codes are used throughout this thesis to develop cosmological simulations that are used for weak lensing analysis (see Appendix B for instructions on how to install GADGET2 and the required libraries). For the purposes of this work, only dark matter particles are modelled so only the N-body function of GADGET2 is used. Setting up a pre-initial particle distribution is discussed in Section 4.2.1 and the generation of initial conditions used by N-GenIC and many other initial conditions generators is introduced in Section 4.2.2. A simple explanation of how to model a dark matter distribution is given in Section 4.2.3 before a brief overview of GADGET2 in Section 4.2.4 and an introduction to TreePM, the dark matter evolution scheme used by GADGET2, in Section 4.2.5.

4.2.1 Pre-Initial Particle Distributions

N-body simulations start with a set of particles placed in a box. It is not possible to represent every object in the Universe with its own particle so in a cosmological simulation, each particle represents a sampling of the volume at that particular

---

[1]GADGET2 http://www.mpa-garching.mpg.de/gadget/

point in space. The particles are generally very massive, adding together to make the total density of the volume equal to the correct average density. A typical medium resolution simulation will have particle masses of the order of $\sim 10^{10}$ M$_\odot$. The distribution of these particles before any initial fluctuations have been imposed is known as the *pre-initial* particle distribution. The placement of the particles at the pre-initial stage is important to ensure the most realistic simulation. A random placement of particles is a poor choice of pre-initial distribution since this leads to random clustering due to the Poisson sampling of the continuous density field. An obvious choice is to order the particles on a grid. However, this has been shown to retain some unrealistic, grid-like structures in simulations at later times (e.g. Bode et al., 2001; Smith et al., 2003). Currently, the most commonly used placement is a distribution known as a *glass* (White, 1994). A glass has sub-Poissonian noise properties (noise that has a lower matter density power spectrum amplitude than a Poisson sample) and no preferred direction with forces on each particle being close to zero. To generate a glass, a random particle distribution is evolved with the sign of gravity reversed, so particles push away from each other. After many time-steps, the distribution reaches a state of equilibrium and if used as the initial condition in a standard integrator, structures do not evolve. Figure 4.1 shows a random particle distribution next to a glass to show the smoothness of the glass distribution.

4.2.2   Generating Initial Conditions

The conditions just after inflation were not random; to begin our simulations from a similar starting point, we need to perturb the positions and velocities of the pre-initial particle distribution to impose a theoretical power spectrum of fluctuations. The initial displacement and velocity fields generated from Gaussian random fields constitute the standard initial conditions for an N-body simulation. These are determined by imposing a power spectrum on the pre-initial particle distribution. Simulations start at a time when the Universe is still linear, so an analytic prediction for the matter density power spectrum can be used to generate the initial conditions. Small particle displacements are imposed manually on the particles in the pre-initial distribution and a velocity field is determined as an initial step to enable structure formation. For CDM, the initial velocity dispersion is negligibly small, but there is a mean streaming velocity which must be imposed as part of the initial conditions. How this is achieved in practice is explained below.
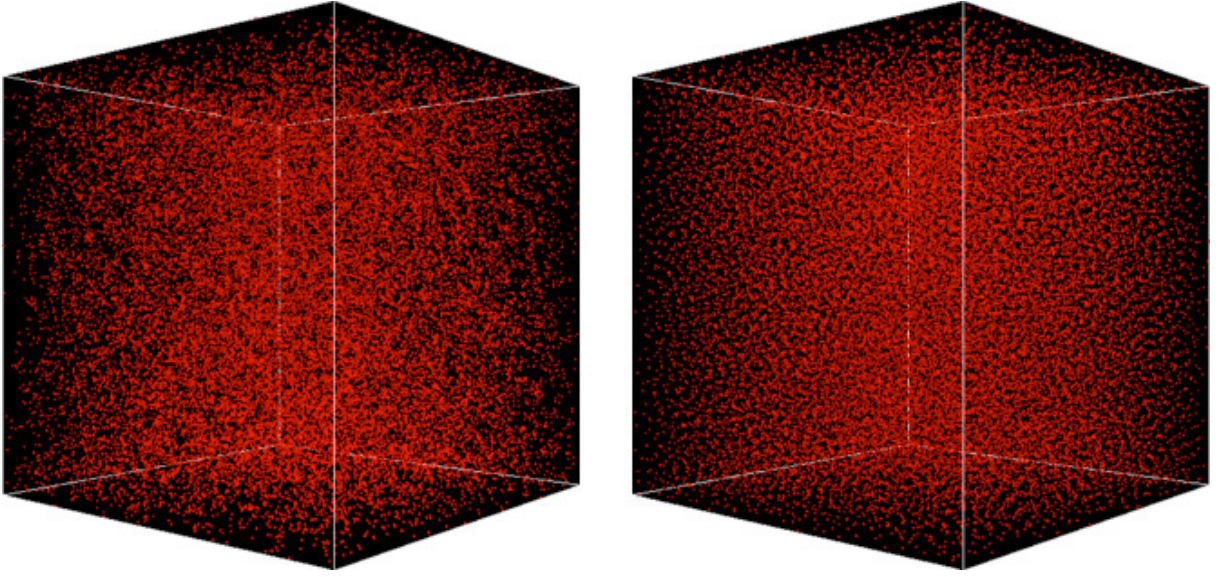
Figure 4.1: **The box on the left is a random pre-initial particle distribution with 32^3 particles. On the right is a glass pre-initial particle distribution with 32^3 particles. When comparing the two distributions in this way, it is possible to see by eye that the glass distribution is smoother then the random distribution.**

Given a linear matter density power spectrum, the initial particle displacement and velocity field is formed by making use of the *Zel'dovich approximation* (Zel'Dovich, 1970b), which states that in a Lagrangian coordinate system[2], a particle with an initial velocity will continue to move in a straight line with a velocity that scales with time in the same way for each particle. To first order, this approximation is very accurate (e.g Yoshisato et al., 2006). To generate these fields in an N-body simulation, a density field is first created on a grid in Fourier space. A random amplitude and phase is assigned for individual modes in Fourier space

$$\delta_{\boldsymbol{k}} = |\delta_{\boldsymbol{k}}| \ e^{i\varphi_{\boldsymbol{k}}}, \tag{4.1}$$

where $\boldsymbol{k}$ is the 3-D wavenumber, $\delta_{\boldsymbol{k}}$ is the overdensity in Fourier space and $\varphi_{\boldsymbol{k}}$ is the phase. For each mode, a random phase is drawn from between $[0, 2\pi]$ and a random amplitude is drawn from a Rayleigh distribution such that

$$\langle |\delta_{\boldsymbol{k}}^2| \rangle = P(k), \tag{4.2}$$

---

[2]In fluid mechanics, a Lagrangian coordinate system follows the evolution of individual particles while an Eulerian coordinate system samples evolution on a fixed grid.

where $P(k)$ is the linear matter density power spectrum at the starting redshift of the simulation. This produces a Gaussian random field. Now, for convenience we define a velocity potential from equation (3.13) such that

$$\phi = \frac{\Phi_N}{4\pi G\rho a^2}. \tag{4.3}$$

From this we get the 3D Poisson equation

$$\nabla^2\phi = \delta \tag{4.4}$$

The Fourier overdensity is related to a Fourier displacement potential by

$$\phi_{\boldsymbol{k}} = -\frac{1}{k^2}\,\delta_{\boldsymbol{k}}, \tag{4.5}$$

which is the Fourier transform of the 3D Poisson equation. Now we have a Fourier potential displacement field on a grid.

The displacement field is given by

$$\boldsymbol{d} = -\nabla\phi. \tag{4.6}$$

So in Fourier space, the potential relates to the Fourier displacement field, $\boldsymbol{d}_k$, by

$$\boldsymbol{d}_k = -i\boldsymbol{k}\phi_{\boldsymbol{k}} = \frac{i\boldsymbol{k}}{k^2}\,\delta_{\boldsymbol{k}}. \tag{4.7}$$

In real space, displacements can now be interpolated to individual particles and a new position can be determined via

$$\boldsymbol{r}_i(t) = \boldsymbol{d}_i(t) + \boldsymbol{q}_i, \tag{4.8}$$

(Zel'Dovich, 1970a), where $\boldsymbol{r}_i(t)$ is the new comoving position of the particle, $\boldsymbol{d}_i(t)$ is the interpolated displacement of the individual particle, and $\boldsymbol{q}_i$ is the initial comoving position of the particle.

The density of the field due to the displacement is

$$\rho(\boldsymbol{r}(q),t)\ d^3r = \rho(\boldsymbol{q})\ d^3q. \tag{4.9}$$

Thus

$$\rho(\boldsymbol{r}) = \rho(\boldsymbol{q})\ \boldsymbol{J}^{-1}, \tag{4.10}$$

where $\boldsymbol{J}$ is the Jacobian, which is given by

$$\begin{aligned}
\boldsymbol{J} &= \det\left(\frac{\partial \boldsymbol{r}_i}{\partial \boldsymbol{q}_j}\right) \\
&= \det\left(\delta_{ij} + \frac{\partial^2 \phi}{\partial q_i\ \partial q_j}\right).
\end{aligned} \tag{4.11}$$

From Equation (4.10) the overdensity of the displacement field can be determined

$$\begin{aligned}
\delta(\boldsymbol{r}(q)) &= \frac{\rho(\boldsymbol{r}) - \rho_0}{\rho_0} \\
&= \boldsymbol{J}^{-1} - 1 \\
&\simeq 1 + \nabla^2\phi - 1 \\
&= \boldsymbol{\nabla}\cdot\boldsymbol{d},
\end{aligned} \tag{4.12}$$

where ρ_0 is the density in the infinitesimal area around the particle before displacement. So, the overdensity field is the gradient of the displacement field and the displacements will produce the required density perturbations.

Velocities can be interpolated onto the particles because they are also related to the displacement field through

$$\dot{\boldsymbol{r}} = H(a)f(\Omega)\boldsymbol{d}, \tag{4.13}$$

where $H(a)$ is the Hubble equation and for a ΛCDM cosmology

$$f(\Omega) = \frac{d\ln D}{d\ln a} \simeq \Omega^{0.55}, \tag{4.14}$$

(Peebles, 1980) where D is the linear growth factor. This interpolation is valid since the particles only move on straight lines in the Zel'dovich approximation. We now have an initial Gaussian displacement and velocity field with the expected power spectrum imposed upon it. When placed into a standard cosmological integrator,

this field should evolve to form a universe of the expected matter density power spectrum.

4.2.3   Modelling Dark Matter in an N-Body Simulation

The evolution of a phase-space distribution of dark matter[3] $f(\boldsymbol{r}, \boldsymbol{v}, t)$ (a Poisson-Vlasov system), where $f d^3 \boldsymbol{r} d^3 \boldsymbol{v}$ is equal to the number of particles in $d^3 \boldsymbol{r}$ and $d^3 \boldsymbol{v}$, can be modelled with the collisionless Boltzmann equation

$$\frac{df}{dt} = \frac{\partial f}{\partial t} + \frac{\partial f}{\partial \boldsymbol{r}} \cdot \boldsymbol{v} + \frac{\partial f}{\partial \boldsymbol{v}} \cdot \left(\frac{\partial \Phi}{\partial \boldsymbol{r}} \right) = 0, \tag{4.15}$$

and the Poisson equation for the gravitational field

$$\nabla^2 \Phi(\boldsymbol{r}, t) = 4\pi G \rho(\boldsymbol{r}, t) - \Lambda, \tag{4.16}$$

where

$$\rho(\boldsymbol{r}, t) = \int f(\boldsymbol{r}, \boldsymbol{v}, t) d\boldsymbol{v}. \tag{4.17}$$

In a naïve Monte Carlo N-body system, the acceleration on each particle is then given by

$$\ddot{\boldsymbol{r}}_i = -\nabla_i \Phi(\boldsymbol{r}_i), \tag{4.18}$$

and the gravitational force on each particle is calculated by the sum of the contributions from all dark matter particles

$$\Phi(\boldsymbol{r}) = -G \sum_{j=1}^{N} \frac{m_j}{[(\boldsymbol{r} - \boldsymbol{r}_j)^2 + \epsilon^2]^{1/2}}. \tag{4.19}$$

where m_j is the mass of the j-th particle and ϵ is the mean softening length. The softening parameter, ϵ, must be introduced to maintain the collisionless nature of the system since when two or more particles are very close together, they exert strong forces on each other. Many numerical integrators, including GADGET2, employ a spherically symmetric cubic spline kernel (Figure 4.2) (e.g. Monaghan & Lattanzio, 1985) used in SPH and set the single particle density distribution function

---

[3]The information in this section was presented in a series of lectures given by Volker Springel in 2009.   The slides for these lectures can be found at http://www.mpa-garching.mpg.de/~volker/PiTP_lectures/
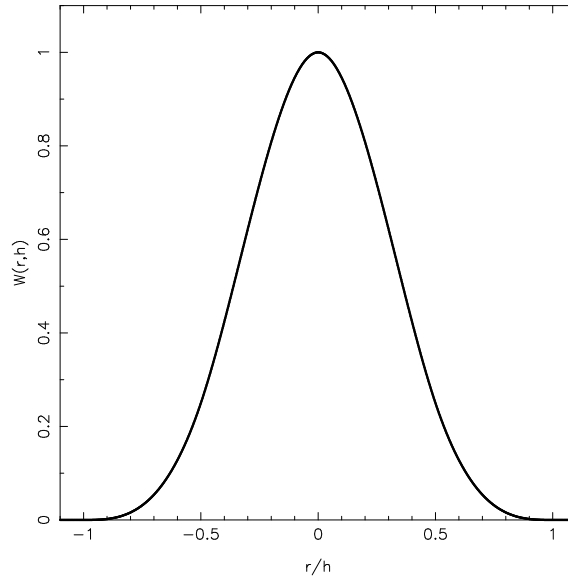
Figure 4.2: Cubic spline kernel used for force smoothing (Monaghan & Lattanzio, 1985).

$\tilde{\delta}(\boldsymbol{r}) = W(|\boldsymbol{r}|, 2.8\epsilon)$, where the smoothing kernel is of the form

$$W(r, h) = \frac{8}{\pi h^3} \begin{cases} 1 - 6\left(\frac{r}{h}\right)^2 + 6\left(\frac{r}{h}\right)^3 & \text{if } 0 \leq \frac{r}{h} \leq \frac{1}{2}, \\ 2\left(1 - \frac{r}{h}\right)^3 & \text{if } \frac{1}{2} < \frac{r}{h} \leq 1, \\ 0 & \text{otherwise}, \end{cases} \tag{4.20}$$

where r is the distance from the particle and h is an individual particle's smoothing length. The smoothing length of each particle is often dynamic and the algorithm ensures that the number of particles within this variable smoothing length remains roughly constant (Figure 4.3). Hence, all points in the fluid have smoothed quantities computed to the same level of mass resolution.

These force terms are used to calculate the new velocity and position in the next time step. The large force due to a close encounter leads to a strong change in the velocities of the particles involved, which requires extremely small time steps in the numerical integration of the equation of the motion. The so-called softening parameter ameliorates the large force change accompanying such a close encounter.

The force calculation described in Equation (4.19) is naïve because it is an N^2 task which is computationally prohibitive in large N systems (the Millennium simulation has 10 billion particles; Springel et al. (2005)). To improve efficiency, approximate
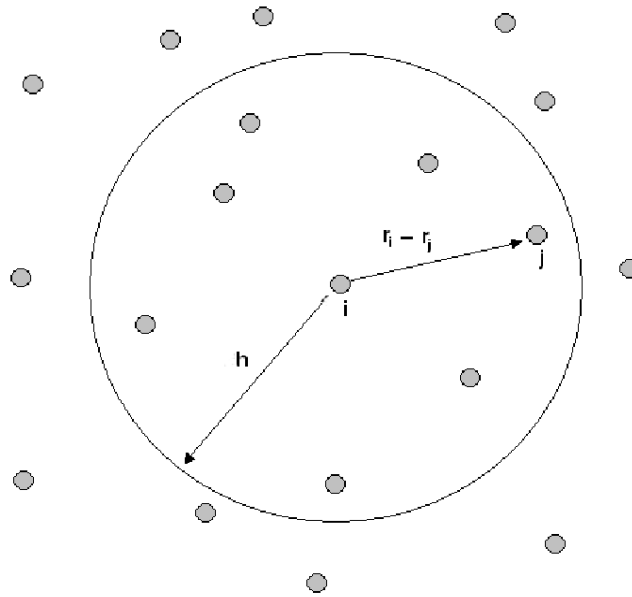
Figure 4.3: The definition of smoothing length h and neighbour particles. In many numerical integrators, the smoothing length is dynamic so that the number of neighbour particles contained within the smoothing length remains roughly constant.

force calculations are sufficient, provided the force errors are random and small.

4.2.4   GADGET2

The cosmological structure formation software package GADGET2 used in this PhD work was originally developed by Springel et al. (2001); Springel (2005). The code can be used for studies of isolated systems as well as simulations that include the cosmological expansion of space. Periodic boundary conditions may be included or not as per the requirements of the simulations. Improvements to this code have been ongoing as new software methodologies for simulating cosmological systems have been developed. GADGET2 represents bodies by a large number, N, of point-like particles. Each particle is 'tagged' with its own unique kinematic and physical properties that evolve with the particle over time. GADGET2 models the dynamics of dark matter and stars using a Tree N-body scheme and gas dynamics are simulated using Smoothed Particle Hydrodynamics (SPH). GADGET2 has the option to calculate the gravitational forces with a TreePM algorithm instead of a pure Tree calculation. The TreePM option calculates the short-range forces as a Tree and

the long range forces as a PM. Both the force computation and the time stepping of GADGET are fully adaptive allowing the user to optimise the settings for their own specific needs. GADGET2 is capable of investigating many different astrophysical problems such as colliding and merging galaxies and the formation of large scale structure in the Universe. The software also has the option to include radiative cooling and heating allowing for studies into the dynamics of the intergalactic medium and star formation. For the purposes of this work, only dark matter particles will be considered.

GADGET2 is vectorised and parallelised. A vector processor will calculate entire arrays (vectors) of numbers in one process rather than calculating each individual scalar value within the array, decreasing the time it takes to run the code. A parallelised code can be subdivided to run on several processors simultaneously, also decreasing the run time. GADGET2 is parallelised using the Message Passing Interface (MPI) library, the industry standard. Thus, the code can run efficiently on any type of computer, including large shared and distributed-memory supercomputers and PC clusters.

4.2.5 The TreePM Method

Computationally, the TreePM gravitational force calculation is based upon the hierarchical tree formalism (e.g. Barnes & Hut, 1986; Pfalzner & Gibbon, 1997) and the PM algorithm (e.g. Hockney & Eastwood, 1988). At high redshifts, it is computationally expensive to obtain accurate forces with the tree algorithm, so the force calculation on each particle is split so long-range forces are determined with the PM algorithm and short-range forces are calculated with the tree. For a more detailed discussion of this method, see Springel (2005).

For a cubic system of volume L^3 with periodic boundary conditions, the interaction potential $\varphi(\boldsymbol{x})$ is the solution of

$$\nabla^2 \varphi(\boldsymbol{r}) = 4\pi G \left[-\frac{M}{L^3} + \sum_{\boldsymbol{n}} \bar{\delta}(\boldsymbol{r} - \boldsymbol{r}_i - \boldsymbol{n}L)m_i \right], \qquad (4.21)$$

where i runs over the particles of mass m_i in the simulation, M is the total mass in the simulation, $\boldsymbol{r}$ is a comoving coordinate, $\boldsymbol{n} = (n_1, n_2, n_3)$ are integer triplets and

$\bar{\delta}(\boldsymbol{r})$ is the particle density distribution function. The solution of this is a peculiar potential that is governed by the Poisson equation

$$\nabla^2 \phi(\boldsymbol{r}) = 4\pi G[\rho(\boldsymbol{r}) - \bar{\rho}], \tag{4.22}$$

where $\rho(\boldsymbol{r})$ is the density of an individual particle and $\bar{\rho}$ is the mean density of the system. The simulations represent the field as discretised particles so the peculiar potential is defined as

$$\phi_{\boldsymbol{r}} = \sum_i m_i \varphi(\boldsymbol{r} - \boldsymbol{r}_i), \tag{4.23}$$

where m_i is the mass of the particle. This potential is explicitly split in Fourier space such that $\phi_{\boldsymbol{k}} = \phi_{\boldsymbol{k}}^{\mathrm{long}} + \phi_{\boldsymbol{k}}^{\mathrm{short}}$, where

$$\phi_{\boldsymbol{k}}^{\mathrm{long}} = \phi_{\boldsymbol{k}} \mathrm{e}^{-\boldsymbol{k}^2 r_s^2}, \tag{4.24}$$

where r_s is the spatial scale of the force-split. This long-range force is solved using the PM algorithm and if r_s is slightly larger than the mesh scale, force anisotropies suppressed to arbitrarily small levels. The short-range force is

$$\phi_{\boldsymbol{k}}^{\mathrm{short}} = \phi_{\boldsymbol{k}} \left[1 - \mathrm{e}^{-\boldsymbol{k}^2 r_s^2} \right], \tag{4.25}$$

which is solved in real space by the tree.

The PM scheme overcomes the N^2 scaling problem by assigning particles to a grid and solving the Poisson equation in Fourier space. The computational scaling is reduced to $N_g^3 \log N_g^3$, where N_g is the number of bins on a side. To solve for the potential, the particles are first binned into the grid using a smoothing algorithm. The smoothing algorithm assigns a 'shape', $S(\boldsymbol{r})$, to the particles and a fraction of mass falls into the surrounding bins. The density of each bin is

$$\rho(\boldsymbol{r}_m) = \frac{1}{h^3} \sum_{i=1}^{N} m_i \, W(\boldsymbol{r}_i - \boldsymbol{r}_m), \tag{4.26}$$

where h is the bin size and

$$W(\boldsymbol{r}_m - \boldsymbol{r}_i) = \int_{cell} \Pi\left(\frac{\boldsymbol{r}' - \boldsymbol{r}_m}{h} \right) S(\boldsymbol{r}' - \boldsymbol{r}_i) \, d\boldsymbol{r}', \tag{4.27}$$

Name	Shape function S(r)	# of cells involved	Properties of force
NGP Nearest grid point	$\delta(\mathbf{r})$	$1^3 = 1$	piecewise constant in cells
CIC Clouds in cells	$\frac{1}{h^3}\Pi\left(\frac{\mathbf{r}}{h}\right) \star \delta(\mathbf{r})$	$2^3 = 8$	piecewise linear, continuous
TSC Triangular shaped clouds	$\frac{1}{h^3}\Pi\left(\frac{\mathbf{r}}{h}\right) \star \frac{1}{h^3}\Pi\left(\frac{\mathbf{r}}{h}\right)$	$3^3 = 27$	continuous first derivative

Figure 4.4: Commonly used particle shape functions. The higher order functions give smoother density fields and forces but are more computationally expensive.

Credit: Volker Springel

where the integral is over a cell centered on $\boldsymbol{r}_m = (r_i, r_j, r_k)$, which is the center of each bin and Π is the step function

$$\Pi(\boldsymbol{r}) = \begin{cases} 1 & \text{for } |\boldsymbol{r}| \leq \frac{1}{2}, \\ 0 & \text{otherwise.} \end{cases} \tag{4.28}$$

The assignment function is a convolution in real space

$$W(\boldsymbol{r}) = \Pi\left(\frac{\boldsymbol{r}}{h}\right) \star S(\boldsymbol{r}), \tag{4.29}$$

Some commonly used shapes include the Nearest Grid Point (NGP), Cloud in Cell (CIC) and Triangular Shaped Cloud (TSC), shown in Figure 4.4. The higher order schemes provide a smoother density field but are increasingly computationally costly as more grid points are involved. Generally a CIC smoothing is chosen as a good compromise between smoothness and efficiency. After the particle masses have been assigned to the grid, the field is Fourier transformed and multiplied by the kernel, W, before inverse Fourier transforming back to real space.

Once back in real space, the force, $f = -\nabla\Phi$, is calculated with a 4-point finite
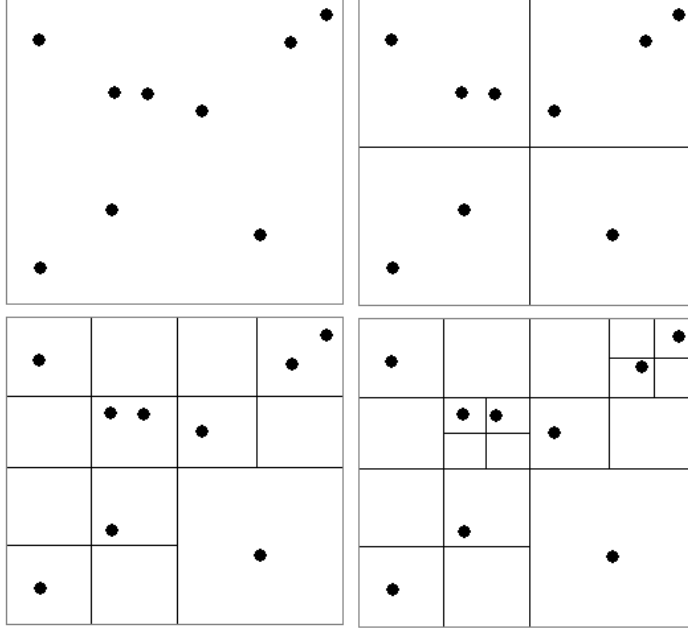
Figure 4.5: Step by Step division of space for a simple 2-D particle distribution.

difference operator

$$f_{i,j,k}^{(x)} = -\frac{4}{3}\frac{\Phi_{i+1,j,k} - \Phi_{i-1,j,k}}{2h} + \frac{1}{3}\frac{\Phi_{i+2,j,k} - \Phi_{i-2,j,k}}{4h}. \tag{4.30}$$

The mesh forces are then interpolated back on to the particle positions

$$F(\boldsymbol{r}_i) = \sum_m W(\boldsymbol{r}_i - \boldsymbol{r}_m)f_m, \tag{4.31}$$

where the kernel W is the same kernel as used in the mass assignment to ensure force anti-symmetry (ie the particles have equal and opposite forces between pairs).

The PM scheme is limited in resolution by the size of the mesh used in the calculations. This becomes particularly apparent on small scales, so GADGET2 uses a tree to calculate the short range forces. The tree scheme starts with a single cubic 'cell' which encloses all the dark matter in the system. In three dimensions, this cell is divided into eight daughter cells. Then the tree algorithm asks the question: How many particles are there in the cell: 0, 1, or > 1? If the cell is empty, it is ignored. If there is one particle in the cell, this is stored and then left alone.
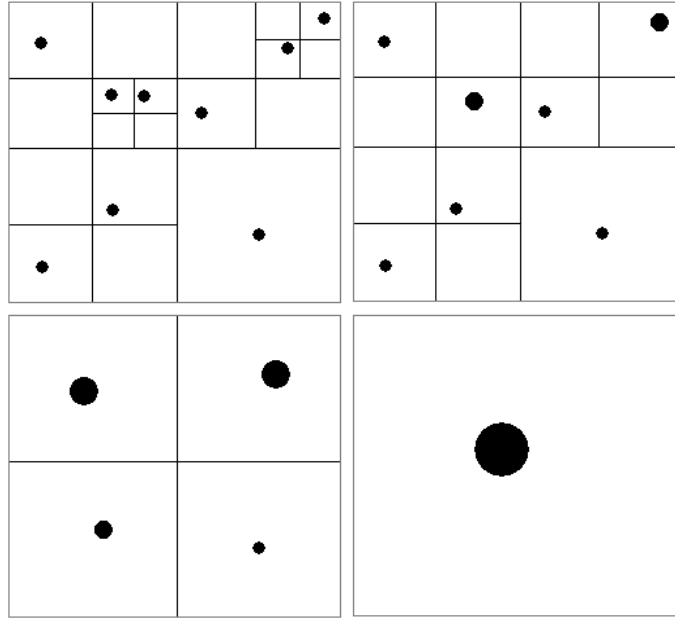
Figure 4.6: Total mass and center of mass of the particles in cells at different levels. The particles can be successively added together to produce pseudo-particles with the general properties of the individual particles they contain. The number of particles added together is dependent on the distance from the i-th particle. The size of the symbol is proportional to the mass of the pseudo-particle.

If there are more particles in a cell, this cell is subdivided in the next level. This subdivision process continues until there are no cells with more than one particle left.

Figure 4.5 shows this step by step division for a two dimensional particle distribution for ease of illustration. The purpose of this tree algorithm is to reduce the time taken to compute the gravitational potential for all the particles from N^2 to $N \log(N)$ by including contributions from near particles by a direct sum, whereas the influence of remote particles is taken into account only by including larger cells (Figure 4.6).

Choosing when to group particles together is decided by first establishing the 'size', s, of the current cell. This is then compared with the distance from the particle d (Figure 4.7). If the criterion

$$s/d \leq \theta \tag{4.32}$$

is fulfilled, where θ is a fixed tolerance parameter, then the force is added to the particle. If not, then cells at the next level are taken, as illustrated in Figure 4.7, and the calculation is done again until criterion of Equation (4.32) is satisfied. This
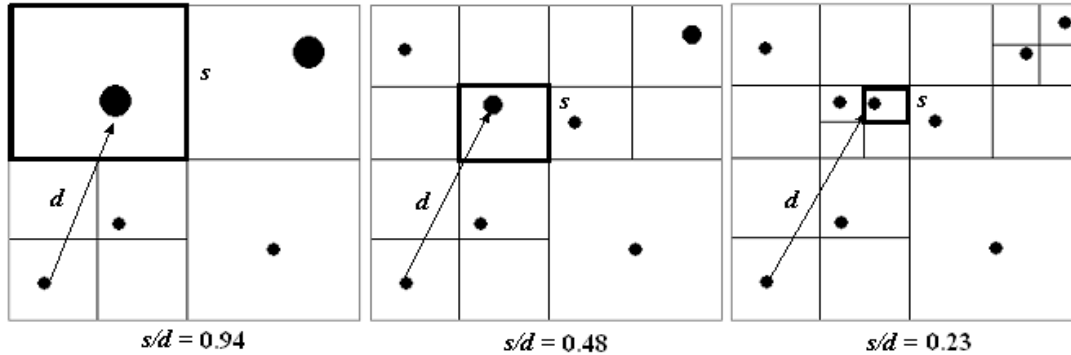
Figure 4.7: **The relation s/d for different levels of the tree.**

generalisation is justified because with all N-body simulations, there is a certain amount of error introduced due to round-off, truncation, and discreteness effects in both space and time, which makes it unnecessary to compute the potential field to extremely high precision. Thus, it is just as accurate to generalise the contribution of particles located far away. The tree structure means that distinguishing between close particles and distant particles without actually calculating the distance between every particle is simplified.

With an appropriate choice of initial condition power spectrum and subsequent dark matter evolution using the methods described above, cosmological N-body simulations are able to produce a particle distribution that resembles the statistical distribution of matter in our Universe today.

4.3   Relevance to Observations and Telescope Surveys

The previous chapters in this thesis have introduced the theories of cosmology and weak gravitational lensing and discussed the technical aspects of creating a simulated universe. In order to relate all of these things to the real world, they must be tested against observations of the Universe. The sophistication of techniques for processing and analysing weak lensing data has progressed rapidly (e.g. Rhodes et al., 2007; Kitching et al., 2008; Massey et al., 2010). The cosmological interpretation of weak lensing surveys is now limited by the *quality* and the *quantity* of
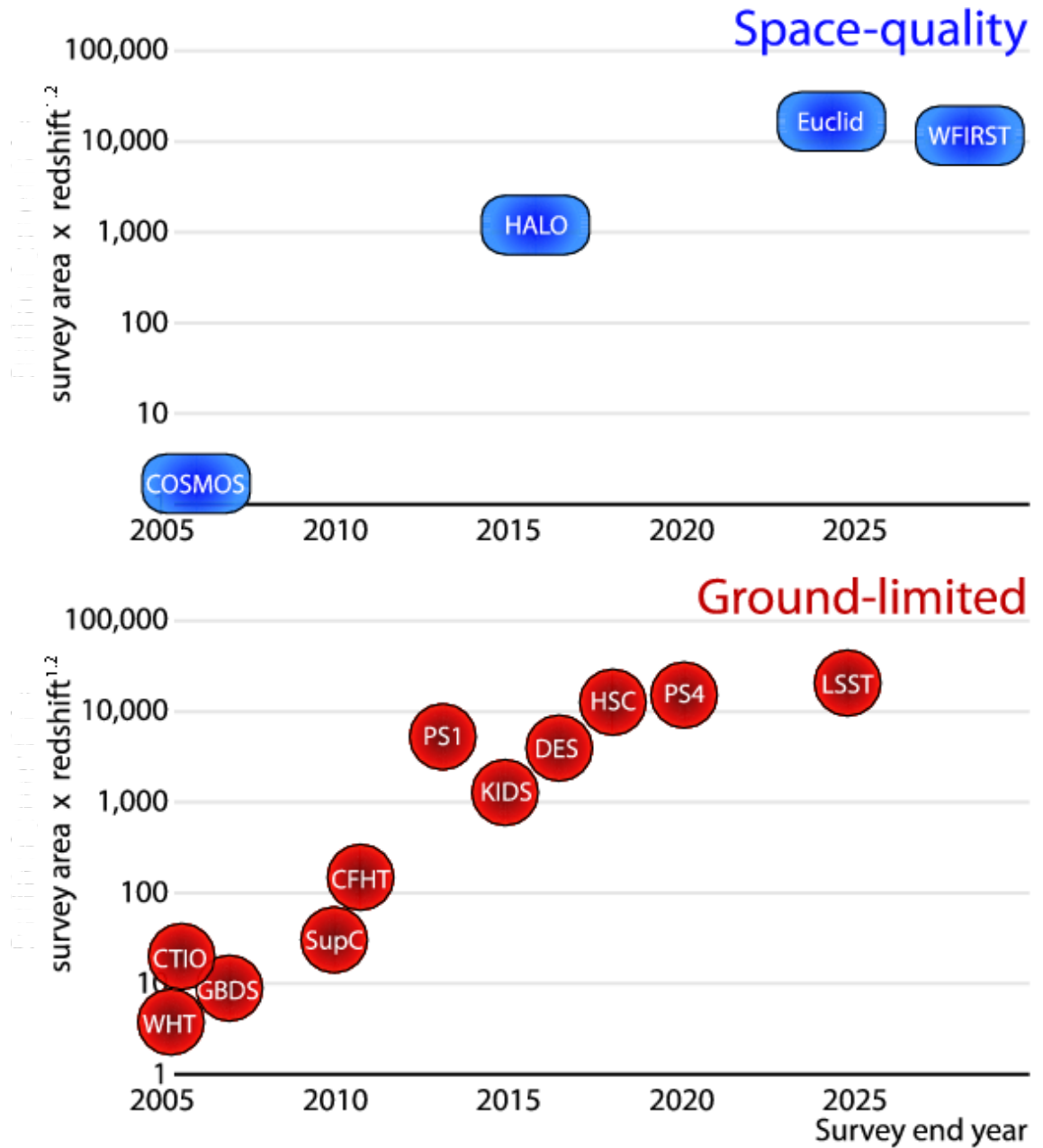
Figure 4.8: Top Panel: Launch dates of existing and future space-based weak lensing surveys as a function of survey area x redshift.
Bottom Panel: Launch dates of existing and future ground-based weak lensing surveys as a function of survey area x redshift.

Credit: Richard Massey

simulated data against which observations can be compared. Future progress will require accurate predictions of the expected signal in any cosmological model - the scientific conclusions of any analysis are only as robust as the underlying theory. Furthermore, any finite survey field will only sample a small region of large-scale structure, and the cosmological information on different scales will be inevitably mixed - for example the large-scale and small-scale distributions of dark matter. Interpreting such observations requires extremely large simulations to quantify the variation possible along the different lines of sight where the survey could have been placed, and the amount of mixing or covariance between scales.

Even for the standard ΛCDM cosmology, high-precision simulations tailored to predict gravitational lensing observables have never been created in sufficient quantity and the exploration of different cosmological models, using cosmic shear or matter density in the non-linear regime, relies on fitting functions (e.g. Smith et al., 2003). For the first time, tailored simulations will be able to provide weak lensing covariance matrices accurate to 1% for ΛCDM through generating upward of 10,000 independent mock galaxy shear catalogues, significantly improving on the 10% accuracy currently achieved with 100 mock catalogues (see Chapter 5), as well as simultaneously exploring different regions of cosmological parameter space and models of gravity.

Lensing surveys can resolve the shapes of galaxies out to high redshift and technological advances are yielding ever larger surveys (Figure 4.8). Maximally exploiting their potential therefore requires fully 3-D analyses, and several innovative techniques have recently been proposed for cosmic shear with a potential factor 2 improvement on parameter constraints (Kitching et al., 2010; Heavens, 2003); 3-D mass mapping (Bacon & Taylor, 2003; Taylor, 2001); the stochastic bias in the galaxy distribution from galaxy-galaxy lensing (Zheng et al., 2009; Jullo et al., 2011); the growth of dark matter structure as a function of physical scale (Bacon et al., 2005); the geometry of a cluster lens system that reflects the large-scale geometry of the Universe (e.g. Gavazzi & Soucail, 2007); and the link between the observed distribution of dark matter with gravitational lensing and baryons with X-ray and visible imaging during mergers (Massey et al., 2010; Powell et al., 2009). Manufacturing analytical predictions for these complex measurements from different cosmological and astrophysical scenarios is often very difficult; the propagation of error analysis is often

impossible. The only realistic path to exploiting complex analysis techniques is to simultaneously apply the analysis techniques to realistic mock catalogs. The mock catalogues in this thesis are produced in a way that is sensitive to these techniques – for example including the overproduction of source galaxies so that they can be resampled with arbitrary bias. These analyses can be directly applied to existing telescope surveys like PS1 and COSMOS.

4.3.1 Completed Telescope Surveys

COSMOS

The Cosmic Evolution Survey, COSMOS, was completed on the Hubble Space Telescope's (HST) Advanced Camera for Surveys (ACS) between 2003 and 2005 and its primary science goal was to obtain weak lensing observations from a stable platform above the Earth's atmosphere. The COSMOS field is a 2 square degree field and the survey has approximately 66 galaxies per square arcminute (Massey et al., 2007; Leauthaud et al., 2007). The survey is one of the deepest weak lensing surveys available with $z_{\mathrm{med}} \simeq 1.2$ and is currently the largest available weak lensing survey from space. However, because the HST has a limited field-of-view, the survey coverage is comparatively small, so sample variance is an important source of bias, which requires simulations to quantify. Simulations from the work in this thesis are currently being used in the analysis of the COSMOS data and have already resulted in a publication (Jullo et al., 2011).

CFHTLenS

The Canada-France-Hawaii Telescope Legacy (Lensing) Survey, CFHTLenS, is a 155 square degree survey that was completed in Hawaii between 2003 and 2009. The CFHT has a 3.6m primary mirror and the survey has a median redshift of $z_{\mathrm{med}} \simeq 0.9$ with 15 galaxies per square arcminute (Fu et al., 2008). The CFHTLenS team have spent the last two years analysing the weak lensing data due to unknown systematics making the interpretation of the data very difficult. The addition of weak lensing simulations to this process has been essential to the understanding of the data.

4.3.2   Current Telescope Surveys

Pan-STARRS PS1

The Panoramic Survey Telescope and Rapid Response System, Pan-STARRS, is a US Air Force funded wide field imaging system that will be able to survey the entire visible sky (3π) every 5 nights and is being located in Hawaii. PS1 is the first stage of the Pan-STARRS project and it will run for 3.5 years. The full Pan-STARRS mission comprises 4 PS1-type telescopes and the second stage with two telescopes, PS2, is already being built. For the PS1 mission, a single prototype telescope has been built and full-time science observations started in May 2010. Pan-STARRS telescope 1 (PS1) is located at Haleakala Observatories in Hawaii. The PS1 system includes the observatory, telescope, camera, hardware and software required to undertake the full scientific studies outlined in the PS1 science case.

The work from this thesis will be used in PS1 Key Project 11, **Cosmological Lensing**, which will analyse data from the 3π survey and the Medium Deep Survey. The 3π survey is both a photometric and astrometric survey that is expected to observe approximately 3 galaxies per square arcminute to a median redshift of $z_{\mathrm{med}} = 0.6$. The cosmological lensing project has outlined several key questions that they hope to address over the course of the PS1 3.5 year lifetime. The main aim is to measure the distortions of galaxy images due to gravitational lensing along the line-of-sight known as cosmic shear. The long term goal is to use the photo-z and shape information from the 3π survey to do an all-sky shear analysis. The information derived from these measurements will be used in an attempt determine the nature of dark energy, constrain cosmological parameters and investigate structure formation. The most ambitious project is to measure the equation of state of dark energy, and its evolution over a redshift range $z = 0$ to 1. Analysis of the data has recently begun and simulations from my pipeline will be used to provide covariance matrices for maximum likelihood analysis.

VST-KIDS

The VLT Survey Telescope Kilo-Degree Survey, VST-KIDS[4], is a ground-based telescope survey located in Cerro Paranal in Chile. The telescope began its testing phase

---

[4]VST-KIDS https://www.astro-wise.org/projects/KIDS/

in 2011 and the survey should begin observations in 2012 for five years and will observe 1500 square degrees. This survey will observe the u,g,r,i bands and will be combined with the VISTA Kilo-Degree Infrared Galaxy Survey, VIKING[5], survey which is observing the Z,Y,J,H,K bands to provide 9-band photometric redshifts that will be reliable over a very wide range of redshifts. The VST-KIDS survey is primarily a gravitational lensing survey that hopes to investigate the big cosmological questions such as the nature of dark matter and dark energy.

4.3.3 Future Telescope Surveys

Future telescopes will obtain larger surveys and aim for greater precision in the measurement of cosmological parameters, which will require ever more accurate simulations to interpret. Furthermore, simulations will be used to optimise telescope designs and survey strategies to maximise scientific potential. Planning future telescope surveys requires a deep understanding of the science that is possible with a particular telescope design and survey strategy. In the design and definition phase of any telescope mission's development, much work must be done to determine whether observations can reach the accuracy required, or if the science goals can be met at all. The research in this thesis works toward this by providing a set of tools that can make predictions for telescopes like the ones mentioned below.

DES

The Dark Energy Survey, DES, is primarily interested in probing the nature of dark energy. In late 2011, the Dark Energy Camera (DECam) will be installed on the Blanco telescope in Cerro Tololo in Chile. Over the next five years high precision observations of 5000 square degrees of the southern sky will be observed. Through observations of galaxy clusters, baryon acoustic oscillations, type Ia supernovae and weak lensing, the nature of dark energy will be deeply probed (The Dark Energy Survey Collaboration, 2005). The DES project has already utilised large suites of simulations in preparation for the mission. The DES simulations provide end-to-end pipelines that produce realistic images from N-body simulations that are then run through the DES analysis pipeline for comparison with the observational data when it arrives.

---

[5]VIKING http://astro-wise.org/projects/VIKING

HALO

The High Altitude Lensing Observatory, HALO, is a planned NASA balloon mission to observe gravitational lensing above 99% of the Earth's atmosphere and is scheduled to launch in 2014. There are several advantages to a balloon survey – the observations are almost entirely out of the atmosphere while the mission only costs a fraction of a full space mission. It is also possible to bring the telescope back to Earth easily to fix any bugs or completely replace instruments for a complementary set of observations. A technology demonstrator for a long duration balloon flight has already been launched and achieved 54 days of continuous flight. By 2013 it is expected that ~ 100 day flights will be achievable. HALO will survey between 200 and 1000 square degrees with $\sim 15-20$ galaxies per square arcminute (Rhodes et al., *in preparation*). The survey area is at least 100 times larger than COSMOS but 100 times smaller than Euclid. However, the time scales mean that HALO will fill the gap between these two surveys. HALO will use simulations from my pipeline to forecast what big cosmological questions the instrument will be able to address with a given survey strategy.

LSST

The Large Synoptic Survey Telescope (LSST) is a wide-field 20,000 square degree ground-based telescope located in Cerro Pachón in Chile. The LSST telescope has an 8.4m mirror, with an effective aperture of 6.7m due to obscuration, that is able to rapidly perform both wide and deep ($z_{\mathrm{med}} \simeq 0.9$) surveys simultaneously (LSST Science Collaborations et al., 2009). Photometric redshifts will be obtained with an accuracy of just 2% (relative error in $1 + z$). Construction of the telescope is currently underway and first light is expected in 2014, followed by a 10 year active observing schedule. The goal of LSST is to answer the big cosmological questions – What is the nature of dark energy and dark matter? Dark energy will be investigated through a combination of probes including weak gravitational lensing, baryon acoustic oscillations, supernovae and cluster counting, all as a function of redshift. The nature of dark matter will be investigated through strong galaxy and cluster lensing. In addition to these cosmological questions, astrophysical questions on a smaller scale will be investigated (solar system, galaxy etc.). Non-lensing specific image simulations for LSST have already been developed from N-body simulations

but the mission will clearly benefit from having simulations with a lensing specific focus.

Euclid

Euclid is a satellite telescope that has been proposed as part of the European Space Agency (ESA) Cosmic Vision program. The Cosmic Vision program is the current cycle of long-term planning for space missions funded by ESA for 2015 - 2025. The final selection should be completed by November 2011 and if Euclid is selected, the planned launch date is in late 2018.

The Euclid mission plan is to map a 15,000 square degree field of the sky with a median redshift of $z_{\mathrm{med}} \simeq 0.9$, including a deeper 40 square degree survey. The survey should see $\sim 30 - 40$ galaxies per square arcminute. The 5-year mission will be undertaken by a 1.2m telescope, located at the L2 Lagrange point on the Earth-Sun line, in the visible and near-infrared bands. The visible r, i and z bands will have a resolution of 0.18 arcseconds and will be used for measuring the shapes of galaxies for weak lensing analysis. The infrared bands y, j and h will have a resolution of 0.3 arcseconds. Photometric redshifts will be obtained with the help of broad-band visible observations and are expected to reach an accuracy of $\sigma(z)/(1+z) = 0.03 - 0.05$. The design of the Euclid telescope is optimised for weak lensing analysis, even though other analyses will be performed, because weak lensing requires very high resolutions to enable measurement of galaxy shapes. The primary science goals of Euclid are to measure the dark energy equation of state parameter w_0 to within 2% and w_a to within ± 0.1 and to test general relativity against modified gravity models (Refregier et al., 2010). The research in this thesis is being utilised in both the weak lensing and simulation working groups that are working together to prepare for the mission. The simulations produced by my pipeline are being used to determine requirements for the instrument and predict errors for cosmological parameter estimation.

WFIRST

The Wide-Field Infrared Survey Telescope, WFIRST, is a space-based NASA mission proposed as part of the US Astronomy and Astrophysics decadal review to answer the fundamental questions in cosmology through weak lensing, supernova

	Area (sq. deg.)	z_{med}	n_g/sq. arcmin.	Start date	AK Sims
Ground					
CFHTLenS	155	0.9	15	2003	
PS1	30000	~ 0.6	~ 3	2010	Yes
DES	5000	~ 0.7	~ 12	2011	
LSST	20000	~ 0.9	~ 40	2014	
Space					
COSMOS	2	1.2	66	2003	Yes
HALO	200 - 1000	~ 0.9	~ 15	2014	Yes
Euclid	15000	~ 0.9	~ 35	2018	Yes
WFIRST	~ 30000	~ 1.0	~ 35	~ 2022	Yes

Table 4.1: Table of parameters for complete, current and future ground- and space-based weak lensing surveys. The final column shows the surveys that are currently, or will be, using my simulations for analysis and development.

distances and baryon acoustic oscillations. WFIRST is not expected to launch before 2022 and will survey approximately 30,000 square degrees to a median redshift of $z_{\mathrm{med}} \simeq 1.0$ with $30 - 35$ galaxies per square arcminute. Preliminary development of the mission is underway with a report due to be presented in June 2011. Simulations from my pipeline will be used in the main development phase to characterise the weak lensing capabilities of the the mission.

4.4   Summary

Observations are only as good as the simulations against which they are interpreted so simulations should be playing a role that is just as important as the observational data in future analyses that aim for high precision. Table 4.1 shows a number of completed, current and future weak lensing surveys and all of these require simulations now, whether it be for data analysis of existing data or forecasting errors for future missions. A start has already been made with the mock shear catalogues from this thesis being provided to correct for sampling variance in COSMOS (Jullo et al., 2011). My simulations will also be used to analyse data from PS1 and to prepare for Euclid, HALO and WFIRST. Future missions should treat the simulations exactly the same as observational data and perform full analyses on all data sets to

generate statistical results that are far more robust than observations can achieve on their own. Future missions will also require a blind analysis of the data, using tools tested exclusively on simulations, for scientific rigour believable by the entire community.

Chapter 5

Simulations and Analysis Software

5.1 Introduction

As discussed in the introductory chapters of this thesis, cosmic shear analysis is
an excellent method for probing the dark Universe. Due to the relative youth of
this field, techniques are still being developed to exploit the weak lensing data from
these surveys to provide further understanding on the nature of the Universe. To
realise the potential of these new telescope surveys and to test new weak lensing
analysis techniques, challenges must be met. To achieve the small statistical errors
required, experiments require full end-to-end simulations of huge volumes which also
probe the non-linear regime to assist in understanding the limitations of the analysis
techniques. Simulations offer data-sets with known parameters which are essential
when testing analysis pipelines. Simulations can also include effects which may be
difficult to model theoretically, such as source clustering and galaxy alignments,
as well as other systematics and real-world effects. An additional role for simu-
lations is in accurate estimation of the covariance of observable quantities. This
is needed for the analysis of surveys and analytic approximations can be wholly
inadequate (e.g. Semboloni et al., 2007). Monte Carlo analyses can be performed
with simulations to provide covariance matrices that are required for data analysis
and cosmological parameter estimation. Simulations are also required for rigorous
testing and development so all analysis methods can be analysed blindly before the
same techniques are applied to real data. To address these challenges, the SUN-
GLASS, Simulated UNiverses for Gravitational Lensing Analysis and Shear Surveys,
pipeline has been developed to produce simulations and mock shear and convergence

catalogues rapidly for weak lensing and cosmic shear analysis. The purpose of this chapter is to introduce SUNGLASS and show rigorous testing of its outputs.

Many weak lensing studies use simulations with very high numbers of particles to run their analysis (e.g. Fosalba et al., 2008; Hilbert et al., 2009; Teyssier et al., 2009; Schrabback et al., 2010). The computational cost of running these simulations is high and consequently there is often only a single realisation available. However, it is very important to ensure that covariance matrices calculated from these simulations are not contaminated by correlations in the simulations (Hartlap et al., 2007). In order to ensure uncorrelated data, a Monte Carlo suite of simulations should be used to determine the covariance matrix (Sato et al., 2009). In this work, 100 independent simulations were constructed using SUNGLASS.

To date, there are still reasonably few weak lensing simulations available. Of the few that are available, many implement a ray-tracing technique where light rays are propagated from an observer to a lensing source plane (e.g. Jain et al., 2000; Vale & White, 2003; Forero-Romero et al., 2007; Hilbert et al., 2009; Teyssier et al., 2009; Sato et al., 2009; Dietrich & Hartlap, 2010; Vafaei et al., 2010). Some alternative ray-tracing methods do not use lensing source planes and instead calculate the full 3-D gravitational potential (e.g. Couchman et al., 1999; Carbone et al., 2008). Ray-tracing is computationally intensive and time consuming when solving the full ray-tracing equations. If the Born approximation is used in the ray-tracing, the time to run the analysis is reduced, but the process is still computationally intensive and the simulation data is still binned in three dimensions to perform the calculations. An alternative to ray-tracing is line-of-sight integration, which uses the Born approximation to calculate rapidly the weak lensing signal through a lightcone (e.g. White & Hu, 2000; Fosalba et al., 2008). This method is not suitable in the strong lensing regime but in the weak lensing regime, it is rapid and requires fewer computational resources than ray-tracing techniques. In this chapter, a new line-of-sight integration technique, implemented in the SUNGLASS pipeline, for measuring convergences in an N-body simulation is introduced. This new method is rapid and after the N-body simulations have been run on a modest computer cluster, the weak lensing analysis can be run on a single processor of a desktop computer. In contrast to ray-tracing, the method does not bin in the radial direction, using all of the redshift information available. Although the catalogues are suitable for real-space analysis, SUNGLASS

analyses and tests the mock weak lensing surveys in Fourier space, using power spectra, as it is possible to cleanly distinguish between linear and nonlinear regimes in Fourier space. It is also possible to easily identify scales where the simulations are reliable by determining the region of the power spectrum in Fourier space that lies between the size of the simulated volume at low wavenumbers and shot-noise due to particle discreteness and pixelization effects at high wavenumbers.

The outline of this chapter is as follows. Section 5.2 introduces the SUNGLASS pipeline. Details of the simulations are in Section 5.2.1 and a test of the 3-D matter density power spectrum is shown in Section 5.2.2. The line-of-sight integration method for determining shear and convergence without radial binning is described in Section 5.2.3. Section 5.2.4 presents the shear and convergence power spectrum analysis and Sections 5.2.5 and 5.2.6 detail tests on the noise properties and B-modes in the lightcones. Section 5.2.7 deals with the generation of the mock galaxy shear catalogues and Section 5.2.8 quantifies the errors introduced by interpolating shear and convergences between source redshift planes to construct the mock catalogues. Section 5.2.9 shows the effect that sampling and binning has on the shear and convergence power spectra in the mock catalogues. Finally, an application of the mock catalogues is discussed in Section 5.3 where Gaussian likelihood estimates of Ω_m and σ_8 are performed before a summary of the pipeline and methods concludes the chapter in Section 5.4.

5.2 Details of the SUNGLASS pipeline

SUNGLASS is a pipeline that generates cosmic shear and convergence catalogues using N-body simulations. The pipeline creates mock galaxy shear catalogues that can be used to test the cosmic shear analysis software used on telescope survey data sets. The nature of the pipeline also allows many simulation realisations to be generated rapidly to produce covariance matrices for data analysis and cosmological parameter estimation. The pipeline begins by creating a suite of cosmological N-body simulations. Lightcones are generated through the simulations and tomographic shear and convergence maps are determined using line-of-sight integrations at multiple lensing source redshifts. Finally, mock galaxy catalogues with fully 3-D shear and convergence information and galaxy redshift distributions are assembled from

the lightcones and the tomographic shear and convergence planes. The following sections detail each step of the SUNGLASS pipeline.

5.2.1   The N-body Simulations

All of the simulations presented in this work were run on a modest Xeon cluster, using 4 nodes with dual Xeon E5520 2.27 GHz quad-core processors per node and 24Gb shared memory per node. The simulations were run using the cosmological structure formation software package GADGET2 (Springel, 2005) (see Section 4.2.4 and 4.2.5 for more detail on GADGET2 and modeling dark matter and Appendix B for detailed instructions on installing GADGET2). For the purposes of this work, only dark matter particles were considered. The pre-initial particle distribution for the simulations used in this work is a *glass* (see Section 4.2.1) and the initial power spectrum was imposed on the particles using the parallel initial conditions generator N-GenIC (see Section 4.2.2).

Multiple medium-resolution simulations were run with 512^3 dark-matter particles, in a box of $L = 512h^{-1}$ Mpc comoving side length with periodic boundary conditions. These parameters were chosen as a compromise between box size and resolution. This combination gives an adequate resolution while still having a box large enough to suitably model large-scale structure. In addition, the time to run these simulations and the amount of space required to store them is also reasonable. It is straight forward to increase (or decrease) the resolution of the simulation by increasing (decreasing) the number of particles. Decreasing the resolution would reduce the scales that are resolved in the simulation which is undesirable since the smaller scales are important to cosmological parameter estimation. Increasing the resolution is desirable but would both increase the time to run the simulation and the amount of space required to store the simulation. Alternatively, the resolution could be increased by decreasing the box size, but this would make modeling large-scale structure difficult with the large-scale modes missing from the simulation. The following cosmological parameters were used for a flat concordance ΛCDM model consistent with the WMAP 7-year results (Jarosik et al., 2011): $\Omega_\Lambda = 0.73$, $\Omega_m = 0.27$, $\Omega_b = 0.045$, $n_s = 0.96$, $\sigma_8 = 0.8$ and $h = 0.71$ in units of 100 km s^{-1} Mpc^{-1}. Note that baryon wiggles are not included in the power spectrum. The particle mass is 7.5×10^{10} M$_\odot$ and the softening length is $33h^{-1}$ kpc, which is 1/30 of the mean interparticle sep-
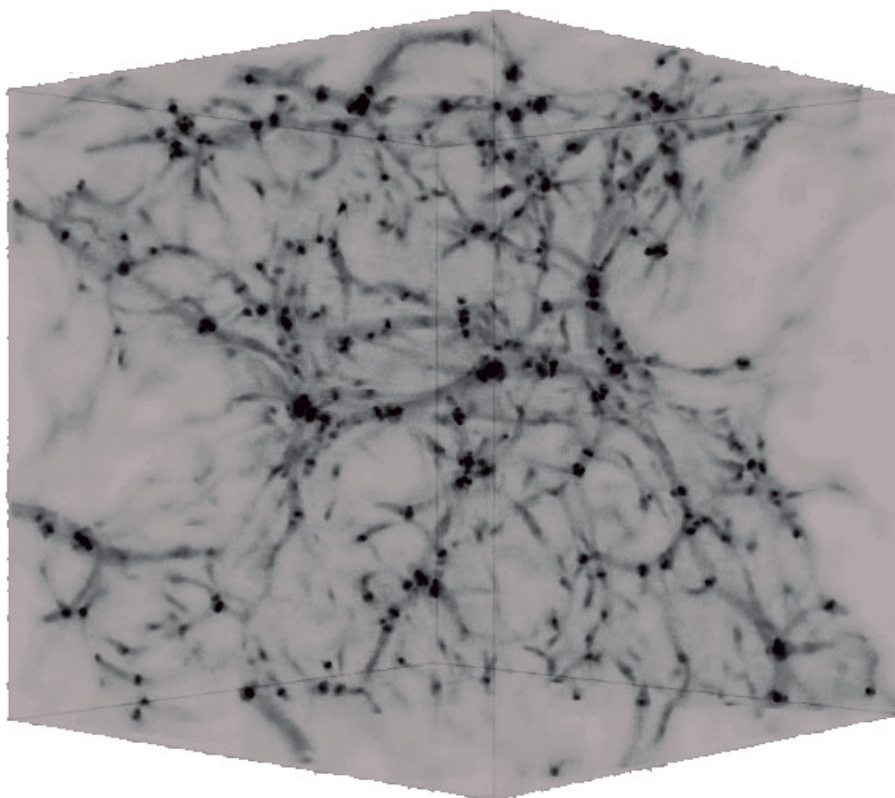
Figure 5.1: **Simulation snapshot at $z = 0$. This shows a typical, fully evolved simulation volume with 512^3 dark matter particles in a box with a sidelength of $512\ h^{-1}$Mpc. The cosmology is a flat concordance ΛCDM cosmology, consistent with the WMAP 7-year results (Jarosik et al., 2011). The web-like nature of the Universe is visible in this image as filaments and voids.**

aration (a standard choice for cosmological simulations). The simulations were all started from a redshift of $z = 60$, which is early enough to fall well within the linear regime but not so early that the perturbations in the initial conditions are too small to evolve numerically. The simulations were all allowed to evolve to the present.

The simulation data were stored at 26 output times corresponding to a $128h^{-1}$ Mpc comoving separation, between $z = 1.5$ and the present. These snapshots were chosen to fall within the photometric redshift error of $\sigma_z < 0.05(1 + z)$ corresponding to a displacement of $\simeq 147h^{-1}$ Mpc at $z = 1$. In a 512^3 particle simulation, this amounts to 100GB data per simulation and takes approximately 21hrs to run on the Xeon cluster's 32 processors. Figure 5.1 shows the $z = 0$ snapshot for one of the realisations. The filaments and voids of the cosmic web are clearly visible in this image.

5.2.2 3-D Matter Density Power Spectra

After the suite of simulations were run, the 3-D matter density power spectrum of the final $z = 0$ snapshots was determined by binning the particles in a 3-D grid using a CIC smoothing algorithm to determine the overdensities (see Section 2.6 for details on the 3-D matter density power spectrum and Section 4.2.5 for more information on particle smoothing). The distribution was then Fourier transformed to determine the dimensionless 3-D matter density power spectrum according to

$$\Delta^2(k) = \sum_{k \text{ in shell}} \frac{|\delta_{\boldsymbol{k}}|^2}{n^3 \Delta \ln(k)}, \tag{5.1}$$

where n^3 is the total number of bins in the simulation box volume. Due to memory restrictions, the number of bins in this calculation is limited to $n = 512$. The Fast Fourier transform used throughout this thesis is FFTW[1] and the convention of this transform sets the form of Equation (5.1). The modes in this power spectrum are arranged in a 3-D grid which leads to mode binning fluctuations when binned into annuli at small k. There are only a very small number of large scale modes, small k, so annular binning on a cartesian grid can cause large fluctuations in the power spectrum due to the measured number of modes not matching with the expected number of modes. To correct for this, the power spectrum is scaled by the ratio of

---

[1]The Fastest Fourier Transform in the West http://www.fftw.org/
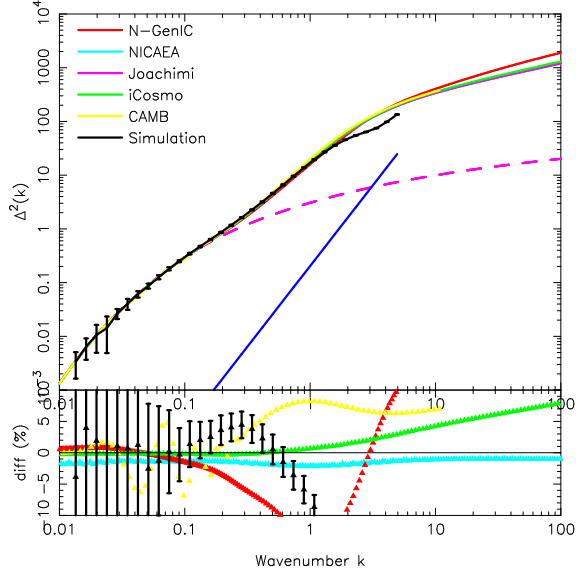
Figure 5.2: The top panel shows the dimensionless 3-D matter density power spectrum. The black line shows the mean power spectrum for the 100 realisations with errors on the mean. A number of theoretical expectations are shown: Red from N-GenIC, light blue from NICAEA, magenta from a code provided by Benjamin Joachimi (the dashed line represents the linear power spectrum expectation), green from iCosmo and yellow from CAMB The dark blue diagonal line is the predicted shot-noise contribution. The bottom panel shows the percentage differences of the various curves from the Joachimi curve.

the measured number of modes to the expected number of modes

$$N_{exp}^k = \frac{4\pi}{3} \, g_3(k_{max}^3 - k_{min}^3), \tag{5.2}$$

where $g_3 = (L/2\pi)^3$ is the density of states, L is the size of the box volume in h^{-1}Mpc and k_{max} and k_{min} are the maximum and minimum wavenumbers in the shell respectively.

The discrete nature of the particles in the simulation volume give rise to a shot-noise contribution to the power spectrum. A Poisson shot-noise contribution can be determined analytically and is given by

$$\Delta_{\rm SN}^2(k) = \frac{k^3}{2\pi^2}\frac{1}{\bar{n}}, \tag{5.3}$$

(e.g. Peacock, 1999), where $\bar{n}$ is the number density of particles in the simulation box.

In Figure 5.2, the top panel shows the mean measured matter density power spec-

trum in black with errors on the mean. The dark blue diagonal line is the expected shot-noise. The measured power spectrum is compared against several different software packages that produce a theoretical expectation for the power spectrum. The red line shows the expectation from N-GenIC which calculates the non-linear power spectrum using a Peacock & Dodds (1996) fitting formula and an Eisenstein & Hu (1998) matter transfer function. The light blue, magenta and green lines are expectations from the NICAEA package[2], a private software package provided by Benjamin Joachimi and the iCosmo package[3] respectively. These all use the Smith et al. (2003) non-linear fitting formula and the Eisenstein & Hu (1998) matter transfer function. The dashed magenta line shows the linear power spectrum expectation from the Joachimi software. The yellow line is from the CAMB package[4] which uses a Smith et al. (2003) non-linear fitting formula and an Eisenstein & Hu (1998) matter transfer function *with baryonic wiggles*. The bottom panel of this figure shows the percentage difference of all of the curves from the Joachimi expectation.

This test was performed to determine both the accuracy of the simulations as well as the accuracy of the software producing the theoretical expectations. As can be seen from the Figure 5.2, none of the theoretical expectations agree with each other, or with the simulated data across a wide range of wavenumbers. At wavenumbers $k > 0.1$, the simulated data power spectrum turns over due to low resolution in the density binning. The very low wavenumbers, $k < 0.1$, are noisy due to the small, discrete, number of modes being sampled. It is difficult to judge how well the simulations and theoretical expectations match in this figure due to the low range of wavenumbers being recovered by the simulations. However, this figure is useful to compare the theoretical expectations. The yellow (CAMB) curve shows oscillations at low wavenumbers because the matter transfer function includes baryonic wiggles which are not included in the simulation. The red (N-GenIC) curve shows that the Peacock & Dodds (1996) fitting formulae are substantially different to the more recent Smith et al. (2003) fitting formulae (green, magenta and light blue lines). This analysis was responsible for identifying an error in NICAEA (light blue) which caused the power spectrum to be underestimated by a constant 2%. The error has now been fixed by its authors and the NICAEA expectation now matches the Joachimi curve.

---

[2] NICAEA http://www2.iap.fr/users/kilbinge/nicaea/
[3] iCosmo http://www.icosmo.org
[4] CAMB http://camb.info/
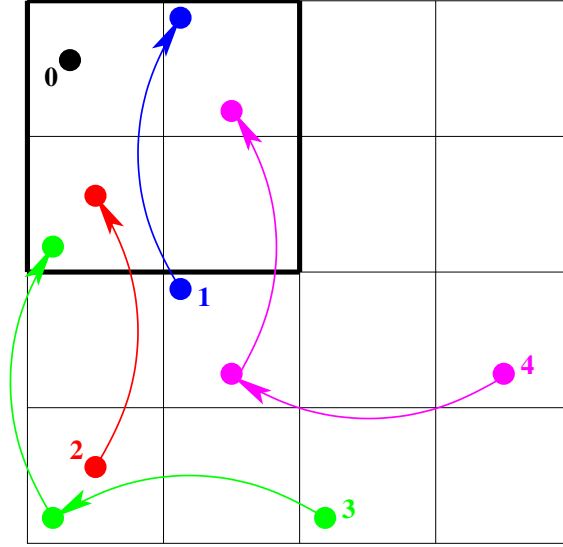
Figure 5.3: Figure demonstrating how 'folded' binning works in 2-D for ease of illustration. In this example the area is folded in half in both the horizontal and vertical axes, so all particles end up in the bins in the bold box at the top left of the area. If the particle coordinate is not $1 < (x, y) \leq n/2^f$, where n is the number of bins on a side (in this case 4) and f is the number of folds (in this case 1), then a shift of $(x, y) - n/2^f$ is performed. This style of binning is undertaken on the simulation volume in 3-D to recover higher wavenumbers in the 3-D matter density power spectrum calculation.

Due to memory restrictions, the number of bins used in the density smoothing is limited and hence the range of wavenumbers recovered in the analysis of the simulations is narrow, $0.01 < k < 0.8$. A way to get around this is to take advantage of the periodic nature of FFTW. To recover the higher wavenumbers, the simulation volume is 'folded' f times before binning the particles (Jenkins et al., 1998). Figure 5.3 demonstrates how this 'folded' binning is implemented in practice (in 2-D for ease of illustration). In this example, the area starts with $n = 4$ bins and is then folded in half, $f = 1$, on both axes. After folding, all particles will end up in the bold box in the top left corner. In the figure, particle 0 (black) is already in this area so it stays where it is. Particles 1 (blue) and 2 (red) are in the correct horizontal axis bins but lie outside $n/2^f$ along the vertical axis. These particles both have $n/2^f$ subtracted from their vertical bin number, which places them in the bold box as demonstrated. Particles 3 (green) and 4 (magenta) both require a shift of $n/2^f$ on both axes to reach the bold box, as demonstrated in the figure.

This style of binning is performed in 3-D on the simulation volumes with $f = 3$
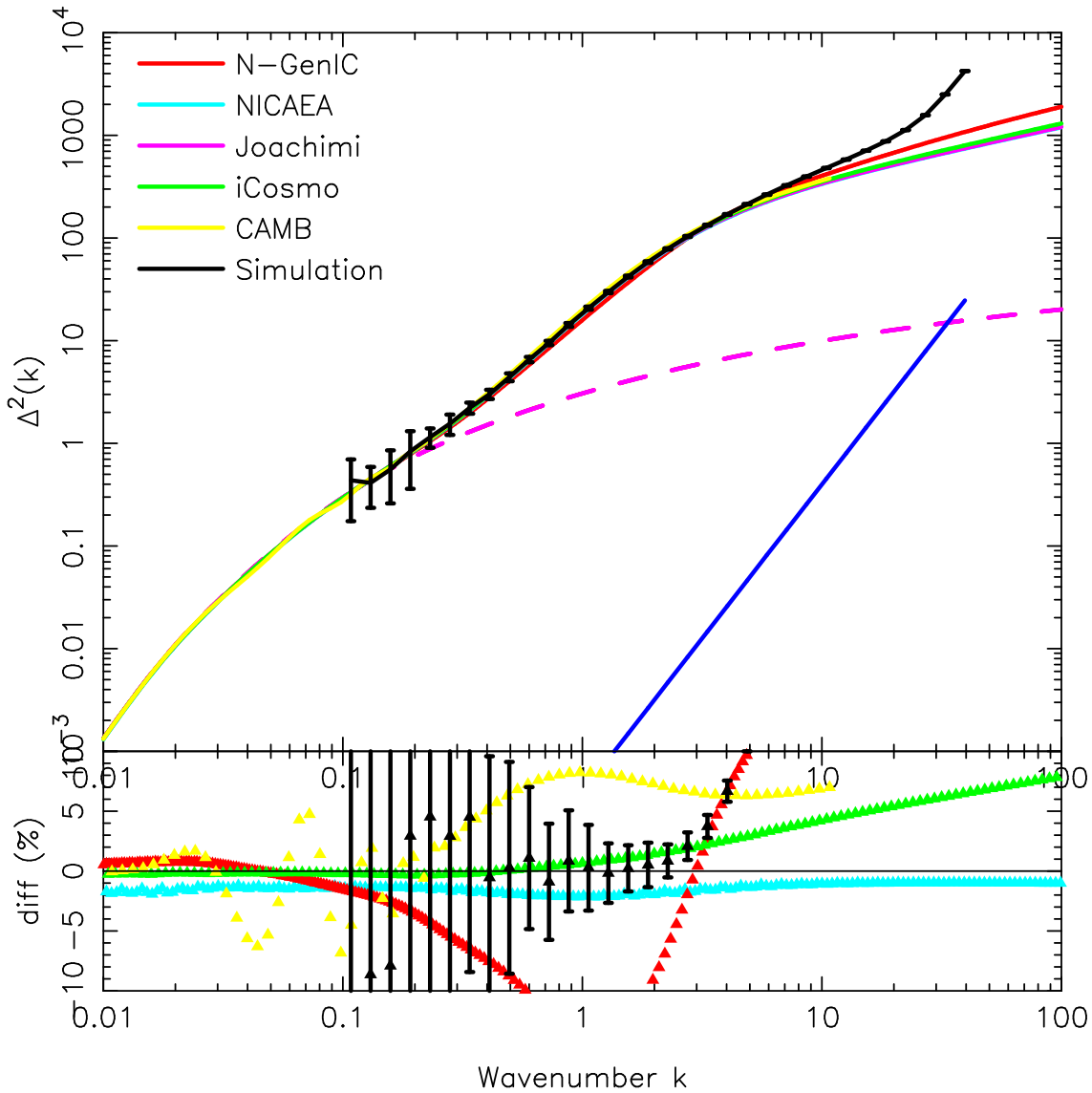
Figure 5.4: **The top panel shows the dimensionless 3-D matter density power spectrum from a volume that has been folded by a factor of 2^3 to recover higher wavenumbers. The black line shows the mean power spectrum for the 100 realisations with errors on the mean. A number of theoretical expectations are shown: Red from N-GenIC, light blue from NICAEA, magenta from a code provided by Benjamin Joachimi (the dashed line represents the linear power spectrum expectation), green from iCosmo and yellow from CAMB. The dark blue diagonal line is the predicted shot-noise contribution. The bottom panel shows the percentage differences of the various curves from the Joachimi curve.**

N_{sims}	Area (sq deg)	n_{pix}	$N_{C\ell}$	z_{max}	n_{planes}
100	100	2048^2	32	1.5	15

Table 5.1: Table of parameters for the source redshift plane lightcones used in this chapter. N_{sims} is the number of independent lightcones, n_{pix} is the number of angular pixels on the sky, $N_{C\ell}$ is the number of bins in the angular power spectrum, z_{max} is the maximum redshift in the lightcone and n_{planes} is the number of source redshift planes in the lightcone.

folds. The number of bins in the final volume is still 512^3 which means that smaller scales are resolved. However, the trade-off is that the large scales are no longer present. Figure 5.4 shows the resulting power spectrum with the same comparisons as in Figure 5.2. The simulation power spectrum is now resolving wavenumbers from $0.01 < k < 13$ and the closest matching theoretical expectation is the Joachimi expectation, which matches the simulations to within $\sim 1\%$ from $0.5 < k < 2$. At higher wavenumbers, the simulations become shot-noise dominated. One thing to note is that the 'bump' in Figure 5.2 at $0.1 < k < 0.8$ is not present in Figure 5.4. This feature is a result of binning and is not a true feature of the simulations which are accurately represented across these wavenumbers in Figure 5.4. All further work in this thesis that requires a theoretical expectation for any power spectra uses the Joachimi expectations.

Although it is difficult to determine from these figures, due to the finite resolution of the simulations and of the density binning, both the Peacock & Dodds (1996) and the Smith et al. (2003) nonlinear correction formulae are known to underestimate the matter-density power spectrum on small-scales. The Smith et al. (2003) produces a more accurate fit but is still underestimating the matter density power spectrum by up to 10% at wavenumbers of $k < 1$ and as great as 50% at $k = 10$ Mpc^{-1} (Giocoli, private communication).

5.2.3 Shear and Convergence Map Generation

The weak lensing analysis begins by determining the shear and convergence for a source redshift plane at fixed comoving distance, r_s. A distribution of sources is considered in Section 5.2.7.

The effects of weak gravitational lensing on a source can be described by two fields, the spin-2 shear, γ, which describes the stretching or compression of an image, and a scalar convergence, κ, which describes its change in angular size. These can be related to a lensing potential field, ϕ, by

$$\kappa = \frac{1}{2}\partial^2\phi, \tag{5.4}$$

$$\gamma = \gamma_1 + i\gamma_2 = \frac{1}{2}\partial\partial\phi, \tag{5.5}$$

where γ_1 and γ_2 are the orthogonal components of the shear distortion, and $\partial = \partial_x + i\partial_y$ is a complex derivative on the sky (see Chapter 3 for more detail on the weak lensing formalism).

The goal of this work is to generate shear and convergence maps along a lightcone through the simulations. Instead of using ray tracing to determine the lightcone (e.g. Wambsganss et al., 1998; Jain et al., 2000; Teyssier et al., 2009; Hilbert et al., 2009), a line-of-sight integration was implemented using the Born approximation where one integrates along an unperturbed path (e.g. Cooray & Hu, 2002; Vale & White, 2003). Fosalba et al. (2008) build their convergence maps by adding slices from their simulation with the appropriate lensing weight and averaging over a pixel;

$$\bar{\kappa}(\boldsymbol{\theta}_i, r_s) = \int_0^{r_s} dr \; K(r, r_s) \; \bar{\delta}(\boldsymbol{\theta}_i, r) \frac{3H_0^2\Omega_m}{2c^2} \sum_j \; \bar{\delta}(\boldsymbol{\theta}_i, r_j) \; \frac{(r_s - r_j)r_j}{r_s a_j} \; \Delta r_j, \tag{5.6}$$

where θ_i is the position if the ith pixel on the sky and j is a bin in the radial direction which is at a distance of r_j and has a width of Δr_j. An overline denotes an average over a pixel on the sky. The expansion factor at each radial bin j is given by a_j and the comoving radial distance of the lensing source plane is given by r_s. In order to make these calculations, the 3-D matter overdensity $\bar{\delta}(\boldsymbol{\theta}, r)$ must be calculated by binning the simulation data in three dimensions.

A limitation of this approach is memory, speed and accuracy (as demonstrated in Section 5.2.2). Here the SUNGLASS pipeline uses a new method for the line-of-sight integration so that no radial binning is required to determine the convergence. The particles are binned in the convergence calculation in a fine angular grid while allowing them to keep their radial co-ordinate. Start with the general equation for

the convergence, Equation (5.6). The overdensity $\delta(\boldsymbol{r})$ is given by

$$\delta(\boldsymbol{r}) = \frac{n(\boldsymbol{r})}{\bar{n}(r)} - 1, \tag{5.7}$$

where $\bar{n}(r)$ is the average density at the comoving radial distance r and is constant in comoving co-ordinates. The particle number density, $n(\boldsymbol{r})$, is given by a sum of 3-D delta functions

$$n(\boldsymbol{r}) = \sum_{k=part} \delta^{3D}(\boldsymbol{r} - \boldsymbol{r}_k) = \sum_k \frac{\delta^{1D}(r - r_k)}{r^2} \delta^{2D}(\boldsymbol{\theta} - \boldsymbol{\theta}_k), \tag{5.8}$$

where *part* are the particles in the pixel with $r_k \leq r_s$. Substituting this sum of delta-functions into Equation (5.6) yields the average convergence per pixel on the sky, p, with no radial binning;

$$\bar{\kappa}_p = \frac{1}{\Delta\Omega} \int_p d^2\theta \, \kappa = \sum_k \frac{K(r_k, r_s)}{\Delta\Omega_p \bar{n}(r_k) r_k^2} - \int_0^{r_s} dr \, K(r, r_s), \tag{5.9}$$

where $\Delta\Omega_p = \Delta\theta_x \Delta\theta_y$ is the pixel area, r_k is the comoving radial distance of each individual particle k in the lightcone and $K(r, r_s)$ is the scaled lensing kernel:

$$K(r, r_s) = \frac{3H_0^2\Omega_m}{2c^2} \frac{(r_s - r)r}{r_s a(r)}. \tag{5.10}$$

Hereafter the overline is dropped and it is assumed that all fields are averaged over an angular pixel. In practice Equation (5.9) can be calculated by a running summation so that it is not necessary to re-calculate the convergence from scratch for each source redshift

$$\sum_k \frac{K(r_k, r_s)}{\Delta\Omega_p \bar{n}(r_k) r_k^2} = \frac{1}{\Delta\Omega_p} \left(\frac{3H_0^2\Omega_m}{2c^2}\right) \times \left[\sum_k \frac{1}{r_k a(r_k)\bar{n}(r_k)} - \frac{1}{r_s} \sum_k \frac{1}{a(r_k)\bar{n}(r_k)}\right]. \tag{5.11}$$

Each of the sums in the square brackets can be calculated as running sums to calculate the first term in Equation (5.9). The second term in Equation (5.9) is constant for each source redshift but can be calculated in the same fashion by splitting the integral into two parts

$$\int_0^{r_s} dr \, K(r, r_s) = \frac{3H_0^2\Omega_m}{2c^2} \times \left[\int_0^{r_s} dr \, \frac{r}{a(r)} - \frac{1}{r_s} \int_0^{r_s} dr \, \frac{r^2}{a(r)}\right]. \tag{5.12}$$
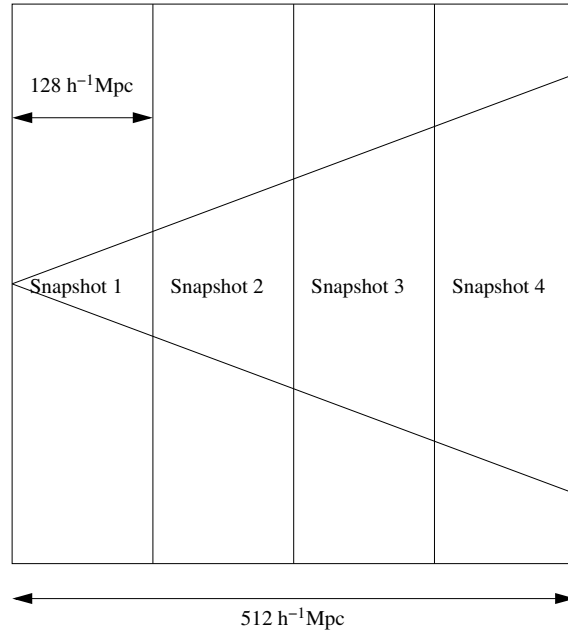
Figure 5.5: Lightcone geometry through a simulation box volume. The lightcone travels through the first $128h^{-1}$ Mpc of the first simulation and then the next $128h^{-1}$ Mpc of the next simulation etc. At the end of the simulation volume, the next volume snapshots have their centroids shifted and are randomly rotated to avoid repeated structures along the lightcone.

The convergence maps are generated by adding the particles that fall within the lightcone to the line-of-sight integration. To show evolution through the lightcone, the simulation volumes are split into $128h^{-1}$ Mpc sections. The first $128h^{-1}$ Mpc of the first ($z = 0$) snapshot is used, the second $128h^{-1}$ Mpc of the second ($z > 0$) snapshot and so on until the end of the simulation box volume is reached at snapshot 4 as shown in Figure 5.5. The centroid of the next simulation box is then shifted and the simulation box is rotated randomly to try to avoid repeated structures along the line-of-sight (e.g. White & Hu, 2000; Vale & White, 2003). The boxes are always periodic in the transverse direction. This continues through all of the snapshots out to a redshift of $z = 1.5$. The source redshifts have been placed at $\Delta z = 0.1$ intervals because the change in convergence between these redshifts is small enough that desired redshift values in between can be accurately determined by interpolation (see Section 5.2.8).

Once the convergences have been calculated at each of the source redshifts, the shear values can be determined on a flat-sky. The flat-sky shear and convergence Fourier

coefficients are related by

$$\gamma_1(\boldsymbol{\ell}) = \kappa(\boldsymbol{\ell})\frac{(\ell_x^2 - \ell_y^2)}{(\ell_x^2 + \ell_y^2)}, \tag{5.13}$$

$$\gamma_2(\boldsymbol{\ell}) = \kappa(\boldsymbol{\ell})\frac{2\ell_x\ell_y}{l_x^2 + l_y^2}, \tag{5.14}$$

where $\kappa(\boldsymbol{\ell})$ is the Fourier transform of the convergence and ℓ_x and ℓ_y are the Fourier variables. The nature of FFTW is such that it has periodic boundary conditions. In this work the lightcone is not periodic and the convergence is calculated with a 1% larger field than the final 100 sq. deg. After Fourier transforming this convergence field to determine the shear, the extra is trimmed away to compensate for any periodic structures in the resulting shear field. To test the algorithm the B-modes were also estimated by calculating the unphysical imaginary part of the convergence $\beta = \mathrm{imag}(\kappa)$, from the shear,

$$\beta(\boldsymbol{\ell}) = \gamma_1(\boldsymbol{\ell})\left(\frac{2\ell_x\ell_y}{l_x^2 + l_y^2}\right) + \gamma_2(\boldsymbol{\ell})\left(\frac{\ell_x^2 - \ell_y^2}{\ell_x^2 + \ell_y^2}\right). \tag{5.15}$$

Figure 5.6 is an example of a convergence and shear map for a field that is 100 square degrees at a source redshift of $z = 0.8$. There are 2048 bins in each transverse direction and no binning in the radial direction. The background of the map shows the integrated convergence along the lightcone up to $z = 0.8$ and the white ticks show the shear at this source redshift. The length of the ticks has been multiplied by an arbitrary constant to make them visible as the magnitude of the shear is at the percent level. The red patches show areas of the highest convergence and the shear ticks clearly trace these regions tangentially. These maps can be generated for the standard simulations at multiple source redshifts quite rapidly once the simulations have been run. The most time consuming module in this code is reading in the snapshots due to their reasonably large size of 100GB. This module can be optimised by using the fastest available data transfer rates on the drive where the snapshot data is stored.

5.2.4 Shear and Convergence Power Spectra

In order to verify the accuracy of the shear and convergence maps, the shear and convergence power spectra are determined for each source redshift. From Equation
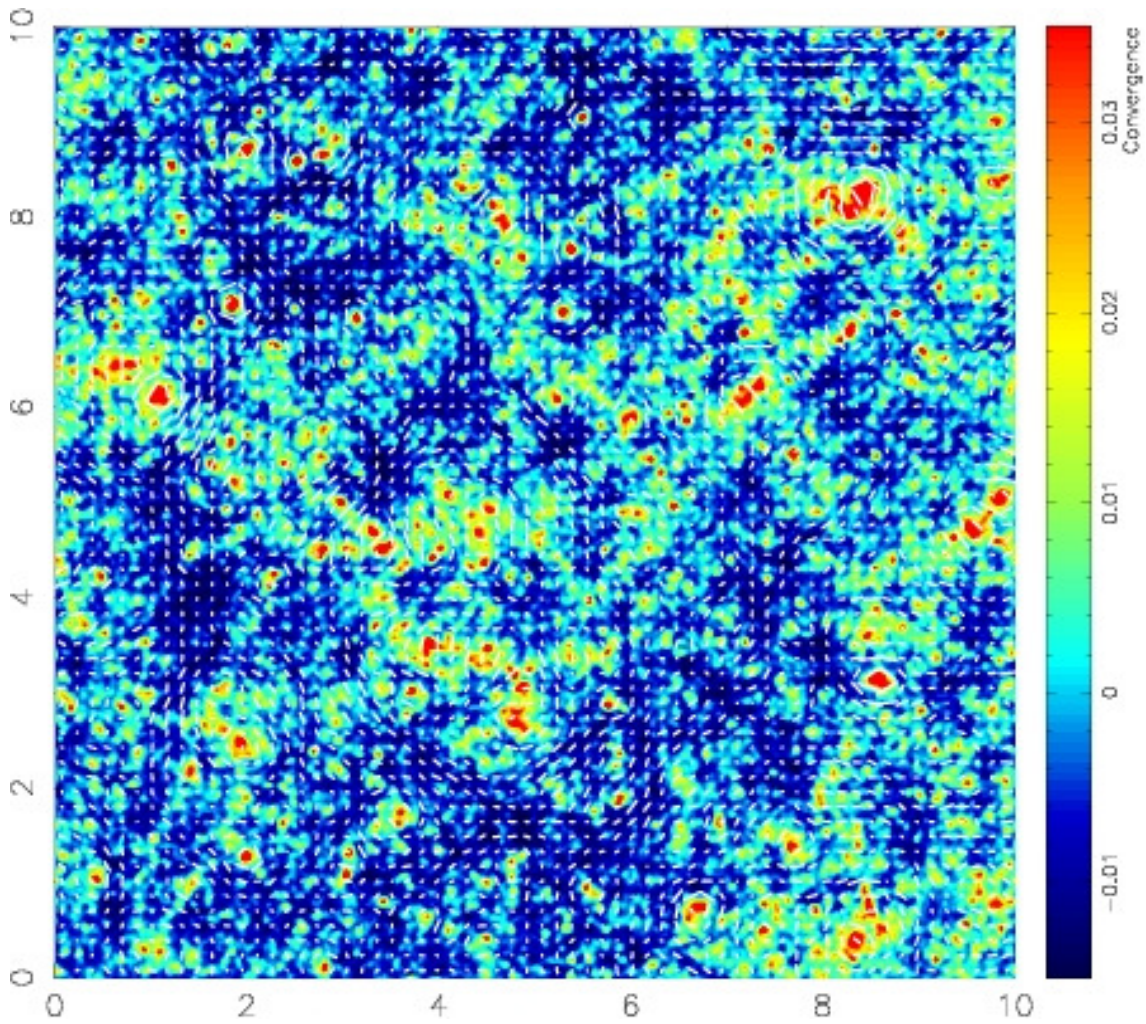
Figure 5.6: Convergence and shear map for a simulated survey of 100 square degrees with a single source redshift of $z_s = 0.8$. The colour-scale background shows the convergence while the white ticks show the shear signal.
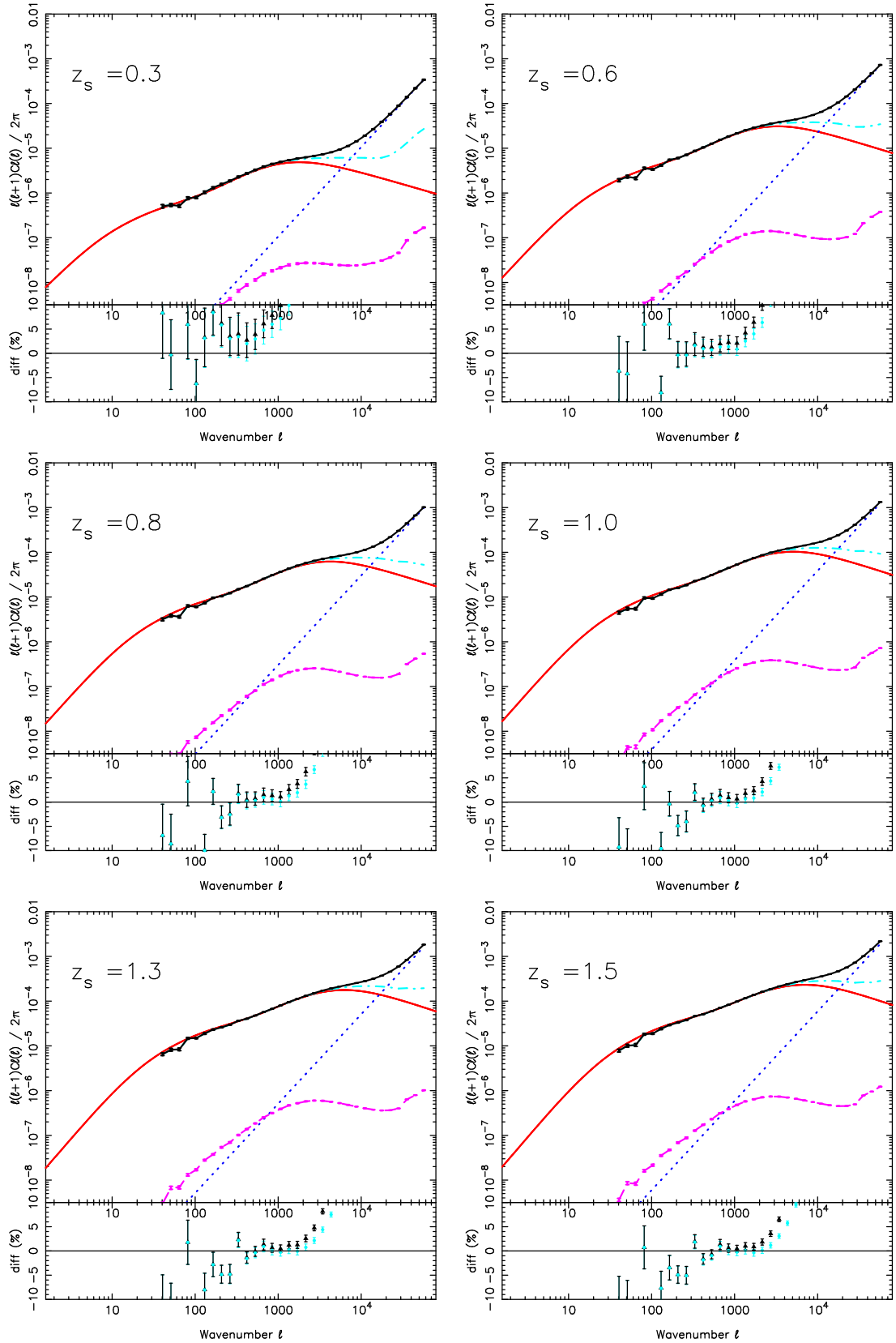
Figure 5.7: **Simulated slices of the shear power spectra for N-body particle data at various source redshifts. The theory power spectrum is in red, the shot-noise prediction in dark blue, the B-modes in magenta and the mean measured signal with errors in black. The light-blue line is the measured signal minus shot-noise. The bottom panel shows the percentage difference of the measured signal from the theoretical expectation.**

(5.6) and using the Limber approximation, the theoretical prediction for the shear and convergence power spectrum for sources at redshift z is given by

$$C_\ell^{\gamma\gamma}(z) = C_\ell^{\kappa\kappa}(z) = \frac{9H_0^4\Omega_m^2}{4c^4} \int_0^{r_s} dr\, P\left(\frac{\ell}{r}; r\right) \frac{[r_s(z) - r]^2}{r_s^2(z)a^2(r)}, \qquad (5.16)$$

(e.g. Munshi et al., 2008) where $P(\ell/r; r)$ is the 3-D matter density power spectrum at a redshift z.

From the simulations it is possible to determine an angle-averaged power spectrum from the convergence and shear calculated in the lightcones. When taking in to consideration the conventions used in FFTW, the discretised convergence power spectrum for a slice in redshift is given as the sum over logarithmic shells in ℓ-space as

$$\frac{\ell(\ell + 1)\hat{C}_\ell^{\kappa\kappa}(z)}{2\pi} = \sum_{\ell\,\text{in shell}} \frac{|\kappa(\boldsymbol{\ell}, z)|^2}{n_{\text{pix}}\, \Delta \ln \ell}, \qquad (5.17)$$

where n_{pix} is the total number of bins in the Fourier transform (2048^2 in this case) and $\Delta \ln \ell$ represents the thickness of the shell in log ℓ-space, and $\hat{C}_\ell^{\kappa\kappa}$ is the estimated power. Similarly the shear power is estimated by

$$\frac{\ell(\ell + 1)\hat{C}_\ell^{\gamma\gamma}(z)}{2\pi} = \sum_{\ell\,\text{in shell}} \frac{|\gamma_1(\boldsymbol{\ell}, z)|^2 + |\gamma_2(\boldsymbol{\ell}, z)|^2}{n_{\text{pix}}\, \Delta \ln \ell}. \qquad (5.18)$$

The B-mode power is estimated in the same way as the convergence.

The lightcone fields are non-periodic 'windows' in the simulation and Fourier transforming a window causes a strong mixing of modes due to edge effects. In the absence of a Pseudo-C_ℓ analysis method (see Chapter 7), apodising the shear and convergence fields will reduce these effects. Apodisation slowly smoothes the discontinuities at the edges of the sample by damping the signal with a smoothly varying function. In this work, the apodisation is performed by multiplying the shear or

convergence with the following kernel

$$
W(x) = \begin{cases}
\frac{1}{2}\left[1 - \cos\left(\frac{\pi x}{\Delta}\right)\right] & \text{for } x < \Delta \\[2ex]
\frac{1}{2}\left[1 - \cos\left(\frac{\pi(n_{pix}-x)}{\Delta}\right)\right] & \text{for } x > n_{pix} - \Delta \\[2ex]
1 & \text{otherwise,}
\end{cases} \tag{5.19}
$$

where x is the bin number and Δ is the size of the region to be apodised, 1/8th of the field in this work. Apodisation does cause the 2-D power spectrum to be slightly damped, but this falls within the 1σ error bars and is not significant.

As with the 3-D matter density power spectrum, the modes in this power spectrum are arranged on a square grid, which causes discreteness errors when binned in annuli at small ℓ. To correct for this, the power is scaled by the ratio of the measured number of modes to the expected number of modes,

$$
N_{exp} = g\pi(\ell_{max}^2 - \ell_{min}^2), \tag{5.20}
$$

where $g = (L/2\pi)^2$ is the density of states, L is the size of the field in radians, ℓ_{max} and ℓ_{min} are the maximum and minimum wave numbers in this shell. The effect of this normalisation correction is about 10% at the lower wavenumbers while the higher wavenumbers remain largely unaffected. The discreteness correction is not perfect which is why the same slight zig-zag of the power spectrum is evident in all of the source redshift planes at wavenumbers $\ell < 100$. The simulated shear and convergence power spectra is compared with the Joachimi theoretical expectation.

Due to the discrete number of particles in an N-body simulation, the measured power spectrum will be the combined real shear and convergence power plus a shot-noise power contribution,

$$
\hat{C}_\ell^{\kappa\kappa} = C_\ell^{\kappa\kappa} + C_\ell^{SN}, \tag{5.21}
$$

where $\hat{C}_\ell^{\kappa\kappa}$ is the power estimated from the simulation. The shot-noise power can be derived from Equation (5.16) using a white-noise power spectrum, $P_{SN}(k,r) = 1/\bar{n}_3(r)$, where $\bar{n}_3(r)$ is the 3-D mean comoving number density of particles in the

simulation. The shot-noise power for the shear and convergence is then given by

$$C_\ell^{SN} = \frac{9H_0^4\Omega_m^2}{4c^4} \int_0^{r_s} dr \, \frac{(r_s - r)^2}{\bar{n}_3(r)r_s^2 a(r)^2}.$$ (5.22)

Usually, for simulated particles, $\bar{n}_3$ will be a constant in comoving coordinates.

Figure 5.7 shows the mean, normalised 2-D shear power spectra estimated from 100 independent simulations (black points and line), with the error bars showing the scatter on the estimated mean. The figures show the shear power for sources at redshifts of $z = 0.3$, 0.6, 0.8, 1.0, 1.3 and 1.5. The smooth (red) line shows the theoretical prediction for the ensemble-averaged shear power spectrum, while the diagonal (dotted blue) lines show the shot-noise power for each source redshift. The (dot-dashed light blue) curve between the simulated data and the theory curve shows the mean power spectrum with the expected shot-noise subtracted and the lower (dashed magenta) curve shows the estimated B-mode power spectrum.

The bottom panel of each figure shows the percentage difference between the measured shear power spectrum and the ensemble-average theory prediction (upper black points), while the lower (light blue) points show the shot-noise subtracted shear power spectrum. Overall the mean shear power agrees well, to within a few percent, with the ensemble-averaged theoretical model over the ℓ-range $\ell < 1000$ for all source redshifts. The difference of a few percent is due to the fact that the theory 3-D matter density power spectrum is a few percent lower than the measured data power spectrum in the corresponding k wavenumber range. Calculating the highly non-linear power spectrum is currently not accurate to a few percent and many calculations of this theory curve do not agree with each other to within a few percent. The Joachimi theory curve was the closest fit to the simulations and was used for all subsequent calculations. At low ℓ the measured signal drops as the size of the simulation box is reached, while at high ℓ, the estimated mean shear power becomes shot-noise dominated before reaching the highest mode allowed by the resolution of the angular pixels beyond $\ell = 1/\theta_{\mathrm{pix}} \simeq 10^4$.

Before reaching pixel-resolution, the measured shear power at high-ℓ agrees well with the predicted shot-noise (see Section 5.2.5 for a more detailed look at the noise power spectrum). This agreement suggests that the shot-noise model works rea-

sonably well in this regime, even though the initial particle distribution is a glass, however we do not expect to be able to model the shot-noise to the percent level accuracies required for future telescope missions (see Baugh et al., 1995, for a discussion). This suggests an improved (but not perfect) estimate of the mean power can be found by subtracting the shot-noise contribution. As expected, the shot-noise subtracted shear power does not follow the ensemble-averaged theoretical power estimated from the theory code. It is likely that as well as not modeling the shot-noise absolutely accurately, this is also a failure of the theoretical model for the matter density power spectrum, which is used to determine the theoretical model of lensing and has been shown to underestimate the shear and convergence power spectrum by up to 30% on scales of $\ell < 10^4$ (Hilbert et al., 2009).

As a test, the 2-D shear power spectrum theory curves were also calculated from the measurement of the 3-D matter density power spectrum from the simulations (see Section 5.2.2), instead of using the theoretical expectation from the Joachimi code. The resulting power spectrum was within 1% of the theory calculation in the wavenumbers that were already being recovered well in the 2-D power spectrum, which is a good validation of the theoretical prediction in this range. At higher wavenumbers, the spectra are affected significantly by shot-noise, which is problematic to model accurately (Baugh et al., 1995). For higher resolution simulations, using the numerical power spectrum may provide more accurate fits than the fitting formulae of Smith et al. (2003). In subsequent analysis in this chapter the analysis will be restricted to the region of the measured power spectrum that agrees with the theoretical prediction.

Figure 5.7 also shows the estimated B-mode power spectra. When galaxies trace the shear signal, we expect the B-mode power to pick up a shot-noise dependence. But here the shear signal is a pixelized field which would be continuous in the limit of infinite pixels or periodic boundary conditions. Therefore a noise-generated B-mode is not expected. However, B-modes can still be generated due to leakage of power from the convergence field caused by the finite window function introduced by the small buffer used when generating the shear field from Equation (5.14). As a consequence the induced B-mode has the shape of the shear power, but suppressed by around three orders of magnitude, showing that the B-mode signal can recovered but giving a signal small enough to not affect any measurements made in the rest

of this work (see Section 5.2.6 for further discussion on the B-modes).

In this section I have shown that the SUNGLASS algorithm for calculating the shear and convergence maps and the power spectra in redshift slices is accurate to a few percent over a wide range of scales and redshifts. Wavenumbers up to $\ell = 1500$ can be modelled accurately for the source redshifts $z \geq 1.1$ with this simulation resolution. For shot-noise subtracted power spectra, the recovered modes increase before the angular pixel resolution cuts off the power.

5.2.5   2-D Noise Power Spectra

The shot-noise contribution to the 2-D angular power spectra in the source redshift analyses is given by the analytic expression in Equation (5.21). This expression predicts the shot-noise for a Poisson sampling of the density field. To test the accuracy of this prediction, ten simulation volumes were randomly populated with the same number of particles as the simulations and weak lensing lightcones were generated using the SUNGLASS pipeline.

Figure 5.8 shows the 2-D angular power spectra for these 'noise' lightcones. The red line is the theoretical expectation for a ΛCDM universe at this source redshift and the lower diagonal (magenta) line shows the B-modes, purely for illustration purposes. It is worth noting that the B-modes are only visible due to the addition of a 1% buffer around the field when calculating the shears (see Section 5.2.6 for further discussion). The diagonal dark blue line is the theoretical expectation for the Poisson shot-noise and the black line shows the measured power spectrum from the suite of noise simulations with errors on the mean. The light-blue line visible in some of the source redshifts shows the expected shot-noise minus the measured shot-noise. The bottom panels show the percentage difference of the measured power spectrum from the expected power spectrum. At all source redshift planes, the measured power spectrum matches the expected power spectrum to within 3%. The reason for the slightly lower measured signal is not known.

While these figures show that the theoretical expectation for the shot-noise contribution match the measured shot-noise in a Poisson distribution well, the noise in the simulations is not Poissonian. The ΛCDM simulations generated in the pre-
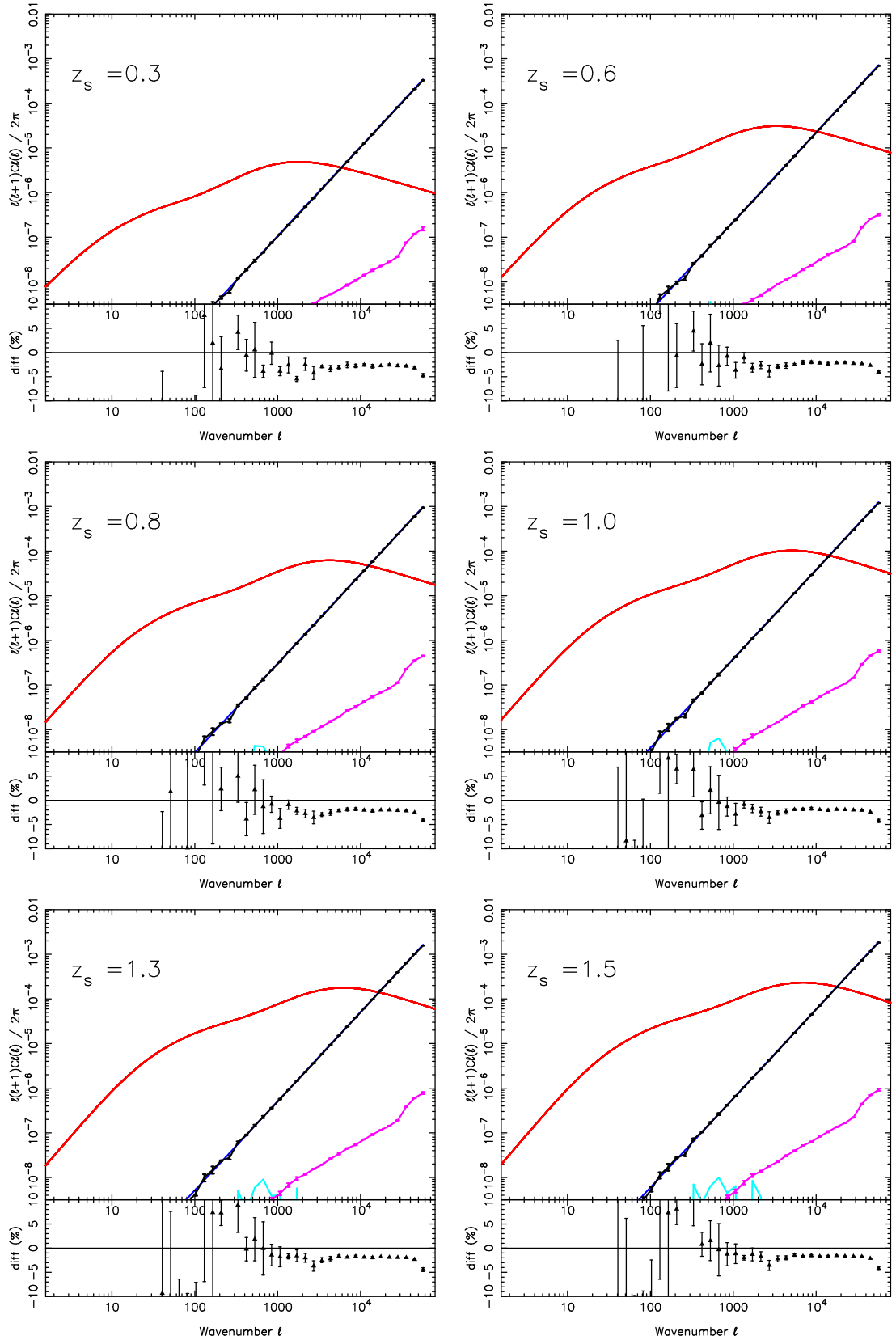
Figure 5.8: **2-D Poisson noise power spectrum at various source redshifts. The theoretical expectation is in red, the analytical shot-noise prediction in dark blue, the measured power spectrum is in black with B-modes in magenta and the analytic shot-noise subtracted signal in light blue. The bottom panel shows the difference between the predicted shot-noise and the measured signal.**

vious section start from a sub-Poissonian glass distribution which evolves toward Poisson noise as the simulations evolve, but this noise evolution is not possible to model accurately. Consequently, although a Poisson noise expectation is shown in this work, it is strictly for visualisation purposes and is not subtracted from the measured signal in any of the analyses in this work.

5.2.6   Source Redshift Plane Weak Lensing B-Mode Test

The B-modes measured from the shear in the source redshift plane analysis are dependent on how the shear is constructed. The ideal scenario available to simulations occurs when the shear field is constructed from the measured convergence through an FFT. The periodic nature of the FFT means that the shear field is also periodic and there should be no B-modes present as there is no mixing of modes in the shear field due to window functions in the FFT. Periodic boundary conditions do not exist in observations which makes this ideal case in the simulations unphysical.

A more realistic scenario occurs when a 'buffer' is added to the convergence field that is trimmed away after the shear field has been constructed. In the simulations, the buffer is simply constructed by selecting a larger field. Trimming away this buffer after the shear field has been constructed removes the periodic boundaries and introduces B-modes to the field. The size of the buffer will have an effect on the size of the B-modes. A very small buffer, like the one used in the previous section, will result in some of the shear effects from the opposite side of the box still appearing in the power spectrum calculation and hence the B-modes should be very small. The purpose of including a buffer like this is to demonstrate how the pipeline measures B-modes, without introducing a signal strong enough to contaminate the physical shear power spectra. A very large buffer should remove all periodicity and is the most representative of observations in the real world. This analysis will have a much larger B-mode signal.

Figure 5.9 shows the B-modes for suites of 10 simulations with three different buffer sizes: no buffer, 1% and 20% buffers. The apodisation of the shear fields at the edges has been switched off in the power spectrum calculation so the buffered fields have sharp cut-offs in the shear signal at their edges while the unbuffered field assumes full periodicity. The mean of the B-modes is shown in magenta, with errors on the
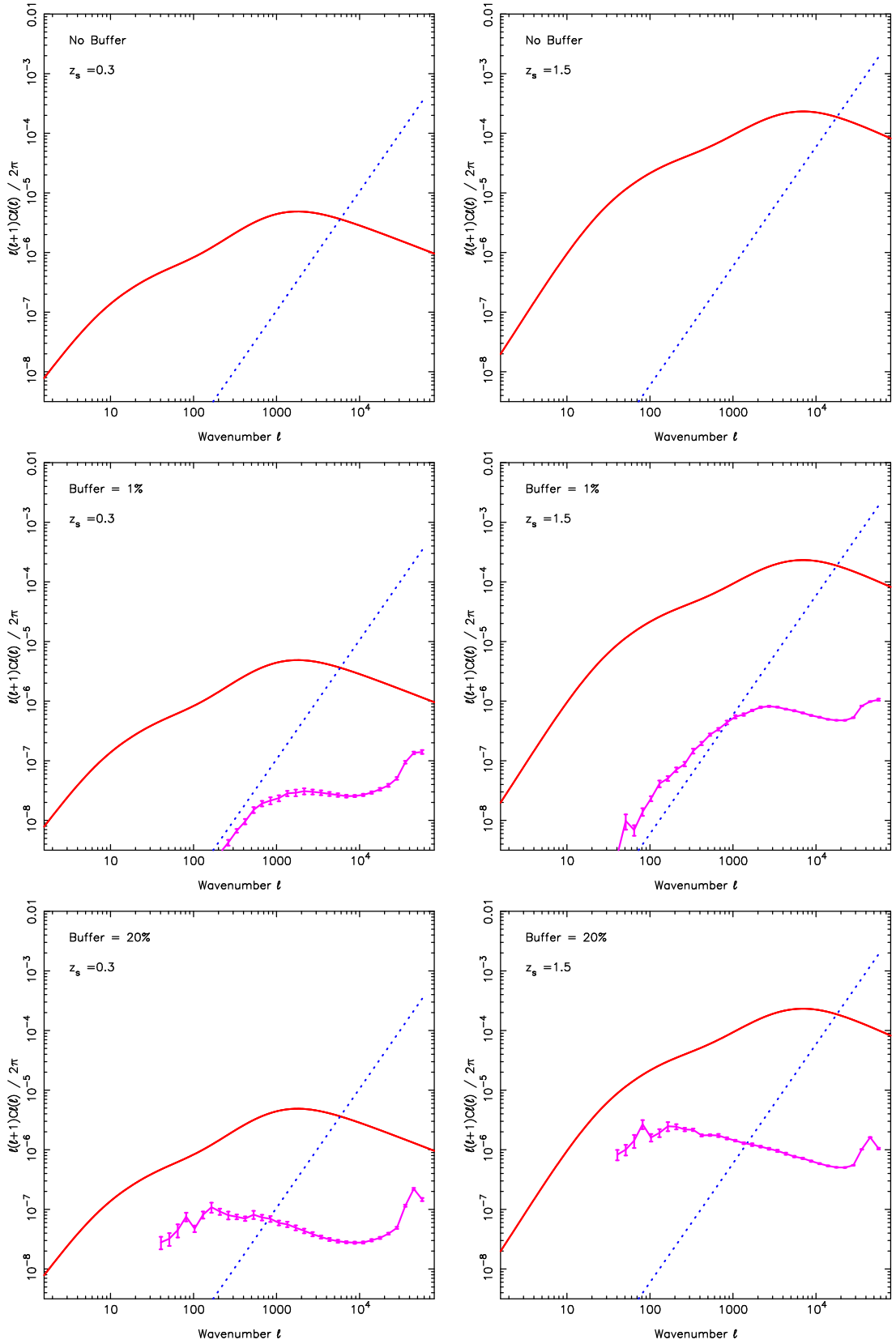
Figure 5.9: B-modes in source redshift plane analysis resulting from various buffer sizes used when calculating the shear field.

n_g ('gals' per sq arcmin)	z_{med}	σ_0	z_{max}	n_{pix}
15	0.82	0.05	1.5	768^2

Table 5.2: **Table of mock weak lensing survey parameters used in this chapter. All 100 lightcones of 100 sq. deg were turned into mock catalogues with the above survey parameters: n_g is the number of 'galaxies' per square arcminute (it is assumed that the galaxies trace the dark matter exactly so the dark matter particle locations are representative of the galaxy distribution), z_{med} is the median redshift of the galaxies in the catalogue, σ_0 is the photometric redshift error estimate, z_{max} is the maximum redshift in the catalogue and n_{pix} is the number of angular pixels on the sky.**

mean. As expected, the unbuffered field shows no B-modes. The field with the 1% buffer has a B-mode signal that is consistent with the shot-noise until wavenumbers $\ell \sim 1000$, where the signal turns over to become almost flat. The field with the 20% buffer has B-modes that are larger than those in the 1% buffered field and are almost flat across all wavenumbers.

The existence of B-modes in the source redshift planes of simulations is user controlled as they can be entirely removed by assuming periodic boundary conditions in the shear field. However, as mentioned earlier, this is unphysical as the Universe does not have periodic boundary conditions. This feature of the simulations can be tailored for the scientific purpose under review. In this work, the 1% buffer is retained for illustrative purposes and the resulting B-modes are visible but not large enough to have an effect on the E-mode signal.

5.2.7   Mock 3-D Weak Lensing Galaxy Catalogues

Real, 3-D weak lensing data analysis is applied to a galaxy catalogue where galaxy angular positions and redshift are added to estimated shears for each galaxy. For a 2-D analysis, individual redshifts are ignored and the theory uses only the redshift distribution. It is straightforward to generate a simple 3-D mock weak lensing galaxy catalogue with the information in the lightcones I have generated from the simulations. Shear and convergence maps are generated for each lensing source redshift and then each particle in the simulation is assigned a shear and convergence by interpolating between adjacent planes. The error introduced by linearly interpolating the shear and convergence between source redshift planes separated
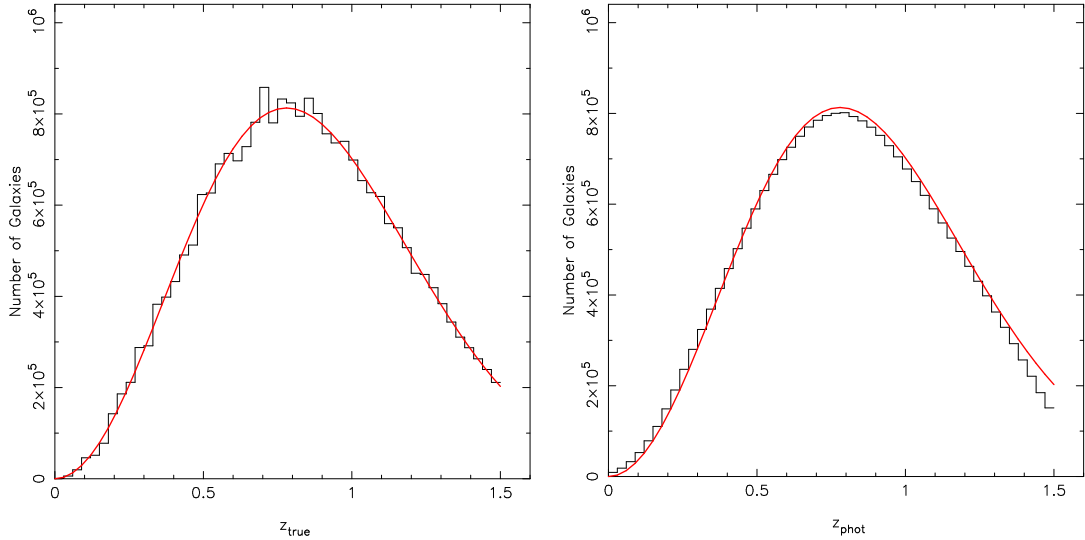
Figure 5.10: Left: The galaxy distribution, $n(z)$, in the mock galaxy catalogue. The smooth (red) line shows the theoretical $n(z)$ and the black histogram shows the distribution from a single simulation lightcone. The histogram shows the clustered nature of the lightcone. Right: The galaxy distribution in the mock galaxy catalogue with photometric redshift errors assigned to each galaxy. The structures visible in the true redshift lightcone have been smoothed out with the addition of the photo-z errors.

by $\Delta z = 0.1$ was estimated by comparing with higher redshift-sampled planes and found to be substantially below the theoretical prediction of the signal except at angular wavenumbers where shot-noise becomes dominant (see Section 5.2.8). With the interpolated shear and convergence assigned to each particle, we now have a fully-sampled 3-D mock weak lensing galaxy catalogue, which can be down-sampled to generate realistic weak lensing surveys.

To down-sample the full 3-D weak lensing simulated lightcone to construct a realistic 3-D weak lensing galaxy catalogue, a galaxy redshift distribution (Efstathiou et al., 1991) is used

$$n(z) \propto z^{\alpha} \exp\left[-\left(\frac{z}{z_0}\right)^{\beta}\right], \tag{5.23}$$

where z_0, α and β set the depth, low-redshift slope and high-redshift cut-off for a given galaxy survey. The parameters are taken as $\alpha = 2$, $\beta = 2$ and $z_0 = 0.78$, yielding a median redshift of $z_m = 0.82$, similar to the CFHTLens Survey (Fu et al., 2008).

As the particles in the simulation are in comoving coordinates, the redshift dis-

tribution is transformed to a probability distribution for the particle to enter the catalogue given its comoving radial distance,

$$p(r) \propto r^\alpha \left(\frac{dr}{dz} \right) \exp\left[-\left(\frac{z(r)}{z_0} \right)^\beta \right], \tag{5.24}$$

where

$$\frac{dr}{dz} = \frac{c}{H(z)}, \tag{5.25}$$

and

$$H(z) = \frac{H_0}{[\Omega_m(1+z)^3 + \Omega_K(1+z)^2 + \Omega_\Lambda]^{1/2}}, \tag{5.26}$$

where H_0 is the current Hubble value, Ω_m is the current matter density, Ω_Λ is the current dark energy density (all defined in Section 5.2.1) and Ω_K is the curvature parameter. Throughout a flat, $\Omega_K = 0$, cosmology for the simulations has been assumed. The particle distribution was sampled so the final galaxy catalogue has a surface density of around 15 galaxies per square arcmin, with a maximum redshift cut-off at $z = 1.5$.

The left panel of Figure 5.10 is an example of a redshift distribution taken from the full particle lightcone. The red line shows the theoretical distribution from Equation (5.24), normalised to the number of particles selected, from which the simulation particles were drawn. The clustered nature of the particles in the distribution is apparent as the peaks and troughs around the theoretical curve can be seen.

The 3-D weak lensing catalogue currently assumes that the redshift of each galaxy is accurately known. This would be appropriate for a spectroscopic redshift survey, but with such large surveys we can expect most weak lensing catalogues will contain photometric redshift estimates for each galaxy. To account for photometric redshift errors, the measured redshift was randomly sampled from the true redshift using a Gaussian distribution with uncertainty

$$\sigma_z = \sigma_0(z_g)(1 + z_g), \tag{5.27}$$

where z_g is the true redshift of the particle. For the purposes of this work a fixed $\sigma_0 = 0.05$ is assumed. The right-hand panel of Figure 5.10 shows what the distri-
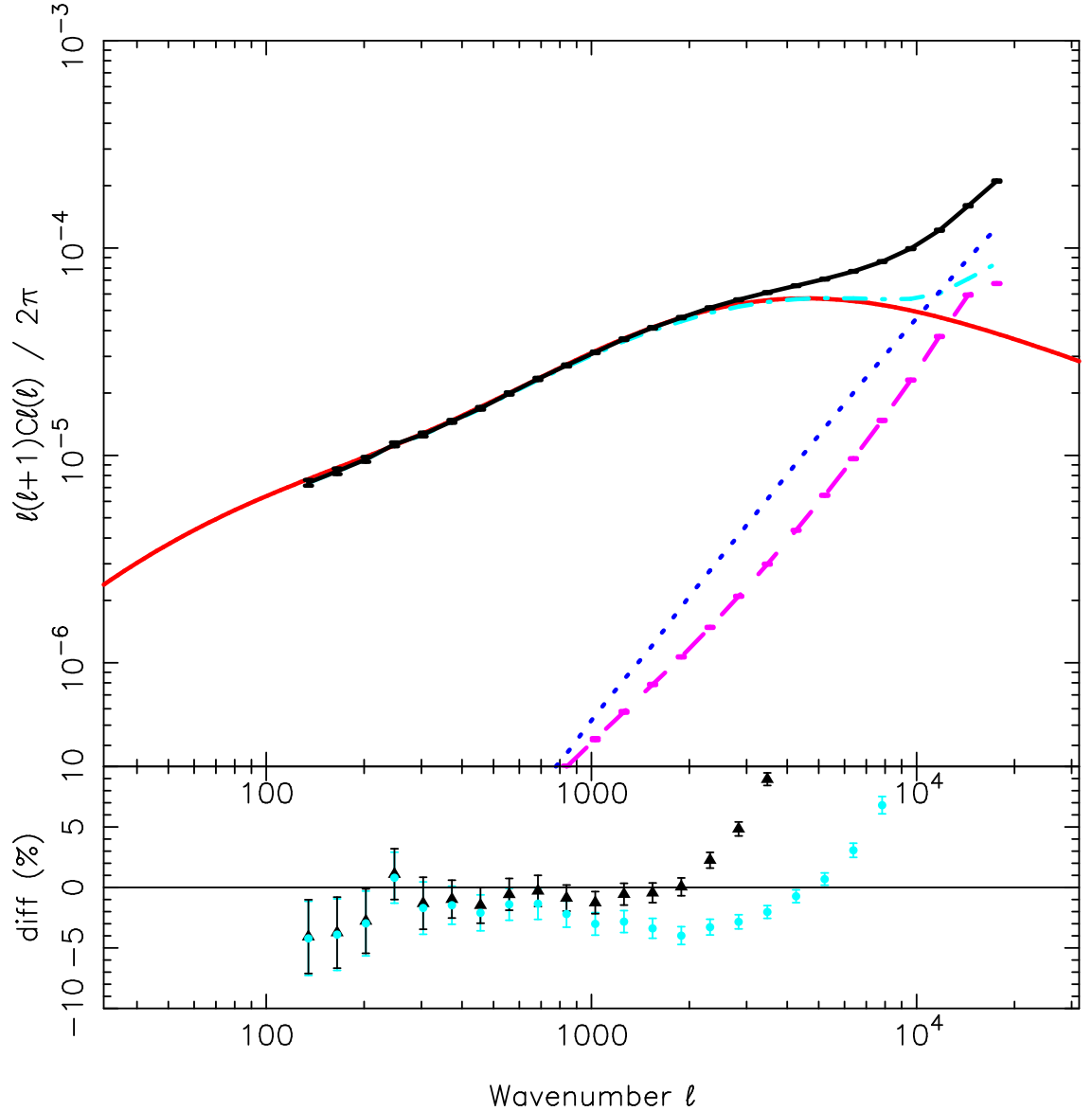
Figure 5.11: **2-D shear power spectrum for the lightcone suite with the $n(z)$ particle distribution. In the upper panel, the long smooth (red) line is the theory prediction and the diagonal (dotted blue) line is the shot-noise prediction. The (black) points and line is the mean measured power spectrum for the suite of mock catalogues with the errors representing the error on the mean and the (dot-dashed light blue) curve between the theory prediction and the measured simulation data is the shot-noise subtracted power spectrum. The diagonal (dashed magenta) line shows the mean of the B-modes for the suite of mock catalogues with errors on the mean. The bottom panel shows the percentage difference of the data from the theory curve with errors on the mean (upper, black) and the (lower, light blue) points represent the shot-noise subtracted data.**

bution on the left looks like with photometric redshift errors. The structures are smoothed out and the distribution becomes featureless. The photometric redshift errors were implemented by specifying a Gaussian error.

Figure 5.11 shows the ensemble-averaged 2-D shear power spectrum estimated from 100 mock weak lensing surveys in the top panel (black line) with errors on the mean, compared the theoretical prediction (long smooth red line), and the ensemble-averaged B-mode power (dashed magenta line). The (blue dotted) diagonal line shows the shot-noise prediction for these galaxy redshift distributed lightcones. The shot-noise was determined by running the SUNGLASS analysis on a number of simulation box volumes filled with randomly distributed particles. The power spectrum of these lightcones represents shot-noise estimate for the simulations and is a remarkably straight power law. The (dot-dashed light blue) curve between the shot-noise and the measured power spectrum is the shot-noise subtracted power spectrum. The bottom panel shows the fractional difference between the average of the mock surveys and the theory curve, with the error on the mean (upper, black) and the shot-noise subtracted points below (lower, light blue). This shows that the mock weak lensing survey agrees with the theoretical expectation from wavenumbers from $\ell = 200$ to $\ell = 2000$, where the disagreement with theory can be ascribed to the uncertainty on the theory curve, and the rise of shot-noise. The shot-noise subtraction in this case is a few percent lower than the theoretical prediction. The reason for this is not well understood and is the subject of ongoing investigation. The analyses in this chapter will use the measured simulation power spectrum only. The B-mode power appears to follow a shot-noise profile which is consistent with the effect of sampling from the full particle lightcone. A secondary source for B-modes is source clustering, which appears to be sub-dominant.

5.2.8 Testing the Accuracy of Interpolating Shear and Convergence Between Source Redshift Planes

The generation of the mock galaxy shear catalogues relies on being able to interpolate shears and convergences between source redshift planes without introducing significant errors. This was tested by generating two identical lightcones, one with source redshift planes at $\Delta z_s = 0.1$ and the other with source redshift planes at $\Delta z_s = 0.05$. The interpolation of the planes is expected to be the least accurate ex-
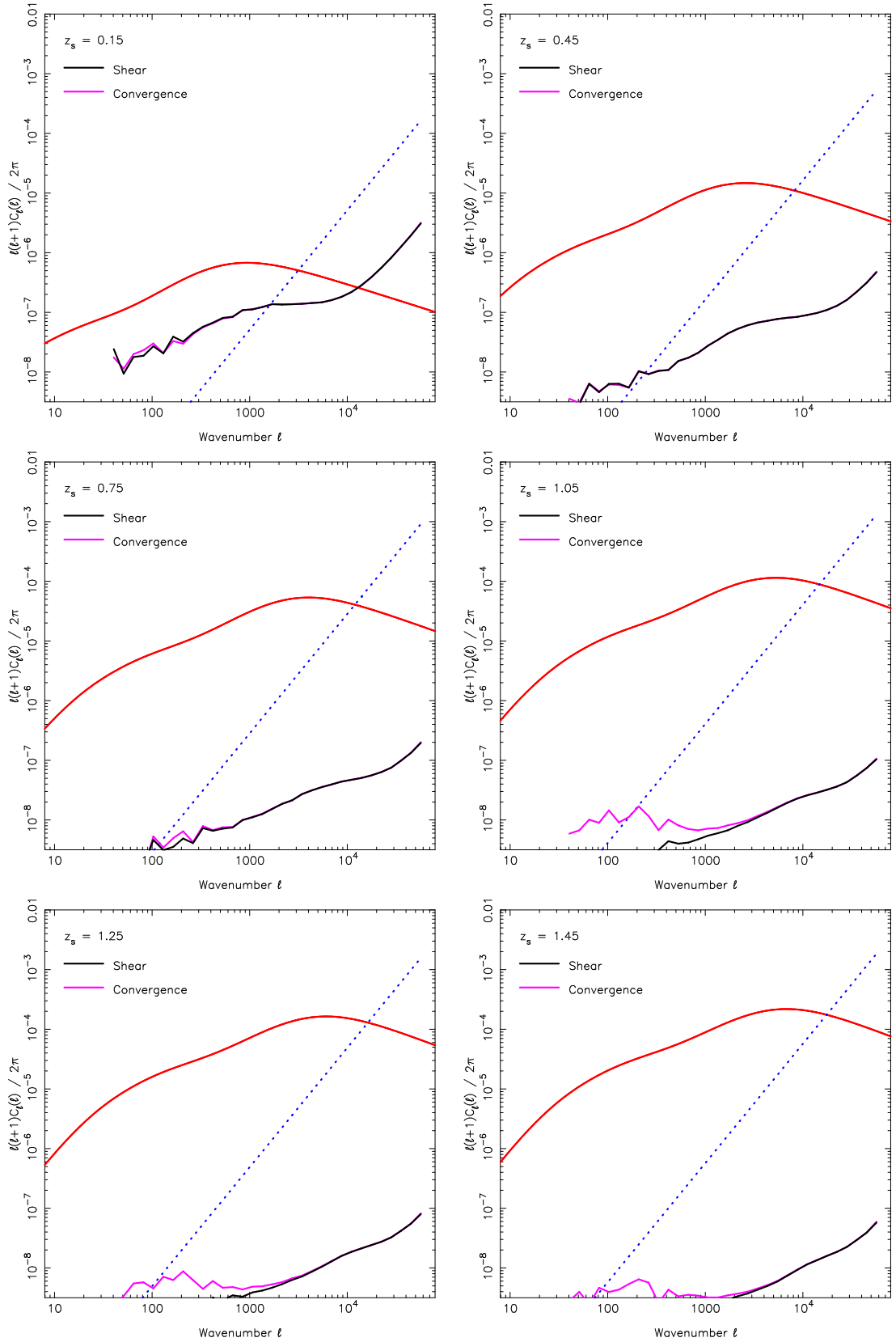
Figure 5.12: **Errors introduced by interpolating shear and convergence between source redshift planes. The theoretical power spectrum is in red and the predicted shot-noise in blue. The power spectrum of the difference between the interpolated and measured shear is in black and convergence in magenta.**

actly half way between the two planes, so this is where the testing was focused. The shears and convergences in the $\Delta z_s = 0.1$ lightcone were interpolated to half way between the planes using a linear interpolation. These fields were then subtracted from the corresponding source redshift planes in the $\Delta z_s = 0.05$ lightcone.

Figure 5.12 shows the 2-D angular power spectrum at a number of source redshift planes of the fields generated by subtracting the interpolated shears and convergences from the corresponding measured fields. The expected ΛCDM power spectrum is shown in red and the shot-noise is represented by the blue dotted line. The black line is the power spectrum of the shear field and the magenta line is the power spectrum on the convergence. The largest errors introduced clearly occur at the lowest source redshift planes where the smallest number of particles are present. However, even at a source redshift of $z_s = 0.15$, the error introduced into the power spectrum is still an order of magnitude lower than the expected signal until the shot-noise begins to dominate. At all redshifts the introduced error $\Delta \frac{\ell(\ell+1)C_\ell^{\gamma\gamma}}{2\pi}$ and $\Delta \frac{\ell(\ell+1)C_\ell^{\kappa\kappa}}{2\pi} < 10^{-7}$ in the non-shot-noise dominated regime. This shows that using source redshift planes separated by $\Delta z_s = 0.1$ is reasonable in the construction of mock galaxy shear catalogues.

5.2.9 Effects of Sampling and Binning on Shear and Convergence in the Mock Catalogues

When generating the mock catalogues, a dependence for the recovered shear and convergence power on the number of pixels used to estimate the 2-D lensing power was found. Figure 5.13 shows the shear and convergence in the mock catalogues with varying numbers of transverse pixels used in the calculation of the power spectrum. In these figures, the red line shows the theoretical expectation for the power spectrum. The black line shows the convergence power spectrum and the green line shows the shear power spectrum. Initially, just focusing on the (green) shear power spectrum, the figure shows that with too many bins, there is a number of empty pixels and this reduces the amplitude of the power spectrum. The amplitude of the power spectrum increases with fewer empty bins before converging at the true amplitude. However, by using too few bins, the number of ℓ modes recovered is reduced due to pixelization effects. From these figures it is clear that 768^2 bins provides a stable amplitude for the shear power spectrum with the largest number
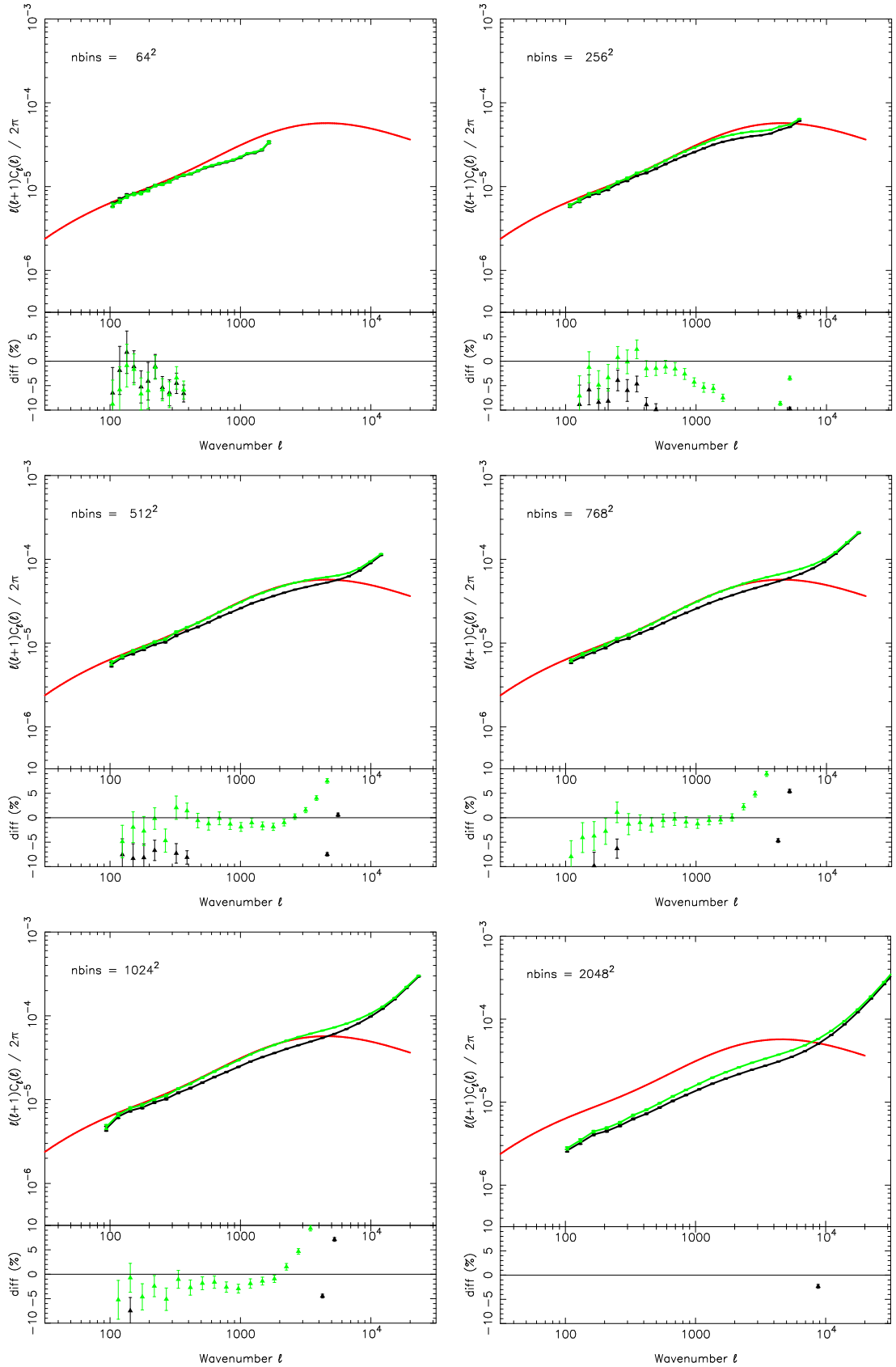
Figure 5.13: Effects of sampling and binning on shear and convergence in mock catalogues. The red line is the theoretical power spectrum, the black line is the convergence and the green line is the shear. The bottom panel shows the percentage difference between the theoretical expectation and the measured signals.

of modes possible without causing this amplitude to fall. In this case, 0.03% of the bins are empty. If this number is increased to 5% empty, the amplitude of the power spectrum drops by up to 10%. This effect will also be important for observational studies and should be considered when binning survey data to determine 2-D lensing power spectra.

Now, looking at both the shear and convergence power spectra, it is clear that they are no longer identical to each other (as in the source redshift plane calculations). The figure with the lowest number of bins does not demonstrate this well but in all subsequent figures, the difference is clear. The cause of this difference is due to the local and non-local forces responsible for generating convergence and shear. Convergence is a local force while shear is a non-local force. When down sampling the particles from the original distribution to create the mock catalogues, a number of particles were discarded. Since shear is a non-local force, the information in these lost particles is still retained in the remaining particles – they are still aware of the objects that are no longer in the catalogue. However, since convergence is local, when the particles were removed from the lightcone, their information was lost. The effect of this loss of information is to damp the convergence signal. This damping of the convergence is not a problem for studies using these mock catalogues because it is the shear signal that is required for the science studies (observers measure a shear signal and perform analyses using this information) and this is unaffected by the sampling in the lightcone.

5.3 Parameter Estimation

As described in Section 5.2.7, 100 simulations have been generated using the SUN-GLASS pipeline. The mock survey parameters are given in Table 5.2.

For each of these mock lensing surveys the shear and convergence power spectra has been estimated, and the ensemble average power and its scatter measured. Here the mock surveys are used to test a maximum likelihood cosmological parameter estimation analysis, typically used to extract parameters from weak lensing surveys. This analysis attempts to recover the amplitude of the matter clustering, σ_8, and density parameter, Ω_m, from a 2-D weak lensing survey.
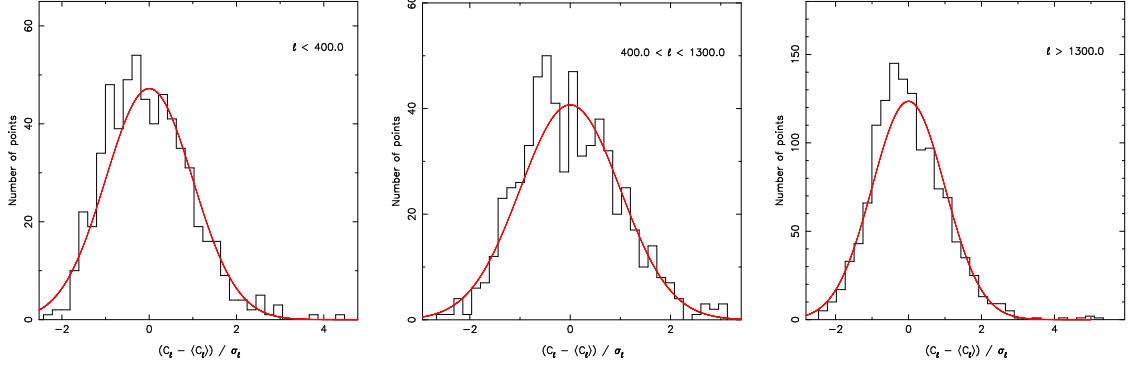
Figure 5.14: Histogram of the distribution of power spectra for the suite of lightcones with the $n(z)$ particle distribution. The left panel shows the distribution of the $C_\ell^{\gamma\gamma}$s less than $\ell = 400$, the middle panel shows the $C_\ell^{\gamma\gamma}$ distribution from $400 < \ell < 1300$ and the right panel shows the distribution from at $\ell > 1300$.

Section 5.2.7 showed that the simulations could produce unbiased estimates of the shear power from a mock survey, $\hat{C}_\ell^{\gamma\gamma}$, over a range of ℓ-modes from 200 to 2000. For parameter estimation we need to know the conditional probability distribution of shear power, $p(\hat{C}_\ell^{\gamma\gamma}|\sigma_8, \Omega_m)$, for the likelihood function, where all other parameters are fixed at their fiducial values. This is usually assumed to be Gaussian (although, see Hartlap et al., 2009, who study non-Gaussian likelihoods). Here, this assumption is tested on the mock catalogues. Figure 5.14 shows the distribution of variations about the mean of the $\hat{C}_\ell$, $\Delta\hat{C}_\ell^{\gamma\gamma}$, divided by the ensemble-averaged scatter in the power, $\sigma(\hat{C}_\ell^{\gamma\gamma})$. If the distribution is Gaussian, these distributions should all lie on the unit-variance Gaussian. The left panel shows a histogram of the distribution of points for modes of $\ell < 400$ which is close to the linear region of the power spectrum. The middle panel shows the distribution of $\hat{C}_\ell^{\gamma\gamma}$ for modes of $400 < \ell < 1300$ which represents the non-linear region of the power spectrum. The final panel shows the distribution for modes $\ell > 1300$ which is the shot-noise dominated regime. The smooth (red) line in each of the panels is a normalised unit-Gaussian curve. In each of the panels, the histogram of points is peaked slightly to the left of the Gaussian peak which indicates a slight non-Gaussianity of the distribution of points. This slight non-Gaussianity may bias the Gaussian likelihood analysis but the dominant effect is currently the inaccurate fitting of the matter power spectrum by the Smith et al. (2003) formula at high k (Giocoli et al., 2010).

The cosmological parameters of the simulations were estimated using a Gaussian

likelihood analysis where the likelihood is given by

$$L(\hat{C}_\ell^{\gamma\gamma}|\sigma_8, \Omega_m) = \frac{1}{(2\pi)^{N/2}(\det M_{\ell\ell'})^{1/2}} \exp\left[\frac{-\chi^2}{2}\right], \qquad (5.28)$$

where

$$\chi^2 = \sum_{\ell\ell'} (\hat{C}_\ell^{\gamma\gamma} - \langle C_\ell^{\gamma\gamma}\rangle) M_{\ell\ell'}^{-1} (\hat{C}_{\ell'}^{\gamma\gamma} - \langle C_{\ell'}^{\gamma\gamma}\rangle), \qquad (5.29)$$

where ℓ and ℓ' are ℓ-bins centred on ℓ and $M_{\ell\ell'}$ is the covariance matrix of the shear power spectra given by

$$M_{\ell\ell'} = \langle \Delta C_\ell^{\gamma\gamma} \Delta C_{\ell'}^{\gamma\gamma}\rangle. \qquad (5.30)$$

The inverse covariance matrix was determined by performing a singular value decomposition (SVD) on the covariance matrix (Press et al., 1992). SVD is a factorisation of a rectangular real or complex matrix. The formalism states that

$$A = USV^T, \qquad (5.31)$$

where A is a rectangular $n \times m$ matrix, U is an $m \times m$ unitary matrix, S is an $n \times m$ diagonal matrix with non-negative real numbers on the diagonal and V^T is the conjugate transpose of an $n \times n$ unitary matrix V. If A is both square and symmetric, then $U = V$. So, the inverse of Equation (5.31) is

$$A^{-1} = U^T S^{-1} U. \qquad (5.32)$$

Consequently, finding the inverse of the covariance matrix $A = C_{\ell\ell'}$ becomes computationally straight forward. The resulting inverse covariance matrix is, however, biased due to noise in the covariance matrix. Hartlap et al. (2007) propose a correction for this bias by multiplying the inverse covariance matrix by a factor:

$$\hat{M}_{\ell\ell'}^{-1} = \frac{N_S - N_p - 2}{N_S - 1} M_{\ell\ell'}^{-1}, \qquad (5.33)$$

where N_S is the number of simulations used to determine the covariance matrix, N_p is the number of bins in the power spectrum and $\hat{M}_{\ell\ell'}^{-1}$ is the unbiased covariance matrix.

The likelihood analysis relies on accurate estimation of the covariance matrix to show the degree of correlations. The correlation coefficients are

$$r_{\ell\ell'} = \frac{M_{\ell\ell'}}{\sqrt{M_{\ell\ell}M_{\ell'\ell'}}}. \tag{5.34}$$

The correlation coefficient matrix is equal to 1 along the diagonal and the off diagonal components will show how correlated the ℓ modes are, with numbers close to zero indicating low correlation and numbers close to (minus) one indicating high (anti-)correlation.

Figure 5.15 shows the correlation coefficient matrix for the ℓ modes being considered between $100 < \ell < 2500$. The modes with a low correlation are represented in black and dark blues and the modes with a high correlation shown in yellows and reds. This shows the the bandpowers at low ℓ have very little correlation between them, as we would expect, since for an all-sky survey the linear power is uncorrelated. At higher ℓ bandpower, the modes become more correlated, due to cross-talk between different scales due to nonlinear clustering in the matter power spectrum. The variations in this coefficient matrix indicate an error of around 10% which is suitable for the studies in this thesis. This error can be reduced by introducing more realisations into the calculations. In the analysis modes up to $\ell = 1500$ are considered, where the correlation coefficient is around $r_{\ell\ell'} \approx 0.6$.

Figure 5.16 shows the χ^2-distribution in the $\Omega_m - \sigma_8$ plane for the ensemble of simulations. These calculations assume that all other cosmological parameters are known. The black lines represent the two-parameter, 1, 2 and 3σ contours (which should contain 68.3%, 95.4% and 99.7% of the points assuming a bivariate Gaussian distribution), contours of parameter space for the cosmological parameters. However, this clearly is not a bivariate Gaussian distribution. The contours shown are representative and come from the simulation that had the best fit parameters that were closest to the true input parameters (the point shown by the red polygon). The blue triangles represent the best fit points for each of the 100 realisations. With this distribution, 68% of the points lie within the 1σ contour, 93% within the 2σ contour and 97% within the 3σ. The black diamond represents the best fit for the combined χ^2 estimate as discussed below.
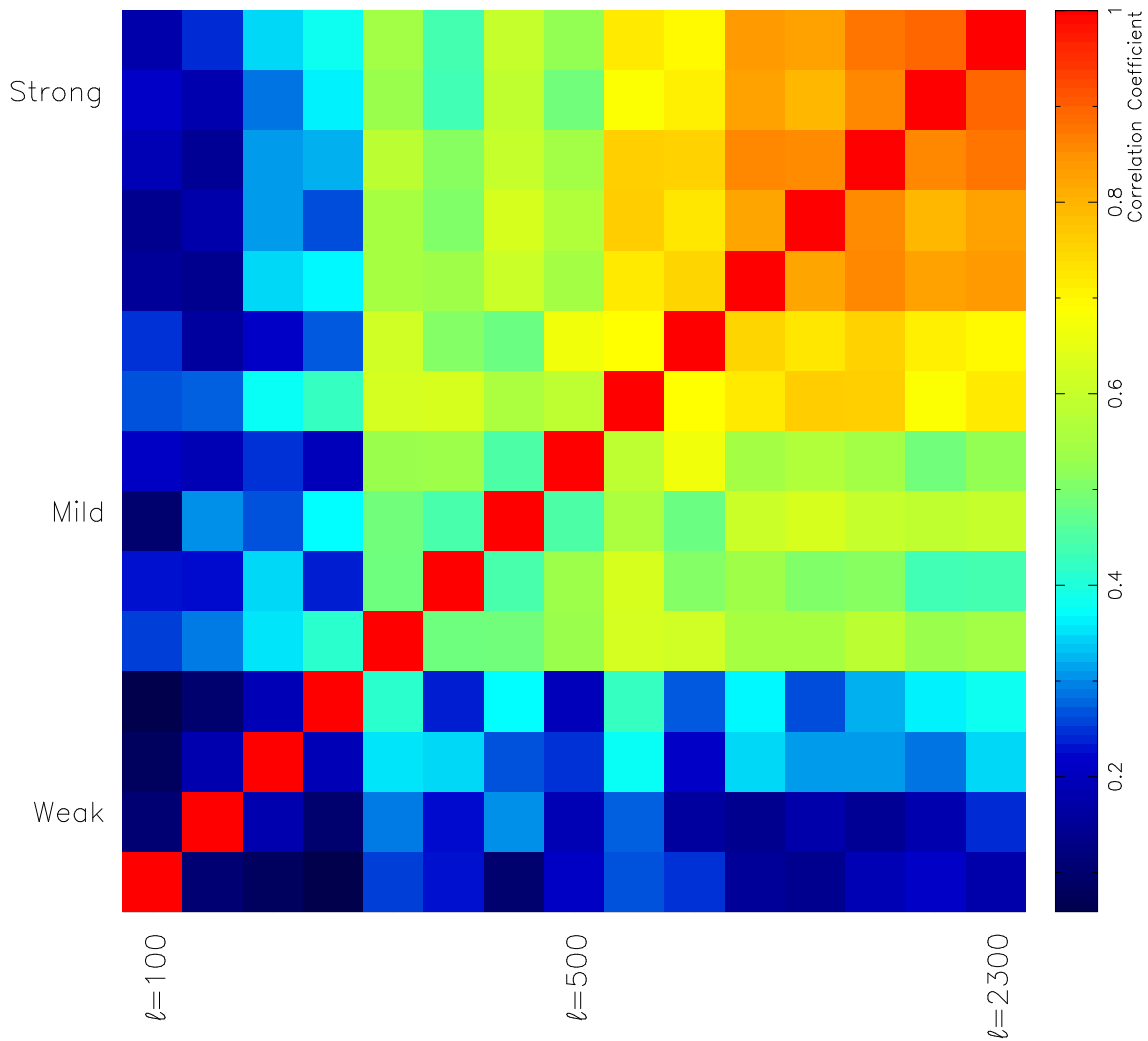
Figure 5.15: Correlation coefficient matrix. This figure shows the correlation between the logarithmically spaced bandpower ℓ-modes in the covariance matrix. The higher ℓ bandpowers are strongly correlated (shown in reds), while the lower bandpowers are only weakly correlated (shown in blues).
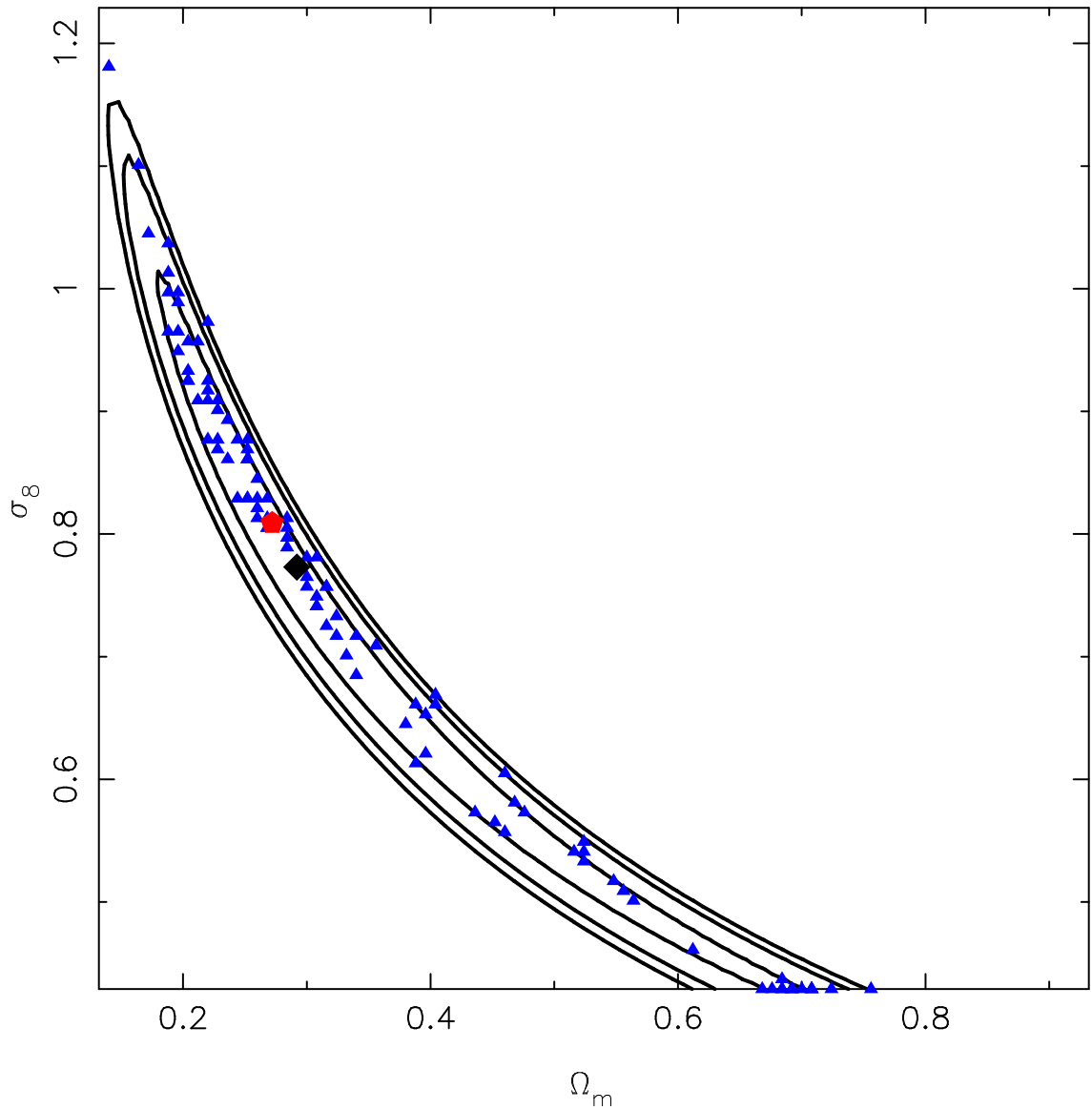
Figure 5.16: **Gaussian likelihood estimate. The black contours come from the simulation with the closest fit to the true cosmological parameters. The blue triangles show the best fit cosmological parameters for the suite of lightcones. The true cosmological parameters are shown at the red polygon and the combined χ^2 best fit parameter is shown at the black diamond.**

The results from this analysis give us very encouraging results for the parameter estimation. Figure 5.17 shows the results of combining the likelihoods for all 100 realisations, as if we have one hundred independent 100 square degree surveys or one 10,000 square degree survey. Even for this test the maximum likelihood recovered parameter values lies within the 1σ confidence contour. The marginalised error on the measured parameters for the combined 100 surveys is $\Delta\Omega_m = 0.012$ and $\Delta\sigma_8 = 0.022$. Any residual bias is below the uncertainty within the 1σ confidence limits. This implies that the inaccuracies in the simulations or theoretical predictions are smaller than the statistical fluctuations over all realisations.

5.4   Discussion and Conclusions

This chapter introduces SUNGLASS – Simulated UNiverses for Gravitational Lensing Analysis and Shear Surveys (Kiessling et al., 2011). SUNGLASS is a new, rapid pipeline that generates cosmological N-body simulations with GADGET2. It computes weak lensing effects along a lightcone using line-of-sight integrations with no radial binning and the Born approximation to determine the convergence and shear at multiple source redshifts. This information is interpolated back on to the particles in the lightcone to generate mock shear catalogues in 3-D for testing weak lensing observational analysis techniques.

In this chapter, SUNGLASS was used to generate 100 simulations with 512^3 particles, a box length of $512h^{-1}$ Mpc and a WMAP7 concordance cosmology. The corresponding mock shear catalogues were 100 sq. degrees with a source redshift distribution with median $z_m = 0.82$ and 15 galaxies per square arcminute. The parameters are easily changed within the SUNGLASS pipeline so that the mock shear catalogues matches the survey of interest. Note that shape noise has not been included in the mock shear catalogues in this chapter, ie this is for a perfect survey.

To show the reliability of the lightcones generated with SUNGLASS, E- and B-mode power spectra were shown at multiple source redshifts. The results show that at low redshifts, the signal becomes dominated by shot-noise at reasonably low ℓ. With increasing source redshift, the power spectrum recovers the theoretical prediction
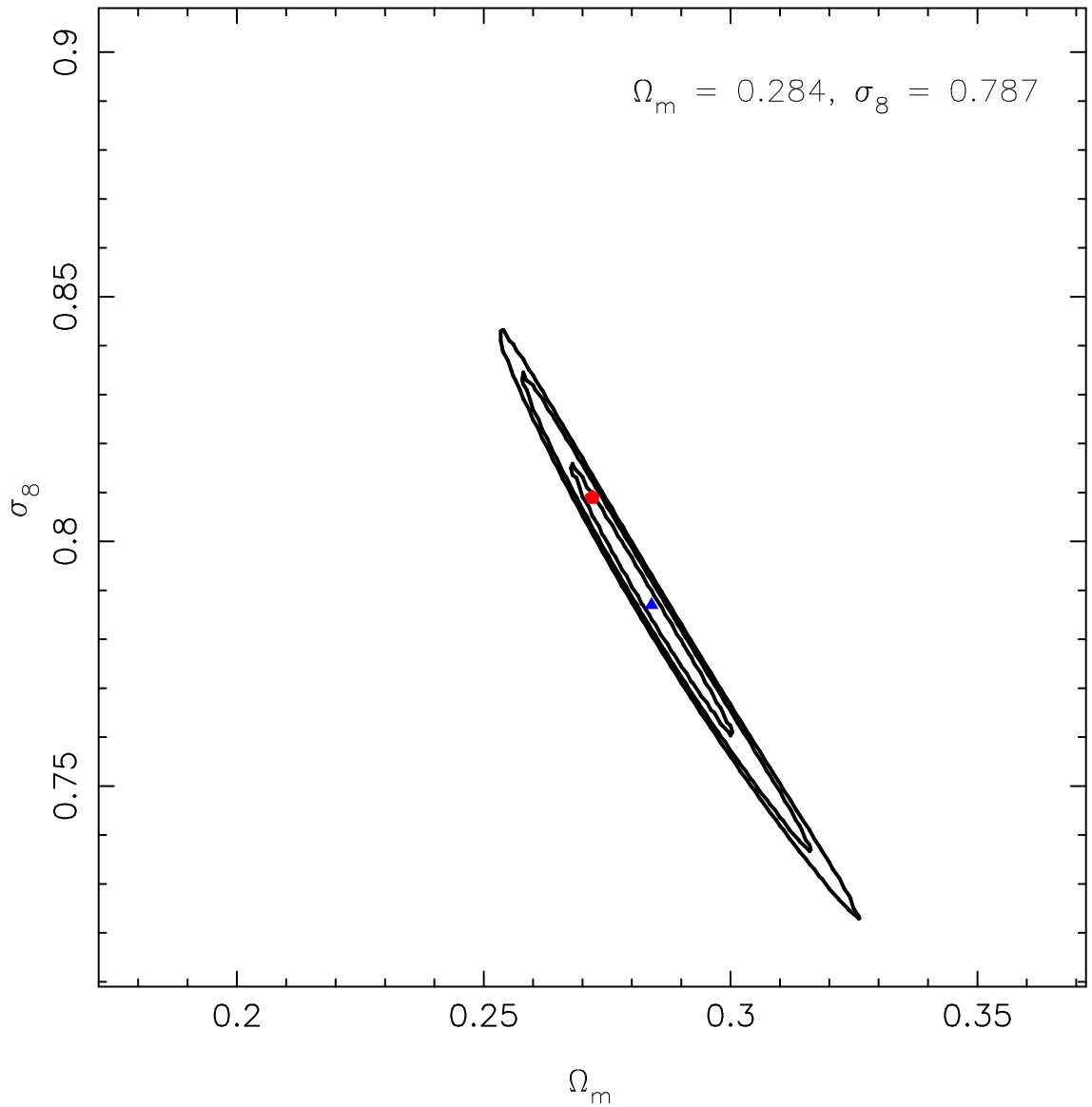
Figure 5.17: Combined χ^2 likelihood. The black lines show the combined χ^2 1, 2 and 3σ contours. The blue triangle shows the best fit parameters for the combined χ^2 and the red star shows the true cosmological parameters.

over a wider range of modes, $\ell < 2500$.

The multiple source redshift plane shear and convergence were interpolated onto the particles in the lightcone to generate a mock shear catalogue. A redshift sampling was also imposed on the lightcone to mimic an observed shear catalogue. Binning this distribution too finely resulted in empty bins which had the effect of suppressing the power spectrum. This has implications for observations where the number of objects per square arcminute should be taken into account, as well as the density of the binning, when determining the accuracy of the power spectrum.

The mock shear catalogues were used to determine a covariance matrix which is essential for both parameter estimation and data analysis. A strength of SUNGLASS is the ability to rapidly produce Monte Carlo realisations of these catalogues, ensuring independent mock data sets for the generation of the covariance matrices.

The mock catalogues were also used to perform a simple parameter estimation using Gaussian likelihood analysis. The distribution of power spectra were shown to be reasonably Gaussian and the resulting parameter estimation contours for a single realisation showed a good agreement with the input parameters within the two-parameter 1, 2 and 3σ error contours.

The combined likelihood from the 100 simulations shows narrow likelihood contours and accurate parameter recovery within the expected errors and any residual bias is below the uncertainty within the 1σ confidence limits.

As already discussed in Chapter 4, current and future telescope surveys promise to provide an enormous amount of data for weak lensing analysis. Weak lensing is still a young field and analysis techniques are still being developed. It is essential that the strengths and weaknesses of these techniques are fully understood before using them on real data with unknown parameters. Using the simulations, lightcones and mock shear catalogues provided by the SUNGLASS pipeline, and demonstrated in this chapter, is an excellent way to test these observational weak lensing analysis techniques. The outputs of this pipeline have been rigorously tested and are well understood, making them ideal for generating covariance matrices that are critical to many observational analysis techniques.

Chapter 6

Fisher Matrix Analysis

6.1 Introduction

Quantities such as the size and depth of a survey (amongst other things) have a significant effect on the ability of a survey to constrain cosmological parameters. Consequently, significant effort must be spent in accurately predicting what these telescopes will see, well before construction begins. This will allow us to both influence the design phase and to understand the capabilities of the instrument once the design has been set. In order to make predictions for these upcoming missions, statistical tools must be used to estimate the accuracy they will be able to achieve. The current standard for prediction uses the Fisher matrix methodology (Fisher, 1935; Tegmark et al., 1997). Traditionally, Fisher matrices have been generated with data covariance matrices that assume an underlying Gaussian matter and radiation distribution (Tegmark et al., 1997; Knox, 1997), which is accurate for CMB estimates when the Universe was still linear. However, this is not an accurate representation of the low-redshift Universe at smaller scales. Error bars generated using these Gaussian assumptions may be biased when compared with those generated using methods that account for the non-Gaussian, non-linear nature of the Universe.

Sources of non-Gaussian errors in the 3-D matter density covariance arise from non-linear mode-coupling (Meiksin & White, 1999; Rimes & Hamilton, 2005; Takahashi et al., 2011) and finite survey areas (the beat-coupling effect, Rimes & Hamilton, 2006; Neyrinck et al., 2006; Takahashi et al., 2009). These errors result in difficulties constraining cosmological parameters in the non-linear regime of the power

spectrum. The weak lensing shear power spectrum is dependent on the matter density power spectrum. Thus, the non-Gaussian errors and challenges constraining cosmological parameters propagate through the weak lensing analysis (Lee & Pen, 2008; Takada & Jain, 2009; Sato et al., 2009).

In this chapter the 1σ, two-parameter $\Omega_m - \sigma_8$ error estimates from the full maximum likelihood analyses in Chapter 5 are compared with a Gaussian Fisher analysis. Using weak gravitational lensing power spectrum analyses of mock galaxy shear catalogues generated with the SUNGLASS pipeline (see Chapter 5), the importance of using accurate non-linear covariance matrices when estimating errors for future experiments is shown. Analytic approximations of the correlation function covariance matrix under these assumptions have been shown to underestimate the errors on sample variance by a factor of up to ~ 30, which makes breaking the $\Omega_m - \sigma_8$ degeneracy more difficult (Semboloni et al., 2007). Simulations are able to provide accurate covariance matrices because they do not make assumptions about the underlying Gaussianity of the Universe and consequently include non-linear mode-coupling so the resulting covariance matrices include the off-diagonal components.

Fisher matrix analyses are attractive because of their relative speed and minimal computational requirements when compared with maximum likelihood estimates. However, this is offset by the loss of accuracy in the predictions due to Gaussian assumptions in the generation of the Fisher matrix. To compensate for some of these Gaussian assumptions, I propose using a non-Gaussian weak lensing shear covariance matrix generated from simulations to calculate the Fisher matrix. The resulting Fisher matrix still assumes a multi-variate Gaussian parameter estimate distribution and power spectrum distribution. However, it now contains the non-linear information found in the off-diagonal components of the covariance matrix from the simulations, giving a 'non-linear' Fisher matrix. In this chapter, the effect of this simple modification to the calculation of the Fisher matrix on the error estimates is shown and the error estimates are compared with the maximum likelihood and Gaussian Fisher error contours in the $\Omega_m - \sigma_8$ plane. Three- (Ω_m, σ_8, n_s), four- (Ω_m, σ_8, n_s, Ω_Λ) and six-parameter (Ω_m, σ_8, n_s, h, w_0, w_a) analyses are also performed and the Gaussian and non-linear Fisher matrix error estimates are compared.

It is possible to produce data vectors for covariance matrices by performing a simple

N	Area (sq deg)	z_{max}	n_g/sq arcmin	z_{med}
100	100	1.5	15	0.82

Table 6.1: Table of parameters for the mock galaxy shear catalogues used in this chapter. N is the number of independent lightcones, z_{max} is the maximum redshift in the lightcone, n_g/sq. arcmin is the number of 'galaxies' per square arcmin in the catalogue and z_{med} is the median redshift of the catalogue. The suite of lightcones is used together to form a survey with an effective area of 10,000 sq. deg.

2-D binning of the galaxies in the survey. However, further information may be gained by splitting the distribution up in to redshift bins and performing a tomographic analysis (e.g. Hu, 1999, 2002; Jain & Taylor, 2003). In this work, both 2-D and 3-bin tomographic analyses are performed in order to generate covariance matrices that are used to calculate the maximum likelihood estimates and the Gaussian and non-linear Fisher matrices.

The outline of this chapter is as follows; Section 6.2 will detail how the simulations and mock galaxy catalogues were generated. Section 6.3 will introduce the Fisher matrix formalism and the maximum likelihood formalism. Section 6.4 shows the results of the analyses on the maximum likelihood estimates and the Gaussian and non-linear Fisher matrices from the 2-D analyses in Section 6.4.1. The 3-bin tomographic shear power spectrum analysis and covariance matrix generation is shown in Section 6.4.2 and the two-parameter Fisher and maximum likelihood error estimates are shown in Section 6.4.3. Section 6.4.4 compares the tomographic multi-parameter Gaussian and non-linear Fisher estimates. Finally, a summary of the findings will be presented in Section 6.5.

6.2 Details of the simulations

The suite of weak lensing simulations used in this work was generated using the SUNGLASS pipeline (for a detailed introduction, see Chapter 5). The work in this chapter uses 100 independent simulations generated with the cosmological N-body simulations code GADGET2 (Springel, 2005). The simulations were made with a flat concordance ΛCDM cosmology, consistent with the WMAP 7-year results (Jarosik et al., 2011): $\Omega_m = 0.272$, $\Omega_\Lambda = 0.728$, $\Omega_b = 0.045$, $\sigma_8 = 0.809$, $n_s = 0.963$ and

$h = 0.71$ in units of 100 km s^{-1} Mpc^{-1}. There are 512^3 particles in a box of $512h^{-1}$ Mpc which leads to a particle mass of $7.5 \times 10^{10} M_\odot$. The simulations were all started from a redshift of $z = 60$ and allowed to evolve to the present with 26 snapshots being stored in redshifts $0.0 \leq z \leq 1.5$.

Lightcones were generated through the simulation snapshots to determine the average convergence in an angular pixel using the 'no radial binning' method introduced in Chapter 5. The convergences were calculated using 2048^2 azimuthal bins, before downsampling, on source redshift planes that were separated by $z = 0.1$ to create 15 planes from $0.0 < z < 1.5$. The mock shear catalogues were generated in the same manner as explained in Section 5.2.7. It is assumed that galaxies trace the dark matter distribution perfectly and the final mock galaxy shear catalogues contain 15 galaxies per square arcminute. There is no ellipticity noise in the catalogues, however there is a shot-noise contribution related to the discrete sampling of the particles in the mock catalogues. Table 6.1 summarises the mock galaxy catalogues used in this work.

6.3   Methodology

In this section, the formalisms introduced in earlier chapters are generalised for tomographic analyses. The shear, γ, convergence, κ, and B-mode, β, fields are related to each other in Fourier-space on a flat-sky by

$$\kappa(\boldsymbol{\ell}) + i\beta(\boldsymbol{\ell}) = e^{2i\varphi_\ell}[\gamma_1(\boldsymbol{\ell}) + i\gamma_2(\boldsymbol{\ell})], \tag{6.1}$$

where φ_ℓ is the angle between the angular wave-vector, $\boldsymbol{\ell}$, and an axis on the sky. For each of the mock galaxy shear catalogues the shear, convergence, and B-mode auto- and cross-power spectra have been estimated. The tomographic weak lensing shear, convergence and B-mode power cross-spectra, for two different source redshifts z and z', are given by

$$
\begin{aligned}
C_\ell^{\gamma\gamma}(z,z') &= \langle \gamma_1(\boldsymbol{\ell},z)\gamma_1(\boldsymbol{\ell},z')\rangle + \langle \gamma_2(\boldsymbol{\ell},z)\gamma_2(\boldsymbol{\ell},z')\rangle, &(6.2)\\
C_\ell^{\kappa\kappa}(z,z') &= \langle \kappa(\boldsymbol{\ell},z)\kappa(\boldsymbol{\ell},z')\rangle, &(6.3)\\
C_\ell^{\beta\beta}(z,z') &= \langle \beta(\boldsymbol{\ell},z)\beta(\boldsymbol{\ell},z')\rangle. &(6.4)
\end{aligned}
$$

The power spectra are related to each other by $C_\ell^{\gamma\gamma}(z, z') = C_\ell^{\kappa\kappa}(z, z') + C_\ell^{\beta\beta}(z, z')$. The auto-spectra are calculated when $z' = z$. In practice the sources are binned into redshift slices. For a survey that has N_z slices the expectation value of the tomographic shear cross-power spectra in redshift bins labeled i and j, is given by

$$C_{ij}^{\gamma\gamma}(\ell) = \frac{9H_0^4 \Omega_m^2}{4c^4} \int_0^{r_{\max}} \frac{dr}{a^2(r)} \, P\left(\frac{\ell}{r}, r\right) g_i(r)g_j(r), \qquad (6.5)$$

(Kaiser, 1992; Joachimi & Schneider, 2009), where r is the comoving distance, $r_{\max}$ is the maximum comoving distance and $P(\ell/r, r)$ is the 3D matter density power spectrum. The lensing efficiency function is

$$g_i(r) = \int_r^{r_{\max}} dr' \, p_i(r') \left(1 - \frac{r}{r'}\right), \qquad (6.6)$$

where p_i is the normalised probability distribution of 'galaxies' in the bin.

When determining the angle averaged shear power spectrum in the simulations, the conventions used in the Fourier transform software FFTW must be taken into consideration. Thus, the discretised tomographic shear power spectrum becomes

$$\frac{\ell(\ell + 1)\widehat{C}_{ij}^{\gamma\gamma}(\ell)}{2\pi} = \sum_{\ell \, in \, shell} \frac{\gamma_1(\boldsymbol{\ell}, z_i)\gamma_1(\boldsymbol{\ell}, z_j) + \gamma_2(\boldsymbol{\ell}, z_i)\gamma_2(\boldsymbol{\ell}, z_j)}{n_b^2 \Delta \ln \ell}, \qquad (6.7)$$

where $\widehat{C}_\ell^{\gamma\gamma}$ is the estimated power, n_b is the total number of bins in the Fourier transform, z_i is the ith redshift slice, and $\Delta \ln \ell$ is the thickness of a shell in log ℓ-space. The modes in this power spectrum are corrected for mode discreteness errors by scaling by the expected number of modes. To compactify the notation, the tomographic shear power is denoted by $C_X^{\gamma\gamma}(\ell)$, where $X = (i, j)$ is a pair of redshift slices. For the 2-D analysis there is only one bin so $i = j$. Using the information from these power spectra, cosmological parameter estimates are possible.

6.3.1 Shear power covariance matrix generation

The shear cross-spectra covariance matrix, $M_{\ell\ell'}^{XX'}$ is defined by

$$M_{\ell\ell'}^{XX'} = \langle \Delta C_X^{\gamma\gamma}(\ell) \Delta C_{X'}^{\gamma\gamma}(\ell') \rangle, \qquad (6.8)$$

where $\Delta C_X^{\gamma\gamma}(\ell) = C_X^{\gamma\gamma}(\ell) - \langle C_X^{\gamma\gamma}(\ell) \rangle$ and angled-brackets denotes ensemble averaging. The covariance matrix is an important element of parameter estimation, containing information on the strength of the correlations between variates, in this case the shear power spectrum modes. The accuracy of this matrix improves by increasing the number of realisations included in the calculation of the matrix. For this work, 100 independent realisations of 2-D power spectra provides an accuracy of $\Delta C_\ell \sim 10\%$ (as shown in Figure 5.15).

Gaussian covariance matrix

If the shear field is isotropic and we assume the shear field is Gaussian, an equation for the tomographic shear power covariance matrix can be written using Wick's theorem (e.g. Matarrese et al., 1997), with a correction for the fraction of the sky covered by the survey:

$$
\begin{aligned}
M_{\ell\ell'}^{ij,kl} &= \frac{\delta_{\ell\ell'}^K}{(2\ell+1)f_{\text{sky}}} \Big([C_{ik}^{\gamma\gamma}(\ell) + N_i(\ell)\delta_{ik}^K][C_{jl}^{\gamma\gamma}(\ell) + N_j(\ell)\delta_{jl}^K] \\
&\quad + [C_{il}^{\gamma\gamma}(\ell) + N_i(\ell)\delta_{il}^K][C_{jk}^{\gamma\gamma}(\ell) + N_j(\ell)\delta_{jk}^K] \Big),
\end{aligned}
\tag{6.9}
$$

where f_{sky} is the fraction of the sky covered by the survey and $N_i(\ell)$ is a shot-noise term due to intrinsic ellipticity in the shear field. For the purposes of this work, although there is a discrete galaxy density, the intrinsic shear variance is set to zero so that $N_i(\ell) = 0$. However, in principle these results can be combined with a Gaussian noise covariance to model different weak lensing surveys.

Simulation covariance matrix estimation

The covariance matrix of the tomographic shear power spectrum for the suite of mock galaxy shear catalogues is estimated by

$$
M_{\ell\ell'}^{XX'} = \frac{1}{N-1} \sum_N \Delta C_X^{\gamma\gamma}(\ell) \Delta C_{X'}^{\gamma\gamma}(\ell'),
\tag{6.10}
$$

where N is the number of mock catalogue realisations and here $\Delta C_X^{\gamma\gamma}(\ell) = \widehat{C}_X^{\gamma\gamma}(\ell) - \langle \widehat{C}_X^{\gamma\gamma}(\ell) \rangle$ where $\langle \widehat{C}_X^{\gamma\gamma}(\ell) \rangle$ is the ensemble average of the tomographic shear power spectrum across all realisations.

The inverse covariance matrix is calculated using singular value decomposition on the covariance matrix (Press et al., 1992). However, the resulting inverse is biased due to noise. To correct for this, we multiply the inverse by a factor (Hartlap et al., 2007):

$$[\widehat{M}_{\ell\ell'}^{XX'}]^{-1} = \frac{N_S - N_p - 2}{N_S - 1}[M_{\ell\ell'}^{XX'}]^{-1},$$ (6.11)

where N_S is the number of realisations, N_p is the total number of bins in all of the power spectra and $[\widehat{M}_{\ell\ell'}^{XX'}]^{-1}$ is an unbiased estimation of the inverse covariance matrix.

6.3.2 Fisher matrix generation

Assuming the power spectra and parameter space are multi-variate Gaussians, the Fisher matrix for $\ell\ell'$ bins and $C_X C_{X'}$ spectra is given by

$$F_{ij} = \frac{1}{2} \sum_{\ell\ell'} \sum_{XX'} \frac{\partial C_X^{\gamma\gamma}(\ell)}{\partial \theta_i} \left[\widehat{M}_{\ell\ell'}^{XX'}\right]^{-1} \frac{\partial C_{X'}^{\gamma\gamma}(\ell')}{\partial \theta_j},$$ (6.12)

(Tegmark et al., 1997) where i and j label cosmological parameters (e.g. Ω_m and σ_8) and the partial derivatives are the gradient of the expectation value of the shear power spectrum in parameter space (the Fisher matrix is defined in terms of the maximum likelihood in Section 6.3.3). In order to determine the gradients of the power spectra, a five-point function is used on the ensemble average power spectra (Equation 6.5). In this work, the five point function is given by

$$\frac{\partial C_X^{\gamma\gamma}(\ell)}{\partial \theta_i} = \frac{1}{\Delta\theta_i} \left(\frac{1}{12} C_{X(-2)}^{\gamma\gamma} - \frac{2}{3} C_{X(-1)}^{\gamma\gamma} + \frac{2}{3} C_{X(1)}^{\gamma\gamma} - \frac{1}{12} C_{X(2)}^{\gamma\gamma} \right),$$ (6.13)

(Abramowitz & Stegun, 1968) where $\Delta\theta_i$ is an incremental change to the given parameter. The theoretical prediction for the power spectrum was generated using a code provided by Benjamin Joachimi and tested in Chapter 5.

The Fisher matrix provides error ellipses in parameter space. In high-dimensions, it is difficult to visualise these hyper-ellipses so two methods are employed to describe them. The first method describes single-parameter marginal errors, which are given by

$$\Delta\theta_i = \left[F^{-1}\right]_{ii}^{1/2}.$$ (6.14)

The second method determines the area of the Fisher matrix error ellipse that encloses a two-parameter 68% confidence limit in the two parameter plane. The inverse of this area is proportional to the Figure-of-Merit that is often quoted in studies (e.g. Albrecht et al., 2006; Wang, 2008; Albrecht et al., 2009; Slosar, 2010).

6.3.3   Maximum likelihood parameter estimation

To perform a maximum likelihood analysis on the suite of mock shear catalogues, a Gaussian likelihood estimator is used. Despite the fact that the simulations are non-Gaussian, using a Gaussian likelihood has been shown to produce accurate results (see Section 5.3). The likelihood is given by

$$L(\hat{C}_\ell^{\gamma\gamma}|\sigma_8, \Omega_m) = \frac{1}{(2\pi)^{N/2}(\det \widehat{M}_{\ell\ell'}^{XX'})^{1/2}} \exp\left[-\frac{\chi^2}{2}\right], \tag{6.15}$$

where N is the number of independent mock catalogue realisations, and

$$\chi^2 = \sum_{\ell\ell'}\sum_{XX'} \Delta C_X^{\gamma\gamma}(\ell) \left[\widehat{M}_{\ell\ell'}^{XX'}\right]^{-1} \Delta C_{X'}^{\gamma\gamma}(\ell'), \tag{6.16}$$

where $\Delta C_X^{\gamma\gamma}(\ell) = \widehat{C}_X^{\gamma\gamma}(\ell) - \langle C_X^{\gamma\gamma}(\ell)\rangle$, and $\langle C_X^{\gamma\gamma}(\ell)\rangle$ is the expected angular power spectrum given by Equation (6.5). While this likelihood analysis is computationally expensive, it takes into account the full non-Gaussian and non-linear nature of the simulations and should provide the most accurate error estimates. Expanding the log-likelihood using a Taylor expansion gives

$$\ln L \simeq \ln L_0 + \Delta\theta_i \left\langle\frac{\partial \ln L}{\partial\theta_i}\right\rangle + \frac{1}{2}\Delta\theta_i\Delta\theta_j \left\langle\frac{\partial^2 \ln L}{\partial\theta_i\partial\theta_j}\right\rangle. \tag{6.17}$$

When the likelihood is maximised, the gradient of the likelihood is zero, so the second term in this equation is zero. The Fisher matrix is defined as the curvature of the log-likelihood surface around the maximum and is given by

$$F_{ij} = \left\langle-\frac{\partial^2 \ln L}{\partial\theta_i\partial\theta_j}\right\rangle. \tag{6.18}$$

6.4 Results

6.4.1 2-D two-parameter analysis

The first step to making parameter estimates from the mock galaxy shear catalogues is to determine the 2-D shear angular power spectra for each realisation. Figure 5.11 in the previous chapter shows the mean power spectra from the suite with the (red) long line showing the theoretical prediction, the (black) line showing the mean measured power spectrum from the suite of catalogues with errors on the mean. The (magenta) triangles show the measured B-modes and the dashed (dark blue) line shows the shot-noise arising from discrete particle sampling in the mock catalogues. The bottom panel shows the percentage difference of the data from the expected power spectrum. The simulations recover the expected power spectrum within 5% between $150 < \ell < 2000$.

A data-vector was constructed from the shear band-power spectra with wavenumbers from $150 < \ell < 1500$. From this, the covariance matrix was determined using Equation (6.10). Similarly, a Gaussian covariance matrix was generated using Equation (6.9).

To test the effect of the non-Gaussian nature of the simulations covariance matrix, the diagonal components of both the simulation and Gaussian field covariance matrices were taken and their ΔC_ℓ values were calculated. For the case of the simulations this is simply the square root of the diagonal components. For a Gaussian field this is

$$\Delta C_\ell = \frac{\sqrt{2}C_\ell}{\sqrt{\ell(2\ell+1)f_{\mathrm{sky}}\Delta \ln \ell}},$$ (6.19)

(Kaiser, 1995; Tegmark et al., 1997) where $\Delta C_\ell = \sqrt{2}C_\ell$ for each mode in a Gaussian field while f_{sky} accounts for the fraction of the sky coverage, $2\ell+1$ accounts for averaging over the azimuthal modes and $\ell\Delta \ln \ell$ accounts for averaging over ℓ bins.

Figure 6.1 shows the diagonals of the covariance matrices as a function of wavenumber ℓ. The (red) dashed line is from the Gaussian error and the (black) line is from the simulations. At low wavenumbers, which are still in the reasonably linear regime, the two errors agree reasonably well. However, in the higher wavenumber,
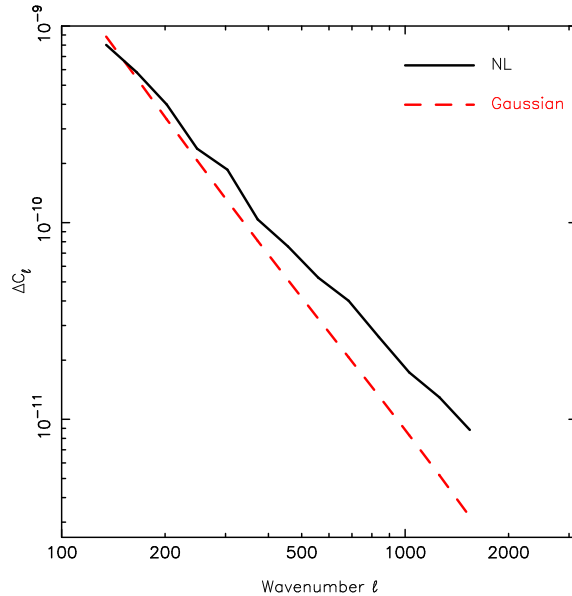
Figure 6.1: Diagonal components of the covariance matrix for the simulations (black line) and a Gaussian field with the same power spectrum (red dashed line).

non-linear regime, there is a factor of three difference between the errors, suggesting that the non-Gaussian contribution to the covariance is significant.

Fisher matrices in the $\Omega_m - \sigma_8$ plane were calculated using Equation (6.12) for both the Gaussian and simulation covariance matrices. The Fisher matrices were multiplied by 100, the total number of independent mock catalogues, to provide an error estimate for a survey of 10,000 square degrees. Additionally, the maximum likelihood was calculated using the simulation covariance matrix and the likelihoods from the 100 mock catalogues were combined (as shown in Section 5.3). For all of these calculations it is assumed that all other cosmological parameters are known.

In Figure 6.2 the two-parameter 1σ contours for the $\Omega_m - \sigma_8$ plane are shown. The inner (orange shaded) ellipse shows the Gaussian Fisher estimate, the outer (grey shaded) ellipse shows the non-linear Fisher estimate and the thick (black) line contour is the combined maximum likelihood estimate. The red point in the middle represents the fiducial Ω_m and σ_8 parameters. The size and shape of the simulation Fisher ellipse and the maximum likelihood contour are very similar, showing that the non-linear Fisher calculation is a good method for making future cosmological parameter estimates, provided the off-diagonal terms are included. The area of the

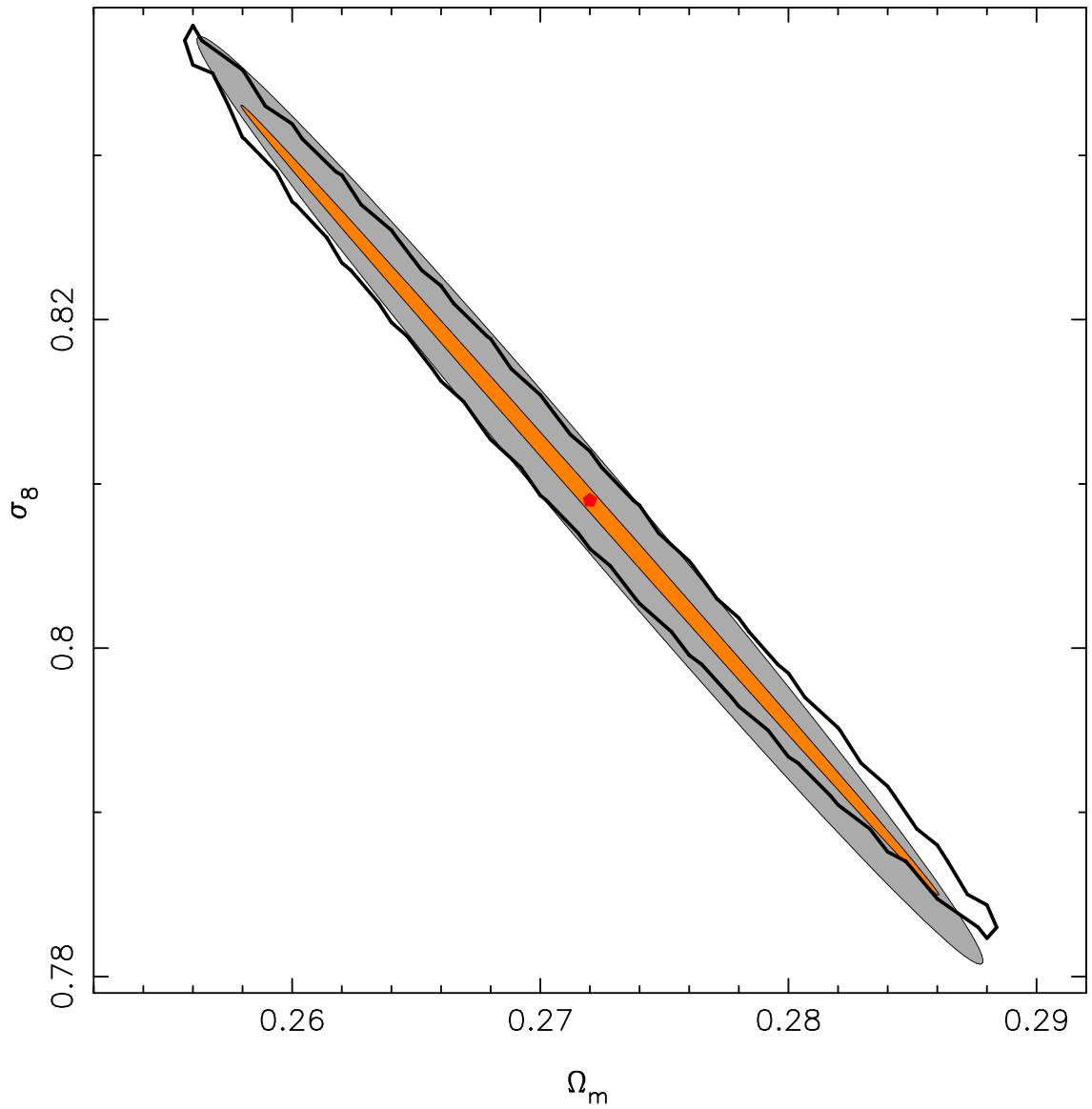Figure 6.2: Comparison of the 1σ two-parameter contours for the $\Omega_m - \sigma_8$ parameters for Gaussian Fisher contour (inner orange shaded ellipse), the non-linear Fisher contour (middle grey shaded ellipse) and the full maximum likelihood analysis (thick black line contour). The (red) point in the middle of the ellipses represents the fiducial $\Omega_m - \sigma_8$ parameters in this calculation.
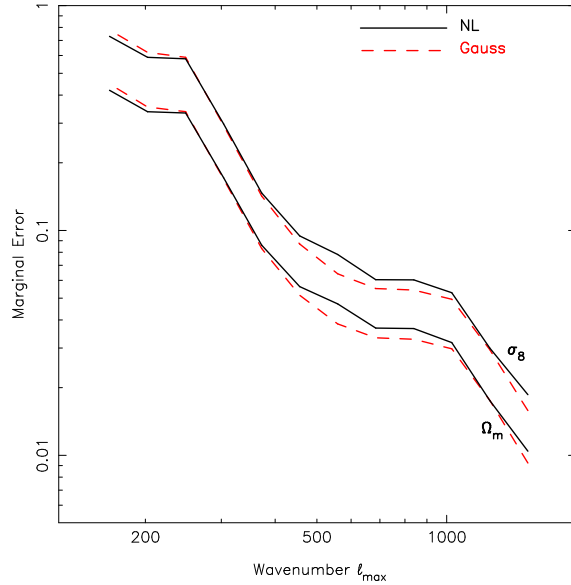
Figure 6.3: Marginal errors of Ω_m and σ_8 as a function of maximum wavenumber in the Fisher calculation. The dashed lines are the marginal errors on Ω_m as a function of maximum wavenumber ℓ_{max} and the continuous lines are for σ_8.

non-linear Fisher estimate is 5.1 times larger than the area of the Gaussian Fisher estimate which is a clear indication that the off-diagonal terms in the covariance matrix are essential for accurate estimation of the parameter errors.

In addition to the area of the contours, the marginal errors on the parameters from the Fisher matrices were also determined. The non-linear Ω_m marginal error is 1.23 times larger than the Gaussian marginal error and σ_8 is 1.17 times larger. From Figure 6.1, we would expect the marginal errors of the non-linear Fisher matrix to be much larger. However, the off-diagonal terms in the simulation covariance matrix act to reduce the marginal errors but increase the total area. This is demonstrated by setting the off-diagonal terms in the simulation covariance matrix to zero. In this case the non-linear Fisher ellipse becomes far narrower but the marginal errors increase significantly.

Figure 6.3 shows how the marginal errors change in the Fisher matrices as a function of maximum wavenumber ℓ_{max}. The marginal errors for both the non-linear and Gaussian Fisher matrices are remarkably similar across all values of ℓ_{max} with the largest gain of information occurring for both Ω_m and σ_8 between $250 < \ell_{max} < 500$ and again at $\ell_{max} > 1000$. This similarity is due to an effect that the off-diagonal

components of the simulation covariance matrix are having on the error ellipse, as discussed earlier. This figure shows that if the marginal error is the value of interest, the Gaussian Fisher matrix appears to provide a result that is comparable with the error obtained with the non-linear Fisher error estimate at wavenumbers between $150 < \ell_{\mathrm{max}} < 1500$. However, when the errors are marginalised over two parameters, the area of the contours shows that the errors are being underestimated by a factor of five.

6.4.2 Tomographic shear power

It is possible to perform the same analysis that was performed in Section 6.4.1 on tomographically-binned mock catalogues. Tomography introduces extra information into the analysis. In this analysis the suite of mock galaxy shear catalogues was split into three redshift bins; bin 1: $0.0 \le z \le 0.5$, bin 2: $0.5 < z \le 1.0$ and bin 3: $1.0 < z \le 1.5$.

Figure 6.4 shows the auto- and cross-power spectra for the 3-bin tomographic analysis of the mock galaxy shear catalogues. Focusing first on the auto-power spectra ($C_{11}^{\gamma\gamma}$, $C_{22}^{\gamma\gamma}$ and $C_{33}^{\gamma\gamma}$), the figure shows that the wavenumbers modelled accurately increase with redshift. For $C_{11}^{\gamma\gamma}$, agreement is found for wavenumbers from $150 < \ell < 700$. The power spectra from $C_{22}^{\gamma\gamma}$ and $C_{33}^{\gamma\gamma}$ are slightly higher than the expected power spectrum but still within 3% and are reliable up to $\ell = 1000$ before shot-noise becomes dominant.

The cross-bins $C_{12}^{\gamma\gamma}$, $C_{13}^{\gamma\gamma}$ and $C_{23}^{\gamma\gamma}$ are damped which is due to the shot noise dominance in the lower redshift bin. Consequently, only the results of these power spectra up to the ℓ range accurately recovered by the auto-power spectra of the lower redshift bin are used.

The power spectra in the auto- and cross-bins were turned into a data-vector with wavenumbers from $150 < \ell < 1800$ included. A data covariance matrix was generated and from this, a correlation coefficient matrix where the correlation coefficients
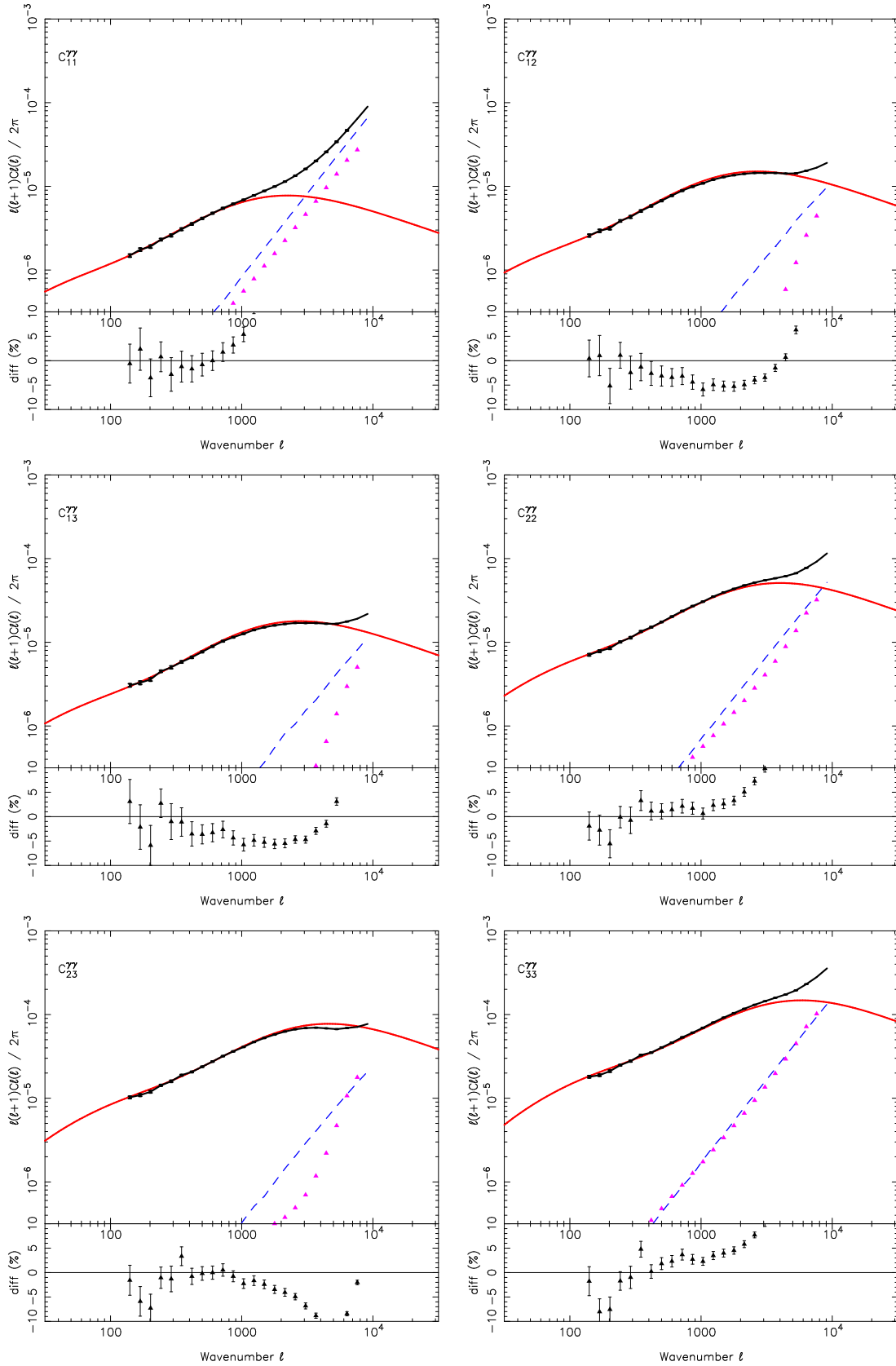
Figure 6.4: **2-D shear power spectra for a 3-bin tomographic analysis of the mock galaxy shear catalogues. The long (red) line is the theoretical prediction for the shear power spectrum, the (black) line is the mean power spectrum for the 100 mock catalogues with errors on the mean, the (dark blue) dashed line is the shot noise estimate and the (magenta) triangles are the measured B-modes.**

are given by

$$r_{\ell\ell'}^{XX'} = \frac{\widehat{M}_{\ell\ell'}^{XX'}}{\sqrt{\widehat{M}_{\ell\ell}^{XX}\widehat{M}_{\ell'\ell'}^{X'X'}}}. \tag{6.20}$$

This matrix shows how (anti-)correlated each of the ℓ modes and spectra are.

Figure 6.5 shows the correlation coefficient matrix for the tomographic data vector. The 'block' nature to the matrix indicates each tomographic bin pair. Each of the blocks along the diagonal represents the auto-correlation between each of the tomographic power spectrum analyses. The off-diagonal blocks show the cross-correlations between the tomographic pair power spectra. As expected, the higher wavenumbers in each block are highly correlated. Additionally, the $C_{11}^{\gamma\gamma}$ auto-power spectrum is highly correlated due to non-linear mode coupling. The $C_{22}^{\gamma\gamma}$ auto-power spectrum is significantly less correlated and the $C_{33}^{\gamma\gamma}$ auto-power spectrum bin has very low correlations between the ℓ modes. The implication of this is that the lower redshift tomographic bins should contribute fewer power spectrum bins to a covariance matrix being used for any kind of analysis.

An alternative visualisation of the correlation coefficient matrix is shown in Figure 6.6. In this figure, each of the blocks represents a wavenumber bin. This alternative visualisation shows how the wavenumbers are correlated in the tomographic power spectra.

With the information gained from these power spectra and the correlation coefficient matrix, a data-vector is assembled that contains the C_ℓ^X from wavenumbers that are accurately reproducing the expected power spectrum and have a reasonably low correlation. Thus, 30 bins are selected in total from the three auto-power spectra, with the highest wavenumber being around $\ell = 1000$ and just 10 bins in total from the cross-power spectra, with the highest wavenumber being around $\ell = 500$. A covariance matrix was generated using this data-vector. A full maximum likelihood analysis was performed with this covariance matrix and a non-linear Fisher matrix was also calculated. An equivalent Gaussian covariance matrix, using the same ℓ-range, was also generated and the Gaussian Fisher matrix determined.
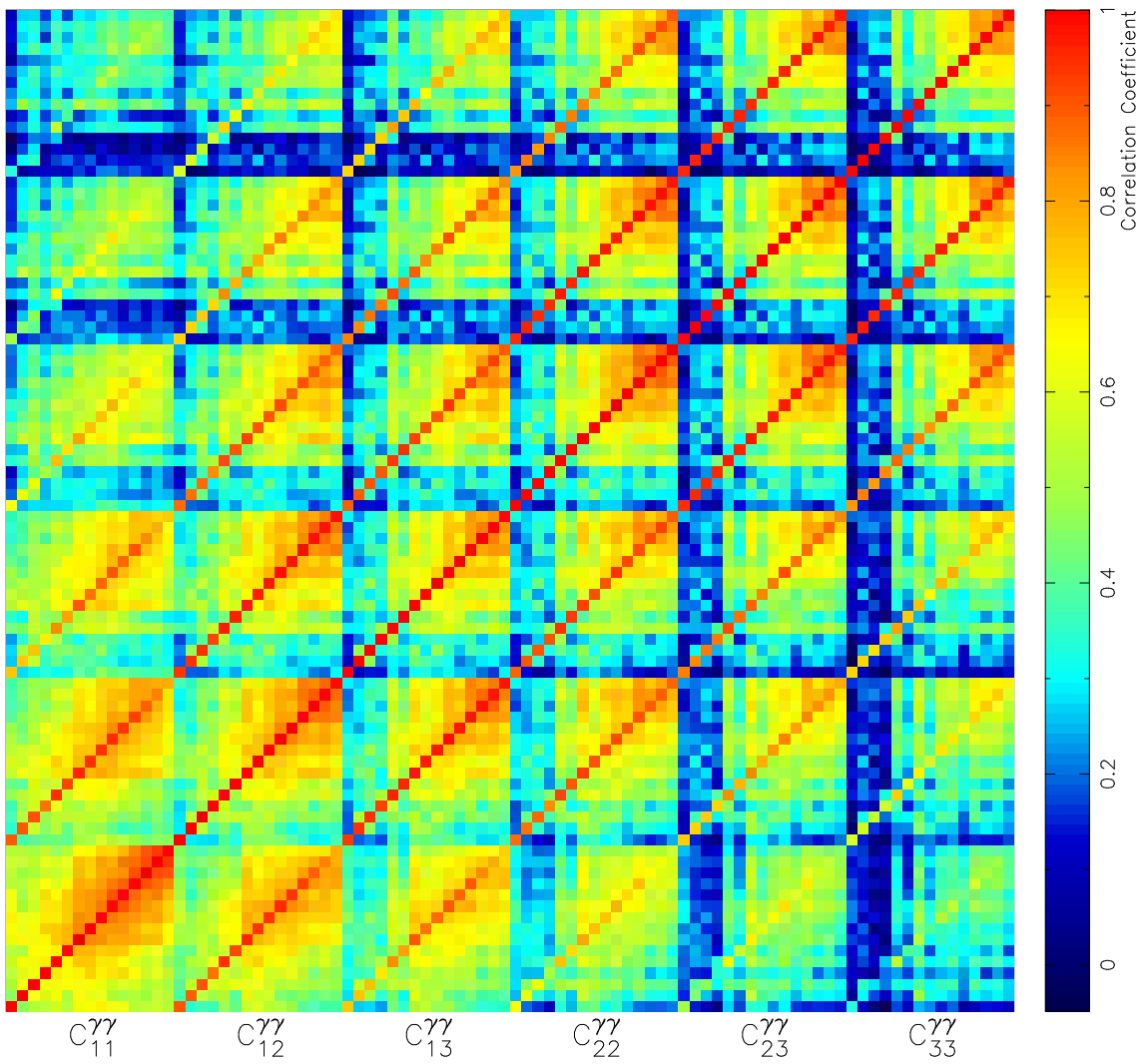
Figure 6.5: Correlation coefficient matrix for 3 tomographic bins. The matrix is arranged so that each sub-square is a tomographic bin pair.
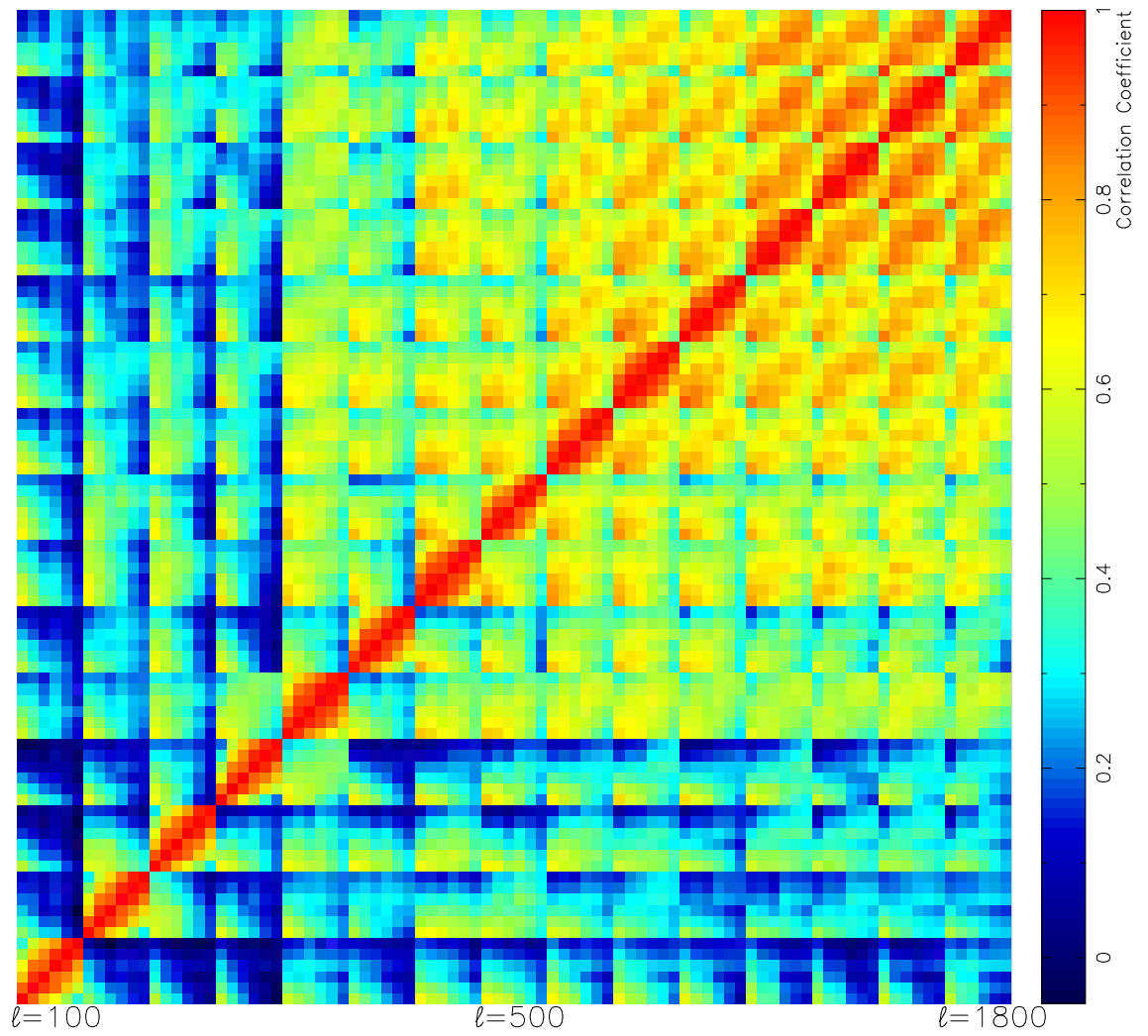
Figure 6.6: **Alternative visualisation for the correlation coefficient matrix for 3 tomographic bins. The matrix is arranged so that each sub-square is an ℓ bin.**
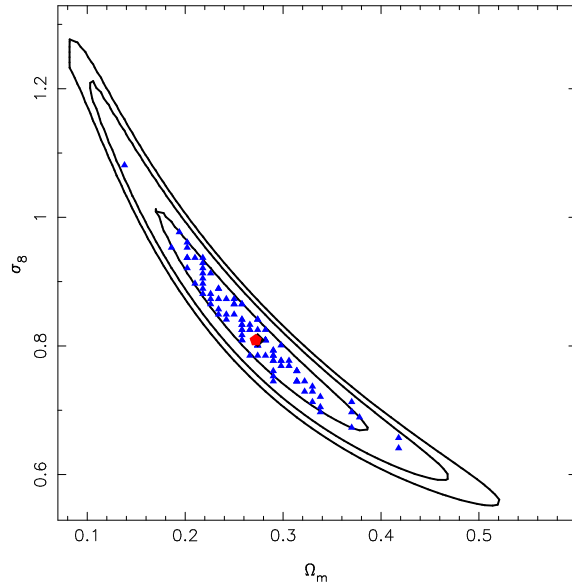
Figure 6.7: Typical χ^2 likelihood. The black lines show the χ^2 1, 2 and 3σ contours for the closest fit realisation to the true input parameters. The blue triangles show the best fit parameters for each realisation and the red star shows the true cosmological parameters.

6.4.3   Two-parameter tomographic analysis

Figure 6.7 shows the maximum likelihood estimate for a single mock catalogue with the 1, 2 and 3σ contours shown in black. The fiducial parameter is shown as the red polygon in the center of the figure. The best fit parameters for all of the 100 realisations are shown as blue triangles. There are 90% of the points falling within the 1σ contour and the full 100% of points within the 2σ contour, which does not follow with Gaussian statistics. The reason for this could lie in the fact that the contours are determined from a single best-fit realisation and do not necessarily represent the true average contours for the suite of mock catalogues, or that the distribution of the data is not Gaussian. However, this typical contour was chosen to be representative as averaging the contours for the 100 realisations is not straightforward.

The combined likelihood estimate for the suite is shown in Figure 6.8. The 1, 2 and 3σ contours are the black ellipses and the best-fit point is the blue triangle. The fiducial input parameters are represented by the red polygon. The best-fit point lies within the 1σ contour showing that any residual bias is within the uncertainty for this calculation.
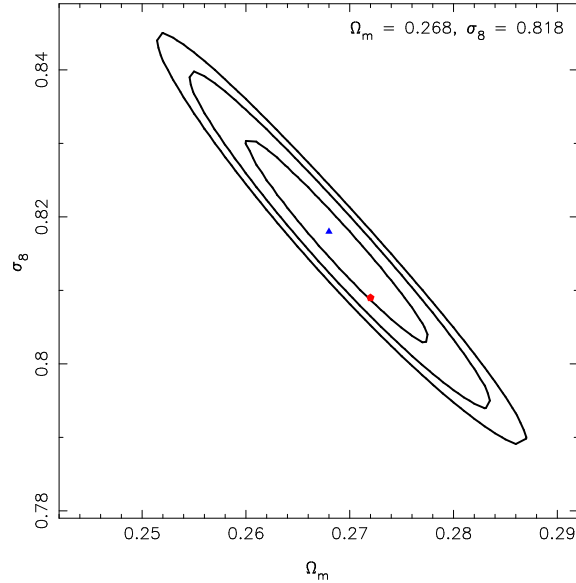
Figure 6.8: Combined χ^2 likelihood. The black lines show the combined χ^2 1, 2 and 3σ contours. The blue triangle shows the best fit parameters for the combined χ^2 and the red star shows the true cosmological parameters.

Figure 6.9 shows the 1σ, two-parameter contours for the Gaussian Fisher (orange shaded ellipse) and the non-linear Fisher (grey shaded ellipse). The thick black line shows the simulation maximum likelihood analysis. As in the case for the 2-D analysis, the non-linear Fisher contour is very close to the maximum likelihood contour. The area of the non-linear Fisher contour is 5.1 times larger than the area of the Gaussian Fisher contour. The marginal error of the non-linear Fisher estimate is 1.39 times larger than the Gaussian in Ω_m and 1.24 times larger in σ_8. These numbers are very similar to those calculated in the 2-D analysis.

The area of the contours and the size of the marginal errors in the tomographic Fisher and likelihood estimates are smaller than those in the unbinned analyses, showing that the tomographic analysis does indeed contain more information.

6.4.4   Multi-parameter Fisher analysis

In the previous section, it was shown that a Fisher matrix analysis in the $\Omega_m - \sigma_8$ plane accurately determines the errors on the parameters when a non-Gaussian data covariance matrix is used in the calculation. This was shown by comparing the 68% error contour with a maximum likelihood analysis of the simulation suite. In this
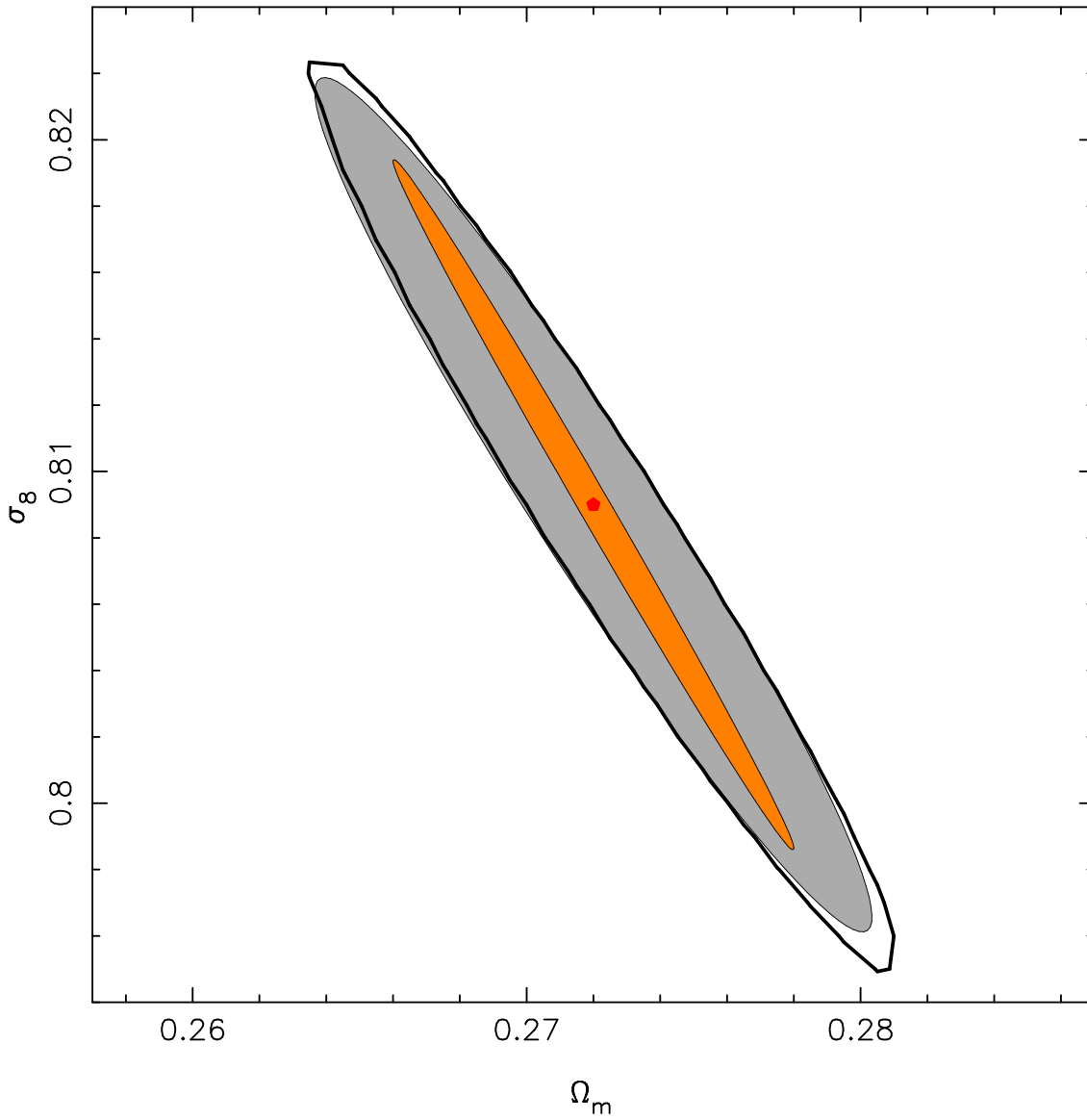
Figure 6.9: **Comparison of the 1σ, two-parameter contours for the $\Omega_m - \sigma_8$ parameters for the Gaussian Fisher contour (inner orange shaded ellipse), the simulation Fisher contour (middle grey shaded ellipse) and the full simulation maximum likelihood analysis (thick black line contour). The (red) point in the middle of the contours represents the fiducial $\Omega_m - \sigma_8$ parameters in this calculation.**

Figure 6.10: Three-parameter Fisher analysis. The (grey) shaded ellipse is the non-linear Fisher contour and the (orange) dashed ellipse is the Gaussian Fisher contour.

Section three different Fisher matrix analyses are performed over multiple cosmological parameters: three parameters (Ω_m, σ_8, n_s), four parameters (Ω_m, σ_8, n_s, Ω_Λ) and six parameters (Ω_m, σ_8, h, n_s, w_0, w_a). Note that Ω_Λ is allowed to vary in the four-parameter analysis, but $\Omega_\Lambda = 1 - \Omega_m$ in the three- and six-parameter analyses. The Gaussian Fisher analysis is compared with the non-Gaussian (simulation) Fisher analysis. Based on the findings in the two-parameter analysis, it is assumed that the Fisher errors calculated with the simulation data covariance matrix are consistent with a maximum likelihood analysis of the simulations over the same multi-parameter space.

For a Euclid-like survey (see Table 6.1), it makes little sense to perform a 2-D analysis over multiple parameters. In the 2-D analysis, the size of the marginal errors was so large as to provide no constraining information (e.g. $\Delta w_0 = 11.3$ and $\Delta w_a = 49.8$ in the six-parameter analysis). However, the additional information provided by per-

forming a tomographic analysis of the power spectra yielded far better constraints and illuminated some features of the Fisher matrix analysis that were not immediately obvious.

Figure 6.10 shows the projected two-parameter 1σ contours marginalised over the three-parameter 3-bin tomographic Fisher analysis. The (grey) shaded ellipse shows the non-linear Fisher contour, the dashed (orange) ellipse is the Gaussian Fisher contour and the (red) point at the center is the fiducial parameter value. Similar to the two-parameter analysis, the Gaussian Fisher contours are smaller than the non-linear Fisher contours as expected. The volume of the non-linear three-parameter space,

$$V \propto \sqrt{\det(F^{-1})}, \tag{6.21}$$

is actually 8 times larger than the Gaussian space and the marginal errors for the non-linear Fisher are 2 times larger than the Gaussian Fisher in Ω_m and 1.5 times larger in σ_8 and n_s. This figure clearly shows that the Gaussian Fisher analysis is underestimating the errors and the addition of the non-linear mode-coupling in the non-linear Fisher analysis gives far more conservative estimates of both marginal errors and 2-D projected areas.

The analysis over four parameters allows marginalisation over curvature with Ω_Λ. Figure 6.11 shows the projected two-parameter 1σ contours marginalised over the four-parameter Fisher analysis. The (red) point is the fiducial parameter value, the (grey) shaded ellipse is the non-linear Fisher contour and the (orange) dashed ellipse is the Gaussian Fisher contour. The projected contours in this figure show the Gaussian Fisher contours appearing to have a larger marginal error for one parameter but smaller areas for each projection as expected. In this case, the volume of the non-linear Fisher four-parameter space is 3.7 times larger than the Gaussian Fisher volume, which matches well with what the 2-D projections show. The non-linear Fisher marginal errors are 1.3 times larger than the Gaussian for n_s and 1.1 times larger for Ω_m and Ω_Λ. However, the Gaussian Fisher marginal errors are 1.2 times larger than the non-linear Fisher for σ_8. While having the marginal errors for σ_8 being larger for the Gaussian is a little unexpected, the size of the marginal errors is so similar for both the Gaussian and non-linear analyses that this is not a significant result. Overall the contours are behaving as expected with larger projected areas in
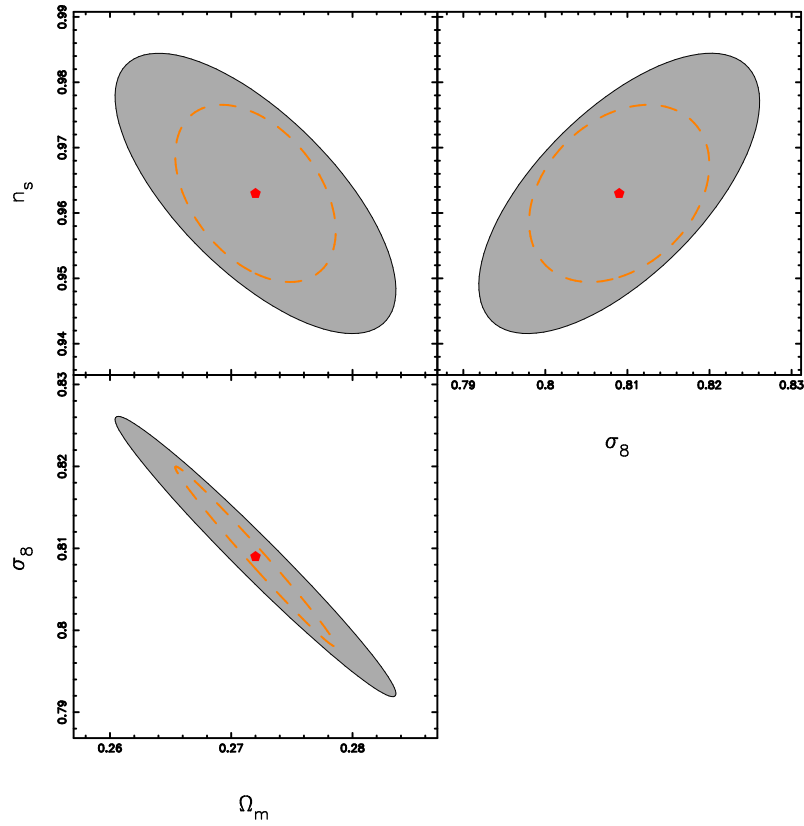
Figure 6.11: **Four-parameter Fisher analysis. The (grey) shaded ellipse is the non-linear Fisher contour and the (orange) dashed ellipse is the Gaussian Fisher contour. The areas of the non-linear Fisher contours are larger than the Gaussian contours as expected.**

Tomographic Six-Parameter Analysis

	NL	Gauss	Gauss / NL
$\Delta\Omega_m$	0.009	0.010	1.11
$\Delta\sigma_8$	0.019	0.021	1.11
Δh	0.198	0.352	1.78
Δn_s	0.143	0.201	1.41
Δw_0	0.107	0.129	1.21
Δw_a	0.343	0.584	1.70

Table 6.2: Marginal errors from a 3-bin tomographic, six-parameter Fisher matrix analysis using both Gaussian and non-linear Fisher matrices. For this configuration, the Gaussian marginal errors are always larger than the non-linear Fisher errors. However, the non-linear Fisher volume is 3.7 times larger than the Gaussian volume.

the non-linear Fisher contours. One unusual thing to note about these projections is the degeneracy in the $\Omega_m - n_s$ plane which is completely different for the Gaussian and non-linear analyses. The reason for this is most likely due to the complex nature of the four-parameter space and highlights the significant effect that the information from the non-linear mode-coupling can have on the Fisher analysis.

Figure 6.12 shows the projected two-parameter, 1σ contours, marginalised over the six-parameter Fisher matrix analysis. The (red) point at the center shows the fiducial parameters used in the analysis, the (grey) shaded ellipses show the non-linear Fisher analysis and the dashed (orange) ellipses show the Gaussian Fisher analysis. In all cases, except the $\Omega_m - \sigma_8$ plane, the projected area of the Gaussian contours is larger than the area of the non-linear Fisher contours which gives the impression that the error estimates from the Gaussian Fisher analysis are more conservative than the non-linear estimates. The marginal errors of the Gaussian contours are larger in all cases (see Table 6.2). However, the volume of the six-parameter space generated shows that the non-linear Fisher volume is 3.7 times larger than the Gaussian volume, which is expected given the off-diagonal terms included in the simulation data covariance matrix. The implication of this is that although the projected areas of the Gaussian Fisher appear larger, the overall volume is smaller. This can be explained with an example (in three dimensions for simplicity of explanation): Take a spherical ball and a thin plate with a slightly larger radius than the ball. Looking at the ball from any of the three axes, the area will appear to be the same circle in
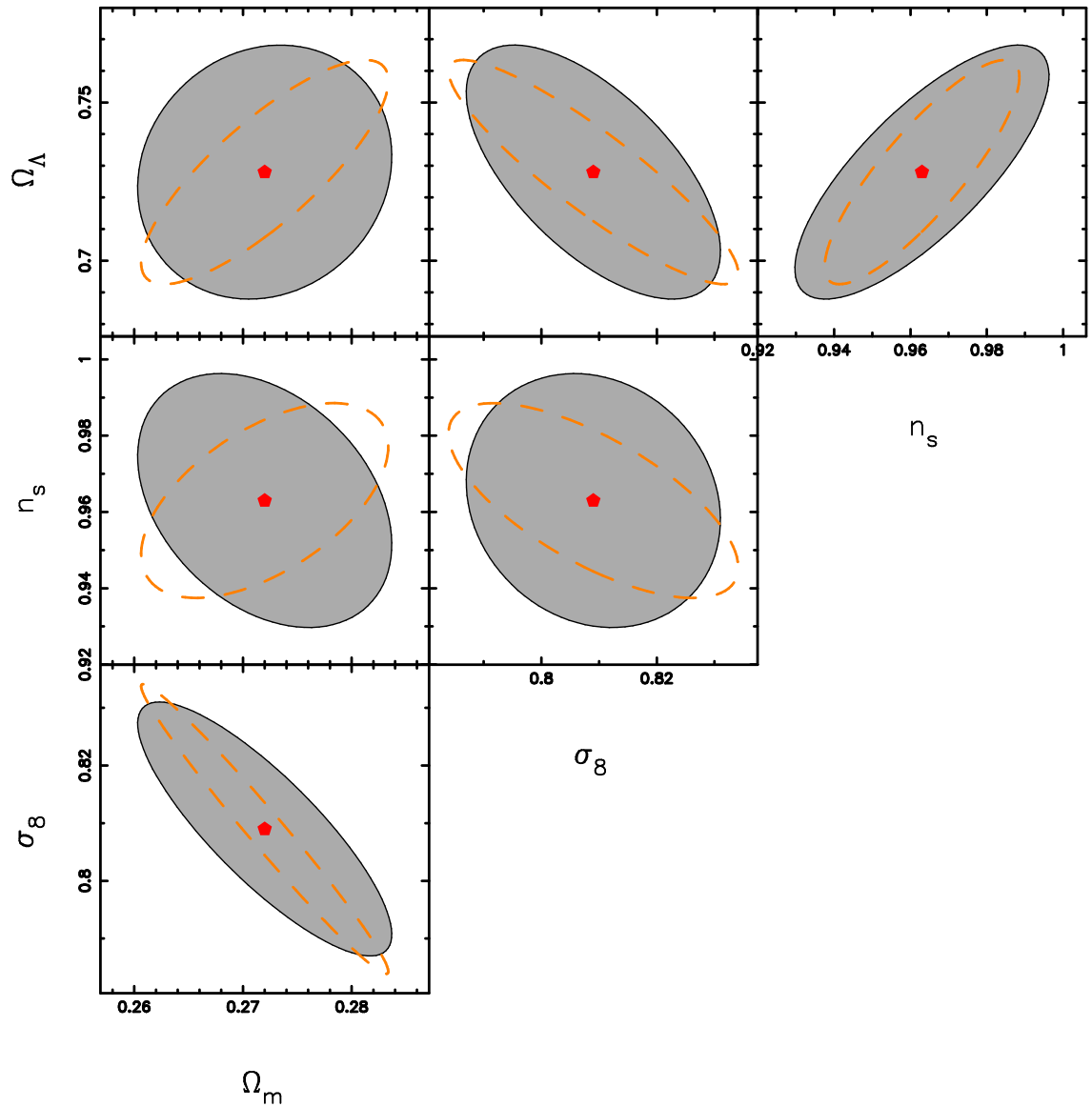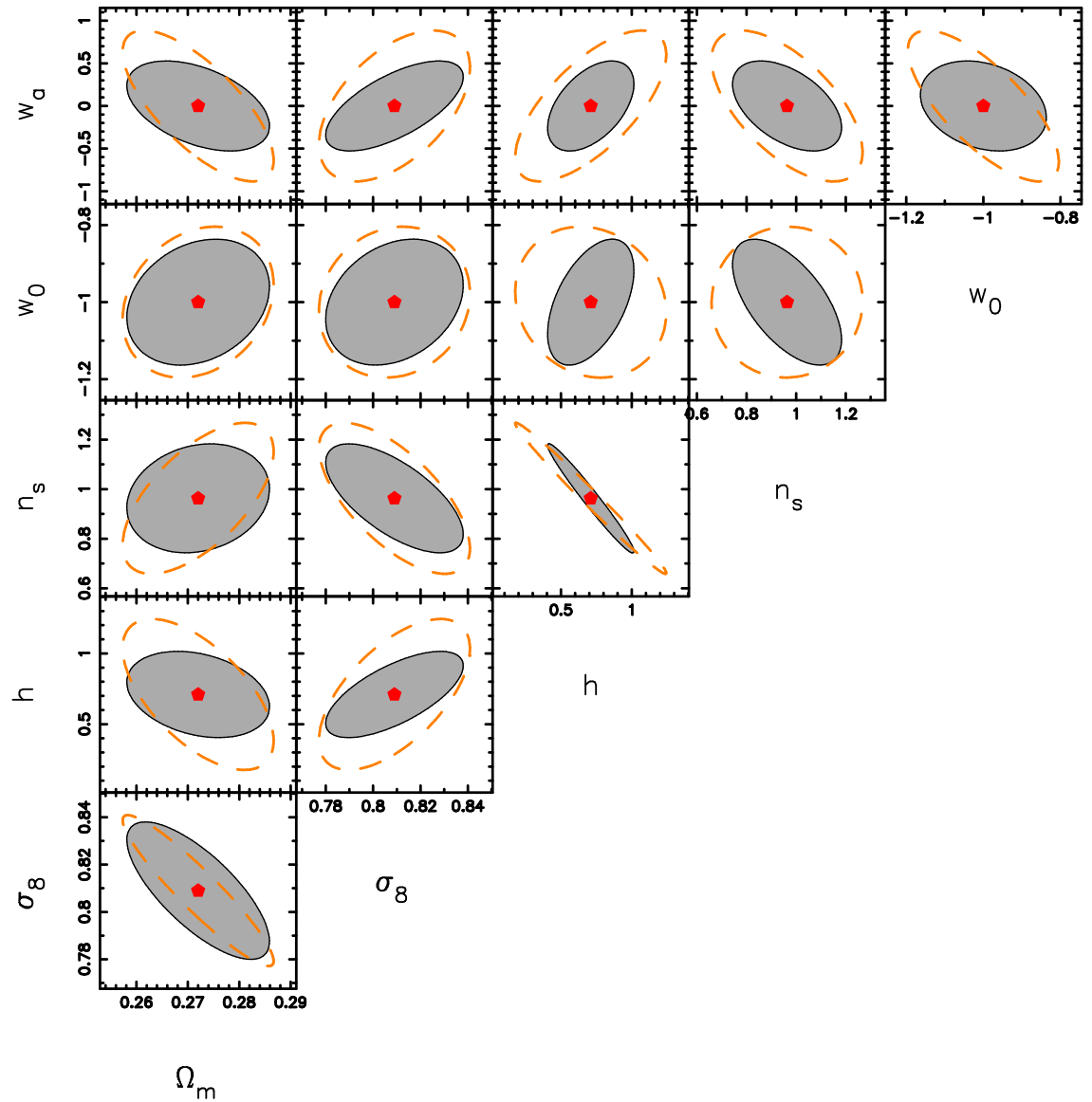
Figure 6.12: **Six-parameter Fisher analysis. The (grey) shaded ellipse is the non-linear Fisher contour and the (orange) dashed ellipse is the Gaussian Fisher contour. The volume of the 6-D space is larger in the non-linear Fisher matrix, however some of the projected contours appear larger for the Gaussian Fisher matrix. This could be very misleading.**

each projection. If the plate is placed at a 45° angle to each of the three axes, in projection it will appear to have a larger area than the ball in all axes, however we know that the volume of the plate is far smaller than the ball. With this knowledge in hand, it is easy to see how misleading the projections of the Fisher matrices can be in these complex multiple-parameter spaces.

The eigenvalues and eigenvectors of the six-parameter Fisher matrices were determined to find the equation for the plane with the most information in the full six-parameter space. They were calculated using a Jacobi rotation of the inverse Fisher matrix. For the Gaussian, this is:

$$
\begin{aligned}
X \quad = \quad & 0.865 \ \Omega_m + 0.498 \ \sigma_8 + 0.049 \ n_s + 0.030 \ h - \\
& 0.035 \ w_0 - 0.006 \ w_a,
\end{aligned}
\tag{6.22}
$$

and for the simulations:

$$
\begin{aligned}
Y \quad = \quad & 0.841 \ \Omega_m + 0.536 \ \sigma_8 + 0.034 \ n_s + 0.028 \ h - \\
& 0.056 \ w_0 - 0.015 \ w_a.
\end{aligned}
\tag{6.23}
$$

When using the fiducial parameters,

$$
X \ = \ 0.741, \tag{6.24}
$$

$$
Y \ = \ 0.771, \tag{6.25}
$$

and the errors on the planes are $\Delta X = 8.6 \times 10^{-8}$ and $\Delta Y = 1.4 \times 10^{-6}$. This shows an order-of-magnitude difference in the thickness between the Gaussian and non-linear Fisher 6-D error ellipses.

6.5 Discussion and Conclusions

This chapter makes a comparison between Fisher matrices in the $\Omega_m - \sigma_8$ plane and three-parameter (Ω_m, σ_8, n_s), four-parameter (Ω_m, σ_8, n_s, Ω_Λ) and six-parameter (Ω_m, σ_8, h, n_s, w_0, w_a) Fisher matrices, generated using covariance matrices from a Gaussian random field and from full N-body simulations. The 1σ two-parameter contours from the two-parameter $\Omega_m - \sigma_8$ Fisher matrices are also compared with

the contour from a maximum likelihood analysis of the full suite of simulations.

This work uses the SUNGLASS pipeline to generate 100 independent simulations of $512h^{-1}$ Mpc with 512^3 particles and a standard ΛCDM cosmology. The pipeline turns these simulations into 100 independent mock galaxy shear catalogues of 100 square degrees and a galaxy redshift distribution with a median of $z_m = 0.82$ and 15 'galaxies' per square arcminute. When these catalogues are combined, they provide an effective survey area of 10,000 square degrees.

Both 2-D and 3-bin tomographic angular shear power spectrum analyses are performed on each of the mock catalogues and covariance matrices from the resulting data-vectors are generated. A Gaussian field covariance matrix is also generated to compare with the more realistic non-Gaussian analyses.

Using these covariance matrices, Fisher matrices are generated for the $\Omega_m - \sigma_8$ plane and it is shown that the 1σ, two-parameter contour for the non-linear Fisher matrix has an area that is 5.1 times larger than the theoretical prediction in both the 2-D and tomographic analyses. This indicates that the theoretical prediction is significantly under-predicting the errors on these parameters (the Figure-of-Merit is over-optimistic), even though their marginal errors are similar.

To quantify if the contours generated using the Fisher matrix are a reasonable estimate of the true errors, these outputs are compared with a combined maximum likelihood analysis of the full simulation suite. The resulting contours in both the 2-D and tomographic analyses closely matched the contours generated with the non-linear Fisher matrix. From this, it can concluded that it is sensible to use a Fisher matrix analysis for parameter estimates, using a covariance matrix with all off-diagonal terms included.

Based on the success of the non-linear Fisher errors in matching the maximum likelihood estimates in the $\Omega_m - \sigma_8$ plane, both 2-D and 3-bin tomographic analyses were performed to generate three-, four- and six-parameter Fisher matrices. The non-linear Fisher matrices were compared with the Gaussian Fisher matrices under the assumption that the non-linear Fisher matrices are providing accurate error estimates. With the survey parameters used in this chapter, the 2-D analysis finds

marginal errors on the parameters that are so large that they provide no constraining power.

The tomographic analyses find reasonable marginal errors and demonstrate the value of the additional information obtained from the tomography. The three-parameter analysis of Ω_m, σ_8 and n_s showed two-parameter projections marginalised over the three parameters that fit expectations with the areas and marginal errors of the non-linear Fisher contours consistently larger than the Gaussian Fisher contours. The four-parameter analysis of Ω_m, σ_8, n_s and Ω_Λ showed projected contours that had a larger area for the non-linear Fisher matrix as expected. The marginal errors were also larger for the non-linear Fisher in all but σ_8 which is understandable given the complex nature of the four-parameter space. However, the marginal errors for the six-parameter Gaussian Fisher matrix were larger than the non-linear Fisher marginal errors for every parameter which is a counterintuitive result. The projected contours from the Gaussian Fisher matrix are also shown to be larger than the non-linear Fisher matrix, even though the volume of the non-linear Fisher is 3.7 times larger than the Gaussian Fisher. This is a warning that the projected Fisher contours can be misleading over complex multi-variate spaces and that larger projected 2-D contours do not necessarily indicate a larger error volume.

The analyses in this chapter show the importance of accounting for mode-coupling in the lensing power spectrum covariance matrix when performing cosmological parameter estimation. To isolate the subject of investigation, we have not included shape noise or intrinsic alignments in this study. These effects will of course degrade the parameter constraints and would need to be included in the analysis of cosmological data.

Chapter 7

Concluding Remarks

This chapter summarises the work completed in this thesis before detailing some future directions and some final comments on the status of the field and this project.

7.1   Summary

This thesis began by giving a broad historical background to the field of weak gravitational lensing, starting with Newton's ideas in 1704 that massive objects may bend light rays and moving through history to the first ever measurements of the cosmic shear signal (Kaiser et al., 2000; Wittman et al., 2000; Van Waerbeke et al., 2000; Bacon et al., 2000) and direct empirical evidence for the existence of dark matter (Clowe et al., 2006).

This historical background provides a framework upon which a more detailed picture is built throughout the next three introductory chapters. Our current view of the Universe is that it is spatially flat with close to critical density, $\Omega_{tot} = 1$. The most recent state-of-the-art observations suggest that 27% of the density of the Universe comes from matter but just 4% of this is made from baryons. The other 23% consists of a non-radiating, non-interacting form of matter, known as dark matter. The remaining 73% of the density is known as dark energy and is believed to be the cause of the accelerated expansion of the Universe. However, the true nature of dark matter and dark energy is poorly understood.

The dark Universe can be investigated through measuring and interpreting the grav-

itational lensing signal, which occurs when a massive object (like a galaxy or cluster of galaxies) bends space-time. Gravitational lensing causes light-rays traveling in the vicinity of massive objects to be distorted and magnified, much like if they were traveling through an optical lens. By measuring the gravitational lensing signal, the dark Universe can be investigated and the true nature of dark matter and dark energy can be probed without relying on luminous tracers. Weak gravitational lensing, where the magnifications and distortions to the light-rays are very small and can only be measured statistically, is the focus of the work in this thesis. In particular this work addresses the cosmic shear signal, which is caused by weak lensing of the large-scale structure.

In order to investigate the Universe with weak lensing, large surveys must be undertaken to observe the phenomenon. However, observations do not provide a complete picture because they suffer from noise and systematics. Weak lensing simulations provide a data set with known parameters that can be used to wholly interpret the weak lensing observations through providing detailed covariance matrices for data analysis. Simulations can also help to prepare for upcoming telescope surveys by forecasting what a particular telescope design and survey strategy will see.

7.1.1 SUNGLASS

Currently, there are very few weak lensing simulation pipelines available in the world. The pipelines that are available often rely on single high-resolution realisations, which may not be suitable for generating independent covariance matrices for data analysis. The need for a pipeline to rapidly generate Monte Carlo suites of weak lensing simulations for analysis lead to the development of the new weak lensing simulations pipeline presented in this thesis – SUNGLASS, Simulated UNiverses for Gravitational Lensing Analysis and Shear Surveys. SUNGLASS generates N-body simulations with GADGET2 (Springel, 2005). It then builds lightcones through the simulations using a new line-of-sight integration with no radial binning to determine weak lensing shear and convergence on multiple lensing source redshift planes. Shears and convergences from the source redshift planes are interpolated back on to the specific particle positions to generate 3-D mock galaxy shear catalogues. Assuming that galaxies trace the dark matter exactly, the SUNGLASS pipeline can impose a redshift distribution on the particles in the lightcone to produce a mock

galaxy shear catalogue that mimics real surveys.

The SUNGLASS pipeline was used to create a suite of 100 independent realisations with a standard ΛCDM cosmology in a 512 h^{-1}Mpc box with 512^3 particles. The mock catalogues generated with the pipeline are 100 square degrees and have a depth of z = 1.5. There are 15 'galaxies' per square arcminute in the catalogue and the distribution has a median redshift of $z_m = 0.82$. The pipeline has been extensively tested and power spectrum analyses of the catalogues show an agreement with the theoretical prediction at wavenumbers $200 < \ell < 2000$. To model wavenumbers lower than $\ell = 200$ in the simulations, larger wavelengths need to be present which requires a larger simulation volume. To model the wavenumbers higher than $\ell = 2000$, smaller wavenumbers need to be resolved which requires a higher number density of particles in the simulations. However, modelling a wider range of wavenumbers is not currently a critical requirement for studies since the realistic range that observational weak lensing surveys can measure is within the range that SUNGLASS is currently modelling. For future work, with very high resolution weak lensing surveys, modelling higher wavenumbers will be more important and SUNGLASS is capable of achieving this.

This thesis shows that the SUNGLASS pipeline is able to produce mock galaxy shear catalogues that are accurately modelling the 2-D shear power spectrum over a reasonably wide range of wavenumbers. The continued development of this pipeline is particularly important to weak lensing studies because to date, observational weak lensing analysis pipelines have not been verified and rigorously checked using data sets with known parameters. The mock galaxy shear catalogues that SUNGLASS produces can be run through observational data analysis pipelines to ensure that the input cosmological parameters are being recovered. Any discrepancies in the parameters being recovered can be used to identify errors and calibrate the analysis. SUNGLASS also has the advantage of being able to produce Monte Carlo realisations which can be used to determine the probabilities of making a particular observation as well as providing fully independent statistical samples to generate accurate covariance matrices that take into account full non-linear mode-coupling. The future of weak lensing lies in a combined analysis of large suites of simulations and high resolution observations.

The simulations provided by SUNGLASS will be used in the analysis of, but not limited to, Pan-STARRS PS1 data and COSMOS data by providing accurate covariance matrices and quantifying sample variance. They will also be used in preparation for the Euclid, HALO and WFIRST surveys by forecasting errors on cosmological parameters, providing images to test the effects of observational defects like charge transfer inefficiency (see Section 7.2) and testing new analysis techniques like Pseudo-C_ℓ (see Section 7.2). The simulations have already contributed to quantifying the sample variance for analysis of COSMOS data, helping to determine the stochastic bias with weak gravitational lensing (Jullo et al., 2011). The convergence fields from SUNGLASS were used to test Box-Cox transformations, used to Gaussianise lensing signals (Joachimi et al., 2011) and finally, images of the N-body simulations generated with the SUNGLASS pipeline were used illustratively in the GREAT10 handbook (Kitching et al., 2010). SUNGLASS has also enabled forecasts of the effect of star masks on a Euclid type survey and shown that when a field is masked by up to 3%, the effect on the power spectrum is negligible.

7.1.2   Maximum Likelihood Analysis

Maximum likelihood analysis was performed on the mock shear catalogues produced by SUNGLASS to forecast cosmological parameter errors in the $\Omega_m - \sigma_8$ plane. Both 2-D and tomographic analyses were performed. In the 2-D analysis, the 1, 2 and 3σ contours for the best-fit realisation showed good agreement with the input parameters. The contours from this realisation were chosen to be representative of the average contours for the full 100 realisations. The best-fit points for each of the realisations showed 68% within the 1σ contour, 93% within the 2σ contour and 97% within 3σ, which is almost Gaussian. However, the banana shape of the contours is confirmation that the distribution of the power spectra is not Gaussian, although this does not appear to bias the error estimates.

The χ^2 values for each of the realisations were added together to provide a likelihood estimate for a Euclid-like survey with an effective area of 10,000 square degrees. The contours provide much smaller errors in this case and appear to be much more elliptical. The best-fit point for this estimate lies within the 1σ error contour so any residual bias in the measurement is below the uncertainty. The marginal errors for the 100 realisations are $\Delta\Omega_m = 0.012$ and $\Delta\sigma_8 = 0.022$.

A 3-bin tomographic analysis was performed by splitting the redshift distribution in the mock catalogues into three equally spaced redshift bins, $0 < z \leq 0.5$, $0.5 < z \leq 1.0$ and $1.0 < z \leq 1.5$. A power spectrum analysis was performed on the auto- and cross-bins and the results show that the auto-power spectra accurately model wavenumbers from $150 < \ell < 700$ for $C_{11}^{\gamma\gamma}$ and $150 < \ell < 1000$ for $C_{22}^{\gamma\gamma}$ and $C_{33}^{\gamma\gamma}$. The cross-power spectra are damped possibly due to shot-noise contamination in the lowest-redshift bin, so only wavenumbers up to the highest accurately modelled wavenumber in the lowest redshift auto-power spectrum are considered. As a result of this, the shear power spectrum data vector that is constructed to perform the maximum likelihood analysis does not contain many bins from the cross-power spectra. The final data vector has 40 bins in total, 10 from each of the auto-power spectra and just 10 from all of the cross-power spectra combined. Despite the low number of cross-bins being utilised, the tomographic analysis still provides parameter constraints that are stronger than the 2-D analysis. The χ^2 contours from the single best-fit realisation have a smaller area than the 2-D analysis and 90% of the best-fit points fall within the 1σ contour while the full 100% lie within the 2σ contour. This does not fit with Gaussian statistics but could be the result of the way that the contours are chosen. Averaging the χ^2 contours does not produce sensible results, which is why the best-fit contour is used. These results suggest that the contours should in fact be even smaller.

As with the 2-D combined analysis, the combined 3-bin tomographic maximum likelihood analysis provides a stronger constraint on the errors with $\Delta\Omega_m = 0.009$ and $\Delta\sigma_8 = 0.014$. The best-fit point also lies within the 1σ contour indicating that any residual bias in the calculation is within the measured uncertainty.

The results in this work are based on catalogues with no shape noise present, ie they are for a perfect survey. This should be taken in to consideration before using these numbers in forecasts for telescope missions.

The maximum likelihood analysis is an attractive way to determine the errors in a suite of simulations because although it makes some assumptions on the Gaussianity of the distribution of the power spectra, it is still taking into account non-linear mode-coupling and bias in the simulations. However, this analysis is computation-

ally very expensive and if extended to a multi-parameter analysis, which would require a Monte Carlo Markov Chain, would become increasingly time consuming. Due to these time issues, the maximum likelihood is a best used as a sanity check on other methods of error estimation (like Fisher matrix analysis), rather than as the primary method.

7.1.3   Fisher Matrix Analysis

Fisher matrix analysis is a computationally cheap method for forecasting cosmological parameter errors. Traditionally, the Fisher matrix was constructed with a Gaussian covariance matrix that is derived from an underlying density field which is a Gaussian random field that contains only diagonal components. In this thesis, both 2-D and 3-bin tomographic Fisher matrix analyses were performed with Fisher matrices generated using Gaussian covariance matrices as well as covariance matrices from the suite of mock shear catalogues. The covariance matrices from the simulations contain non-linear mode-coupling and consequently have all of the off-diagonal components present.

As a sanity check, the two-parameter error estimates for the $\Omega_m - \sigma_8$ plane were checked against the maximum likelihood estimates. In both the 2-D and tomographic analyses, the Gaussian Fisher contours had an area that was far smaller than the maximum likelihood while the non-linear Fisher matrix fit the maximum likelihood almost perfectly. While the area of the non-linear Fisher contour was 5 times larger than the Gaussian contour, the marginal errors are quite similar. In the 2-D analysis, the non-linear Fisher marginal error, $\Delta\Omega_m$, is 1.23 times larger than the Gaussian and $\Delta\sigma_8$ is 1.17 times larger. In the tomographic analysis, the non-linear Fisher marginal error $\Delta\Omega_m$ is 1.39 times larger than the Gaussian and $\Delta\sigma_8$ is 1.24 times larger. These results show that a Fisher matrix calculation that takes non-linear mode-coupling into account produces an error estimate that is far more accurate than the Gaussian Fisher estimates. However, if only the marginal errors are of interest, the Gaussian Fisher analysis supplies an adequate estimate provided acknowledgment is made that the resulting errors will be slightly underestimated.

Given the success of the two-parameter non-linear Fisher matrices in matching the maximum likelihood analysis, three-, four- and six-parameter Fisher analysis of

$(\Omega_m,\ \sigma_8,\ n_s)$, $(\Omega_m,\ \sigma_8,\ n_s,\ \Omega_\Lambda)$ and $(\Omega_m,\ \sigma_8,\ h,\ n_s,\ w_0,\ w_a)$ were performed. The non-linear Fisher matrix estimates were compared with the Gaussian Fisher estimates to determine the differences. A 2-D analysis was performed initially but the error estimates were so large that they did not provide any sensible constraints (e.g. $\Delta w_0 = 11.3$ and $\Delta w_a = 49.8$ in the six-parameter analysis). However, the 3-bin tomographic analysis provided far stronger constraints, demonstrating the value of tomography. The three- and four-parameter analyses produced results that were expected with the non-linear Fisher projected two-parameter contours, marginalised over all parameters, having a larger area and marginal errors than the Gaussian Fisher contours. The volume of the three- and four-parameter non-linear Fisher spaces was also significantly larger than the Gaussian Fisher volume. The volume of the six-parameter non-linear Fisher was 3.7 times larger than the volume of the Gaussian Fisher, once again showing that the characterisation of the non-linear mode-coupling makes a substantial difference the the error volume. However, when this volume was projected into 2-D to show two-parameter error ellipses, the areas of the Gaussian Fisher ellipses were larger than the non-linear Fisher ellipses in all but the $\Omega_m - \sigma_8$ plane. The marginal errors in these planes are once again very similar, but the projections are clearly very misleading. The indication of this work is that the Figure of Merit (FOM), which is related to the inverse of the area of the Fisher projections, can be misleading. The projections in a complex multi-parameter space do not necessarily provide an adequate representation of the errors unless the total volume of the space is taken into account. Studies relying on the FOM to provide strong constraints for future telescope missions should be very careful in how they state their errors and should provide as much information as possible to clarify the full extent of the errors.

7.2 Future Directions

While the SUNGLASS pipeline is a useful tool in its current state, there is much expansion possible. This section will give some details of some future directions for SUNGLASS and a brief overview of the extended development plans.

Initially, I will develop and incorporate a realistic treatment of the two specific

effects that most pollute current interpretation of wide-field lensing data: finite-field masking and intrinsic galaxy shape alignments. The development of realistic weak lensing simulation pipelines is critical to reliably interpret weak lensing survey data. This programme will enable current and future observers to

1. Include non-linear mode-coupling and sampling variance, including the covariance between measurements on different angular scales, without which current errors in cosmological parameter estimation and forecasting may be underestimated by a factor of 5 (see Chapter 6).

2. Correctly implement and interpret several innovative analysis techniques that will remove intrinsic alignments and account for windows and masks in the survey data.

7.2.1   Motivation

Surveys suffer from window functions, both in terms of their finite survey regions and the masking of bright stars or scattered light. In survey areas of limited depth (e.g. the gaps between chips), or in the presence of photometric redshift errors, the window function can become a complex three-dimensional volume. Measurement of the shear-shear power spectrum $C_\ell^{\gamma\gamma}$, whose Fourier space representation is theoretically preferred over real-space correlation functions because of the lower covariance between measurement bins, has long been an observational goal (e.g. Hu, 1999; Brown et al., 2003). However, power spectrum analysis is especially restricted by masked data, because ringing of a window function in Fourier space simultaneously degrades measurements on all scales. I shall incorporate exact window functions and photometric redshift errors into my mock galaxy catalogs, to precisely measure and correct for their effect on the interpretation of the real data from surveys such as Pan-STARRS PS1 and Euclid. The windowed mock catalogs will also enable the development of the Pseudo-C_ℓ technique to measure the power spectrum in a way that is more resilient to specific window function shapes (Taylor & Kitching, 2011, *in preparation*; Hikage et al., 2010).

Most weak gravitational lensing analyses implicitly assume that the intrinsic shapes of galaxies are randomly aligned. However, tidal gravitational effects can cause galaxies physically near each other to become aligned (and a more subtle effect can

align the observables of galaxy pairs along a line of sight). Such effects can be modelled in 3-D, and I shall incorporate them into my mock shear catalogs. However, they are difficult to correct in 2-D observational data, after the effects of (catastrophic) photometric redshift errors have been overlaid. Spurious residual effects can dominate the weak lensing signal (Hirata & Seljak, 2004). Understanding residuals so they can be corrected during the blind analysis of real data can only be done via the full end-to-end pipeline that I propose.

Developing the SUNGLASS pipeline to include more realistic effects will optimize the scientific return of existing lensing surveys like Pan-STARRS PS1 and COSMOS. Interpreting the more sophisticated, 3-D analysis techniques proposed will require full mock catalogs. This will be the first time that realistic window functions and intrinsic alignments have been included in a weak lensing simulations pipeline and investigations into their effects will yield invaluable insight into the problems of systematics and real world effects for all future lensing analyses. These investigations will be of immediate use to weak lensing data analysis, increasing the scientific return from existing lensing data. They will also be a useful resource for the wider community and will support development of future observing programs like the Euclid mission and HALO.

7.2.2 Development Plan

The more immediate development of the pipeline is detailed in this section.

End-to-End Simulated Pipelines

The SUNGLASS pipeline currently generates mock galaxy shear catalogues the provide a position of a 'galaxy' and the shear associated with that position. In order to provide an output that can be used to test observational analysis pipelines, the SUNGLASS pipeline needs to be extended to produce observational images that will then feed straight in to the observational pipelines. To do this, postage stamps of galaxies with appropriate colour, shape and clustering properties need to be pasted on to the positions of the particles in the mock catalogues. I will liaise with observers to generate these observational images to ensure their accuracy. Once the images have been generated, observational analysis pipelines can analyse them blindly to see if the true input shear can be recovered accurately. An end-to-end simulations pipeline

like this is essential to the analysis of observational data sets like Pan-STARRS PS1
and will provide much insight into the strengths and weaknesses of the observational
analysis.

Introducing galaxy ellipticities, window functions and photo-z errors into the mock data

Currently, the mock galaxy shear catalogs from SUNGLASS are perfect with all of
the information available in any 3-D location. In order to mimic the real surveys,
our catalogs need to have intrinsic random galaxy ellipticities, a window function
and complex masks imposed on them, then realistic photometric redshift errors to
be added. This process will involve modifying the SUNGLASS pipeline to include
random galaxy ellipticities on each particle. Then, blank patches on the shear field
or regions of reduced depth will be imposed. For the case of the HST COSMOS
field, I already have vectorised masks of bright stars and ghosting (painstakingly
produced by hand), whose properties I will model as representative of extragalactic
HST observations. I will liaise with the zCOSMOS team, whose spectroscopic ob-
servations are now public (Lilly et al., 2009), to characterise the typical photometric
redshift errors present in HST surveys with different numbers of bands. Due to the
flexibility of SUNGLASS, I am able to tailor this process to other existing surveys
like Pan-STARRS PS1 and future surveys like Euclid as well.

Testing the Pseudo-C_ℓ analysis technique on windowed surveys

The Pseudo-C_ℓ analysis technique (Taylor & Kitching, 2011, *in preparation*; Hikage
et al., 2010; Brown et al., 2005) is a method proposed to obtain the true shear-
shear power spectrum, $C_\ell^{\gamma\gamma}$, signal from a measured power spectrum signal that is
contaminated by windows and masks. If windows and masks are not taken into
account when we perform analyses, the resulting cosmological parameter estimates
will be biased. Pseudo-C_ℓ also offers the potential to improve cosmic shear measure-
ments. While the Pseudo-C_ℓ method has been tested on Gaussian random fields
and a single simulated source redshift plane, the method has never been applied to
a more realistic galaxy shear catalog. In order to test its robustness to masking, I
will write new software that will use the Pseudo-C_ℓ power spectrum analysis on re-
alistic mock galaxy shear catalogs generated by the SUNGLASS pipeline. The power
spectrum analysis with masked mock shear catalogs and Pseudo-C_ℓ will be tested

against a traditional power spectrum analysis with an unmasked catalog. Through these comparisons I will be able to make adjustments to the technique to improve its reliability and test the range of wavenumbers that the Pseudo-C_ℓ analysis can recover accurately.

Introducing intrinsic alignments into the mock data

Weak lensing analysis assumes that galaxies are randomly aligned on the sky, so their mean ellipticity is zero. However, this is not the case in the real Universe. There are two types of intrinsic alignment, the first describes galaxies that are close together in distance and have a mean shape alignment due to tidal forces during their formation. The effect of these alignments is to spuriously increase the lensing signal. The second type of intrinsic alignment is more difficult to detect (and remove). A galaxy that is formed close to the lensing object may be stretched toward it radially. Background objects lensed by this object will be gravitationally distorted tangential to the lens, the overall effect being an anti-correlation in shape that dilutes the lensing signal. Using an analytic prescription (Bridle & King, 2007), I will paint these intrinsic alignments in to the mock galaxy shear catalogs generated by SUNGLASS, so that each type of intrinsic alignment can be included individually or both together.

Testing the removal of intrinsic alignments

The intrinsic alignment signal contaminates the cosmic shear signal by up to 20%, which could result in parameter estimates for the dark energy equation of state being biased by up to a 50% (Bridle & King, 2007). Removing intrinsic alignments efficiently is essential for future weak lensing analyses.

Both the nulling technique (Joachimi & Schneider, 2008) and the path integral technique (Kitching & Taylor, 2011) can be tested on the mock shear catalogs with intrinsic alignments generated by the SUNGLASS pipeline. The effectiveness of the techniques will be tested against a traditional power spectrum analysis on catalogs with no intrinsic alignments. These comparisons will allow me to identify the strengths and weaknesses of each technique to ascertain the conditions that produce the best results for a particular method.

Beyond End-To-End Simulations, Pseudo-C$_\ell$ and Intrinsic Alignments

I will continue to augment the simulations with real world effects such as baryons, neutrinos and atmospheric effects, bringing us closer to having simulation data that is indistinguishable from the real data. My analysis will also be extended to investigate more general cosmological and modified gravity models including alternative dark matter models.

7.3 Concluding Remarks

Weak lensing simulations pipelines are essential to analysis of weak lensing data and in preparation for future weak lensing missions. The SUNGLASS pipeline provides Monte Carlo suites of simulations for weak lensing analysis and fulfills this critical role. The pipeline has been rigorously tested and has already been used to perform both data analysis (Jullo et al., 2011) and parameter estimations (Chapter 6). While the pipeline is very useful in its current state, the prospects for development are vast and continued improvements will make SUNGLASS more valuable to the weak lensing community.

'The physicist may be satisfied when he has the mathematical scheme he knows how to use for the interpretation of the experiments. But he has to speak about his results also to non-physicists who will not be satisfied unless some explanation is given in plain language. Even for the physicist, the description in plain language will be the criterion of the degree of understanding that has been reached'

Werner Heisenberg
Physics & Philosophy, 1962

'For I am not so enamored of my own opinions that I disregard what others may think of them'

Copernicus
De Revolutionibus Orbium Coelestium, 1543

'At the last dim horizon, we search among ghostly errors of observations for landmarks that are scarcely more substantial.
The search will continue. The urge is older than history. It is not satisfied and it will not be oppressed'

Edwin Hubble
Public Lecture, Pasadena, 1951

References

Aarseth S. J., Turner E. L., Gott III J. R., 1979, ApJ, 228, 664

Abell G. O., 1965, ARA&A, 3, 1

Abramowitz M., Stegun I. A., 1968, Handbook of mathematical functions with formulas, graphs and mathematical tables. New York: Dover, 1968, edited by Abramowitz, Milton; Stegun, Irene A.

Albrecht A., Amendola L., Bernstein G., Clowe D., Eisenstein D., Guzzo L., Hirata C., Huterer D., Kirshner R., Kolb E., Nichol R., 2009, ArXiv e-prints

Albrecht A., Bernstein G., Cahn R., Freedman W. L., Hewitt J., Hu W., Huth J., Kamionkowski M., Kolb E. W., Knox L., Mather J. C., Staggs S., Suntzeff N. B., 2006, ArXiv Astrophysics e-prints

Allgood B., Flores R. A., Primack J. R., Kravtsov A. V., Wechsler R. H., Faltenbacher A., Bullock J. S., 2006, MNRAS, 367, 1781

Amendola L., Tsujikawa S., 2010, Dark Energy: Theory and Observations

Appel A. W., 1985, SIAM Journal on Scientific and Statistical Computing, 6, 85

Armendariz-Picon C., Mukhanov V., Steinhardt P. J., 2000, Physical Review Letters, 85, 4438

Armendariz-Picon C., Mukhanov V., Steinhardt P. J., 2001, Phys. Rev. D, 63, 103510

Astier P., Guy J., Regnault N., et al. 2006, A&A, 447, 31

Bacon D. J., Goldberg D. M., Rowe B. T. P., Taylor A. N., 2006, MNRAS, 365, 414

Bacon D. J., Massey R. J., Refregier A. R., Ellis R. S., 2003, MNRAS, 344, 673

Bacon D. J., Refregier A. R., Ellis R. S., 2000, MNRAS, 318, 625

Bacon D. J., Taylor A. N., 2003, MNRAS, 344, 1307

Bacon D. J., Taylor A. N., Brown M. L., Gray M. E., Wolf C., Meisenheimer K., Dye S., Wisotzki L., Borch A., Kleinheinrich M., 2005, MNRAS, 363, 723

Barnes J., Hut P., 1986, Nature, 324, 446

Bartelmann M., 2010, ArXiv e-prints

Bartelmann M., Schneider P., 2001, Phys. Rep., 340, 291

Bass S. D., 2011, Journal of Physics G Nuclear Physics, 38, 043201

Battaglia G., Helmi A., Morrison H., Harding P., Olszewski E. W., Mateo M., Freeman K. C., Norris J., Shectman S. A., 2005, MNRAS, 364, 433

Baugh C. M., Gaztanaga E., Efstathiou G., 1995, MNRAS, 274, 1049

Begeman K. G., 1987, PhD thesis, , Kapteyn Institute, (1987)

Bertone G., 2010, Nature, 468, 389

Bertschinger E., Gelb J. M., 1991, Computers in Physics, 5, 164

Blandford R. D., Narayan R., 1992, ARA&A, 30, 311

Blandford R. D., Saust A. B., Brainerd T. G., Villumsen J. V., 1991, MNRAS, 251, 600

Blumenthal G. R., Faber S. M., Primack J. R., Rees M. J., 1984, Nature, 311, 517

Bode P., Ostriker J. P., Turok N., 2001, ApJ, 556, 93

Bolton A. S., Burles S., Koopmans L. V. E., Treu T., Moustakas L. A., 2005, ApJ, 624, L21

Bond J. R., Efstathiou G., Silk J., 1980, Physical Review Letters, 45, 1980

Booth C. M., Schaye J., 2009, MNRAS, 398, 53

Brainerd T. G., Blandford R. D., Smail I., 1996, ApJ, 466, 623

Bridle S., King L., 2007, New Journal of Physics, 9, 444

Brown M. L., Castro P. G., Taylor A. N., 2005, MNRAS, 360, 1262

Brown M. L., Taylor A. N., Bacon D. J., Gray M. E., Dye S., Meisenheimer K., Wolf C., 2003, MNRAS, 341, 100

Cabanac R. A., Valls-Gabaud D., Jaunsen A. O., Lidman C., Jerjen H., 2005, A&A, 436, L21

Caldwell R. R., Kamionkowski M., Weinberg N. N., 2003, Physical Review Letters, 91, 071301

Carbone C., Springel V., Baccigalupi C., Bartelmann M., Matarrese S., 2008, MN-RAS, 388, 1618

Carlberg R. G., Yee H. K. C., Ellingson E., Abraham R., Gravel P., Morris S., Pritchet C. J., 1996, ApJ, 462, 32

Chandrasekhar S., 1931, ApJ, 74, 81

Chang T.-C., Refregier A., Helfand D. J., 2004, ApJ, 617, 794

Chapman G. N. F., Geller M. J., Huchra J. P., 1988, AJ, 95, 999

Chen D. N., Jing Y. P., 2002, MNRAS, 336, 55

Chwolson O., 1924, Astronomische Nachrichten, 221, 329

Clowe D., Bradač M., Gonzalez A. H., Markevitch M., Randall S. W., Jones C., Zaritsky D., 2006, ApJ, 648, L109

Cole S., Percival W. J., Peacock J. A., et al. 2005, MNRAS, 362, 505

Cooray A., Hu W., 2002, ApJ, 574, 19

Cooray A., Sheth R., 2002, Phys. Rep., 372, 1

Côté P., McLaughlin D. E., Cohen J. G., Blakeslee J. P., 2003, ApJ, 591, 850

Couchman H. M. P., 1991, ApJ, 368, L23

Couchman H. M. P., Barber A. J., Thomas P. A., 1999, MNRAS, 308, 180

Cowie L. L., Songaila A., Hu E. M., Cohen J. G., 1996, AJ, 112, 839

Dalla Vecchia C., Schaye J., 2008, MNRAS, 387, 1431

Daniel S. F., Linder E. V., 2010, Phys. Rev. D, 82, 103523

Das D., Goudelis A., Mambrini Y., 2010, J. Cosmology Astropart. Phys., 12, 18

Dashevskii V. M., Slysh V. I., 1966, Soviet Astronomy, 9, 671

Dashevskii V. M., Zel'dovich Y. B., 1965, Soviet Astronomy, 8, 854

David L. P., Jones C., Forman W., Daines S., 1994, ApJ, 428, 544

Davis M., Efstathiou G., Frenk C. S., White S. D. M., 1985, ApJ, 292, 371

de Blok W. J. G., 1997, PhD thesis, AA(Kapteyn Astronomical Institute, Groningen, The Netherlands)

Deb S., Goldberg D. M., Heymans C., Morandi A., 2010, ApJ, 721, 124

Debattista V. P., Moore B., Quinn T., Kazantzidis S., Maas R., Mayer L., Read J., Stadel J., 2008, ApJ, 681, 1076

Dicke R. H., Peebles P. J. E., Roll P. G., Wilkinson D. T., 1965, ApJ, 142, 414

Dickinson C., Battye R. A., Carreira P., et al. 2004, MNRAS, 353, 732

Diemand J., Kuhlen M., Madau P., 2007, ApJ, 667, 859

Dietrich J. P., Hartlap J., 2010, MNRAS, 402, 1049

Dine M., Kusenko A., 2003, Reviews of Modern Physics, 76, 1

Dubinski J., Carlberg R. G., 1991, ApJ, 378, 496

Eastwood J., Hockney R. W., 1974, Journal of Computational Physics, 16, 342

Efstathiou G., Bernstein G., Tyson J. A., Katz N., Guhathakurta P., 1991, ApJ, 380, L47

Efstathiou G., Davis M., White S. D. M., Frenk C. S., 1985, ApJS, 57, 241

Einstein A., 1916, Annalen der Physik, 354, 769

Einstein A., 1917, Sitzungsberichte der Königlich Preußischen Akademie der Wissenschaften (Berlin), Seite 142-152., pp 142–152

Einstein A., 1936, Science, 84, 506

Eisenstein D. J., Hu W., 1998, ApJ, 496, 605

Eisenstein D. J., Zehavi I., Hogg D. W., et al. 2005, ApJ, 633, 560

Etherington A. M. M., 1933, Phil. Mag., 15, 761

Fisher R. A., 1935, J. Roy. Stat. Soc, 98, 39

Fomalont E. B., Sramek R. A., 1975, ApJ, 199, 749

Fomalont E. B., Sramek R. A., 1976, Physical Review Letters, 36, 1475

Fontanot F., De Lucia G., Monaco P., Somerville R. S., Santini P., 2009, MNRAS, 397, 1776

Forero-Romero J. E., Blaizot J., Devriendt J., van Waerbeke L., Guiderdoni B., 2007, MNRAS, 379, 1507

Fort B., Prieur J. L., Mathez G., Mellier Y., Soucail G., 1988, A&A, 200, L17

Fosalba P., Gaztañaga E., Castander F. J., Manera M., 2008, MNRAS, 391, 435

Freedman W. L., Madore B. F., Gibson B. K., Ferrarese L., Kelson D. D., Sakai S., Mould J. R., Kennicutt Jr. R. C., Ford H. C., Graham J. A., Huchra J. P., Hughes S. M. G., Illingworth G. D., Macri L. M., Stetson P. B., 2001, ApJ, 553, 47

Frieman J. A., Turner M. S., Huterer D., 2008, ARA&A, 46, 385

Fu L., Semboloni E., Hoekstra H., et al. 2008, A&A, 479, 9

Gamow G., 1948, Nature, 162, 680

Gamow G., 1949, Reviews of Modern Physics, 21, 367

Gavazzi R., Soucail G., 2007, A&A, 462, 459

Gentile G., Salucci P., Klein U., Vergani D., Kalberla P., 2004, MNRAS, 351, 903

Giannantonio T., Scranton R., Crittenden R. G., Nichol R. C., Boughn S. P., Myers A. D., Richards G. T., 2008, Phys. Rev. D, 77, 123520

Giocoli C., Bartelmann M., Sheth R. K., Cacciato M., 2010, MNRAS, 408, 300

Girardi M., Borgani S., Giuricin G., Mardirossian F., Mezzetti M., 2000, ApJ, 530, 62

Goldberg D. M., Bacon D. J., 2005, ApJ, 619, 741

Gorbunov D., Khmelnitsky A., Rubakov V., 2008, Journal of High Energy Physics, 12, 55

Gott III J. R., Miller J., Thuan T. X., Schneider S. E., Weinberg D. H., Gammie C., Polk K., Vogeley M., Jeffrey S., Bhavsar S. P., Melott A. L., Giovanelli R., Hayes M. P., Tully R. B., Hamilton A. J. S., 1989, ApJ, 340, 625

Gottlöber S., Łokas E. L., Klypin A., Hoffman Y., 2003, MNRAS, 344, 715

Götz M., Sommer-Larsen J., 2003, Ap&SS, 284, 341

Gregory R., Kaloper N., Myers R. C., Padilla A., 2007, Journal of High Energy Physics, 10, 69

Gunn J. E., 1967a, ApJ, 147, 61

Gunn J. E., 1967b, ApJ, 150, 737

Guth A. H., 1981, Phys. Rev. D, 23, 347

Hamuy M., Phillips M. M., Maza J., Suntzeff N. B., Schommer R. A., Aviles R., 1995, AJ, 109, 1

Hamuy M., Phillips M. M., Suntzeff N. B., Schommer R. A., Maza J., Smith R. C., Lira P., Aviles R., 1996, AJ, 112, 2438

Hartlap J., Schrabback T., Simon P., Schneider P., 2009, A&A, 504, 689

Hartlap J., Simon P., Schneider P., 2007, A&A, 464, 399

Heavens A., 2003, MNRAS, 343, 1327

Hetterscheidt M., Simon P., Schirmer M., Hildebrandt H., Schrabback T., Erben T., Schneider P., 2007, A&A, 468, 859

Hikage C., Takada M., Hamana T., Spergel D., 2010, ArXiv e-prints

Hilbert S., Hartlap J., White S. D. M., Schneider P., 2009, A&A, 499, 31

Hinshaw G., Nolta M. R., Bennett C. L., et al. 2007, ApJS, 170, 288

Hirata C. M., Seljak U., 2004, Phys. Rev. D, 70, 063526

Hockney R. W., Eastwood J. W., 1981, Computer Simulation Using Particles. Computer Simulation Using Particles, New York: McGraw-Hill, 1981

Hockney R. W., Eastwood J. W., 1988, Computer simulation using particles

Hoekstra H., Franx M., Kuijken K., Carlberg R. G., Yee H. K. C., 2003, MNRAS, 340, 609

Hoekstra H., Mellier Y., van Waerbeke L., Semboloni E., Fu L., Hudson M. J., Parker L. C., Tereno I., Benabed K., 2006, ApJ, 647, 116

Hoekstra H., Yee H. K. C., Gladders M. D., 2004, ApJ, 606, 67

Hogg D. W., 2000, astro-ph/9905116

Hu W., 1999, ApJ, 522, L21

Hu W., 2002, Phys. Rev. D, 66, 083515

Hubble E., 1929, Proceedings of the National Academy of Science, 15, 168

Hubble E., Humason M. L., 1931, ApJ, 74, 43

Huff E. M., Hirata C., Mandelbaum R., Padmanabhan N., Schlegel D., Seljak U., 2010, in American Astronomical Society Meeting Abstracts #215 Vol. 36 of Bulletin of the American Astronomical Society, Cosmic Shear in the Sloan Digital Sky Survey. pp 603.02–+

Jain B., Seljak U., White S., 2000, ApJ, 530, 547

Jain B., Taylor A., 2003, Physical Review Letters, 91, 141302

Jamil M., 2010, International Journal of Theoretical Physics, 49, 144

Jarosik N., Bennett C. L., Dunkley J., et al. 2011, ApJS, 192, 14

Jenkins A., Frenk C. S., Pearce F. R., Thomas P. A., Colberg J. M., White S. D. M., Couchman H. M. P., Peacock J. A., Efstathiou G., Nelson A. H., 1998, ApJ, 499, 20

Joachimi B., Schneider P., 2008, A&A, 488, 829

Joachimi B., Schneider P., 2009, A&A, 507, 105

Joachimi B., Taylor A. N., Kiessling A., 2011, ArXiv e-prints

Jones W. C., Ade P. A. R., Bock J. J., et al. 2006, ApJ, 647, 823

Jullo E., Rhodes J., Kiessling A., J. B., Massey R., Taylor J., Scoville N., 2011, ApJ submitted

Kaiser N., 1992, ApJ, 388, 272

Kaiser N., 1995, ApJ, 439, L1

Kaiser N., Squires G., 1993, ApJ, 404, 441

Kaiser N., Squires G., Broadhurst T., 1995, ApJ, 449, 460

Kaiser N., Wilson G., Luppino G. A., 2000, astro-ph/0003338

Kiessling A., Heavens A. F., Taylor A. N., Joachimi B., 2011, MNRAS, 414, 2235

Kitching T., Amara A., Gill M., et al. 2010, ArXiv e-prints

Kitching T. D., Heavens A. F., Miller L., 2010, ArXiv e-prints

Kitching T. D., Miller L., Heymans C. E., van Waerbeke L., Heavens A. F., 2008, MNRAS, 390, 149

Kitching T. D., Taylor A. N., 2011, MNRAS, 410, 1677

Klimov Y. G., 1963, Sov. Phys. Doklady, 8, 119

Knebe A., Libeskind N. I., Knollmann S. R., Yepes G., Gottlöber S., Hoffman Y., 2010, MNRAS, 405, 1119

Knox L., 1997, ApJ, 480, 72

Komatsu E., Smith K. M., Dunkley J., et al. 2011, ApJS, 192, 18

Kowalski M., Rubin D., Aldering G., et al. 2008, ArXiv e-prints, 804

Kubo J. M., Allam S. S., Drabek E., et al. 2010, ApJ, 724, L137

Kubo J. M., Annis J., Hardin F. M., Kubik D., Lawhorn K., Lin H., Nicklaus L., Nelson D., Reis R. R. R., Seo H., Soares-Santos M., Stebbins A., Yunker T., 2009, ApJ, 702, L110

Kuo C. L., Ade P. A. R., Bock J. J., et al. 2004, ApJ, 600, 32

Larson D., Dunkley J., Hinshaw G., et al. 2011, ApJS, 192, 16

Larson R., 1992, in G. Tenorio-Tagle, M. Prieto, & F. Sanchez ed., Star Formation in Stellar Systems Galaxy Formation and Evolution. pp 125–+

Leahy D. A., Yin D., 2000, MNRAS, 313, 617

Leauthaud A., Massey R., Kneib J., et al. 2007, ApJS, 172, 219

Leavitt H. S., Pickering E. C., 1912, Harvard College Observatory Circular, 173, 1

Lee J., Pen U.-L., 2008, ApJ, 686, L1

Lemaître G., 1931, Nature, 127, 706

Liebes S., 1964, Physical Review, 133, 835

Lilly S. J., Le Brun V., Maier C., et al. 2009, ApJS, 184, 218

Linde A. D., 1982, Physics Letters B, 108, 389

LSST Science Collaborations Abell P. A., Allison J., Anderson S. F., Andrew J. R., Angel J. R. P., Armus L., Arnett D., Asztalos S. J., Axelrod T. S., et al. 2009, ArXiv e-prints

Macfarland T., Couchman H. M. P., Pearce F. R., Pichlmeier J., 1998, New Astronomy, 3, 687

Maller A. H., Dekel A., 2002, MNRAS, 335, 487

Mandelbaum R., Hirata C. M., Broderick T., Seljak U., Brinkmann J., 2006, MN-RAS, pp 684–+

Massey R., Kitching T., Nagai D., 2010, ArXiv e-prints

Massey R., Kitching T., Richard J., 2010, Reports on Progress in Physics, 73, 086901

Massey R., Rhodes J., Leauthaud A., et al. 2007, ApJS, 172, 239

Matarrese S., Verde L., Heavens A. F., 1997, MNRAS, 290, 651

Meiksin A., White M., 1999, MNRAS, 308, 1179

Mellier Y., 1999, ARA&A, 37, 127

Miller L., Kitching T. D., Heymans C., Heavens A. F., van Waerbeke L., 2007, MNRAS, 382, 315

Miralda-Escude J., 1991, ApJ, 380, 1

Monaghan J. J., Lattanzio J. C., 1985, A&A, 149, 135

Mulchaey J. S., Davis D. S., Mushotzky R. F., Burstein D., 1993, ApJ, 404, L9

Munshi D., Valageas P., van Waerbeke L., Heavens A., 2008, Phys. Rep., 462, 67

Narayan R., Bartelmann M., 1997, astro-ph/9606001

Navarro J. F., 1998, ArXiv Astrophysics e-prints

Navarro J. F., Frenk C. S., White S. D. M., 1995, MNRAS, 275, 56

Navarro J. F., Frenk C. S., White S. D. M., 1996, ApJ, 462, 563

Navarro J. F., Frenk C. S., White S. D. M., 1997, ApJ, 490, 493

Neistein E., van den Bosch F. C., Dekel A., 2006, MNRAS, 372, 933

Neyrinck M. C., Szapudi I., Rimes C. D., 2006, MNRAS, 370, L66

Oguri M., Takada M., Okabe N., Smith G. P., 2010, MNRAS, 405, 2215

Olive K. A., 1990, Phys. Rep., 190, 307

Ostriker J. P., Peebles P. J. E., 1973, ApJ, 186, 467

Peacock J. A., 1999, Cosmological Physics. Cosmological Physics, by John A. Peacock, pp. 704. ISBN 052141072X. Cambridge, UK: Cambridge University Press, January 1999.

Peacock J. A., Dodds S. J., 1996, MNRAS, 280, L19

Peebles P. J. E., 1970, AJ, 75, 13

Peebles P. J. E., 1980, The large-scale structure of the universe. Research supported by the National Science Foundation. Princeton, N.J., Princeton University Press, 1980. 435 p.

Peebles P. J. E., Ratra B., 1988, ApJ, 325, L17

Pello R., Sanahuja B., Le Borgne J., Soucail G., Mellier Y., 1991, ApJ, 366, 405

Penzias A. A., Wilson R. W., 1965, ApJ, 142, 419

Percival W. J., Reid B. A., Eisenstein D. J., et al. 2010, MNRAS, 401, 2148

Perlmutter S., Aldering G., Goldhaber G., et al. The Supernova Cosmology Project 1999, ApJ, 517, 565

Pfalzner S., Gibbon P., 1997, Many-Body Tree Methods in Physics. Many-Body Tree Methods in Physics, ISBN 0521495644, Cambridge University Press, 1997.

Pospieszalska-Surdej A., Surdej J., Detal A., Jean C., 2001, in ASP Conf. Ser. 237: Gravitational Lensing: Recent Progress and Future Go The GL Bibliography and an Interactive Database. pp 55–+

Powell L. C., Kay S. T., Babul A., 2009, MNRAS, 400, 705

Prada F., Vitvitska M., Klypin A., Holtzman J. A., Schlegel D. J., Grebel E. K., Rix H.-W., Brinkmann J., McKay T. A., Csabai I., 2003, ApJ, 598, 260

Press W. H., Schechter P., 1974, ApJ, 187, 425

Press W. H., Teukolsky S. A., Vetterling W. T., Flannery B. P., 1992, Numerical recipes in FORTRAN. The art of scientific computing

Ratra B., Peebles P. J. E., 1988, Phys. Rev. D, 37, 3406

Readhead A. C. S., Mason B. S., Contaldi C. R., et al. 2004, ApJ, 609, 498

Refregier A., 2003a, MNRAS, 338, 35

Refregier A., 2003b, ARA&A, 41, 645

Refregier A., Amara A., Kitching T. D., Rassat A., Scaramella R., Weller J., Euclid
   Imaging Consortium f. t., 2010, ArXiv e-prints

Refsdal S., 1964a, MNRAS, 128, 307

Refsdal S., 1964b, MNRAS, 128, 295

Refsdal S., 1966a, MNRAS, 134, 315

Refsdal S., 1966b, MNRAS, 132, 101

Refsdal S., Surdej J., 1994, Reports of Progress in Physics, 57, 117

Rhodes J. D., Massey R. J., Albert J., Collins N., Ellis R. S., Heymans C., Gardner
   J. P., Kneib J., Koekemoer A., Leauthaud A., Mellier Y., Refregier A., Taylor
   J. E., Van Waerbeke L., 2007, ApJS, 172, 203

Riess A. G., Filippenko A. V., Challis P., et al. 1998, AJ, 116, 1009

Riess A. G., Macri L., Casertano S., Sosey M., Lampeitl H., Ferguson H. C., Filip-
   penko A. V., Jha S. W., Li W., Chornock R., Sarkar D., 2009, ApJ, 699, 539

Riess A. G., Press W. H., Kirshner R. P., 1995, ApJ, 438, L17

Riess A. G., Press W. H., Kirshner R. P., 1996, ApJ, 473, 88

Riess A. G., Strolger L., Casertano S., et al. 2007, ApJ, 659, 98

Rimes C. D., Hamilton A. J. S., 2005, MNRAS, 360, L82

Rimes C. D., Hamilton A. J. S., 2006, MNRAS, 371, 1205

Robertson D. S., Carter W. E., Dillinger W. H., 1991, Nature, 349, 768

Romanowsky A. J., Napolitano N. R., Capaccioli M., Douglas N. G., Merrifield
   M. R., Kuijken K., Gerhard O., Arnaboldi M., Freeman K. C., 2004, American
   Astronomical Society Meeting Abstracts, 205,

Rubin V. C., Ford W. K. J., 1970, ApJ, 159, 379

Sachs R., 1961, Royal Society of London Proceedings Series A, 264, 309

Sachs R. K., Wolfe A. M., 1967, ApJ, 147, 73

Salucci P., Burkert A., 2000, ApJ, 537, L9

Sandage A., 1962, ApJ, 136, 319

Sarazin C. L., 1986, Reviews of Modern Physics, 58, 1

Sato M., Hamana T., Takahashi R., Takada M., Yoshida N., Matsubara T., Sugiyama N., 2009, ApJ, 701, 945

Schaeffer R., Silk J., 1988, ApJ, 332, 1

Schmidt M., 1963, Nature, 197, 1040

Schneider P., 2006, in Meylan G., Jetzer P., North P., Schneider P., Kochanek C. S., Wambsganss J., eds, Saas-Fee Advanced Course 33: Gravitational Lensing: Strong, Weak and Micro Part 3: Weak gravitational lensing. pp 269–451

Schneider P., Ehlers J., Falco E. E., 1992, Gravitational Lenses. Gravitational Lenses, XIV, 560 pp. 112 figs.. Springer-Verlag Berlin Heidelberg New York. Also Astronomy and Astrophysics Library

Schrabback T., Hartlap J., Joachimi B., et al. 2010, A&A, 516, A63+

Schwarzschild M., 1954, AJ, 59, 273

Seitz C., Schneider P., 1997, A&A, 318, 687

Seljak U., Makarov A., Mandelbaum R., Hirata C. M., Padmanabhan N., McDonald P., Blanton M. R., Tegmark M., Bahcall N. A., Brinkmann J., 2005, Phys. Rev. D, 71, 043511

Semboloni E., Hoekstra H., Schaye J., van Daalen M. P., McCarthy I. G., 2011, ArXiv e-prints

Semboloni E., Schrabback T., van Waerbeke L., Vafaei S., Hartlap J., Hilbert S., 2011, MNRAS, 410, 143

Semboloni E., van Waerbeke L., Heymans C., Hamana T., Colombi S., White M., Mellier Y., 2007, MNRAS, 375, L6

Sikivie P., 2011, Physics Letters B, 695, 22

Silk J., Szalay A. S., Zeldovich Y. B., 1983, Scientific American, 249, 72

Slipher V. M., 1917, Proceedings of the American Philosophical Society, 56, 403

Slosar A., 2010, ArXiv e-prints

Smith R. E., Peacock J. A., Jenkins A., White S. D. M., Frenk C. S., Pearce F. R., Thomas P. A., Efstathiou G., Couchman H. M. P., 2003, MNRAS, 341, 1311

Smoot G. F., Bennett C. L., Kogut A., et al. 1992, ApJ, 396, L1

Sofue Y., Rubin V., 2001, ARA&A, 39, 137

Sommer-Larsen J., Dolgov A., 2001, ApJ, 551, 608

Soucail G., Mellier Y., Fort B., Mathez G., Cailloux M., 1987, The Messenger, 50, 5

Splinter R. J., Melott A. L., Linn A. M., Buck C., Tinker J., 1997, ApJ, 479, 632

Springel V., 2005, MNRAS, 364, 1105

Springel V., White S. D. M., Jenkins e., 2005, Nature, 435, 629

Springel V., Yoshida N., White S. D. M., 2001, New Astronomy, 6, 79

Strumia A., 2010, Journal of High Energy Physics, 6, 36

Szapudi I., 2005, astro-ph/0505391

Takada M., Jain B., 2009, MNRAS, 395, 2065

Takahashi R., Yoshida N., Takada M., Matsubara T., Sugiyama N., Kayo I., Nishimichi T., Saito S., Taruya A., 2011, ApJ, 726, 7

Takahashi R., Yoshida N., Takada M., Matsubara T., Sugiyama N., Kayo I., Nishizawa A. J., Nishimichi T., Saito S., Taruya A., 2009, ApJ, 700, 479

Taylor A. N., 2001, ArXiv Astrophysics e-prints

Tegmark M., Taylor A. N., Heavens A. F., 1997, ApJ, 480, 22

Tereno I., Schimd C., Uzan J., Kilbinger M., Vincent F. H., Fu L., 2009, A&A, 500, 657

Teyssier R., Pires S., Prunet S., Aubert D., Pichon C., Amara A., Benabed K., Colombi S., Refregier A., Starck J., 2009, A&A, 497, 335

The Dark Energy Survey Collaboration 2005, ArXiv Astrophysics e-prints

The Planck Collaboration 2006, ArXiv Astrophysics e-prints

Thomas S. A., Abdalla F. B., Lahav O., 2010, Physical Review Letters, 105, 031301

Tikhonov A. V., Gottlöber S., Yepes G., Hoffman Y., 2009, MNRAS, 399, 1611

Tyson J. A., Wenk R. A., Valdes F., 1990, ApJ, 349, L1

Vafaei S., Lu T., van Waerbeke L., Semboloni E., Heymans C., Pen U., 2010, Astroparticle Physics, 32, 340

Vale C., White M., 2003, ApJ, 592, 699

van Daalen M. P., Schaye J., Booth C. M., Dalla Vecchia C., 2011, ArXiv e-prints

Van Waerbeke L., Mellier Y., Erben T., Cuillandre J. C., Bernardeau F., Maoli R., Bertin E., Mc Cracken H. J., Le Fèvre O., Fort B., Dantel-Fort M., Jain B., Schneider P., 2000, A&A, 358, 30

Wagoner R. V., Fowler W. A., Hoyle F., 1967, ApJ, 148, 3

Walker T. P., Steigman G., Kang H.-S., Schramm D. M., Olive K. A., 1991, ApJ, 376, 51

Walsh D., Carswell R. F., Weymann R. J., 1979, Nature, 279, 381

Wambsganss J., Cen R., Ostriker J. P., 1998, ApJ, 494, 29

Wang Y., 2008, Phys. Rev. D, 77, 123525

Warren S. J., Hewett P. C., Lewis G. F., Moller P., Iovino A., Shaver P. A., 1996, MNRAS, 278, 139

Weinberg S., 1972, Gravitation and Cosmology: Principles and Applications of the General Theory of Relativity

Weinberg S., 1989, Reviews of Modern Physics, 61, 1

White M., Hu W., 1997, A&A, 321, 8

White M., Hu W., 2000, ApJ, 537, 1

White S. D. M., 1976, MNRAS, 177, 717

White S. D. M., 1994, arXiv:astro-ph/9410043

White S. D. M., Frenk C. S., 1991, ApJ, 379, 52

White S. D. M., Frenk C. S., Davis M., 1983, ApJ, 274, L1

Wiersma R. P. C., Schaye J., Smith B. D., 2009, MNRAS, 393, 99

Willis J. P., Hewett P. C., Warren S. J., 2005, MNRAS, 363, 1369

Wittman D., 2002, LNP Vol. 608: Gravitational Lensing: An Astrophysical Tool, 608, 55

Wittman D. M., Tyson J. A., Kirkman D., Dell'Antonio I., Bernstein G., 2000, Nature, 405, 143

Wood-Vasey W. M., Miknaitis G., Stubbs C. W., et al. 2007, ApJ, 666, 694

Woosley S. E., Heger A., Weaver T. A., 2002, Reviews of Modern Physics, 74, 1015

Xu G., 1995, ApJS, 98, 355

Yoshisato A., Morikawa M., Gouda N., Mouri H., 2006, ApJ, 637, 555

Zel'dovich Y. B., 1964, Soviet Astronomy, 8, 13

Zel'Dovich Y. B., 1970a, Astrophysics, 6, 164

Zel'Dovich Y. B., 1970b, A&A, 5, 84

Zheng Z., Zehavi I., Eisenstein D. J., Weinberg D. H., Jing Y. P., 2009, ApJ, 707, 554

Zwicky F., 1933, Helvetica Physica Acta, 6, 110

Zwicky F., 1937a, Physical Review, 51, 290

Zwicky F., 1937b, Physical Review, 51, 679

Zwicky F., 1938, PASP, 50, 218

Zwicky F., 1957, Morphological astronomy. Berlin: Springer, 1957

Zwicky F., Herzog E., Wild P., 1961, in CGCG1 "Catalogue of Galaxies and of Clusters of Galaxies", 1961, Volume i Pasadena: California Institute of Technology. pp 0–+

Appendix A

Deriving the Deflection Angle $\hat{\alpha}$

The deflection angle $\hat{\alpha}$ of a point source is a fundamental quantity in the gravitational lensing equations. The following shows a derivation expanded from notes by Andy Taylor for the deflection angle.

Starting with the relativistic line element: a line element describes the relationship between one co-ordinate system and another. The relationship can be found using Pythagoras' theorem and Figure A.1 shows how we determine this line element in Minkowski space, which is

$$c^2 d\tau^2 = c^2 dt^2 + dr^2, \tag{A.1}$$

where $d\tau$ is the *proper* time, which is the time experienced by an observer moving through the Universe, and dt is the *co-ordinate* time, which is the time experienced by observers in an inertial frame and dr is the comoving distance.

It is also possible to generalise to a relativistic line element in a static, spatially flat, Minkowski Universe with small Newtonian potential variations, $\tilde{\Phi}$, which is given by

$$c^2 d\tau^2 = g_{\nu\mu} dx^\nu dx^\mu = (1 + 2\tilde{\Phi})c^2 dt^2 - (1 - 2\tilde{\Phi}) \delta^K_{ij} dr^i dr^j, \tag{A.2}$$

where $\tilde{\Phi} = \Phi/c^2$ and $x^\mu = (ct, x, y, z)$.

The *relativistic equation of motion* is the geodesic equation that describes the motion of an object through curved space;

$$a^\mu = u^\mu_{;\nu} u^\nu = \dot{u}^\mu + \Gamma^\mu_{\nu\lambda} u^\nu u^\lambda = 0, \tag{A.3}$$

where a^μ is the 4-acceleration, $u^\mu = (c, u^i)$ is the 4-velocity, u^i is the 3D velocity and

$$\cdot \equiv \frac{d}{dp}, \tag{A.4}$$

where p is an affine parameter. For a massive particle $p = \tau$ and for a massless
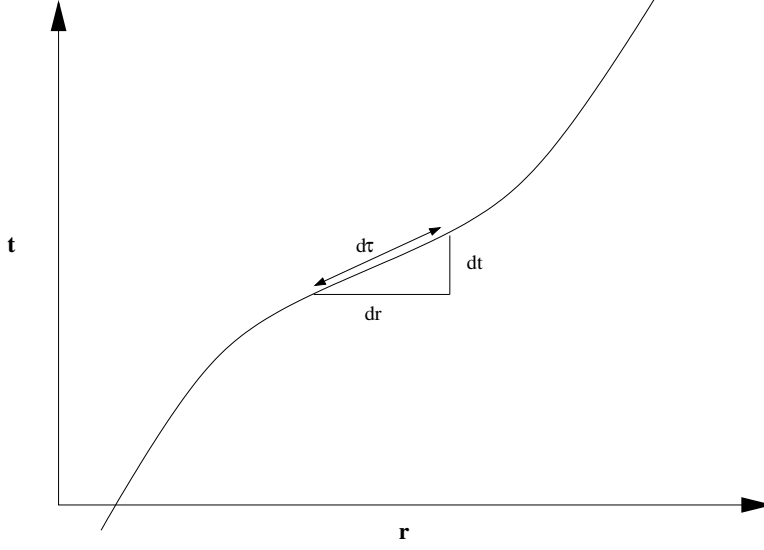
Figure A.1: Determination of a line element. $d\tau$ is the time experienced by an observer moving through the Universe. This is the proper time. dt is the co-ordinate time, the time experienced by observers in comoving co-ordinates and in freefall.

particle $p = t$. Finally,

$$\Gamma^{\mu}_{\nu\lambda} = \frac{1}{2}g^{\mu\eta}\left(g_{\nu\eta,\lambda} + g_{\lambda\eta,\nu} - g_{\nu\lambda,\eta}\right) \tag{A.5}$$

is the Christoffel connection matrix where

$$g_{\mu\nu} = \begin{bmatrix} (1+2\tilde{\Phi}) & 0 & 0 & 0 \\ 0 & -(1-2\tilde{\Phi}) & 0 & 0 \\ 0 & 0 & -(1-2\tilde{\Phi}) & 0 \\ 0 & 0 & 0 & -(1-2\tilde{\Phi}) \end{bmatrix} \tag{A.6}$$

is a metric tensor defined in a perturbed universe.

Substituting the Christoffel matrix into the equation of motion gives

$$0 = \dot{u}^{\mu} + \Gamma^{\mu}_{\nu\lambda}u^{\nu}u^{\lambda} \tag{A.7}$$

$$\Rightarrow \dot{u}^{\mu} = -\Gamma^{\mu}_{\nu\lambda}u^{\nu}u^{\lambda} \tag{A.8}$$

$$= -\frac{1}{2}g^{\mu\eta}\left(g_{\nu\eta,\lambda} + g_{\lambda\eta,\nu} - g_{\nu\lambda,\eta}\right)u^{\nu}u^{\lambda} \tag{A.9}$$

$$= \left(-g^{\mu\eta}g_{\nu\eta,\lambda} + \frac{1}{2}g^{\mu\eta}g_{\nu\lambda,\eta}\right)u^{\nu}u^{\lambda}, \tag{A.10}$$

since $g^{\mu\eta}g_{\nu\eta,\lambda} = g^{\mu\eta}g_{\lambda\eta,\nu}$. So

$$\Rightarrow \dot{u}^\mu = -g^{\mu\eta}\left(g_{\nu\eta,\lambda} - \frac{1}{2}g_{\nu\lambda,\eta}\right)u^\nu u^\lambda. \tag{A.11}$$

Expanding the metric, but keeping all the terms in u^i, first let $\mu = (0, i)$ and $\eta = (0, j)$. All of the cross terms are ignored under the assumption that there is no vortical frame dragging (Lens-Thirring) effects and the $\mu = 0$ and $\eta = 0$ terms are also ignored because only the 3-velocity acceleration is of interest:

$$\dot{u}^i = -g^{ij}\left(g_{\nu j,\lambda} - \frac{1}{2}g_{\nu\lambda,j}\right)u^\nu u^\lambda. \tag{A.12}$$

Now sum over $\nu = (0, k)$

$$\dot{u}^i = -g^{ij}\left(\cancel{g_{0j,\lambda}} - \frac{1}{2}g_{0\lambda,j}\right)\cancel{u^0}u^\lambda - g^{i,j}\left(g_{kj,\lambda} - \frac{1}{2}g_{k\lambda,j}\right)u^k u^\lambda, \tag{A.13}$$

since $g_{0j,\lambda}$ is a cross-term and $u^0 = 1$. Finally, sum over $\lambda = (0, m)$

$$\dot{u}^i = -g^{ij}\left(-\frac{1}{2}g_{00,j}\right)\cancel{u^0} - g^{ij}\left(\cancel{-\frac{1}{2}g_{0m,j}}\right)u^m$$
$$-g^{ij}\left(g_{kj,0} - \frac{1}{2}\cancel{g_{k0,j}}\right)u^k\cancel{u^0} - g^{ij}\left(g_{kj,m} - \frac{1}{2}g_{km,j}\right)u^k u^m \tag{A.14}$$

$$\Rightarrow \dot{u}^i = -g^{ij}\left[-\frac{1}{2}g_{00,j} + g_{kj,0}u^k + \left(g_{kj,m} - \frac{1}{2}g_{km,j}\right)u^k u^m\right] \tag{A.15}$$

$$\dot{u}^i = g^{ij}\left[\frac{1}{2}g_{00,j} - g_{kj,0}u^k - \left(g_{kj,m} - \frac{1}{2}g_{km,j}\right)u^k u^m\right]. \tag{A.16}$$

The first term in Equation (A.16), $\frac{1}{2}g_{00,j}$, relates to Newtonian gravity while the second term, $g_{kj,0}u^k$ relates to the Integrated Sachs Wolfe (ISW) effect. ISW is caused by gravitational redshift between the surface of last scattering and the Earth. The gravitational redshifting causes the potential wells to decay, allowing photons to escape easier.

The components of the metric

$$g_{00} = (1 + 2\tilde{\Phi}) \tag{A.17}$$
$$g_{ij} = -(1 - 2\tilde{\Phi})\delta^K_{ij}, \tag{A.18}$$

and the component $g^{ij} = -(g_{ij})^{-1} = (1 - 2\tilde{\Phi})\delta^{ij}_K$ can be plugged into the equation

of motion. Remembering that $A_{i,j} = \frac{\partial}{\partial x_j} A_i$ and $A_{i,0} = \frac{1}{c} \frac{\partial}{\partial t} A_i$,

$$g_{00,j} = 2\tilde{\Phi}_{,j} = 2\nabla_j \tilde{\Phi}, \tag{A.19}$$

$$g_{kj,0} = (2\tilde{\Phi}\, \delta^K_{kj})_{,0} = 2\dot{\tilde{\Phi}}\, \delta^K_{kj}, \tag{A.20}$$

$$g_{kj,m} = 2\nabla_m \tilde{\Phi}\, \delta^K_{kj}, \tag{A.21}$$

$$g_{km,j} = 2\nabla_j \tilde{\Phi}\, \delta^K_{km}, \tag{A.22}$$

which gives

$$\dot{u}^i = -(1 - 2\tilde{\Phi})\, \delta^{ij}_K \left[\nabla_j \tilde{\Phi} c^2 - 2\dot{\tilde{\Phi}} c\, \delta^K_{kj} u^k - (2\nabla_m \tilde{\Phi}\, \delta^K_{kj} - \nabla_j \tilde{\Phi}\, \delta^K_{km}) u^k u^m \right]. \tag{A.23}$$

The $2\tilde{\Phi}$ in the first term is ignored because it will give $\tilde{\Phi}^2$ terms when multiplied through the bracket and we are only interested in the first order $\tilde{\Phi}$ terms. So,

$$\begin{aligned}
\dot{u}^i &= -\left[\nabla_j \delta^{ij}_K \tilde{\Phi} c^2 - 2\dot{\tilde{\Phi}} c\, \delta^K_{kj} \delta^{ij}_K u^k - 2\nabla_m \tilde{\Phi}\, \delta^K_{kj} \delta^{ij}_K u^k u^m \right. \\
&\qquad \left. + \nabla_j \tilde{\Phi}\, \delta^K_{km} \delta^{ij}_K u^k u^m \right] \tag{A.24} \\
&= -\left[\nabla^i \tilde{\Phi} c^2 - 2\dot{\tilde{\Phi}} c u^i - 2\nabla_m \tilde{\Phi} u^i u^m + \nabla^i \tilde{\Phi} u^k u_k \right] \tag{A.25} \\
&= -\left[\nabla^i \tilde{\Phi}(c^2 + u^k u_k) - 2\nabla_m \tilde{\Phi} u^i u^m - 2\dot{\tilde{\Phi}} c u^i \right]. \tag{A.26}
\end{aligned}$$

Given that we are only interested in the spatial parts, $u^k = u_k$, we find

$$\dot{u}^i = -\left[\nabla^i \tilde{\Phi}(c^2 + u^2) - 2\nabla_m \tilde{\Phi} u^i u^m - 2\dot{\tilde{\Phi}} c u^i \right]. \tag{A.27}$$

When $u_i \ll c$, the velocities are slow so the time derivative $\dot{\tilde{\Phi}}$ and the terms of order $(O(u^2))$ are ignored, which leaves the **Newtonian equation of motion**,

$$\dot{u}_i = -\nabla_i \Phi. \tag{A.28}$$

This slow motion limit equation can be traced back to the $\frac{1}{2} g_{00,j}$ term in the equation of motion.

On the other hand, there is the ultra-relativistic limit where $u_i \to c n_i$, where n_i is the unit photon direction vector with $|\boldsymbol{n}| = 1$. Rewriting the equation of motion,

$$\begin{aligned}
\dot{u}^i &= -\left[\nabla^i \tilde{\Phi}(c^2 + u^2) - 2\nabla_m \tilde{\Phi} u^i u^m - 2\dot{\tilde{\Phi}} c u^i \right] \tag{A.29} \\
&= -\left\{ \left[(c^2 + u^2)\, \delta^K_{mi} - 2u^i u^m \right] \nabla_m \tilde{\Phi} - 2\dot{\tilde{\Phi}} c u^i \right\}, \tag{A.30}
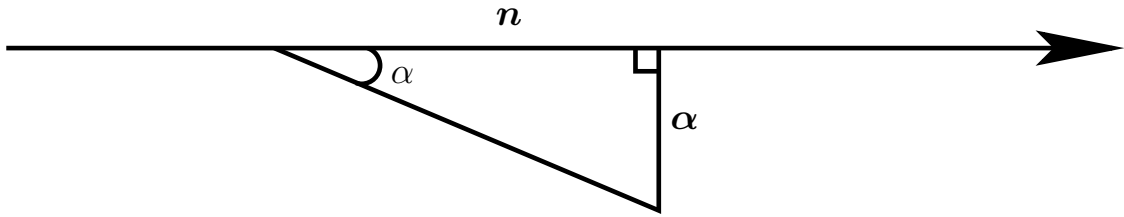\end{aligned}$$

Figure A.2: Figure showing how the deflection angle α relates to the unit photon vector n.

we can determine the relativistic acceleration equation where $u_i \rightarrow c n_i$,

$$c \dot{n}_i = - \left\{ \left[(1 + |\boldsymbol{n}|)c^2 \, \delta_{mi}^K - 2c^2 n_i n_m \right] \nabla_m \tilde{\Phi} - 2\dot{\tilde{\Phi}} c n_i \right\}. \tag{A.31}$$

The final term in this equation is proportional to the rate of change of the curvature metric perturbation and is parallel to the photon motion. Therefore it does not have any effect on the acceleration because a photon can not travel faster than the speed of light. Thus, only acceleration that is perpendicular to the motion of the photon is allowed. So

$$\dot{n}_i = -2(\delta_{mi}^K - n_i n_m) \frac{\nabla_m \Phi}{c} = -\frac{2}{c} \nabla_i^\perp \Phi, \tag{A.32}$$

where

$$\nabla_i^\perp = (\delta_{mi}^K - n_i n_m) \nabla_m. \tag{A.33}$$

The ultra-relativistic case has two effects that differ from the Newtonian equation of motion. The first is the factor of 2 in front of the potential gradient. This can be traced back to the spatial curvature terms proportional to u^2. This means that the ultra-relativistic particles feel an extra force due to the curvature of space which is not felt by the slow moving particles. This is analogous to rapidly moving charged particles in an electromagnetic field feeling both electric and magnetic forces while slow moving particles only feel the electric force. The second effect is that the force along the particle trajectory is canceled out by the spatial curvature term, with the parallel force proportional to $(1 - u^2)$, so only a transverse deflection is felt by the particle. This makes sense in the limit $u = c$ as a particle moving at the speed of light cannot be accelerated faster. These two effects combine so that for a particle approaching the speed of light, the force felt in the direction of propagation vanishes while the transverse force is doubled.

So, in the small-angle approximation, the deflection of $\boldsymbol{n}$, known as $\boldsymbol{\alpha}$, is equal to the deflection angle (see Figure A.2)

$$\boldsymbol{n} = |\boldsymbol{\alpha}| = \alpha. \tag{A.34}$$

$-\infty$ ∞

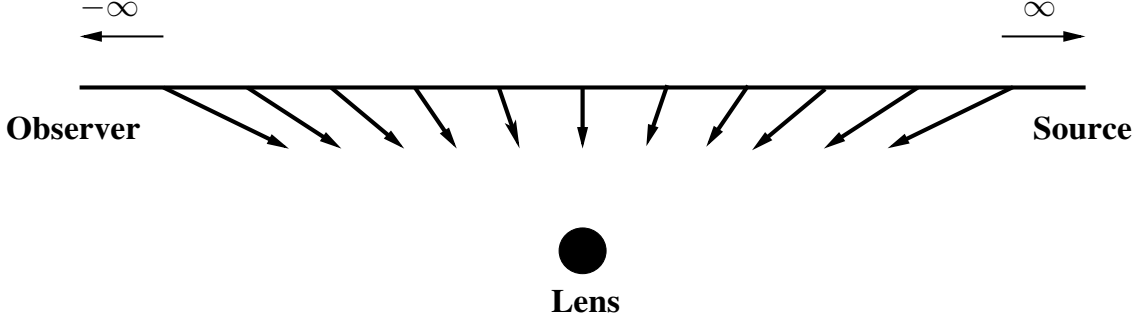**Observer**   **Source**

Lens

Figure A.3: The deflection angle can be approximated by integrating the deflection over the entire z direction.

Solving for the acceleration $\dot{\boldsymbol{n}}$ by integrating, we get

$$\hat{\boldsymbol{\alpha}} = 2c \int dt \nabla_\perp \tilde{\Phi}. \tag{A.35}$$

The Newtonian potential for a point mass is

$$\tilde{\Phi} = -\frac{GM}{c^2 r}, \tag{A.36}$$

where $r = \sqrt{D_L^2 \theta^2 + z^2}$ is the distance from the point, z is the distance along the line of sight from the lens, D_L is the angular diameter distance from the observer to the lens and θ is the angle on the sky seen by the observer.

For photons, the distance traveled is $z = ct$ and the transverse gradient for a circularly symmetric lens is

$$\nabla_\perp = \hat{\boldsymbol{\theta}} \frac{1}{D_L} \frac{\partial}{\partial \theta}, \tag{A.37}$$

so the deflection angle can be written as

$$\hat{\boldsymbol{\alpha}} = 2 \int_{-\infty}^{\infty} -dt \hat{\boldsymbol{\theta}} \frac{1}{D_L} \frac{\partial}{\partial \theta} \frac{GM}{r} \tag{A.38}$$

and for an integral over z, $dz = c\, dt + t\, dc$,

$$\hat{\boldsymbol{\alpha}} = -\hat{\boldsymbol{\theta}} \frac{2}{cD_L} \int_{-\infty}^{\infty} dz \frac{\partial}{\partial \theta} \frac{GM}{r}, \tag{A.39}$$

where we have assumed that the integration from the source to the observer can be approximated by an integration over the entire z direction (see Figure A.3). To

solve this integral, first differentiate inside the integral

$$\frac{\partial}{\partial\theta}\left(-\frac{GM}{c^2 r}\right) = \frac{\partial}{\partial r}\left(-\frac{GM}{c^2 r}\right)\frac{\partial r}{\partial\theta}, \tag{A.40}$$

where

$$\frac{\partial}{\partial r}\left(-\frac{GM}{c^2 r}\right) = \frac{GM}{c^2 r^2}, \tag{A.41}$$

and

$$\begin{aligned}
\frac{\partial r}{\partial\theta} &= \frac{\partial}{\partial\theta}\left(\sqrt{D_L^2\theta^2 + z^2}\right) \tag{A.42} \\
&= \frac{1}{2}\left(D_L^2\theta^2 + z^2\right)^{1/2} 2D_L^2\theta \tag{A.43} \\
&= r^{-1}D_L^2\theta. \tag{A.44}
\end{aligned}$$

So

$$\frac{\partial}{\partial\theta}\left(-\frac{GM}{c^2 r}\right) = \frac{GM}{c^2 r^3}D_L^2\theta. \tag{A.45}$$

Then, integrating along z,

$$\begin{aligned}
\int_{-\infty}^{\infty} dz\frac{1}{(D_L^2\theta^2 + z^2)^{-3/2}} &= \left[\frac{2z}{D_L^2\theta^2\sqrt{D_L^2\theta^2 + z^2}}\right]_0^{\infty} \tag{A.46} \\
&= \frac{2}{D_L^2\theta^2}. \tag{A.47}
\end{aligned}$$

Putting Equations (A.45) and (A.47) back into Equation (A.38), the equation for the deflection angle becomes

$$\begin{aligned}
\hat{\boldsymbol{\alpha}} &= \hat{\boldsymbol{\theta}}\frac{2\cancel{c}}{c^2 D_L}\frac{2}{\cancel{D_L^2}\theta\cancel{c}}GM\cancel{D_L^2}\cancel{\theta} \tag{A.48} \\
&= \frac{4GM}{c^2 D_L\theta}\hat{\boldsymbol{\theta}}, \tag{A.49}
\end{aligned}$$

which is the deflection angle of a point source.

Appendix B

Detailed Instructions on Installing the GADGET2 Simulation Package

The cosmological simulation package GADGET2 requires a number of libraries to run and is non-trivial to install. The following instructions are correct for the libraries that I have listed and the Intel compiler suite. It is possible that there are newer versions of the libraries available that could also be used, but no guarantee is made on whether these instructions will work for different packages or different compilers. These instructions should work on both Linux machines and Macs.

These instructions assume that none of the libraries are available on the system, which may not be true. However, even when libraries are available, they may not have been compiled to include all of the options required for GADGET2. The easiest way to get things running quickly is to install everything yourself.

This guide is incredibly verbose, which I feel is necessary to ensure total clarity. After originally writing these notes in 2008, they have continued to be useful to me on many different machines and have been used by other people all over the world. This experience has taught me that the more detail in the instructions, the higher the success rate on installation. The guide starts by installing each of the libraries required for GADGET2 before installing GADGET2 itself. Follow the instructions in the order that they are written as the later packages sometimes have dependencies on the earlier packages.

Note: `Instructions in this font indicate text to be entered in a file` `or when preceded by '>', are command line arguments.`

B.1   OpenMPI-1.3.2

OpenMPI is a Message Passing Interface (MPI) that enables parallel computing.

Step 1:   Download OpenMPI-1.3.2 from:
            http://www.open-mpi.org/software/ompi/v1.3/
            Click on the openmpi-1.3.2.tar.gz link.

Step 2:   Put the tarball in the desired directory

Step 3:   Untar the tarball
            `> tar -xzvf openmpi-1.3.2.tar.gz`
            This creates a directory called openmpi-1.3.2

Step 4:   Move into the source directory and set the compiler variables.
            `> setenv FC ifort`
            `> setenv F90 ifort`
            `> setenv F77 ifort`
            `> setenv CC icc`
            `> setenv CXX icpc`

Step 5:   Configure OpenMPI
            `> ./configure --prefix='pwd'`
            This configures the package to run from the source directory. Note
            the two different apostrophes around '`pwd`'.

Step 6:   After configuring, compile the source
            `> make`

Step 7:   Check the compilation and install the libraries
            `> make check`
            `> make install`
            The check should return no errors and the install should put the
            directories /bin, /include and /lib in the openmpi-1.3.2 directory.

Step 8:   If you have another MPI installed on your system, set this latest
            version to be your executable in your path
            `> emacs  /.cshrc`
            or `.tcshrc`, depending on your default shell.
            In this file,
            `> set path = (./  /bin $path /path/to/openmpi-1.3.2/bin)`
            Save and close the file.
            `> source  /.cshrc`

Check that the correct MPI is being used
```
> which mpicc
```
This should return the directory that you just installed.

Now OpenMPI should be installed and should execute mpirun and mpicc from any directory.

B.2   FFTW-2.1.5

The Fastest Fourier Transform in the West, FFTW, is a fast Fourier transform code. It is essential that you install FFTW-2 as FFTW-3 does not currently support parallel processing.

Step 1:   Download FFTW-2.1.5 from
              http://www.fftw.org/download.html
              Click on the file fftw-2.1.5.tar.gz

Step 2:   Put the tarball in the desired directory

Step 3:   Untar the tarball
```
> tar -xzvf fftw.2.1.5.tar.gz
```
              This creates a directory called fftw-2.1.5

Step 4:   Move into the source directory and set the compiler variables.
```
> setenv FC 'ifort -nus'
> setenv F90 'ifort -nus'
> setenv F77 'ifort -nus'
> setenv CC icc
> setenv CXX icpc
```

Step 5:   Configure FFTW
```
> ./configure --prefix='pwd' --enable-MPI
    --enable-type-prefix
```

Step 6:   After configuring, compile the source
```
> make
```

Step 7:   Check the compilation and install the libraries
```
> make check
> make install
```

Step 8:   Compile the other FFTW libraries
```
> make clean
```

```
> ./configure --prefix=`pwd' --enable-mpi
    --enable-type-prefix --enable-float
> make
> make check
> make install
> make clean
```

Now FFTW-2.1.5 should be installed with libraries in this directory in /bin, include and /lib.

B.3   GSL-1.9

The GNU Scientific Library, GSL, is a set of numerical libraries.

Step 1:   Download gsl-1.9 from
ftp://www.mirrorservice.org/sites/ftp.gnu.org/gnu/gsl
Click on the file gsl-1.9.tar.gz

Step 2:   Put the tarball in the desired directory

Step 3:   Untar the tarball
```
> tar -xzvf gsl-1.9.tar.gz
```
This creates a directory called gsl-1.9

Step 4:   Move into the source directory and set the compiler variables.
```
> setenv FC 'ifort -nus'
> setenv F90 'ifort -nus'
> setenv F77 'ifort -nus'
> setenv CC icc
> setenv CXX icpc
> setenv CFLAGS '-O2 -m64 -mieee-fp -Wpointer-arith
-fno-strict-aliasing'
```

Step 5:   Configure GSL
```
> ./configure --prefix=`pwd'
```

Step 6:   After configuring, compile the source
```
> make
```

Step 7:   Check the compilation and install the libraries
```
> make check
```

```
> make install
```

The libraries are found in /bin, /include and /lib in this directory.

B.4 HDF5-1.6.9

HDF5 is a file format for storing and managing data. It can be useful when reading GADGET2 files in IDL.

Step 1: Download hdf5-1.6.9 from
http://www.hdfgroup.org/ftp/HDF5/current16/src/
Click on the file hdf5-1.6.9.tar.gz

Step 2: Put the tarball in the desired directory

Step 3: Untar the tarball
```
> tar -xzvf hdf5-1.6.9.tar.gz
```
This creates a directory called hdf5-1.6.9

Step 4: Move into the source directory and set the compiler variables.
```
> setenv FC 'ifort -nus'
> setenv F90 'ifort -nus'
> setenv F77 'ifort -nus'
> setenv CC icc
> setenv CXX icpc
```

Step 5: Configure HDF5
```
> ./configure --prefix='pwd' --enable-fortran
    --enable-cxx
```

Step 6: After configuring, compile the source
```
> make
```

Step 7: Check the compilation and install the libraries
```
> make check
> make install
```

The libraries can now be found in /bin, /include, and /lib in this directory.

B.5   GADGET2

Now that all of the libraries are installed, GADGET2 can be installed.

Step 1: Download GADGET2 from
http://www.mpa-garching.mpg.de/gadget
Click on the file gadget-2.0.3.tar.gz

Step 2: Put the tarball in the desired directory

Step 3: Untar the tarball
```
> tar -xzvf gadget-2.0.3.tar.gz
```
This creates a directory called Gadget-2.0.3

Step 4: Move into the directory ./Gadget-2.0.3/Gadget2/ and open the Makefile in a text editor like emacs
```
> emacs Makefile &
```
Edit Line 22
```
-DPMGRID = 512
```

Step 5: Edit the Makefile to the correct values for your setup.
Line 82 `cc = mpicc`
Line 83 `#OPTIMIZE = -O2 -Wall -g` (comment out)
Line 84 `#MPICHLIB = -lmpich` (comment out)

Create a SYSTYPE on Line 89
```
SYSTYPE = 'NewSystype'
```

Now add your own SYSTYPE on starting at Line 102, before SYSTYPE='MPA'
```
ifeq($(SYSTYPE),'NewSystype')
CC = mpicc
OPTIMIZE = -O3 -Wall -g
GSL_INCL = -I/path/to/gsl-1.9/include
GSL_LIBS = -L/path/to/gsl-1.9/lib
FFTW_INCL = -I/path/to/fftw-2.1.5/include
FFTW_LIBS = -L/path/to/fftw-2.1.5/lib
MPI_INCL = -I/path/to/openmpi-1.3.2/include
MPICHLIB = -L/path/to/openmpi-1.3.2/lib
HDF5INCL = -I/path/to/hdf5-1.6.9/include
HDF5LIB = -L/path/to/hdf5-1.6.9/lib -lhdf5 -lz
endif
```

Save the Makefile

Step 6: Compile the source code
> make
This will create an executable in the Gadget2 directory.

Step 7: Create an executable to generate a glass pre-initial particle distribution. In the Makefile, uncomment
Line 71 `OPT += -DMAKEGLASS = 262144`
This will create a 64^3 particle glass. Change the name of the executable
Line 225 `EXEC = Gadget2_glass`

Step 8: Compile the 'glass' Gadget
> make
This will create an executable called Gadget2_glass in this directory.

Now GADGET2 is installed on your system and ready to use.

Appendix C

Publications

The following papers are all a result of work completed as part of this PhD.

Simulating the Effect of Non-Linear Mode-Coupling in Cosmological Parameter Estimation,
A. Kiessling, A. N. Taylor, A. F. Heavens, 2011, *MNRAS, Accepted*, arXiv:1103.3245

SUNGLASS: A New Weak Lensing Simulation Pipeline,
A. Kiessling, A. F. Heavens, A. N. Taylor, B. Joachimi, 2011, *MNRAS*, 414, 2235

Stochastic Bias Measurement in COSMOS with Weak Lensing,
E. Jullo, J. Rhodes, **A. Kiessling**, J. Berge, R. Massey, J. Taylor, N. Scoville, 2011, *ApJ, submitted*

Gravitational Lensing Accuracy Testing 2010 (GREAT10) Challenge Handbook,
T. Kitching, A. Amara, M. Gill, S. Harmeling, C. Heymans, R. Massey, B. Rowe, T. Schrabback, L. Voigt, S. Balan, G. Bernstein, M. Bethge, S. Bridle, F. Courbin, M. Gentile, A. Heavens, M. Hirsch, R. Hosseini, **A. Kiessling**, D. Kirk, K. Kuijken, R. Mandelbaum, B. Moghaddam, G. Nurbaeva, S. Paulin-Henriksson, A. Rassat, J. Rhodes, B. Schölkopf, J. Shawe-Taylor, M. Shmakova, A. Taylor, M. Velander, L. van Waerbeke, D. Witherick, D. Wittman, 2011, *Annals of Applied Statistics, Submitted*, arXiv:1009.0779

Cosmological Information in Gaussianised Weak Lensing Signals,
B. Joachimi, A. N. Taylor, **A. Kiessling**, 2011, *MNRAS, submitted*